EUROPEAN ORGANIZATION FOR NUCLEAR RESEARCH

PS213
The n_TOF Collaboration

CERN/INTC-O-011
INTC-2002-037
CERN-SL-2002-053 ECT

CERN n_TOF Facility: Performance Report

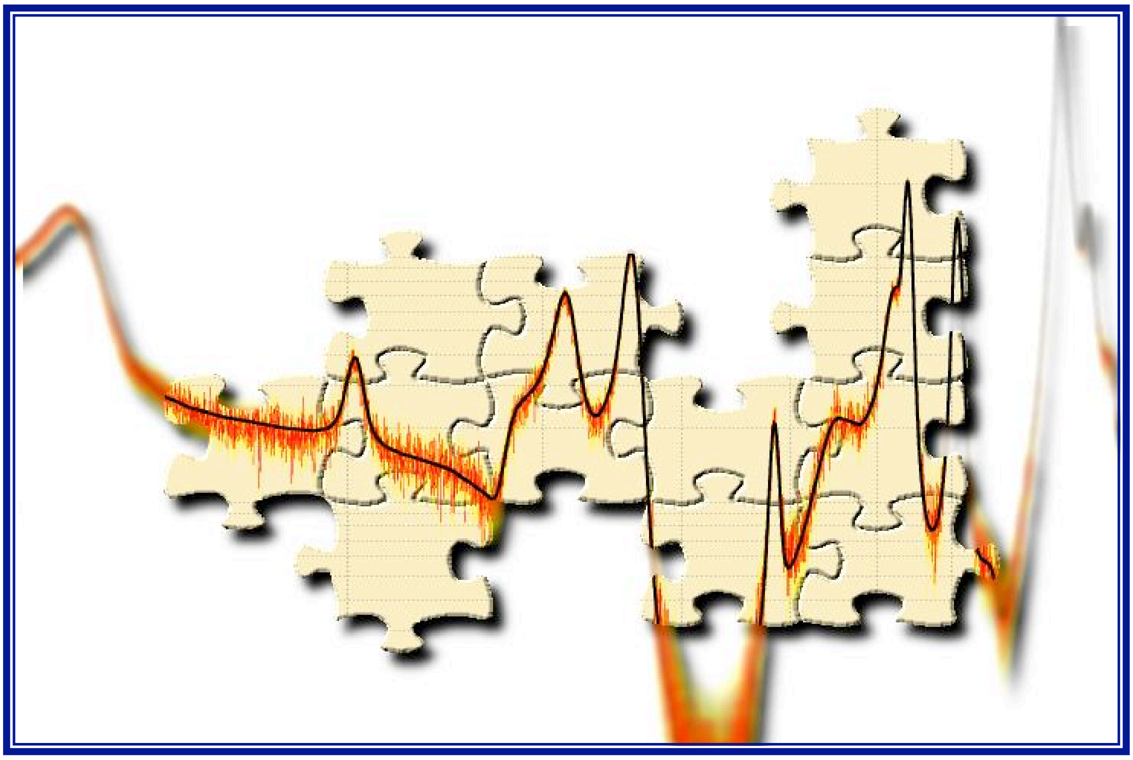

Geneva, 31 January 2003

CERN n_TOF Facility: Performance Report

EDITORIAL BOARD:

E. Chiaveri	Chairman
M. Dario	Secretary
S. Andriamonje	
P. Cennini	
Y. Kadi	
A. Mengoni	
P. Pavlopoulos	
F. Saldana	
V. Vlachoudis	
H. Wendler	

LIST OF AUTHORS

U. Abbondanno[1], G, Aerts[2], H. Alvarez[3], S. Andriamonje[2], A. Angelopoulos[4], P. Assimakopoulos[4], C. O. Bacri[5], G. Badurek[6], P. Baumann[5], F. Becvar[7], H. Beer[8], J. Benlliure[3], B. Berthier[5], E. Berthoumieux[2], J. P. Bertuzzi[9], D. Blanc[9], R. Bonzano[9], C. Borcea[9], P. Bourquin[9], N. Bustreo[10], J. Buttkus[9], F. Calvino[11], D. Cano-Ott[12], R. Capote[13], R. Cappi[9], J. C. Carlier[9], P. Carlson[14], E. Cennini[9], P. Cennini[9], D. Chapuis[9], V. Chepel[15], E. Chiaveri[9], V. Chohan[9], C. Coceva[16], N. Colonna[17], J. P. Come[9], G. Cortes[11], D. Cortina[3], A. Couture[18], J. Cox[18], S. Dababneh[8], G. Daems[9], M. Dahlfors[9], V. Dangendorf[19], S. David[5], T. Dobers[9], R. Dolfini[20], C. Domingo-Pardo[21], I. Duran-Escribano[3], L. Durieu[9], C. Eleftheriadis[4], M. Embid-Segura[12], A. Ferrari[9], L. Ferreira-Lorenco[22], R. Ferreira-Marques[15], C. Flament[9], H. Frais-Koelbl[23], W. I. Furman[24], M. Gaidon[9], J. Gascon[9], D. Gasser[9], Y. Giomataris[2], M. Giovannozzi[9], I. F. Goncalves[22], E. Gonzales-Romero[12], I. Goulas[9], A. Goverdovski[25], F. Gramegna[10], E. Griesmayer[23], F. Gunsing[2], R. Haight[26], M. Heil[8], A. Herrera-Martinez[9], K.G. Ioannides[4], N. Janeva[27], E. Jericha[6], Y. Kadi[9], F. Kaeppler[8], D. Karamanis[4], A. Kelic[5], V. Ketlerov[25], G. Kitis[4], P.E. Koehler[28], V. Konovalov[24], E. Kossionides[4], G. Kowalik[9], J. Kuhnl-Kinel[9], V. Lacoste[9], J. M. Lacroix[9], H. Leeb[6], A. Lindote[15], I.M. Lopes[15], M. Lozano[13], S. Lukic[5], R. Magnin[9], E. Mahner[9], F. Marie[2], S. Markov[27], S. Marrone[17], J.M. Martinez-Val[29], P. Mastinu[10], A. Mengoni[9], R. Messerli[9], G. Metral[9], P. Milazzo[1], E. Minguez[29], A. Molina-Coballes[13], J. Monteiro[9], C. Moeau[1], F. Neves[15], B. Nicquevert[9], R. Nolte[19], H. Oberhummer[6], S. O'Brien[18,] J. Pancin[2], C. Paradela-Dobarro[3], A. Pavlik[30], P. Pavlopoulos[31], A. Perez-Parra[12], J.M. Perlado[29], L. Perrot[2], V. Peskov[14], R. Plag[8], A. Plompen[32], A. Plukis[2], A. Poch[11], M. Poehler[9], A. Policarpo[15], C. Pretel[11], J.M. Quesada[13], E. Radermacher[9], U. Raich[9], S. Raman[28], W. Rapp[8], T. Rausher[31], R. Reifarth[8], F. Rejmund[5], J. P. Riunaud[9], G. Rollinger[9], M. Rosetti[16], C. Rubbia[20], G. Rudolf[5], P. Rullhusen[32], F. Saldana[9], J. Salgado[22], E. Savvidis[4], M. Silari[9], J.C. Soares[22], C. Stephan[5], G. Tagliente[17], J.L. Tain[21], C. Tapia[11], L. Tassan-Got[5], L.M.N. Tavora[22], R. Terlizzi[17], M. Terrani[20], N. Tsangas[4], W. Van Baaren[9], G. Vannini[33], P. Vaz[22], A. Ventura[16], D. Villamarin-Fernandez[12], M. Vincente-Vincente[12], V. Vlachoudis[9], R. Vlastou[4], F. Voss[8], M. Weierganz[19], H. Wendler[9], M. Wiescher[18], K. Wisshak[8], L. Zanini[9], M. Zanolli[9].

---

[1] Istituto Nazionale di Fisica Nucleare, INFN, Trieste, Italy

[2] Commissariat a l'Energie Atomique (CEA), France

[3] Universidad de Santiago de Compostela, Spain

[4] Astro-Particle Consortium (APC), Greece

[5] Centre National de la Recherche Scientifique/IN2P3 - IPN, Orsay, France

[6] Atominstitüt der Österreichischen Universitäten, Technische Universität Wien, Austria

[7] Charles University, Prague, Czech Republic

[8] Forschungszentrum Karlsruhe, Institüt für Kernphysik (FZK), Germany

[9] CERN, Geneva, Switzerland

[10] Istituto Nazionale di Fisica Nucleare, INFN, Laboratori Nazionali di Legnaro, Italy

[11] Universidad Politecnica de Catalunya, Barcelona, Spain

[12] Centro de Investigaciones Energeticas Medioambientales y Technologicas (CIEMAT), Madrid, Spain

[13] Universidad de Sevilla, Spain

[14] Kungliga Tekniska Hogskolan, Physics Department (KTH), Stockholm, Sweden

[15] Laboratorio de Instrumentacao e Phisica Experimental de Particulas (LIP), and Departamento de Fisica da Universidade de Coimbra, Portugal

[16] ENEA, Bologna, Italy

[17] Istituto Nazionale di Fisica Nucleare, INFN, Bari, Italy

[18] University of Notre Dame, USA

[19] Physikalisch Technische Bundesanstalt, Braunschweig, Germany

[20] Università di Pavia, Italy

[21] Consejo Superior de Investigaciones Cientificas (CSIC), Universidad de Valencia, Spain

[22] Instituto Tecnologico e Nuclear (ITN), Lisbon, Portugal

[23] Fachhochschule Wiener Neustadt, Wiener Neustadt, Austria

[24] Joint Institute for Nuclear Research, Frank Laboratory of Neutron Physics, Dubna, Russia

[25] Institute of Physics and Power Engineering, Kaluga region, Obninsk, Russia

[26] Los Alamos National Laboratory, New Mexico, USA

[27] Institute for Nuclear Research and Nuclear Energy, Sofia, Bulgaria

[28] Oak Ridge National Laboratory, Physics Division, Oak Ridge, USA

[29] Universidad Politecnica de Madrid, Spain

[30] Institut für Isotopenforschung und Kernphysik, Universität Wien, Austria

[31] Department of Physics and Astronomy - University of Basel, Basel, Switzerland

[32] CEC-JRC-IRMM, Geel, Belgium

[33] Dipartimento di Fisica and INFN, Bologna, Italy

ABSTRACT

This report describes the basic characteristics and the performances of the new neutron time-of-flight facility, n_TOF, recently set in operation at CERN.

The report is divided into three parts. In the first part, a description of the characteristics of the installation, up to the experimental area (EAR-1) is presented. This includes the proton extraction line from the PS, the spallation module (the lead target and its cooling and moderation systems) and the neutron beam window. A description of the neutron time-of-flight line with the vacuum system, shielding and collimation is also included in this part.

In the second part, matters related to safety issues, including radiation and dose estimates and measurements in the target area are discussed.

In the third part, a description of the experimental set up in EAR-1 is presented. This includes the data acquisition systems, the beam monitoring systems and the detectors for capture and for fission measurements. The measurements performed in order to derive the major beam characteristics (neutron fluence, energy resolution and background conditions), are described in details. For all these quantities, comparisons with Monte Carlo simulations are provided.

A summary table with all the most important parameters of the n_TOF installation and neutron beam characteristics is enclosed in the Appendix.

TABLE OF CONTENTS

INTRODUCTION

The world-wide increasing energy demand in general, and electricity demand in particular, with the increased concern for the environmental impact of energy consumption and the foreseen limitations of fossil fuel call for a re-evaluation of fission energy as a long-term energy source compatible with the goals of sustainable development. Although present light water reactors (LWRs) are capable of covering the nuclear energy demand for the decades to come, the longer-term need has triggered in the last decade active fields of research looking at innovative options. Important development goals for such advanced systems are environmental friendliness, resource efficiency, and cost-effectiveness, while accounting for socio-political concerns such as proliferation. Several factors such as transmutation of nuclear waste, energy with reduced nuclear waste production, as well as long-term energy sustainability, have led to an interest in the innovative Accelerator Driven Systems (ADS) that has emerged at CERN [1] and elsewhere.

The design of any ADS prototype requires the complete and precise knowledge of basic nuclear data in the form of cross sections for neutron induced processes. It might be argued that the presently available databases for this application are just adequate for conceptual studies but it is certainly not accurate enough for the design and simulation of ADS devices. Nuclear data contained in these databases stem from compilations of numerous distinct experiments, which by being inherently dedicated to specific energy domains and elements each time, are often not in perfect agreement or even mutually incompatible. The discrepancies are worse in the case of minor actinides, fission products and the isotopes of the Th cycle, their intrinsic radioactivity being one of the reasons.

The European Commission approved [2] within the 5th EURATOM program the n_TOF-ND-ADS project proposed by the n_TOF Collaboration. The main advancement of the state-of-the-art offered by the n_TOF experiment lies exactly in the dissemination of a complete and consistent set of high accuracy cross-sections, extending over eight orders of magnitude in the neutron energy and satisfying the aforementioned demanding research and industrial requirements. Due to the flexible configuration of the CERN accelerator complex and the innovative technological concepts that are exploited within the n_TOF project, the quality of the n_TOF measurements is superseding that of those at any other neutron source.

The concept of the n_TOF neutron beam [3] makes use of both the specifically high flux of neutrons attainable using the spallation process of 20 GeV protons on an extended lead target containing practically the whole spallation shower and the remarkable beam density of the CERN Proton Synchrotron (PS), which can generate high intensities up to $7□10^{12}$ ppp (protons per pulse) - high enough to produce the vast number of $2□10^{15}$ neutrons per pulse - in the form of short (6□ns width) pulses with a repetition time varying from 2.4 s to 16.7 s and a prompt “flash” considerably smaller compared to electron machines. The high neutron flux, the low repetition rates and the excellent energy resolution of $3x10^{-4}$ open new possibilities to high precision cross section measurements in the energy range from 1 eV to 250 MeV, for stable and, moreover, for radioactive targets.

In the scope of our program we have dedicated special effort to the geometry, material and size of the neutron beam collimators, in order to allow a large flexibility to the choice of the size and the intensity of the neutron beam. Presently only two different beam configurations are in operation with the possibility to be interchanged within two hours only. Different forms of shielding and the geometry of the experimental area have been optimized, in order to keep the background to a level compatible with the operation of large calorimeters and neutron sensitive detectors. The experimental area is equipped with all necessary infrastructures to provide flexible and safe operation in the running of the individual measurements.

At first phase we consider for the measurements of capture cross sections the use of liquid C_6D_6 detectors and of a 1□segment of BaF_2. We envisage in a second phase the construction of a highly segmented BaF_2 calorimeter. The measurement of the (n,f) reactions are performed with a set of sixteen high efficiency FIC [4] chambers and of ten high spatial resolution PPAC [5] chambers. The innovative Data Acquisition System (DAQ) based on 1 GHz flash ADCs, developed jointly with the industry, was performing without dead time even at a peak data rate of 18 MBytes/s.

The recorded capture, fission and ^{6}Li(n,α) data, exceeding 6.5 TBytes in 2002, allowed the determination of the neutron beam intensity and profile at the experimental area, as well as the evaluation of the weighting functions required for the analysis of the capture measurements with the C_6D_6 detectors. The results of the analysis [6] provided the neutron flux in a range of neutron energies spanning over eight orders of magnitude, the determination of the various background components and the resolution function, allowing thus the determination of the measured ^{151}Sm(n,γ), ^{232}Th(n,γ), ^{204,206,207,208}Pb(n,γ), ^{209}Bi(n,γ), the ^{232}Th(n,f) and ^{234}U(n,f) cross sections. The achieved energy resolution is excellent and fully compatible with the Monte Carlo simulations.

The scientific program related to the n_TOF-ND-ADS project within the 5th EURATOM framework will continue in the years 2003 and 2004. The measurements at the CERN Neutron TOF facility on different types of cross sections will trigger the critical task of neutron cross section theoretical evaluation and the development of an advanced software system concerning the storage and dissemination of the results in a form of a Database proper to ADS.

Several of the proposed cross section measurements are within the central interest of the field of Nuclear Astrophysics. Astrophysics is approaching a stage where a number of long-standing central questions about our Universe can finally be addressed within a consistent and quantitative way. The so-called Standard Model describes satisfactorily the hot Big Bang cosmology. In this context, the quest for the origin of the chemical elements plays a prominent role: The production of ^{2}H, ^{3}He, ^{4}He and ^{7}Li (200 s after) in the Big Bang bears important consequences for cosmology and particle physics. On the other hand, the heavy elements beyond Fe witness ongoing neutron capture nucleosynthesis in evolved stars and supernova explosions with immediate constraints for the galactic chemical evolution. The difficult task is to understand the formation of these heavy elements, where not only the nuclear physics is complicated but also the mechanisms and thermodynamics are not completely understood yet. Advances in our understanding of these processes and of the astrophysical sites where they occur demand also advances in laboratory measurements of neutron cross sections. Cross section measurements comprising the crucial input for models of those astrophysical processes are planned by the n_TOF Collaboration. The high precision of new abundance measurements, primarily in meteorites, is a strong motivation for these new, precise measurements of neutron capture cross-sections by our Collaboration.

Moreover, the thorium-cycle isotope ^{232}Th attracted the scientific interest twenty years ago with the nuclear phenomenon named “the thorium anomaly”. It has raised new fundamental questions on the nuclear fission process, the role of shell and pairing effects, the fine structure of potential energy surface at high- and hyper-deformations in a wide region of nuclear temperature. Other nuclei, ^{230}Th, ^{231}Pa, ^{234}U and ^{236}U, have similar properties due to their potential energy surface. It’s interesting, that the main part of those nuclei is involved into the thorium-uranium fuel cycle. Therefore, the n_TOF Collaboration devoted particular attention to the physics aspects of detailed and high-resolution measurements of the fission barrier through a series of fission cross-sections measurements.

The experimental set-up allowed the full evaluation of the performances of the nTOF neutron beam and has confirmed the potentialities of the proposed method and the predictions of the Monte Carlo simulations. The determination of the neutron flux, the neutron profile and the energy resolution has been performed with the data collected in 2001 and partially in 2002 confirming the expectations in both the quantity and quality of the neutron beam in a range of neutron energies spanning over eight orders of magnitude, i.e. from 1 eV to over 250 MeV.

PART I

TECHNICAL DESCRIPTION OF THE FACILITY

1 THE PS BEAM

1.1 General Considerations

The spallation mechanism [3] is a remarkably powerful source of neutrons, furthermore, lead has a high transparency for neutrons of energy ≤ 1 MeV. In the beam used for the neutron spallation source, the CERN PS accelerator is capable of accelerating up to 7x10^{12} protons per cycle. This extraordinarily prolific source can be concentrated in short time pulses (7 ns r.m.s.), offering the added feature of a tremendous potential accuracy in the time of flight (TOF) determination for high energy neutrons.

The neutrons produced by spallation are canalized to an experimental area located at ~ 185 m downstream through a vacuum pipe, making use of the existing TT2-A tunnel about 7 m below the ISR tunnel (see Figure 1.1).

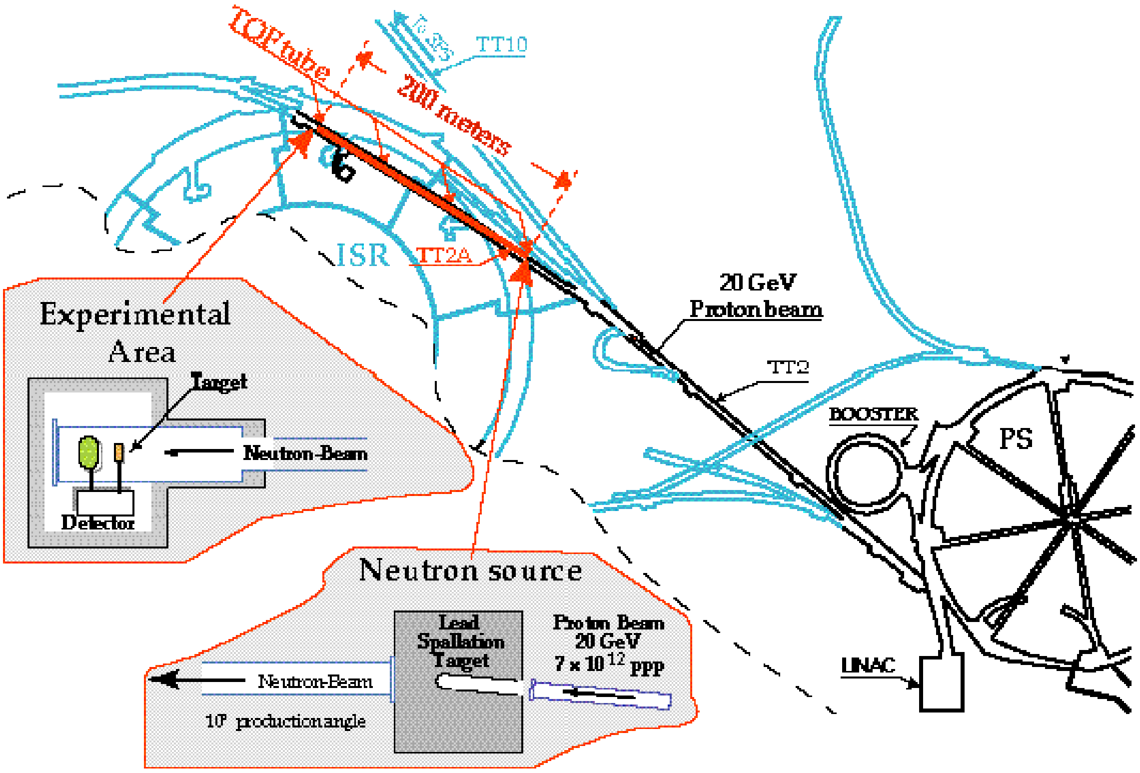

Figure 1.1: General layout of the experiment. The proton beam is extracted via the TT2 transfer line and hits the lead target. At the end of the TOF tunnel (TT2-A), neutrons are detected about 185 m from the primary target.

We report here the main characteristics of the proton beam dedicated to the Facility:

- Momentum of 20 GeV/c corresponding to the maximum attainable energy with a PS magnetic cycle of 1.2 s;
- a single proton bunch of 7x10^{12} particles with a width of 7 ns r.m.s;
- possibility to have up to 6 bunches per Supercycle of typically 16.8 s. This parameter is limited at 5 bunches every 16.8 s by the maximum power dissipation allowed on the Spallation Target and by the radiation level in the target area.

The beam will be fast extracted and sent onto the Spallation Target by using the present Fast Extraction FE16 with no modifications in the PS ring. The proton beam for n_TOF can be considered as a record for the PS machine in terms of peak intensity, using the procedures briefly described below.

A single bunch in a single Booster ring is accelerated and injected into the PS at 1.4 GeV/c. This higher injection energy (recently modified for the LHC beam requirements) allows the self-field space charge tune shift to be kept to a reasonable value of <0.3 on the 20 ms injection flat bottom. The bunch is injected and then accelerated with the RF frequency at harmonic number $h = 8$. The horizontal and vertical working points are precisely adjusted during the acceleration to avoid, as much as possible, resonance crossings. Head-tail transverse instabilities at low energy are cured using linear coupling with skew quadrupoles. The horizontal and vertical chromaticities are set to -1 before transition and to $+0.1$ after transition, to avoid head-tail instabilities at high energy. The RF voltage is adjusted during the acceleration to decrease the longitudinal acceptance and to improve Landau damping and minimize longitudinal instabilities. Preventing beam break-up instabilities at transition, destroying 50% of the beam, requires increasing the longitudinal emittance from 2 to 2.5 eVs, using the standard longitudinal blow-up and a 200 MHz cavity on the injection flat bottom.

Once on the 20 GeV/c flat top, a phase jump RF gymnastic squeezes the bunch length, just before extraction, from 13 to 7 ns (r.m.s.). The normalized r.m.s. transverse emittances are 40 and 30×10^{-6} m in the horizontal and vertical plane respectively. The total transmission efficiency is better than 90%.

Two modes of operation are foreseen: the Dedicated Mode and the Parasitic Mode.

In the Dedicated Mode one or more 20 GeV/c – 1.2 s cycles are dedicated to the TOF experiment. This mode achieves the best performance in beam quality; namely the highest bunch intensity.

In the Parasitic Mode, the TOF bunch is accelerated together with a much lower intensity bunch, which is slow-extracted at 24 GeV/c to the East Hall experimental area. The high intensity TOF bunch is fast-extracted onto an intermediate flat top at 20 GeV/c. The small bunch goes through a bunch compression as well, and has to be decompressed, with a reverse RF gymnastic to recover its normal shape well-suited for the slow extraction.

In the Dedicated Mode an intensity of 7×10^{12} particles/bunch and a r.m.s. bunch length of 7 ns r.m.s can be achieved (see Figure 1.2). In the Parasitic Mode the bunch length will be the same but the maximum intensity will be ~ 4×10^{12} particles/bunch. The advantages of running in “parasitic mode” are in an easier TOF scheduling (e.g. setting up’s) as the slow extraction cycles are present almost all of the time.

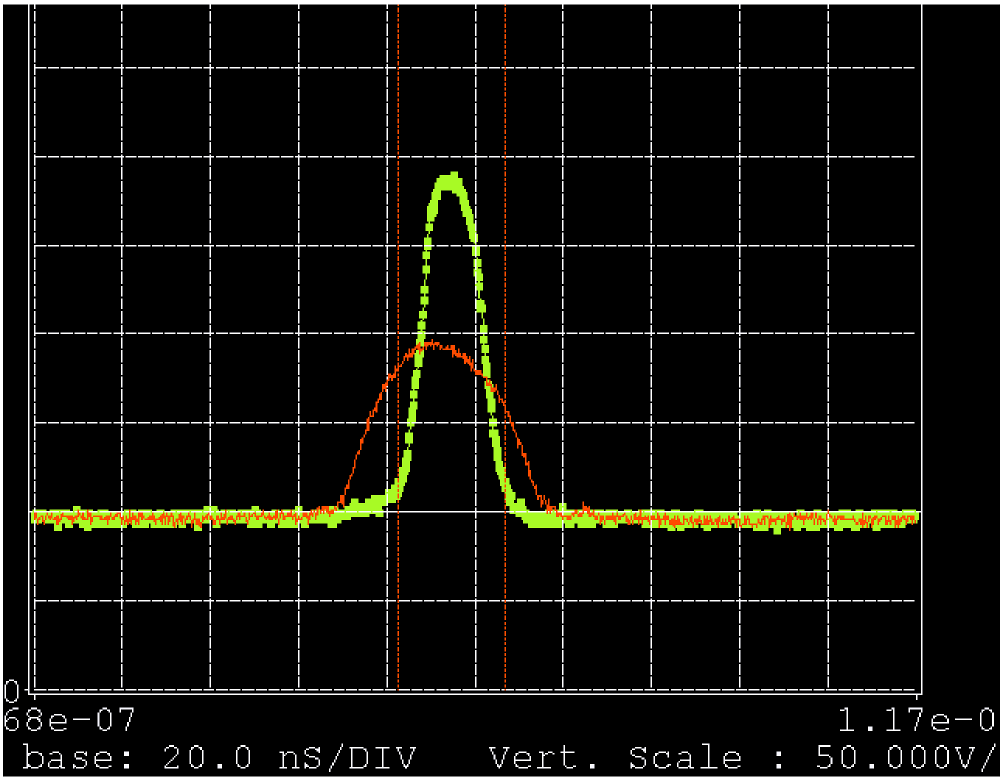

Figure 1.2: TOF proton bunch before and after compression. $N_b = 0.7 \times 10^{13}$ *particles/bunch, r.m.s. bunch length ~6 ns. Time scale 20 ns per divisions.*

1.2 Beam Line Layout

The geometry of the new layout of the FTN transfer line can be summarized as follows [7]:

- three bending magnets (of type MCA) to deflect the beam to the left-hand side of the dump D3. Each magnet generates a bending angle of 2° at the maximum beam momentum of 20 GeV/c;
- six quadrupoles are used to focus the beam. Three of them (QFS type) are used to focus the beam, the other three (QD type) are used for defocusing. Since the quadrupoles of the same type have the same strength, it is possible to connect them in series;
- three bending magnets (MCA type) are used to deflect the beam to the right by an overall bending angle of 6°. Each of them generates the same deflection angle;
- two correction magnets (M100 type) are installed to control the beam trajectory.

With this choice of geometry, the proton beam intersects the axis of the TOF pipe at an angle of 10°. The layout of the FTN transfer line is shown in Figure 1.3 and Figure 1.4.

1.3 Beam Line Optics

As described in previous reports [8,9], the starting point for the optics study of the new transfer line is the standard optics configuration, used for the fast extracted beam at 26 GeV/c delivered by the PS machine [10]. This optics have been scaled down for the 20 GeV/c operation foreseen for the TOF Facility.

The quadrupole FT16.QFO375 is powered by an independent power supply. It has been separated from the string of focusing quadrupoles of the TT2 line since the installation of the stripper foil for the ion beam, just upstream. Hence, this magnetic element can be used to focus the proton beam on the target. The six quadrupoles installed in the FTN line are divided into two families (focusing and defocusing).

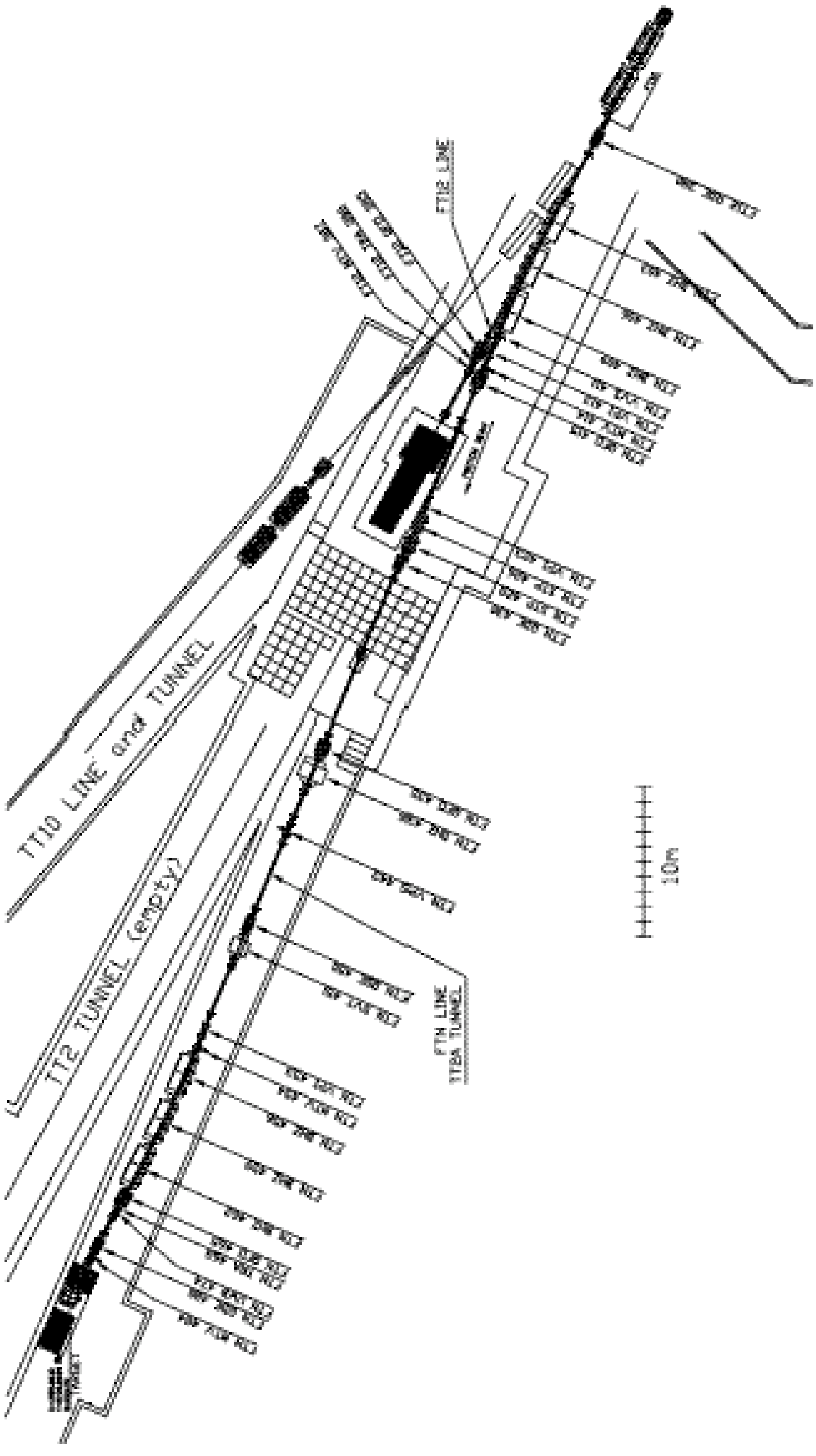

Figure 1.3: Layout of the FTN transfer line.

Figure 1.4: Picture of the FTN transfer line installed in the TT2-A tunnel.

To improve the control of the beam size and dispersion function at the target location, it has been decided to install two quadrupoles downstream from the last group of three bending magnets.

The computation of the optics has been carried out by using the *MAD* program [11]. In Table 1.1 the beam parameters used for the computation of the beam envelope are reported, together with the beam size at the target location.

TRANSVERSE PARAMETERS		**LONGITUDINAL PARAMETERS**		**BEAM SIZE AT TARGET**	
eH (1s) [mm mrad]	1.88 p	$\Delta p/p$	$\pm 3 \cdot 10^{-3}$	σH [mm]	7.8
eV (1s) [mm mrad]	1.41 p			σV [mm]	5.6

Table 1.1: Beam parameters used for computation of beam envelope.

The location of the two correcting magnets has been optimized by taking into account the optics and the available power converters (see next section for more details). The horizontal corrector has been placed near the second focusing quadrupole to exploit the large value of the β-function. For the same reason, the vertical corrector has been installed near the second defocusing quadrupole. Two magnets of type M100 have been chosen, due to their magnetic strength: they will be used with a gap of 140 mm. The maximum variation in the beam position at the target location is about ±33 mm and ±36 mm in the horizontal and vertical planes respectively for a maximum current of 20 A.

The first beam position monitor is installed at the entrance of the first focusing quadrupole of the FTN beam line. It will be used to control the beam trajectory at the exit of the first group of three bending magnets. The second monitor is placed at the entrance of the fourth bending magnet, while the third monitor is located just downstream from the last quadrupole.

The first two bending magnets, which are powered in series, can be used to steer the beam on the first monitor to allow a well-corrected horizontal trajectory. Using the first string of two bending magnets one can center the beam on the second monitor. Then, the horizontal corrector allows the final steering on the target to be performed using the third monitor.

The vertical trajectory can be corrected by using the magnet FT16.DVT353 to center the beam on the second monitor in the FTN transfer line and then using the vertical corrector installed in FTN together with the last monitor.

In Table 1.2 are reported the coordinates of the intersection point between the proton beam and the TOF axis as computed by the *MAD* program and then translated into the standard CERN co-ordinate systems.

X [m]	Y [m]	H [m]
1595.9564	2198.2357	434.2401

Table 1.2: Co-ordinates of the intersection point of the FTN axis and the axis of the TOF tube computed using the MAD *program and expressed in the standard CERN co-ordinate system.*

1.4 Power Converters

One power converter (type R22.01), formerly used for Dump D2, is used to power the first two bending magnets. This will allow the power converter to be operated in ppm mode with a switching time shorter than 1.4 s, but not faster than 1.2 s, between the operational value of 895 A and the zero value used to send the beam to the dump D3. A second power converter (type R22.02), also used formerly for dump D2, is used for the remaining bending dipoles, i.e. the four MCA elements. The total resistance of the whole string of magnets does not allow a ppm operation, but this does not seem to be a serious limitation.

As far as the quadrupoles are concerned, they cannot be connected in series with the two strings of focusing and defocusing elements of the TT2 transfer line. In fact, as already mentioned in [9], the existing power converter is not able to ensure a fast cycling of the magnet string. On the other hand, two power converters of type N can be recuperated from the PS stock. They power the string of three focusing quadrupoles and the string of three defocusing respectively.

The two corrector magnets are powered by using power converters of type L10, supplying a maximum current of 10 A. This type of power converter works around zero-current and has been modified in order to deliver up to 50 A.

The rearrangement of building 269 combined with the rejuvenation of the low voltage distribution system allows all power converters of the FTN transfer line to be housed in that building.

The actual values of the current needed by the main magnetic elements (dipoles and quadrupoles) used to generate the nominal optics are listed in Table 1.3. In addition to the elements in the FTN transfer line, the quadrupole FT16.QFO375 is also included.

ELEMENT TYPE	**CURRENT** [A]
Quadrupole FT16.QFO375 (TT2)	246.15
Dipole MCA (FTN)	895.00
Quadrupole QD (FTN)	167.70
Quadrupole QFS (FTN)	236.80

Table 1.3: List of the actual values of the current for the various magnetic elements in the FTN line, including the last quadrupole of the TT2 line.

1.5 Instrumentation Related to the PS Beam

The following devices are available for the users:

- Beam Current Transformers (BCT), to monitor pulse by pulse the proton intensity sent onto the Target;
- Wall Current Monitor (WCM or pick-up), to provide a pulse in the n_TOF control room proportional to the instantaneous proton beam intensity;
- Beam Position Monitors (BPM), to monitor the position of the proton beam along the FTN line;
- Timing Pulses;
- Beam Request Box, to request the proton beam;
- Visistar PS, to visualize on a video screen the status of the PS Complex.

1.5.1 Beam Current Transformers

A current transformers (TRA 468) similar to those used in the FT12 line is installed downstream from the second group of bending magnets. Its location is at ~ 6 m before the end of the FTN line. The digitized value of the beam intensity is available for the users in the PS control system through Ethernet.

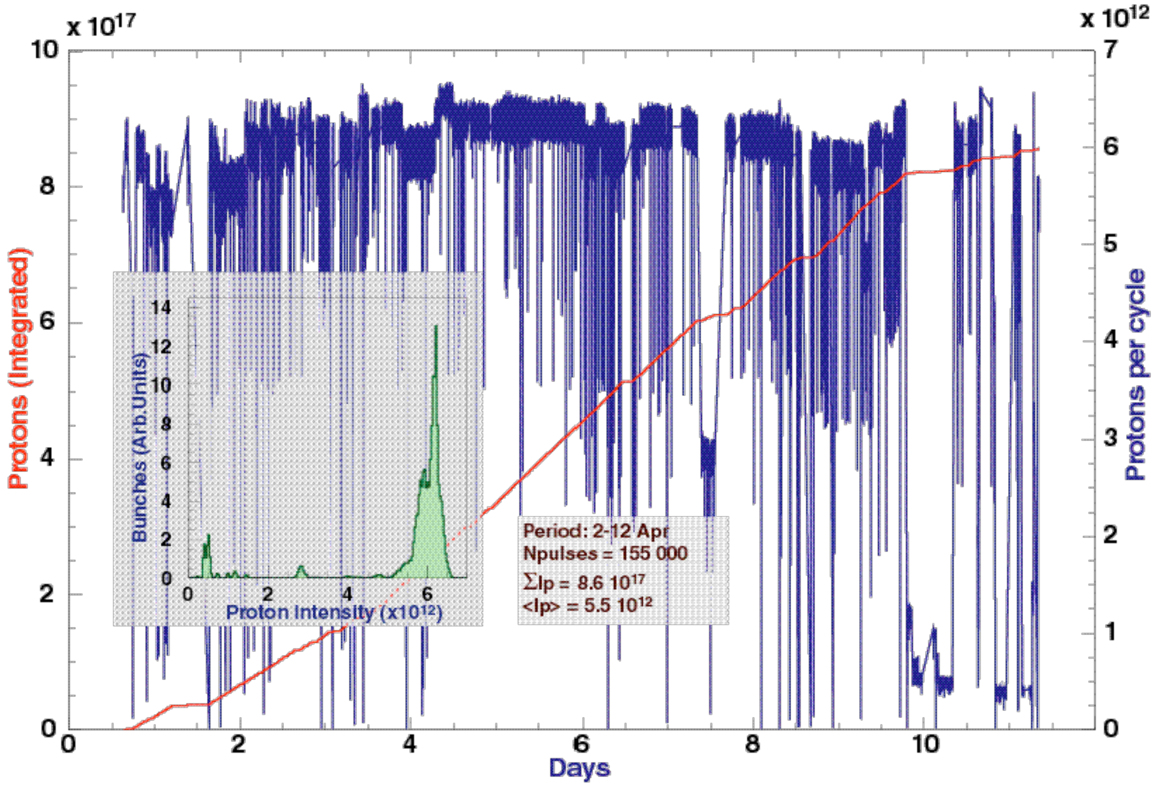

Figure 1.5: Proton intensity delivered to n_TOF during second Commissioning.

As all the other transformers in the PS complex, the value of the proton intensity is normalized by making periodical calibration procedures. This normalization takes in account as reference the measurement made in the PS ring with the so-called DC Beam Current Transformers. Under this condition the accuracy of the value of the beam current, for bunches of 10^{12} protons, is ± 0.3% whilst its absolute value is ± 1%. In Figure 1.5 is reported one example of the recorded beam intensity taken during the commissioning. It has to be noted that in this period almost all protons were delivered in Dedicated Mode (> 6×10^{12} p/pulse).

1.5.2 *Wall Current Monitor*

The resistive Wall Current Monitor (WCM) is mounted immediately after the BCT. This device provides in the n_TOF Control Room a signal proportional to the proton beam current and could be used either for timing purposes or to monitor directly the proton beam intensity.

1.5.3 *Beam Position Monitors*

To monitor the proton beam position three scintillating screens, coupled to three video cameras (MTV 414, 454 and 484), are mounted in the FTN line. The operation of these devices is under the control of the MCR. The screens are inserted in the proton beam only during the beam setting-up and are removed in normal operation. The visual information of the beam position is available on TV screens in the MCR and in the n_TOF Control Room.

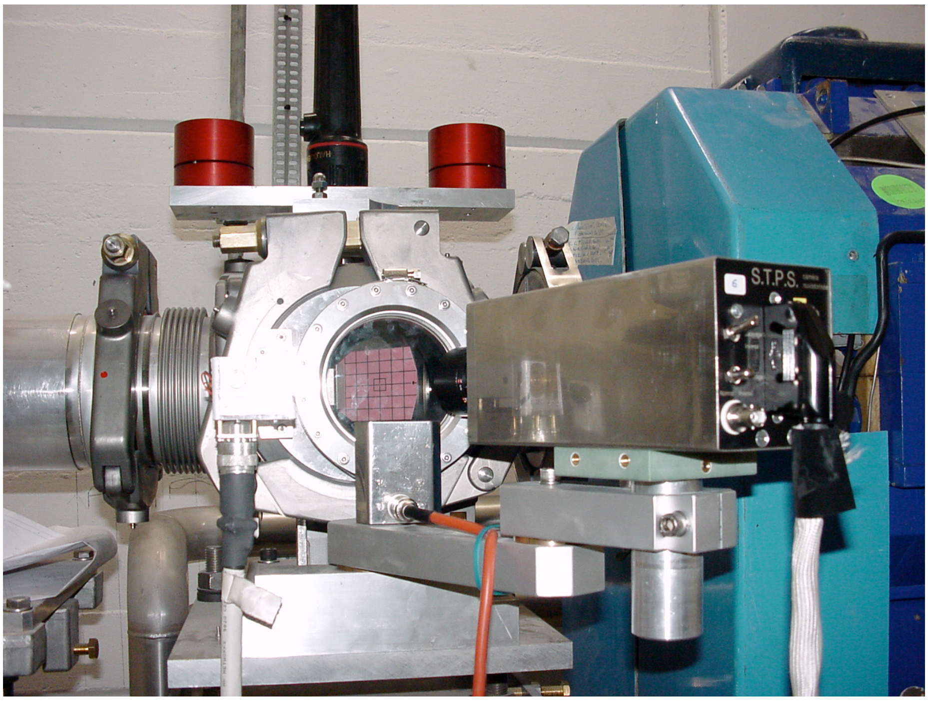

Figure 1.6: Beam Position Monitor

The last screen, immediately before the spallation target (MTV 484), can be "read" through Ethernet. The position to respect to the nominal beam axis and the beam dimension (x,y) are extracted by analyzing the video signal of the camera. This parameter is only available on request and can not be used to monitor the beam position of every proton shot delivered to n_TOF.

1.5.4 *Timing*

There are two timing signals available in the Control Room: Prompt Pulse for the Dedicated Mode and Prompt Pulse for Parasitic Mode. Both are standard PS Timing signals (20 V, 2 μs wide positive pulses on 50 Ω).

The timing of these pulses, compared to the signal from the detectors sent the Data Acquisition (DAQ), can be adjusted in advance with a precision of 5 ns. Even if this resolution could be considered sufficient for almost the entire neutron energy range, it is preferable to use the signal produced at t_0 in the detectors by the so-called "gamma flash".

It has to be noticed that the Timing Pulses are provided by the PS even for magnetic cycles without protons. The user must detect the presence of the beam by using the information of the WCM or by any other method.

1.5.5 *Beam Request Box*

This device, located in the Control Room, send a Beam Request to the MCR. The request can be set or reset manually by pushing two buttons on the box, or by applying a TTL signal (2 μs) on the appropriate connectors on the rear panel. The request is sent to the MCR only if two conditions are present simultaneously:

- the status of the Proton Beam Stopper (STP 428) indicates that the Beam Stopper is in the up position;
- the toggle switch on the Request Box is in the position “Enable”.

In response to a request the MCR provides an acknowledge signal visualized by a Led on the front panel. It is recommended to monitor the Beam Request by checking its status through Ethernet.

1.6 Cooling and Ventilation

A summary of the power dissipated by the different magnet elements used for the FTN line is listed in Table 1.4. In this Table, the maximum power dissipated by the different magnets is reported, which is obtained by taking the minimum value between the maximum current delivered by the power converter and the maximum current sustainable by the magnet.

	MAGNETIC ELEMENT	Imax [A]	R [Ohm]	Pmax [kW]
TT2 tunnel	Three DC dipoles (MCA)	1500	0.016	72.00
	One DC quadrupole (QFS)	470	0.064	30.08
	One DC quadrupole (QD)	300	0.062	18.60
	Total Pmax			120.68
TT2A tunnel	Two DC quadrupoles (QFS)	470	0.064	60.16
	Two DC quadrupoles (QD)	300	0.062	37.20
	Two DC correctors (M100)	20	0.200	8
	Three DC dipoles (MCA)	1500	0.016	72.00
	Sweeping magnet (M200)	800	0.200	128.00
	Total Pmax			305.36

Table 1.4: Summary of maximum power dissipated in TT2 and TT2A tunnel.

In order to accommodate the heat loads coming from the magnets and electronic equipment, a ventilation system must be provided for the section of the FTN line inside the TT2A tunnel. The air handling unit will operate on full recirculation air and it will be equipped with a chilled water cooling coil (for mode “BEAM ON”), an electric heating coil (for mode “BEAM OFF”) and filter class EU4. In Table 1.5 the parameters concerning the water flow and the pressure drop for the different magnetic elements in the FTN transfer line are listed.

ELEMENT TYPE	**WATER FLOW**[1] [l/min]	**PRESSURE DROP** [bar]
Dipole MCA	20	5
Dipole M100	44	3.5
Quadrupole QD	10	6
Quadrupole QFS	10	8

Table 1.5: Details concerning the water flow and the pressure drop of the magnetic elements installed in FTN.

The demineralized water must be supplied to the magnets located in both the TT2 and TT2A tunnels. Since one of the magnets installed in the TT2 tunnel represents higher-pressure losses, the water will come from Booster station (higher Δp available). For the

---

[1] The water flow is referred to a temperature increase of 30°.

rest of the magnets, the water will be supplied from ISR cooling station (located in building 378).

A water flow measurement, connected to the Technical Control Room (TCR), is provided for the two tunnels. The same source of demineralized water is used as a primary source of cooling for the lead Spallation Target located in the TT2-A tunnel.

1.7 Vacuum System in the FTN Line

The situation of the vacuum system installed in the PS transfer line FT16 can be summarized as follows:

- p(FT16-10.VGP1) ~ 3 x 10^{-8} mbar;
- p(FT16-10.VGP2) ~ 4 x 10^{-9} mbar;
- p(FT16-20.VGP1) ~ 8 x 10^{-9} mbar;
- p(FT16-30.VGP1) ~ 4 x 10^{-9} mbar.

The elements installed in the FTN line are the following:

- a sector valve (FTN.VVS411), is installed directly downstream from the three MCA bending magnets, in order to separate the transfer line FT16 from FTN;
- one pumping group (FTN.VPG443), used for the pre-vacuum, is positioned approximately in the middle of the beam line. It consists of a standard 600 l/s turbo-molecular pump and a 25 m^3/h primary pump;
- two vacuum gauges are foreseen for measurements;
- one manual valve is foreseen for venting the sector;
- numerical simulations have shown that at least three 410 l/s ion pumps (FTN.VPI413/433/453) are necessary to guarantee an average H2 pressure of about 2 10-8 mbar in the FTN line, which is in total agreement with the FT16 line layout.

The calculated pressure distribution along the transfer line FTN is shown in Figure 1.7.

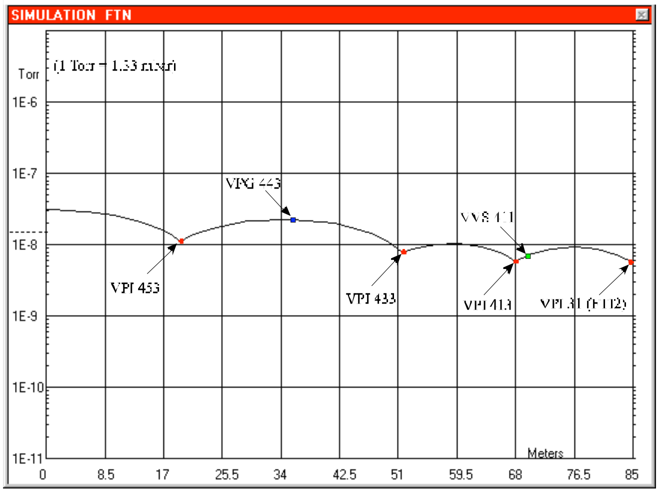

Figure 1.7: Pressure simulation for the FTN transfer line.

1.8 Safety Aspects on the Proton Beam

To comply with the safety rules in force at CERN, two Beam Stoppers have been installed in the FTN transfer line (STP 426, STP 428). They are located downstream from the dump D3 at the end of the TT2 tunnel (see Figure 1.3).

The Beam Stoppers are automatically pushed down as soon as the key giving access to the n_TOF Experimental Area is removed from the Access Control Box located in the n_TOF Control Room.

2 THE LEAD TARGET

The choice of the specific geometry of the spallation target is a compromise between several parameters. On one hand, there is choice between the neutron flux and the neutron energy resolution, related to the uncertainty due to the neutron moderation path fluctuations. On the other hand, the requirements on the dimension of the neutron beam and its halo at the detector station imply also strong constraints on the lateral size of the spallation target and on its collimation. Finally, the energy dependence of the neutron spectrum depends also on the dimension of the spallation target.

2.1 Optimization of the Design

We have performed an overall optimization on the size of a cylindrical spallation target of length h and radius R, followed by a water moderator layer of thickness d, which is added in order to improve the TOF energy resolution. All calculations are performed for the CERN-PS proton beam with an intensity of 7x10^{12} ppp at 20 GeV/c.

The spallation cascade is directed forward and spreads out over a large volume. Spallation neutrons emanating from the cascade slow down through isolethargic moderation naturally achieved within a volume of radius R and length h. Since a target with a larger radius would contain a larger fraction of the lateral component of the spallation cascade and its outer layer would act as reflecting cavity, it would also provide a higher neutron flux. A target of smaller radius would produce a smaller neutron flux but with a harder neutron energy spectrum due to the reduced mean moderation path available for the neutrons. On the other hand, the influence of the target length, h, on the neutron flux exiting the beam-downstream surface is an interplay between the containment of the longitudinal component of the spallation cascade, i.e. the proton to neutron conversion efficiency, and the loss of neutrons due to the solid angle reduction of the beam-downstream surface of the target.

The thin water layer will reduce in both cases the uncertainty due to the moderation path fluctuations by an equal amount. However, the smaller target involves shorter moderation paths and consequently a smaller uncertainty. Therefore, a smaller spallation target would provide better precision in the neutron energy TOF determination at the price of reduced neutron flux. The target size optimization considers the interplay between the resulting neutron flux and the sharpness in determining the neutron energy by TOF.

Good quality experimental conditions at the detector station require a neutron beam with a well-defined spot of homogeneous neutron flux density and the absence of a penumbra or halo around this beam spot. In particular, for the experiments using a 4π total absorption calorimeter the small size of the neutron beam and the beam penumbra are crucial. In a realistic set-up the size of the penumbra depends directly on the lateral size of the spallation target, vanishing only for a point-like target. For an extended spallation target only a complex system of double collimators can minimize the size of this halo ring.

By means of the FLUKA [12] and the EA-MC [13] programs, we simulated all physics processes for different sizes of the cylindrical lead target followed by a thin (5 cm) water moderator. Figure 2.1a shows the integrated neutron flux at a TOF distance L = 200 m as function of the target length, h, for different radii, R. The neutron flux increases with increasing radius as expected. For each target radius there is an optimum length, h, where the neutron flux, Φ, exhibits a maximum value. Figure 2.1b shows the monotonic dependence on the target length, h, of the uncertainty due to the moderation path fluctuations, $\Delta\lambda$, calculated in the neutron energy domain between 1 eV and 10 keV. This uncertainty $\Delta\lambda$ decreases with decreasing target size. By comparing Figure 2.1 and Figure 2.2, the target lengths with values above 50 cm can be excluded, since both, the neutron flux and the resolution are deteriorating.

In addition to the lead simulations, we considered also other materials for the spallation target. A clear advantage has been established for tungsten, having practically the same absorption and elastic cross sections as lead, but with the double density of atoms per unit volume. This fact would allow for the same flux a reduction by factor two of the lateral target size and the corresponding increase of the neutron intensity in the experimental area for the same spot surface of the neutron beam. However, the price and delivery of such a target would introduce delays in the neutron beam construction, not acceptable in our time schedule.

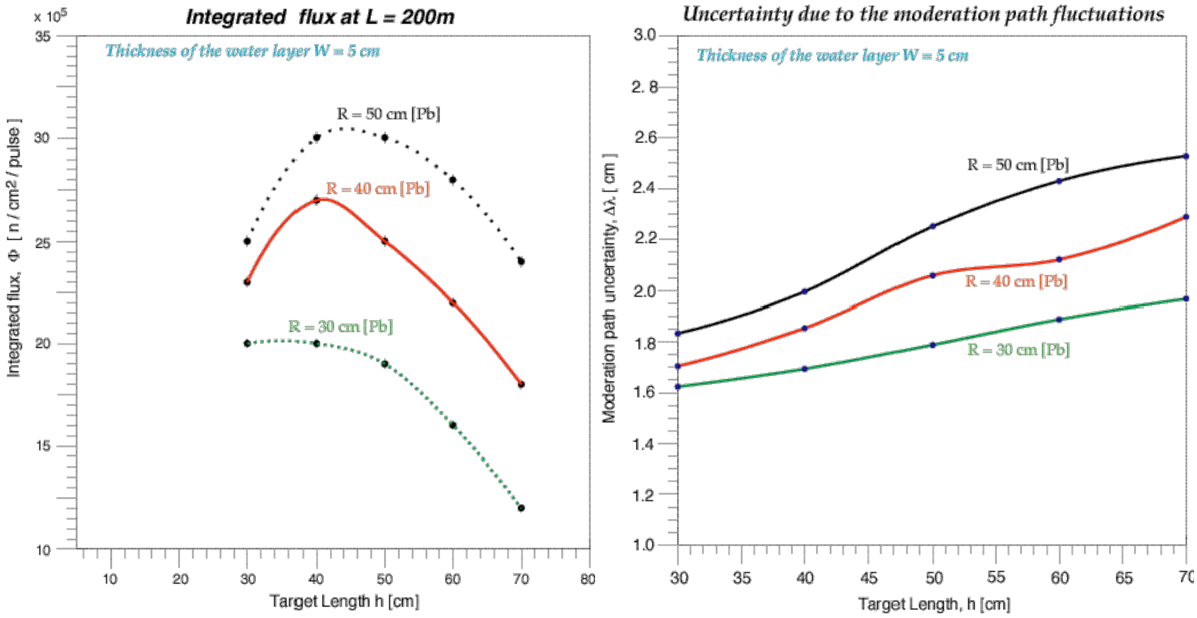

Figure 2.1: (a) The neutron flux as function of different sizes of the Pb spallation target. (b) The uncertainty due to the moderation path fluctuations in the energy range between 1 eV and 10 keV for different lead spallation target sizes.

Since for a given target the neutron flux decreases inversely proportional to the square of the TOF distance, L^2, but the TOF resolution decreases only inversely proportional to the TOF distance L, the quantity □□/√□ would be a measure of the target quality, independent of L. Since the optimization requires the smallest value for □□ and the maximum value for □, the quantity □□/ □ should be minimum for the optimum target dimensions. Figure 2.2a shows this quantity for different target dimensions, where the uncertainty □□ is calculated in the energy range between 1 eV and 10 keV. The optimum size corresponds to the minimum at a radius of R = 40 cm and a length h = 40 cm.

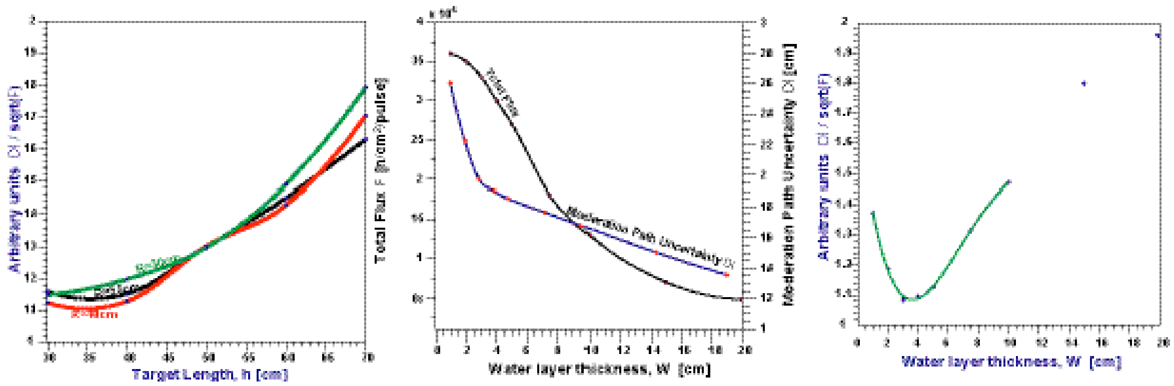

Figure 2.2: (a, left) The parameter □□/ □ representing the trade-off between the neutron flux and the energy resolution, for different target sizes. (b, center) The neutron flux and the uncertainty due to the moderation path fluctuations for different thickness of the water moderator. (c, right) The parameter □□/ □ representing the trade-off between the neutron flux and the energy resolution, for different water thickness. The uncertainty □□ is calculated in the energy range between 1 eV and 10 keV.

With the same criteria and the same simulation tools, we study the influence of the water layer thickness at the beam-downstream side of the target. Figure 2.2b shows the dependence of the neutron flux and of the uncertainty □□, between 1 eV and 10 keV, on the water thickness W for the chosen lead target geometry. The change in the first derivative of the uncertainty □□ at W = 4 cm indicates the optimum thickness of the water layer. This value can also be determined in Figure 2.2c, showing the quantity □□/ □ as function of the water layer thickness.

By simulating all physics processes, we studied the spallation lead target geometry requiring an optimum between a maximum neutron flux and a minimum neutron TOF energy resolution. We conclude that the optimum target has a radius of 40 cm and a length of 40 cm. The thickness of the water moderator is optimal at 4 cm.

2.2 The Spallation Source

The actual design of the lead spallation target differs slightly from the above values for practical reasons. A detailed description of the properties of the lead spallation target can be found in reference [14]. The simulations have been based on the real geometry of the target. This section is devoted only to those characteristics of the target that have an impact on the definition of the neutron beam. The study of the CERN neutron source has, among other, two major goals: i) to evaluate the most relevant properties of the spallation source, such as the flux and its spectral function; ii) to parameterize these properties in order to implement them in time-efficient but realistic Monte Carlo simulations necessary for most of the studies [15].

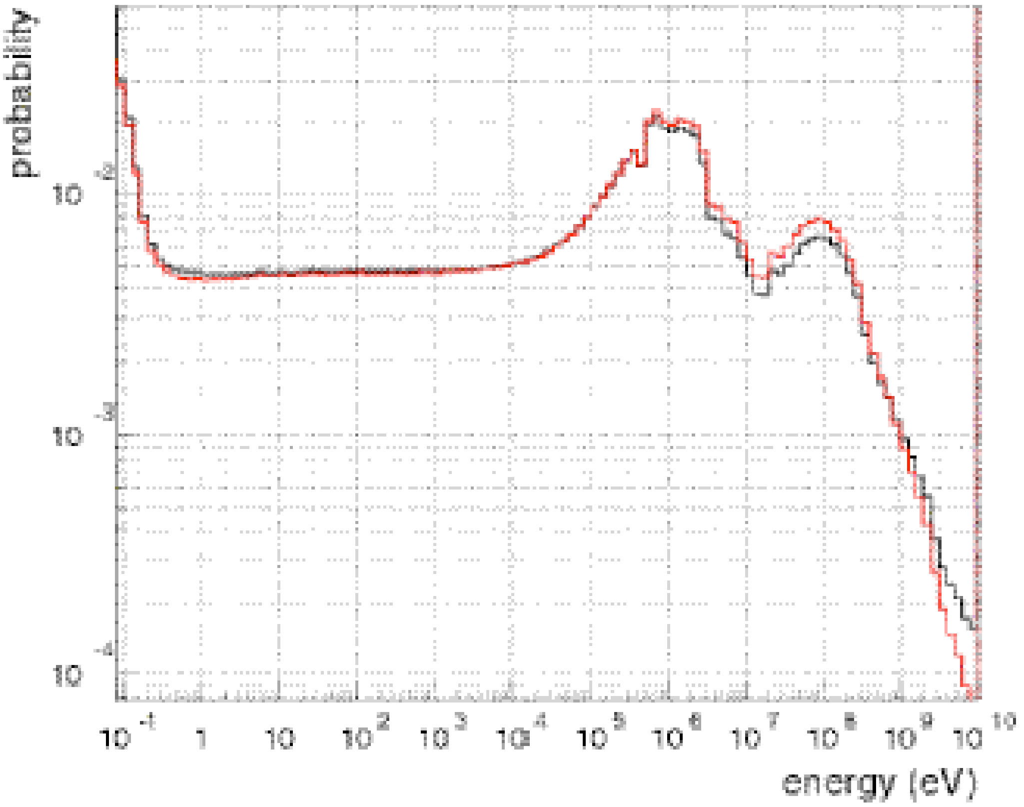

Figure 2.3: Energy distribution (normalized to unit area) of the neutrons at the exit of the Pb target after the water moderator (black) and at the sample position in the experimental area (red).

An important element of the TOF facility is that the neutron energies - due to the 20 GeV/c momentum of the PS proton beam - extend up to 20 GeV. The FLUKA Monte Carlo simulated energy spectrum of the neutrons at the exit of the water moderator of the spallation target and at the sample position in the experimental area is plotted in Figure 2.3 and shows that 38% of the neutrons emerge from the water moderator with energies below 0.3 eV. The range from 0.3 eV to 20 keV accounts for 23% of all neutrons and evidences an almost exact isolethargic behavior as a consequence of the moderation in the water. However, there is still a significant fraction of 32% of the neutrons having energies between 20 keV and 20 MeV, and a further 7% at neutron energies above 20 MeV. Obviously the two spectra in Figure 2.3 show small deviations only in the high-energy region. This hard component, the signature of the spallation reactions, differentiate substantially the energy distributions at the CERN facility from those of alternative neutron production mechanisms used in other neutron TOF facilities. As discussed later, it has important consequences on the design of the collimators and shielding elements.

The simulation of the spallation process in each of the comprehensive Monte Carlo studies would have been excessively time-consuming. In order to perform all the subsequent calculations for the background studies and the other issues effectively, the spallation neutron source was parameterized by constructing an *event generator*. The goal is to properly model the energy, the time as well as the spatial and angular distributions of the spallation neutrons. The interactions of the protons with the lead spallation target (80 x 80 x 40 cm^3) were simulated by means of FLUKA and EA-MC. A very detailed geometry of the target, the surrounding water moderator, the mechanical parts and the shielding was included. The position, energy, time, and the direction cosines of the particles emanating from the target surface linked to the TOF tube were recorded on data summary tapes (DST).

We report in this chapter the results obtained for neutrons, but details about other emerging particles can be found in references [14] and [15].

Figure 2.4 shows the reference system adopted in our parameterization as well as the variables involved. The proton beam lies in the y/z plane and enters into the target at x=y=0 cm and z=-40 cm, forming an angle of □=10° with respect to the z-axis. Such an incident angle was adopted in order to avoid the contamination of the neutron beam with the forward-directed high-energy charged particles and □-rays. However, it introduces an asymmetry in the spatial distribution of the neutron source along the y-axis. The analysis of the DST provided the one-dimensional probability distributions of the neutron x- and y-positions, p(x) and p(y), the angular distributions of their momenta, p(□) and p(□), the time, p(t), and the energy, p(E), distributions. For practical reasons, the projections of the spatial and angular distributions were grouped into eleven bins.

The strong correlation of all single-variable distributions with the neutron energy has been considered in the parameterization. Some illustrative examples can be found in Figure 2.5. The energy-time relation in the upper left panel is of fundamental importance for the precision of the TOF determination. However, for the study concerning the beam optics and the background only, this correlation can be neglected in first order approximation. The influence of the time resolution due to the different optical elements was comparatively studied by assuming that all neutrons are simultaneously emitted.

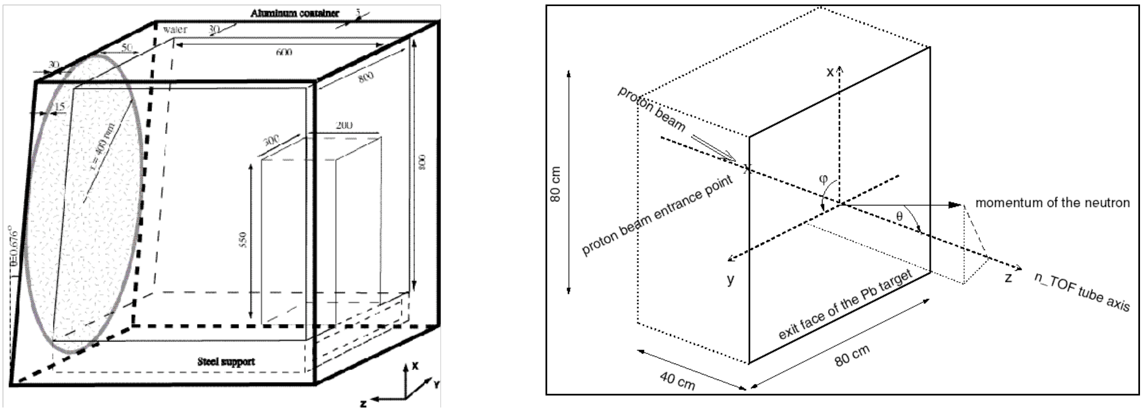

Figure 2.4: Left: Schematic view of the lead spallation target [14]. Right: The reference system defined for the neutron source parameterization. The z-axis corresponds to the axis of the time of flight tube. The x/y plane defines the exit face of the lead target. An oversimplified view of the target and its dimensions is also shown in dotted lines. The azimuthal □ angle is defined with respect to the z-axis. The polar □ angle is defined in the positive sense starting from the x-axis. The direction of the proton beam is coplanar to the y/z plane and forms an angle of □=10° with respect to the z-axis.

In the upper right panel of Figure 2.5 the spatial distributions in x and y directions are shown for the neutron energies interval between 1 MeV and 10 MeV. Both distributions are clearly not uniform and present pronounced peaks with similar r.m.s. values. As an effect of the incidence angle of the protons, the centroid of the y-distribution is displaced towards positive values, while the x-distribution remains centered at x=0. The displacement varies with neutron energy ranging from 4.1 cm for energies below 1 eV, to 6.6 cm for energies between 10 MeV and 100 MeV, and 9.8 cm for energies above 1 GeV. The r.m.s of both distributions depends on energy. For neutrons below 1 eV a broad distribution is obtained with a r.m.s of 15.9 cm, which reduces to 12.9 cm for energies between 1 MeV and 10 MeV and to 5 cm for energies above 1 GeV.

In the lower left panel, the cos(θ) distribution for energies between 10 keV and 100 keV shows that the distribution is not uniform and that there is a clear preference of the neutrons to be emitted in the forward direction. This effect is enhanced for the highest neutron energies. However, the consequences are of minor importance since only small emission angles with θ much smaller than 1° are relevant for the flux in the experimental area 185 m downstream of the target.

The lower right panel of Figure 2.5 shows the ϕ distribution for neutron energies between 100 MeV and 1 GeV. It can be seen that these neutrons are emitted more likely in the ϕ=90° direction corresponding to the direction of the proton beam, and this tendency is enhanced for neutrons above 1 GeV. However, the ϕ distributions for neutron energies below 100 MeV present a uniform behavior. This effect has the positive consequence that the neutrons of the highest energies do not follow the beam pipe direction, avoiding thus the production of a background close to the experimental area, situated 185 m away.

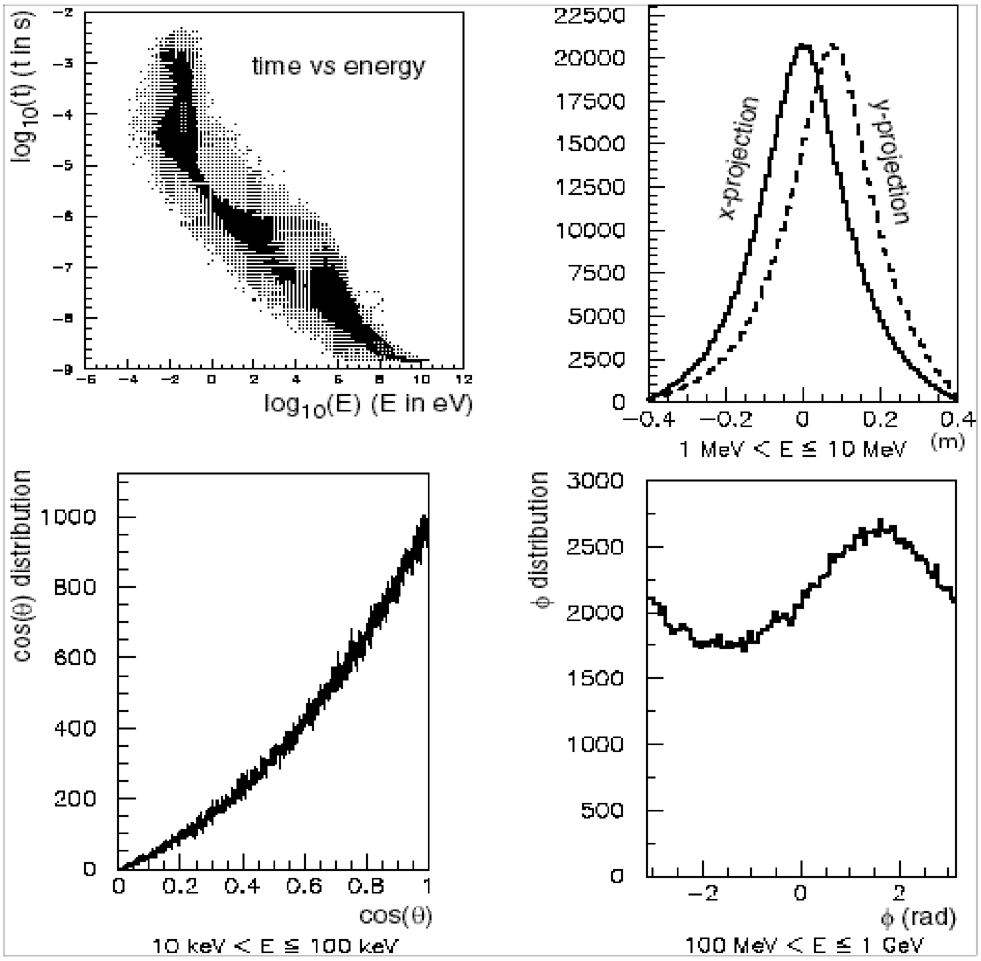

Figure 2.5: Upper left: Time-energy relation of the spallation neutrons. Upper right: x and y projections of the spatial distribution of neutrons with energies between 1 MeV and 10 MeV. Lower left: cos(θ) distribution for neutron energies between 10 keV and 100 keV. Lower right: ϕ distribution for neutron energies between 100 MeV and 1 GeV.

The influence of other correlations between the variables was found to be negligible for small emission angles. Therefore, to first order, the neutron source can be parameterized for the purpose of an *"event generator"*, as the product of the single-variable distributions depending on the energy.

Additional Monte Carlo simulations of the n_TOF target-moderator assembly have been performed independently by interfacing FLUKA with the CAMOT [16] codes, exploiting thus the FLUKA capability of dealing with high-energy nuclear interactions and the CAMOT capability of calculating the resolution function and the target-moderator efficiency.

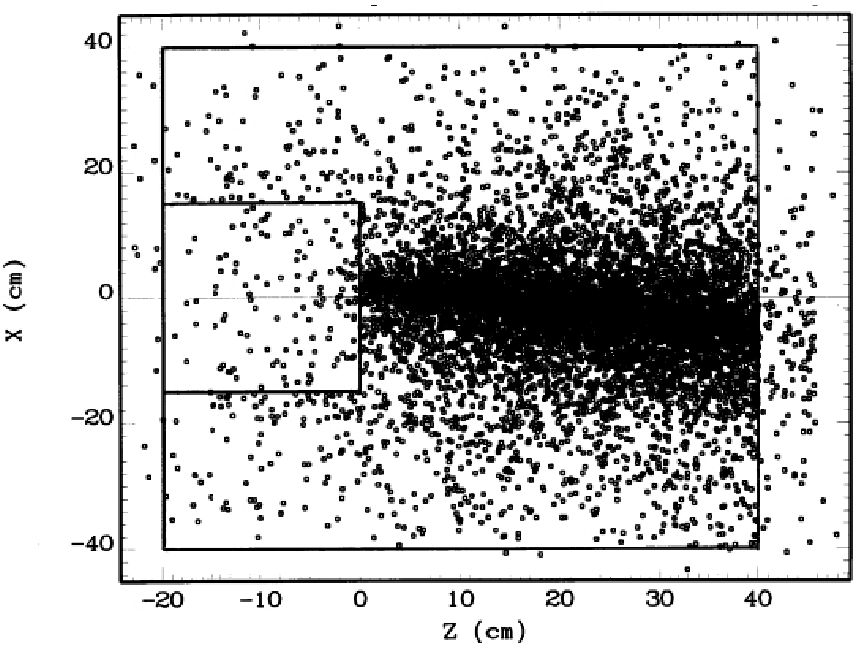

Figure 2.6: Geometrical distribution of all the neutrons with $E_n < 20$ MeV generated by 15'000 incident protons with momentum 20 GeV/c. The protons hit the target at the origin of the x-z coordinates axis.

If a neutron is generated above 20 MeV, FLUKA keeps following its history until the lower energy threshold of 20 MeV is reached, where CAMOT takes over, making use of 30-group cross-section libraries. The spatial distribution of the neutrons with energy < 20 MeV generated in the target-moderator assembly in the spallation and subsequent reaction processes is shown in Figure 2.6. All the positions shown in the figure are the result of the FLUKA simulation. From that point on, the Monte Carlo trajectories are followed by CAMOT.

Neutrons escaping from the target-moderator system are sorted by CAMOT according to their direction, energy and moderation time. The neutron energy range is divided into bins, where CAMOT assigns all neutrons with directions smaller than 0.12 steradiant around the direction of the flight-path. In this way, one obtains the number of neutrons emitted by the moderator per unit solid angle, per unit energy interval, and per incident proton, as a function of neutron energy. The resulting average neutron flux at the experimental area was found in good agreement with the data given in reference [3].

2.3 Target Zone

The target zone is the most demanding part of the TOF project since it requires not only the critical coupling of the water moderator with the vacuum of the TOF tube by means of a special window, but also a sophisticated shielding and a highly performing removal procedure.

The target zone is surrounded by marble and concrete blocks, some molded and fixed and some removable to give access to the area. Marble has the advantage over concrete in that it becomes less radioactive.

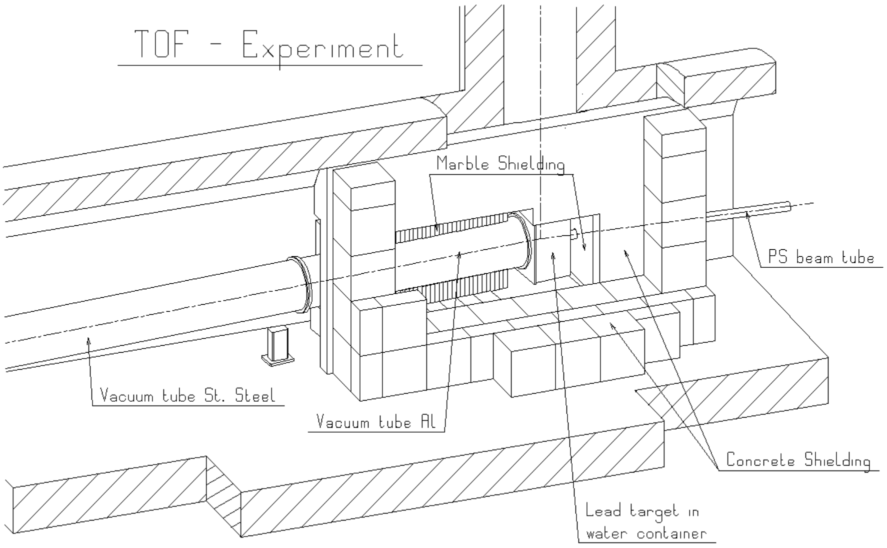

Figure 2.7: View of the target zone with the different shielding parts.

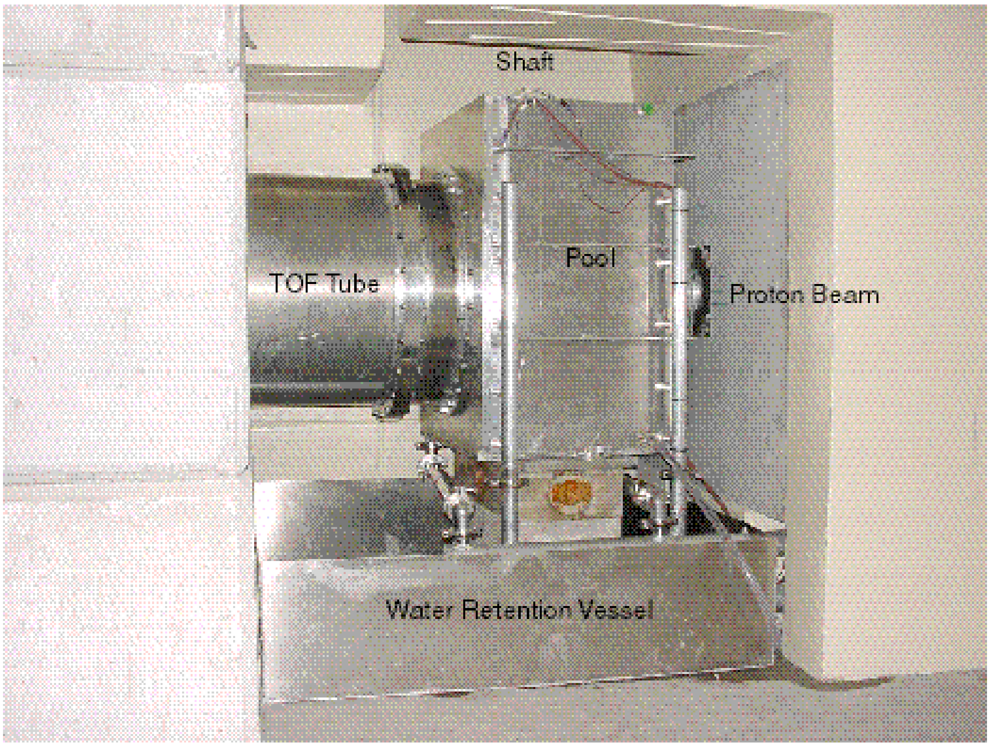

Figure 2.8: Picture of the target zone.

The fixed part of the shielding is made with concrete loaded with 1% of boron in order to capture neutrons outside of the direction of the time of flight tube more efficiently. This shielding is shown in Figure 2.7. The target is placed and removed from the pool through a vertical Shaft, of 1.3 m in diameter (Figure 2.8), joining an ISR gallery on top of it. After irradiation the target could be placed in a concrete repository located near the top of the shaft or transported in a storage zone to be defined in agreement with the recommendations of TIS (Radioprotection).

2.4 Lead Target and Support

The lead target is mounted into a stainless steel support (Figure 2.9), which is an integral part of the whole target assembly.

The lead for the target was taken from the TARC experiment [17]. Pure lead (99.99%) was chosen to ensure that impurities have a negligible effect on the neutron flux. Information on the concentration levels for 11 elements was obtained by measurements (see Table 2.1).

Although the target size optimization favored a circular cross section in the beam direction, a square shape of 80 cm length of side was constructed because of the extreme difficulty to machine lead to a round shape.

Figure 2.9: Picture of the Target Assembly.

Therefore nine blocs of 300×300×600 mm^3 has been used to construct such a target and to reach the optimal size as defined in [3]. For this, the length of the central block and of the block below will be reduced to 400 mm. The shorter central block now provides the right depth. The shorter block below the central block is needed in order to extract the target from the water tank. In order to cope with the 1.18% of slope of the time of flight tube in the tunnel, all the lead blocks are machined to 0.676° with respect to the vertical line at the outlet face.

Element	**Concentration** (ppmw)	**Error Spread** (ppmw)	**Systematic Error** (ppmw)	**Total Error** (ppmw)
Na	0.006	0.007	0.0001	0.0075
Mg	0.003	0.005	0.0006	0.005
Al	0.02	0.01	0.004	0.01
Cu	0.09	0.2	0.01	0.2
Ag	3.78	0.6	0.07	0.6
Cd	0.09	0.04	0.006	0.045
Te	0.215	0.09	0.025	0.09
Sb	0.14	0.14	0.006	0.14
Tl	4.6	1.3	0.3	1.4
Bi	19.0	2.8	0.3	2.8
Au	0.0009	0.0002	0.00035	0.0004

Table 2.1: Summary of measured impurity concentrations for manufactured lead blocks. The systematic error is the error quoted by the laboratory, which performed the measurement; the third column shows the spread between all measurements of a given sample. The total error is the quadratic sum of the two contributions.

The complete target is put on a stainless steel support, which allows handling and transportation. The support is part of the target and has to be changed if a new target is to be installed.

2.5 The Cooling System

The heat dissipation in the target is expected to reach a maximum of 10 kW if 5 Dedicated Pulses from the PS reach the lead target during 16.8s. The cooling system has been designed for the nominal conditions defined in the proposal, namely 4 Dedicated Pulses of 7×10^{12} protons every Supercycle of 14.4 s.

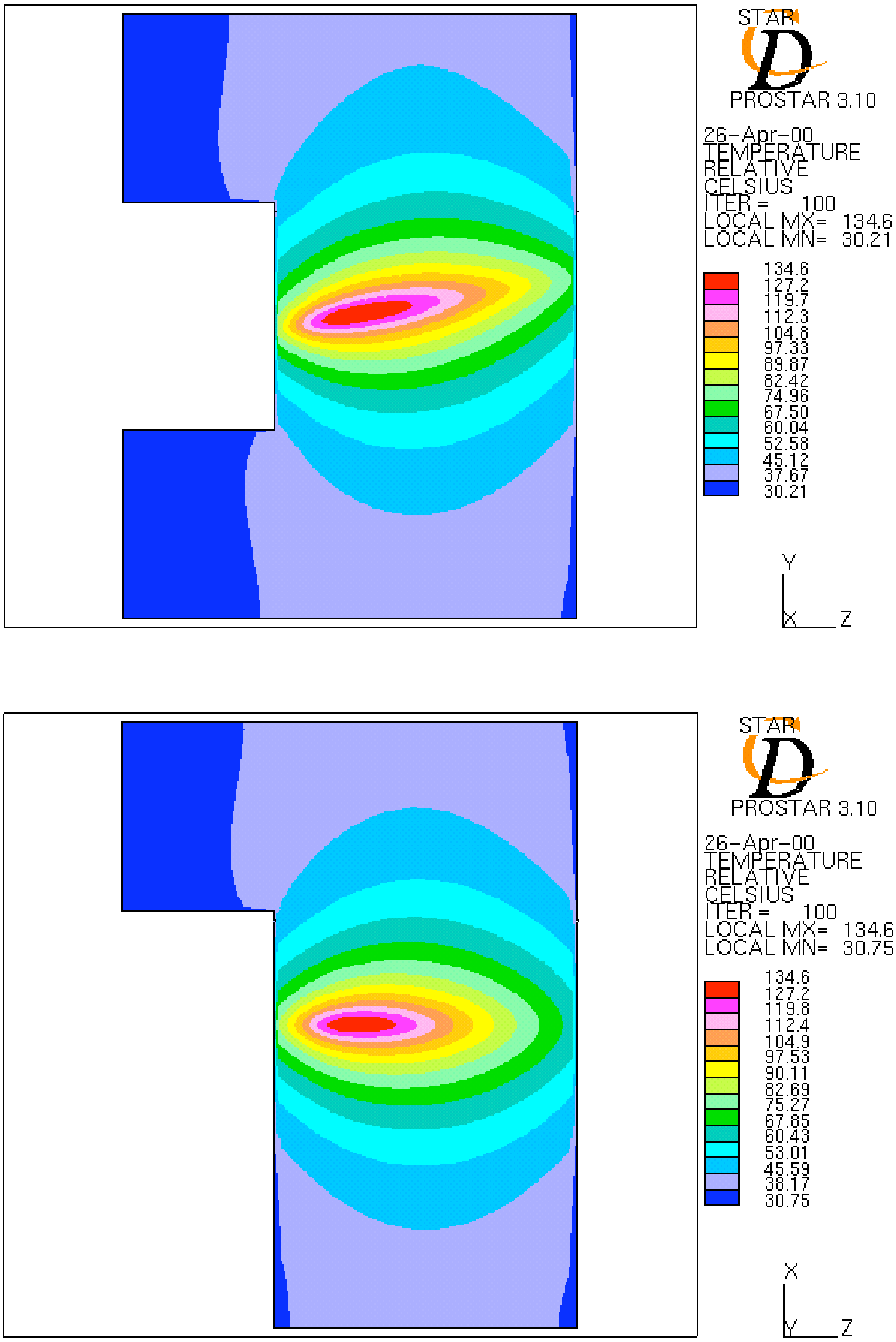

Figure 2.10: Temperature distribution inside the lead target for a water flow of 6 l/s and a water temperature of 30 °C.

The temperature inside the target and the heat of the target's outer face have been simulated for a water flow of 6 l/s and a water temperature of 30°C, with the result shown in Figure 2.10. The lead Target is plunged in a pool with a water circulation in closed loop used to remove the heat and as neutron moderator. The maximum temperature inside the target does not exceed ~140°C. The target assembly is put into a pool filled with demineralized water. To avoid unnecessary activation the tank is made out of an aluminum alloy (ISO Al-Si1-Mg-Mn 6082). At the entrance side a cylindrical niche ending with a 2 mm thick window, reduces the proton beam path in water to only 30 mm to avoid unnecessary interaction. At the exit face of the tank the distance between the wall and the lead target is 50 mm, providing the necessary amount of water for the moderation of the neutrons. The water tank is covered by an aluminum alloy plate mounted directly onto the target support and will be removed with it (see Figure 2.9).

2.5.1 *Principle of the Target Cooling System*

The principle of the cooling system is described in Figure 2.11.

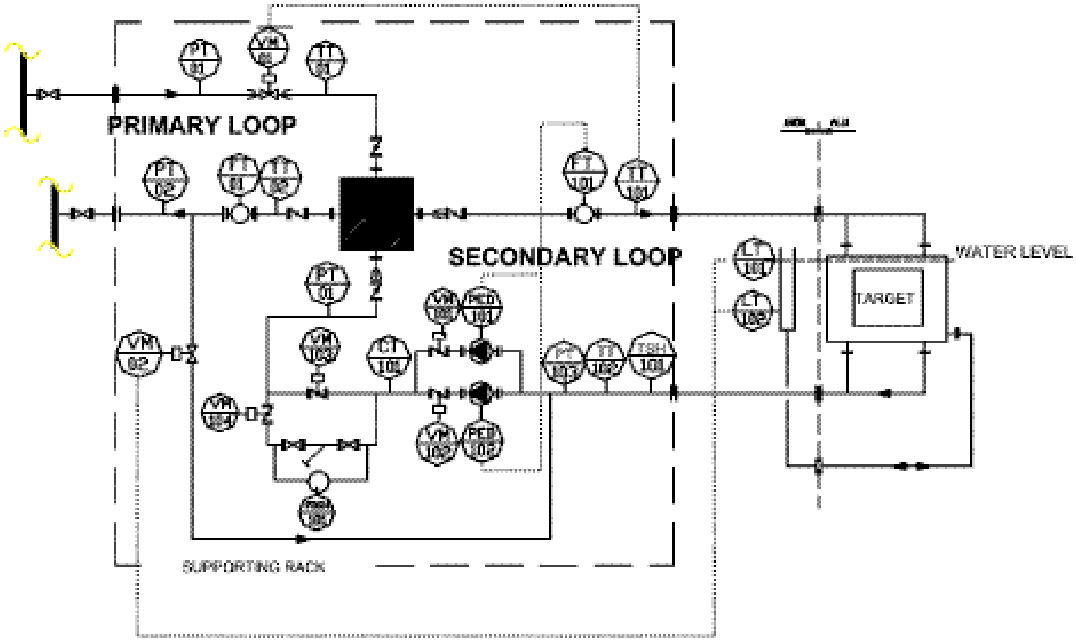

Figure 2.11: Schematic principle of the cooling circuit.

The hydraulic circuit is mainly constituted of a heat exchanger and two independent loops:

- the first one (primary loop) is connected to the inlet and return lines of the magnet cooling circuit;
- the second one (secondary loop) is connected to the target's tank and provides the water flow in it.

The water, demineralized in both loops, is supplied by the same circuit used for the cooling of the FTN line.

On the primary loop side, the heat exchanger is connected to the inlet and the return line of the magnet cooling circuit. The differential pressure between these two lines is about 8-12 bar with an absolute pressure of 10-14 bar at inlet line and 2-3 bar at return line.

On the secondary loop side, the heat exchanger is connected to the target tank, which will be open to the atmosphere. The target tank will act as an expansion vessel. The pressure is about 1 to 1.5 bar in the secondary loop.

The water temperature at the primary loop inlet is about 28-31°C. This loop is on the cold side of the heat exchanger and cools the water down in the secondary.

The flow rate in the secondary loop is set at a constant value (about 22 m^3/h). The secondary loop is filled-up via a derivation coming from the primary loop. It has been decided to make this operation only manually (VM2 not connected) to avoid any run over. During three running periods it has not been necessary to refill the secondary loop. At the end of the run the secondary loop is emptied into a dedicated container located near the station and the same water is used for the next running period.

All the precautions (retention vessels) have been taken to avoid any spill of contaminated water in the sewer.

2.5.2 *Main Features of the Control and Regulation System*

The control system will use a PLC monitored, via Ethernet, by a PC located in the control room. This PC will use the Wizcon supervision Software. The cooling system works independently from the status of the Ethernet connection.

The regulation valve (VM01) controls the flow rate on the primary loop in order to obtain the right temperature (measured by the temperature transmitter TT101).

Two identical pumps (PED101 and PED102) are installed in parallel. Only one will be in operation normally and will be backed up by the other in case of breakdown; two electrically actuated butterfly valves (VM101 and VM102) allow the flow in one pump or the other.

A flowrate meter transmitter (FT101), installed in the secondary loop, controls the pump velocity – via the PLC – in order to have a flow rate in the loop of about 22 m^3/h.

A cut-off differential thermostat (TSH101) will be installed to prevent any temperature rise over 50°C. The free potential contact will be dealt with by the regulation and control system.

The Control System provides hardware interlock signal to automatically cut off the proton beam in case of problems.

2.5.3 *Measurement of the Target Temperature*

To monitor the temperature inside the lead 6 thermocouples are fixed on the target. The most useful information is coming from that located in the centre where the heat is reaching its maximum. In Figure 2.12 is reported a measurement made during the commissioning. The reported cycle shows the temperature increase in the centre of the target in response of one, two, three and four Dedicated Pulses of ~ 7x10^{12} protons every Supercycle of 16.8 s.

In the enlarged image is reported the fine structure of the temperature change for one pulse per Supercycle.

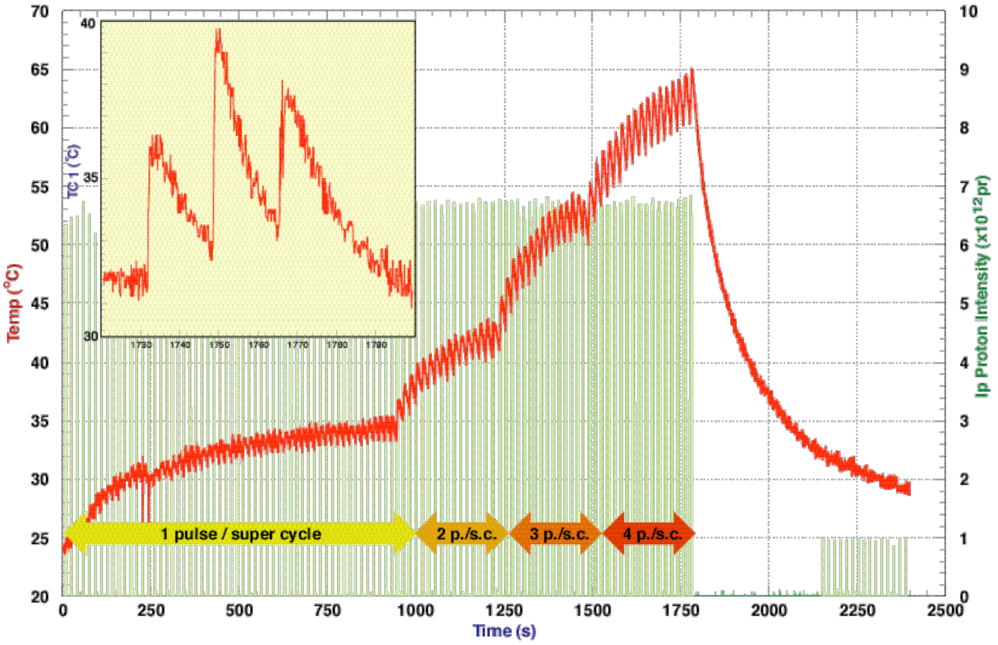

Figure 2.12: Temperature behavior in the center of the Target.

2.6 The Window

The aluminum alloy (AA 6082) window of 800 mm diameter is fixed onto the face of the water tank (Figure 2.13) which separates it from the time of flight tube. The window is welded directly onto a 250 mm long aluminum alloy tube. A Helicoflex ring provides the necessary leak tightness between the water and the vacuum inside the time of flight tube. A flange is welded onto the end of this, which connects directly to the time of flight tube. This construction allows the easy mounting of the window from the outside of the tank and the easy removal of the tank from the target zone.

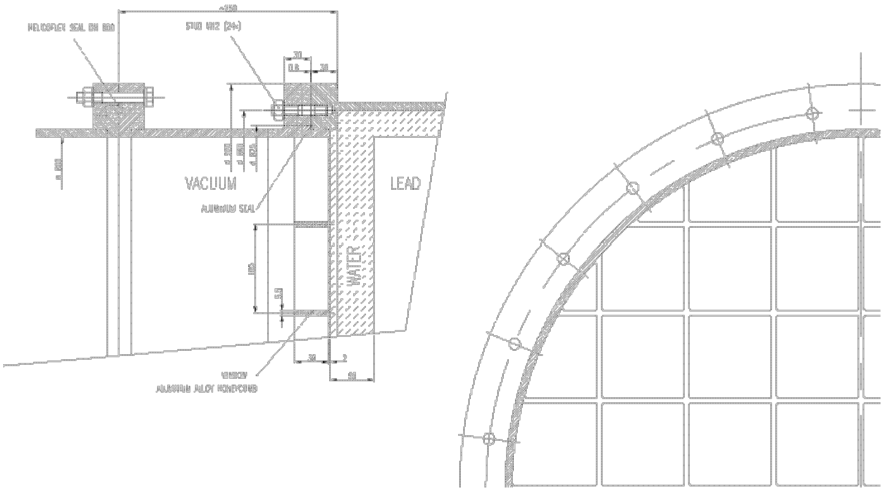

Figure 2.13: Aluminum alloy window welded to a 250 mm long aluminum alloy tube and fixed on the tank and the time of flight tube. On the right side the grid structure of the window is shown.

The window itself represents a critical part of the project. On one hand it must be solid enough to separate the water from the vacuum (pressure difference = 1.2 bar) and remain flat (maximum deflection allowed in the center ≤ 2 mm) in order to guarantee a constant water moderation of 5 cm, therefore not affecting the energy resolution. On the other hand it should be as light as possible to avoid neutron scattering and made of the right material not to absorb too many neutrons. Furthermore, it should be radiation resistant since the dose rate accumulated in one year could reach a few 10^6 Gray depending on the running period.

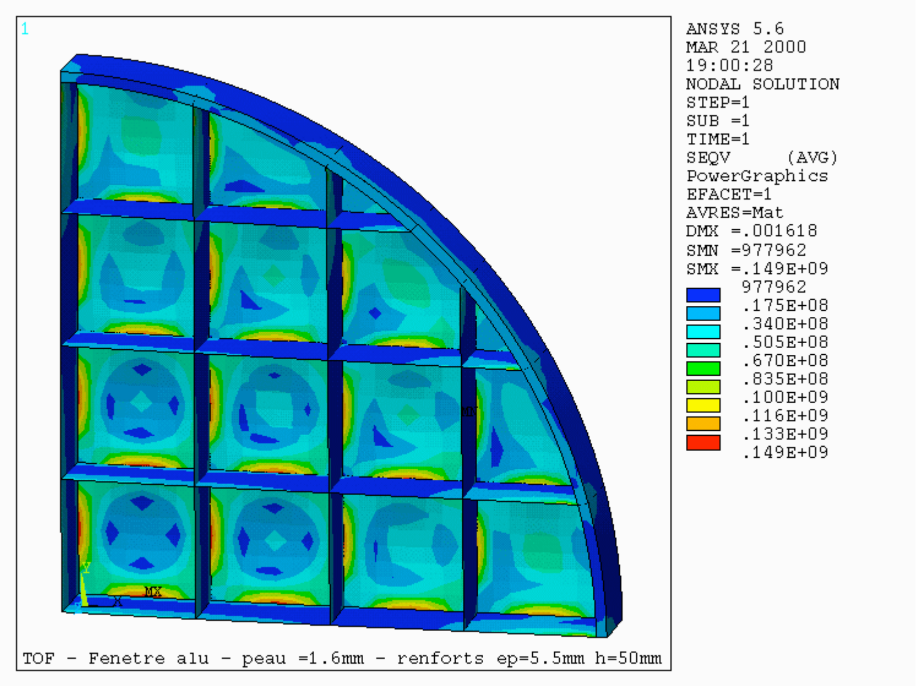

Figure 2.14: ANSYS Simulation of the Window.

We have chosen the aluminum alloy as material for the window instead of carbon fiber because of the lack of information on the resin and glue used in its construction. The Al alloy window has the advantage that the material composition is known, therefore also the neutron spectrum, and that the mechanical stability is not influenced by the radiation.

The window itself is made of a 1.6 mm thick plate, reinforced by a grid 50 mm thick with sides of 100 mm in length. The struts of the grid have a thickness of 5.5 mm. This window will be machined in one piece from a thick Al alloy plate. The "equivalent" total thickness of the Al alloy is 6.17 mm. The face of the window with the grid is mounted towards the vacuum tube. The deformation of the window amounts to 1.96 mm in the center. The mechanical simulation of the window is reported in Figure 2.14.

2.7 The Handling of the Target

The target on its stainless steel support will be lowered through the 1.3 m diameter shaft inside the water tank. During the operation of the TOF facility, this shaft is completely closed off by concrete blocks and on top an additional iron shielding is added to keep the radiation below 1 μSv/h. During the yearly shutdown, the target might be extracted if maintenance work is necessary at the target station.

2.7.1 Displacements of the Target

In Figure 2.15 is shown the layout of the area. The various levels concerned by the target handling are:

- TT2-A Level (TT2-A-L), where the target stays during data taking;
- TT-2 Level (TT-2-L);
- ISR-I8 Lower Level (ISR-LL), practically equal to that of the I8 entrance;
- Service Gallery Cellar (SG-C), about 60 cm lower than ISR-LL;
- Service Gallery (SG), where the monorail is located, about 250 cm higher than ISR-LL.

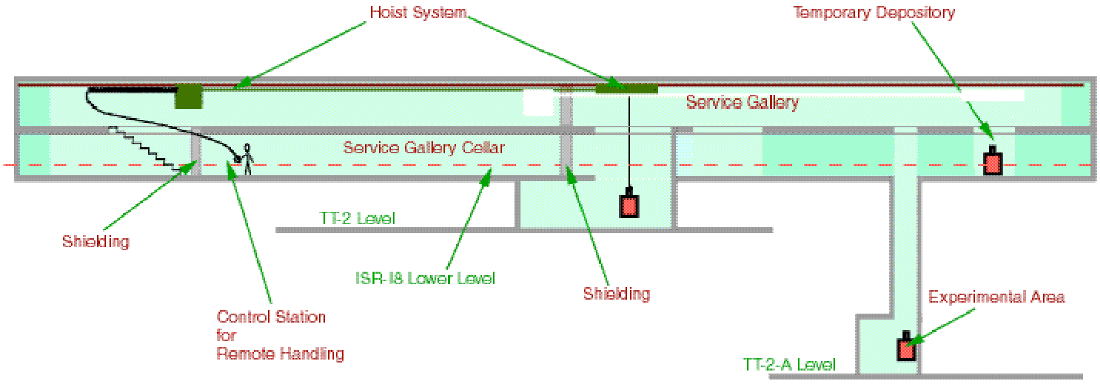

Figure 2.15: Lay out of the displacements of the Lead Target Assembly.

For practical reasons the movements of the target are limited to the existing monorail axis, such an approach presenting the advantage to concentrate the efforts to have a reliable hoist system with only two movements, longitudinal and vertical.

The various movements of the target can be described as follows:

- installation of the target (presumably non-radioactive) in TT2-A through the existing shaft from the SG;
- removal of the radioactive target from TT2-A through the existing shaft up to the SG;

- installation of the radioactive target in the temporary repository SG-C located at the SG end;
- removal of the radioactive target from the temporary repository SG-C located at the SG end for permanent storage. For this operation the radioactive target must be removed from TT2-A-L up to ISR-LL passing through the SG.

2.7.2 *Remote Handling with Video Cameras*

It has been agreed by the Radioprotection Group (TIS) that a system using several video cameras can be used to do all the required movements of a radioactive Target.

There is a set of video cameras, equipped with a remote control on the view angle and the zoom, mounted in SG to monitor the movements of the target in the gallery itself. At every place where a vertical movement is required, a fixed camera monitors the displacement. A small camera mounted on the hook provides the fine positioning of the hook inside the inlet supporting the lead.

The operator has the possibility to control the cameras by using a joystick and a TV monitor with four different views on the same screen.

A back-up solution is also foreseen and the indication of the status of micro-switches giving the crane position in various strategic points is also available. The video monitoring is shown in Figure 2.16.

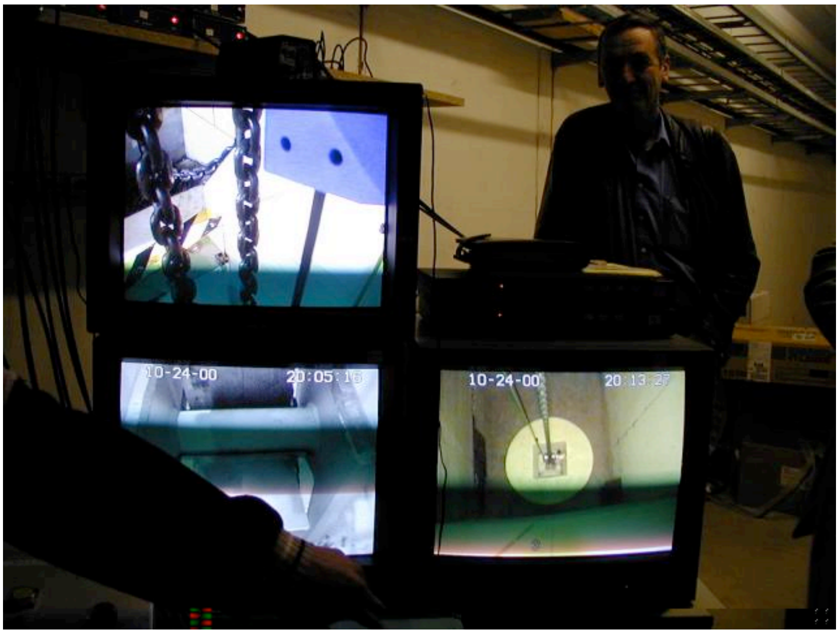

Figure 2.16: Remote control for the Target Handling.

2.7.3 *The Temporary Repository*

After the analysis of the first measurement, it has been agreed that a Temporary Repository for one target is sufficient as there is no evidence to plan the replacement of the existing target. The other important reason not to foresee additional storing places for irradiated targets, is to limit the accumulation in the CERN site of radioactive waste. A pit accessible with the existing crane, has been constructed at the end of the Service Gallery. A stainless steel container is installed inside the pit to avoid contamination in case of water flood.

2.7.4 *The Crane Modification*

The system available today is not certified for the handling of a target irradiated at the nominal intensity. The main concern is to face the situation in which the crane stops while the target is hanging in the air without the possibility of any intervention.

The problem could be divided in two parts:

- concerning the horizontal displacement there are no problems because the movement and related controls are 25 m away from the hook. The shielding built in the Service Gallery is sufficient to protect against the target radioactivity the person in charge of the maintenance;
- concerning the vertical movement a solution using a crane certified for the handling of radioactive loads must be envisaged. A design made by a specialized firm has already been done and this solution could be implemented as soon as a budget will be allocated for this item.

2.7.5 Removal of the Irradiated Target to a Permanent Storage

The activated target will be removed from the temporary repository after cooling down (or directly from TT2-A) using the monorail and the remote control system. It should be placed in a container at the level of the SG-C or at the level of TT-2. The container must satisfy the international rules for transportation of radioactive materials.

The date of removal of the irradiated target (hot or cooled down) directly influences the dimension of the container but, in both cases, the container will be closed with a cover put in place through the evacuation hole.

This operation needs complete study in tight co-operation with the Radioprotection group in the TIS Division.

3 THE TOF TUBE

The Time of Flight tube will starts directly behind the window and ends 200 m away at the end of the Escape Lane. It is ideally divided in two parts: the Primary Area (up to 150 m) and the Secondary Area having different access procedures as described in a following chapter. Due to the geometry of the existing tunnel, the tube is not located in the same position in the cross section. To reach the nominal length of 200 m, the tube has a slope of 1.16 % with respect to the flat part of the tunnel. The angle on the horizontal plane between the proton beam axis and the neutron beam is 10° in order to minimize the collection of unwanted secondary particles in the Experimental Area. A Sweeping Magnet at a distance of ~ 150 m is used to remove all the remaining charged particles.

3.1 The n_TOF Tube Sectors

As described in 3.6, the window and the 250 mm long aluminum alloy tube (AA6082) ø=800 mm, is directly mounted onto the water tank. Then a 3.9 m sector of the same material and dimension is flanged onto this short tube and traverses the 2 m of marble in front of the target. From there, a stainless steel tube (304 L) with different diameters, as shown in Figure 3.1 and Figure 3.2, goes up to the end of the Facility. The distances are referred from center of the lead target, to have the Time of Flight path 0.35 m must be subtracted.

The first 24 m of the stainless steel tube is divided into two parts with vacuum flanges at the end. This allows their removal during shutdown to access the target area with a forklift. In one 12 m long sector, three additional windows of diameter ø=600 mm are mounted on the side to eventually insert equipment for measurements at very high neutron flux.

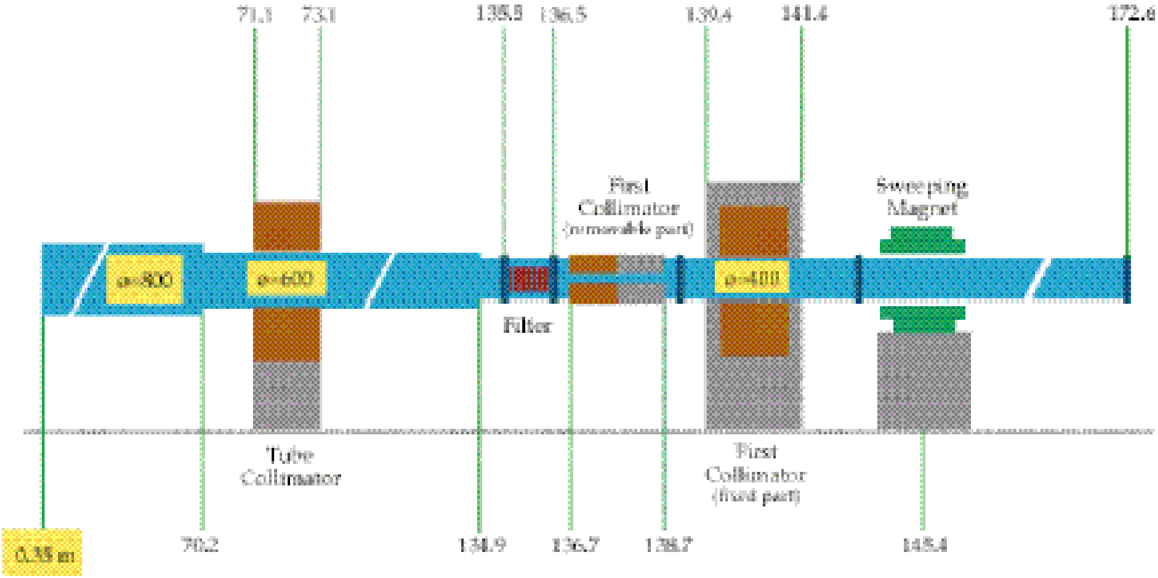

Figure 3.1: Elements of the TOF Tube in the first 172 m.

At the end of the ø=800 mm tube (~ 70 m from the target), a reduction piece of ø=600 mm is welded. Immediately after there is an iron shielding with a cross section of $1.80 \times 1.80\ m^2$ where the left side (seen in the beam direction) is reduced to the available space to the tunnel wall. This iron shielding is embedded in 40 cm of concrete.

At ~ 140 m from the target, there is the second diameter reduction from ø=600 mm to ø=400 mm and immediately after is installed the First Collimator with ø=110 mm. An iron shielding of $1.20 \times 1.20\ m^2$ and 1 m long is embedded in concrete with a total thickness of 2 m. In this region the shielding fills the whole tunnel in order to remove the background produced by the Collimator. On the free side of the tunnel, a 1.6 m wide concrete shielding mounted on wheels allow a forklift to go through. The Primary Area of the Facility ends at this point. When in operation, the access to the Secondary Area is made via a chicane closed by a door.

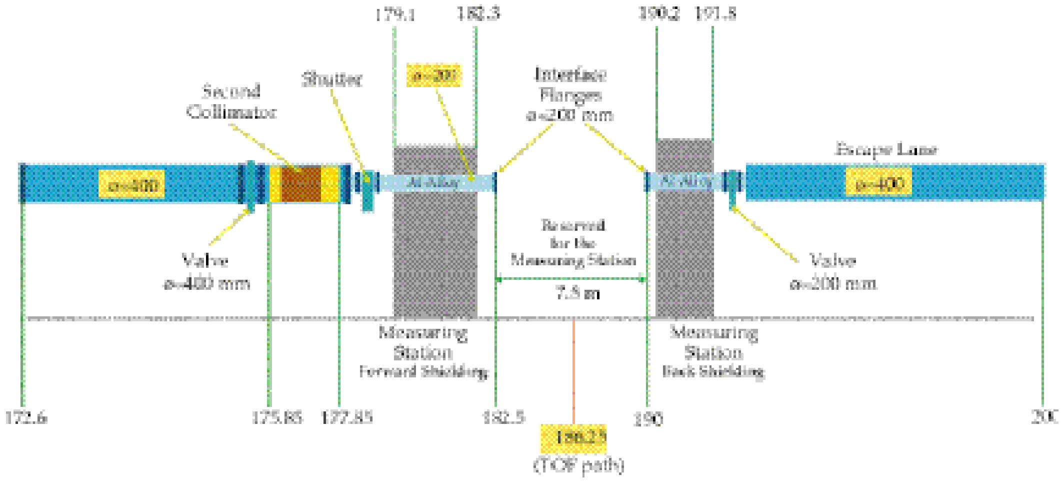

Figure 3.2: Elements of the TOF Tube after the first 172 m.

In the Secondary Area (Figure 3.3) the ø=400 mm tube runs through the Sweeping Magnet and the Muon Shielding ending with a valve at 175 m. At this point a reduction ø=400 mm to ø=200 mm precede the Second Collimator.

Starting from this point the TOF tube is made with an aluminum alloy. Before entering in the Experimental Area the tube crosses a 3.2 m deep concrete shielding equipped with a removable part to allow the passage of a forklift. A chicane equipped with a door is used to link these two zones.

The Experimental area is defined by two flanges of diameter ø=200 mm distant 7.5 m from one another. The lay out in this zone depends on the type of detector installed.

At the exit of the area there is an additional concrete shielding with a simple chicane giving access to the tube end. There, a valve ø=200 mm is installed to define the tube sector in the Experimental Area.

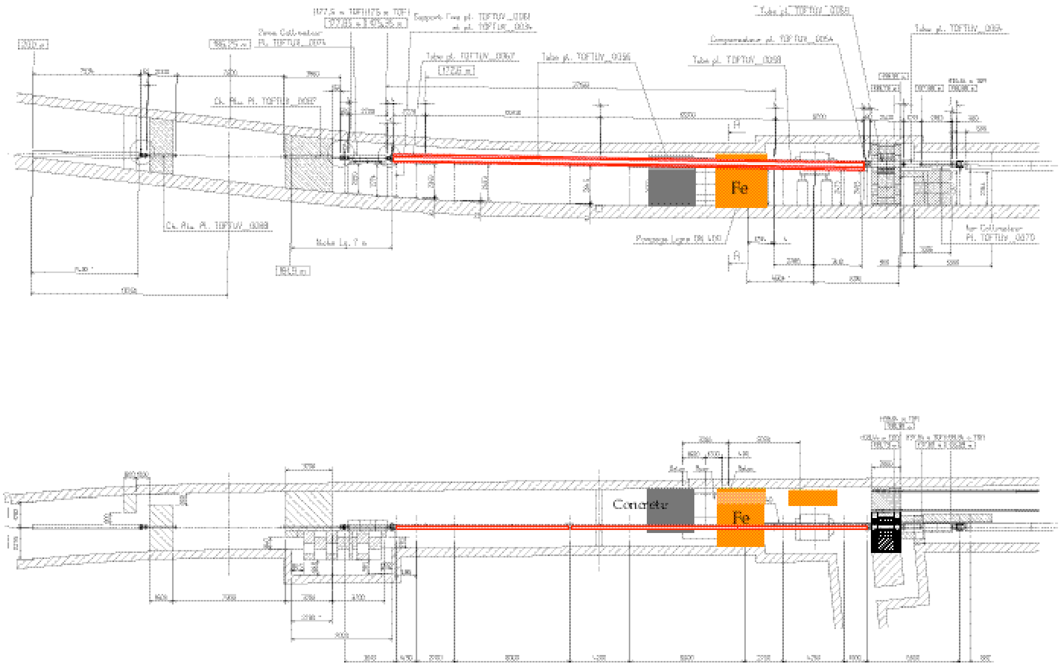

Figure 3.3: Lay out of the last 50 m of the TOF tube highlighting the Muon Shielding.

Finally, the last 8 m of the TOF tube are made with a sector of ø=400 mm called the Neutron Escape Lane (NEL).

3.2 The Vacuum System

The vacuum requirement for the TOF tube is only 1 mbar. There are three defined vacuum sectors:

- sector 1: from the target up to the ø=400 mm valve at ~ 175 m, defined as TOF Tube. Three double stage, rotary vane pumps (35 m^3/h) are used to pump this sector;
- sector 2: from the valve at ~ 175 m up to the valve (ø=200 mm) at ~ 192 m, defined as Experimental Area. One rotary vane pump is dedicated to this sector;
- sector 3: from the valve at ~ 192 m up to the end, defined as Neutron Escape Lane. One additional rotary vane pump is dedicated to this sector.

The time necessary to reach the nominal working pressure in Sector 1 is shown in Figure 3.4. A typical vacuum of few 10^{-2} mb is reached in less than 12 hours. For the other sectors the pumping time is of few hours.

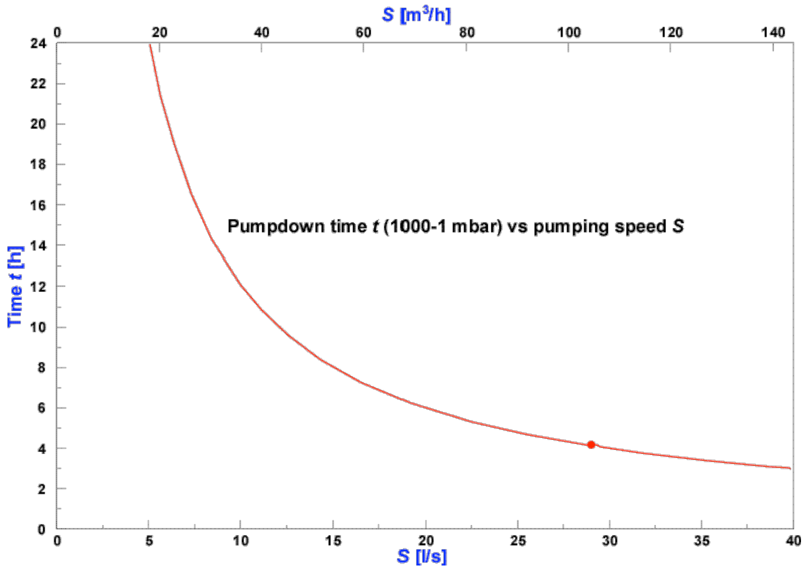

Figure 3.4: Pumping time for the time of flight tube.

For safety reasons the two valves defining the Experimental Area are automatically closed by the Control Access System in case a person access the area.

The pressure value in the three sectors and the status of the valves is permanently monitored in the Control Room. This information is also available through Ethernet in the equipment dedicated to the Facility Slow Control.

3.3 The Sweeping Magnet

The natural choice consists in using a dipole magnet to sweep away the charged particles that contaminate the neutron beam. This magnet is a standard M200 magnet used in the beam transfer lines at the PS. Only the gap has been opened to 410 mm in order to allow the time of flight tube to pass through.

3.3.1 General Characteristics of the Sweeping Magnet

The angular acceptance of the beam line can be computed under the assumption that the decays in flight of the charged particles generated by the spallation process can be neglected. Using this hypothesis, the geometry of the beam line allows estimating the maximum angle θ_{max} of a charged particle reaching the sweeping magnet located *L* meters from the beginning of the line, namely

$$\theta_{max} \approx \frac{d_i + d_{mag}}{2L}$$

where di represents the diameter of the beam pipe at the entrance of the beam line and dmag the diameter at the magnet location. Furthermore, a deflection angle given by

$$\theta_{\mathrm{def}} \approx \frac{d_{\mathrm{mag}}}{(l-L)}$$

allows the deflection of charged particles traveling parallel to the beam pipe axis and near its walls so that they hit the opposite side of the pipe *(l-L)* meters downstream from the sweeping magnet. Hence, the maximum deflection angle to be produced by the magnet should be given by

$$\theta_{\mathrm{mag}} = \theta_{\mathrm{max}} + \theta_{\mathrm{def}} \approx \frac{(l-L)d_i + (l+L)d_{\mathrm{mag}}}{2L(l-L)}$$

Neither the position *L* of the sweeping magnet nor the parameter *l* can be chosen freely. In the new version of the TOF channel, the position of the sweeping magnet has been changed with respect to the previous layout. Realistic values of the parameters *L* and *l* are now 140 m and 15 m respectively. Then one obtains

$$\theta_{\mathrm{mag}} = 26.67\ \mathrm{mrad}$$

To determine the actual strength of the required magnetic field, it is necessary to evaluate the maximum kinetic momentum p_{max} of the charged particles to be deflected. According to the simulations reported in PART III, it has been decided to define the cut-off at the value pmax = 10 GeV/c. From this, one obtains the integrated magnetic field of the sweeping magnet, namely

$$(Bl)_{mag} = \theta_{mag} \cdot (B\rho)_{\mathrm{max}} = 1.03\ Tm$$

As a remark, a hypothetical secondary particle having a kinetic momentum equal to 20 GeV/c would reach the pipe walls about 30 m downstream from the sweeping magnet under the effect of the computed angular kick $(Bl)_{mag}$.

3.3.2 Performance Simulation of an Electromagnetic Sweeping Magnet

To reduce the costs, the approach has been to look for a suitable magnet among those available in the CERN stock. The best candidate is the M200-type magnet [18]. This is a 2m long magnet with a variable height gap. The gap size can be changed by varying the width of a special spacing plate installed in the iron yoke.

Figure 3.5: The M200-type magnet used as sweeping magnet.

This would allow the gap to be increased up to 440 mm by simply inserting a specially designed ARMCO spacing plate 330 mm thick (Figure 3.5).

TYPE	2 M BENDING MAGNET. STRAIGHT POLES.
Pole face [mm2]	2000×520
Gap height [mm]	110, 140 (nominal), 170, 200
Bending power [T m]	3.63
Resistance at 20 °C [Ohm]	0.195
Max. temperature	40°C at inlet and 80°C at outlet
Max. power [kW]	140
Water flow [l/min]	66
Weight of magnet [Kg]	30000
Weight of base [Kg]	6000

Table 3.1: Main parameters of the M200-type magnet (unmodified).

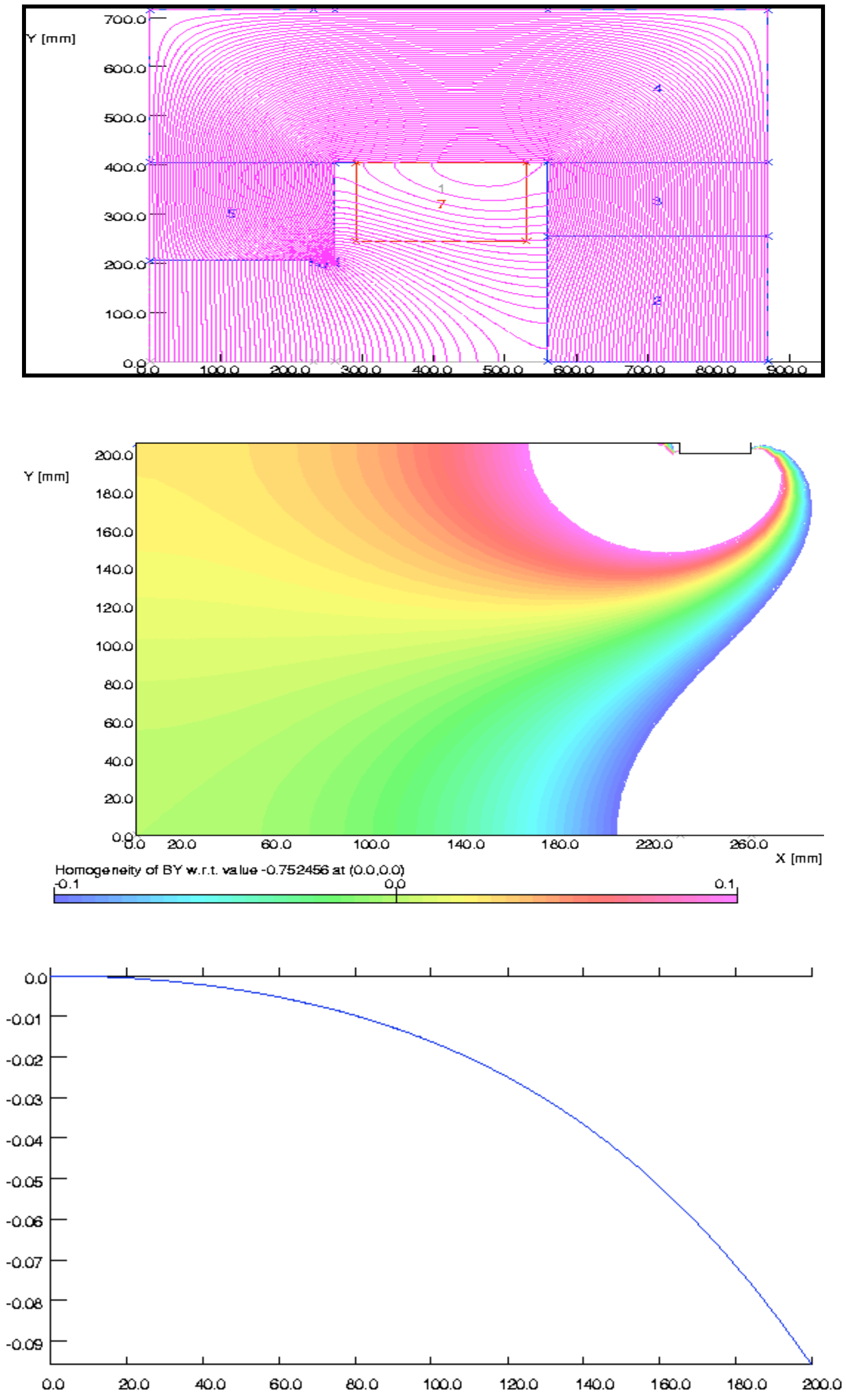

Figure 3.6: Magnetic properties of the M200-type with 410 mm gap. The field lines are shown in the upper part. In the center, the contour plot of the field distribution in the magnet gap is plotted. In the lower part, the field homogeneity is presented.

As far as the magnetic field is concerned, the maximum integrated field is about 3.63 T m. A simulation of the magnetic performance of this type of magnet has been carried out using the OPERA program (for more details on the results of the numerical simulations see Ref. [19]). The measured peak field is 1.73 T and this value agrees with the result of the numerical simulations within 2%. Therefore, one can be confident that the model used is also capable of correctly simulating the situation with an increased gap size. The main parameters of the M200-type magnet are summarized in Table 3.1.The increase in the gap size will result in a drop of the magnetic field produced, which is approximately proportional to the ratio of the two gap sizes. Therefore, it is expected to have an overall reduction by a factor of three with respect to the nominal layout (140 mm gap size). The numerical simulations shown in Figure 3.6 confirm this trend.

The peak field reaches a value of 0.75 T, thus giving an integrated field of about 1.5 T m. This is a rather conservative estimate, as the magnetic length will be bigger than the mechanical length of the magnet, due to the very large gap size. The field homogeneity is about 10%, but this is not a major source of concern in this specific case. In fact, the field quality is not relevant as long as the minimum integrated field is high enough to deflect the charged particles and this is certainly the case for the field drop obtained with numerical simulations. For this reason, the possibility of modifying the shims in order to improve the field quality has not been taken into account.

An important point is that such a magnet has already been installed in regions with a high degree of radioactivity (primary areas of the East Hall). However, one should keep in mind that the weak point, as far as radiation hardness is concerned, is the resin used for the magnet coils. Typical values of integrated doses sustainable by the resins used to build coils are of the order of 5×10^{7} Gy [20].

3.4 The Filter Station

In order to facilitate background studies in n_TOF experiments, a filter station with eight positions was installed at 140 m from the neutron target, just in front of the first collimator. Each position can hold a filter consisting of materials with strong neutron resonances. The filters are chosen thick enough that the neutron beam is completely absorbed at the energies of these resonances. Since the filter station cannot be accessed during the runs, it is remotely operated from the control room.

The individual filters can be moved in and out of beam by means of pneumatic drives. Their actual positions are monitored by switches at the respective end positions, which are recorded and automatically documented in the software protocols. Figure 3.7 illustrates the mechanics of the filter station, showing the three flanges, which carry the pneumatic drives with the filters.

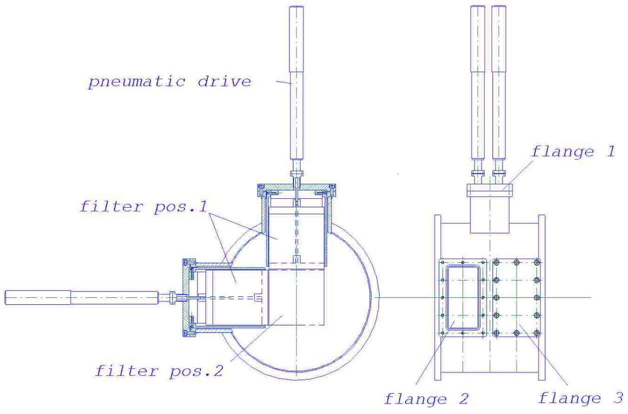

Figure 3.7: The filter station. The position of the filter foils and the pneumatic drives are indicated in the front view (left), whereas the side view (right) shows the arrangement of the flanges.

At present, silver, tungsten, cobalt, molybdenum, and aluminum filters are installed, which are effective at neutron energies of 5.1, 18.8, 45, 132, $3.5 \cdot 10^{4}$, and $8.7 \cdot 10^{4}$ eV.

4 THE EXPERIMENTAL AREA

4.1 The Experimental Area Layout

The experimental area is situated after the shielding of the BSC collimator at 182.5 m downstream from the spallation target and extends up to 190 m. The detectors, the front-end electronics and the necessary auxiliary equipment are situated in this low background area, called the Measuring Station. After the measuring station the neutron beam enters in the Neutron Escape Line (NEL).

Between the two ends of the TOF tube, at 182.5 and 190 m, a specially designed "Reaction Chamber" (RC) (Figure 4.1) comprising the monitor detectors, the samples to be measured, the sample exchanger, the PPACs and FIC detectors, etc., will provide the mechanical support and the required vacuum. The flux monitor detectors and the samples will be installed in vacuum. All flanges in the experimental area are in general of ISO-K NW 200 type and can accept 200 mm O-rings or Helicoflex vacuum seals. The flanges of the sample exchanger are of 50 mm type with O-rings. The RC will be connected downstream of the beam with the NEL, which is a 4.15 m vacuum tube of 40 cm diameter with appropriate shielding, which prevents neutrons from backscattering towards the samples.

Since the experimental area is situated in the rising part of the tunnel, a false floor of aluminum grating was installed in order to have a horizontal working area. A central aluminum I-beam consisting of two I-beams of 176 mm by 179 mm in the axis of the beam for the whole length of the area, fixed to the concrete floor of the tunnel, provides a support of 352 mm width for the fixation of the various detectors (two fixation grooves spaced 244 mm) and the central part of the false floor. Nevertheless, some of the detectors might require to be fixed to the concrete floor for additional stability. Part of this floor is removable in case some equipment has to be changed upstream to provide access for heavy-duty engines.

The electricity supply in the experimental area (20 kW) is sufficient for the electronics, the two vacuum pumps (RC and NEL), detector systems and networking. It can be switched off in emergencies from inside the experimental area as well as from the control room or from outside the control access gate.

There are four optical fiber links for data transfer between the front-ends, the control room and also for the local LAN in the experimental area. This LAN provides also for a low-level access system for all PCs (TCP/IP access via PASSaPort units). The trigger signal is generated in the control room and sent via a high quality coaxial cable to the experimental area where it will be pass via a BUSY logic and then distributed to the front-ends. All emergency switches and security detectors, gas systems, dosimeters, protection of the samples in case of prompt vacuum accident, have been designed in co-operation with the EP safety officers and TIS. Adequate grounding of all electrical equipment is provided as well as the prescribed safety equipment.

The gas cupboard, which houses the Isobutane bottle (B1, the maximum size permitted by TIS) for the PPAC detectors is situated next to the NEL, equipped with an adequate ventilation system with the exit to the outside of the underground area. The gas supply to the detector as well as the exhaust line is kept in copper. The exhaust of the PPAC is fed into the exit of the ventilation system at the level of the gas cupboard. A gas alarm system with four measuring heads (one in the gas cupboard, three in the experimental area under the false floor in strategic positions) and an airflow detection system provide their alarm signals to the control

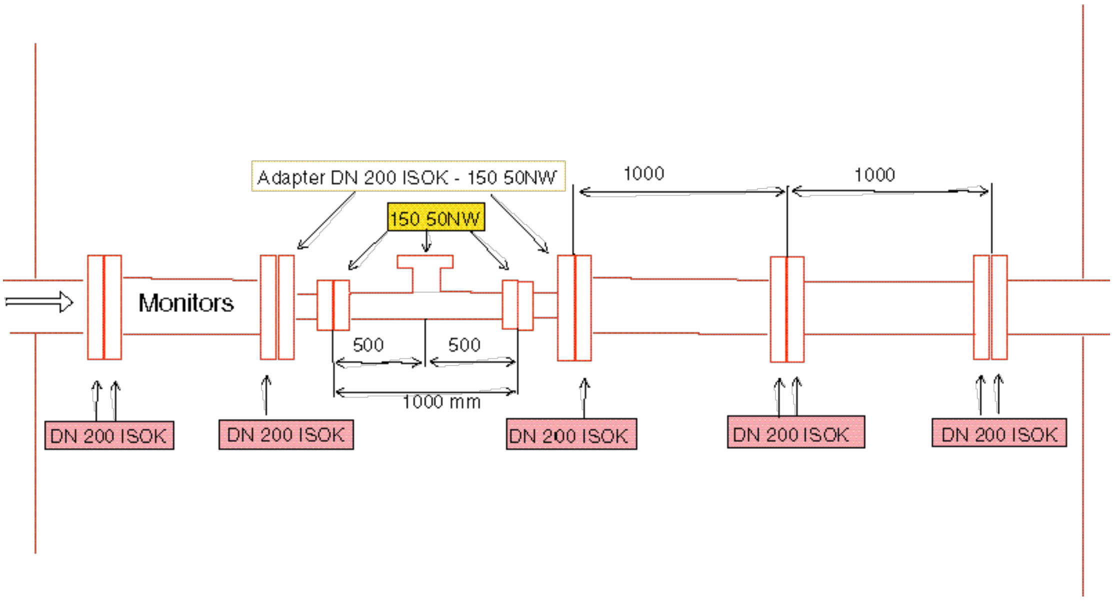

Figure 4.1: Layout of the "Reaction Chamber".

4.2 The Neutron Escape Lane

This part of the n_TOF tube is used to avoid neutron backscattering in the Measuring Station. After the shielding upstream, defining the experimental area, the tube of diamater ø=200 mm stops with a valve. The tube continues with a ø=400 mm diameter for ~ 8 m and ends at the nominal distance from the spallation target of 200 m. Figure 4.2 shows the end of the n_TOF tube at 200 m from the Spallation Target. Due to the tunnel slope, the tube ends practically on the floor.

After the tube window, neutrons are absorbed by a hydrogen rich device equipped with BF_3 gas counters to monitor the neutron beam position.

Figure 4.2: View of the Neutron Escape Line.

5 SHIELDING AND COLLIMATION

5.1 The Target Zone

After a year of run, it has been decided to increase the shielding in the direction of the Measuring Station. The motivations for this shielding upgrade are: minimization of the μ production affecting the □ background in the Measuring Station and the reduction of the Radioactivity due to the production of ^{7}Be.

Figure 5.1: View of the additional Shielding installed after the Target Area.

Starting from the end of the marble shielding installed immediately after the lead Target, a C-shaped concrete elements surrounded by standard shielding blocks has been installed over a distance of ~ 15 m (Figure 5.1). The effects of this upgrade are reported in PART III.

5.2 The TOF Line

Along the n_TOF tube there are various shieldings to reduce the background in the Experimental Area. The implementation of these infrstructures is made complex due to three contradictory requirements: (i) completely fill the tunnel cross section for the best shielding efficiency, (ii) leave a passage for heavy engines to do the maintenance and, finally, (iii) provide a permanent passage for personnel in case of fire.

Figure 5.2: View of the Iron Shielding from the opening in the separation wall between Primary and Secondary Area.

The most important elements of shielding along the flying path are:

- shielding at ~140 m separating the Primary Area from the Secondary Area. This element is a concrete wall 2.4 m deep partially equipped with iron around the tube. A passage for the access of the forklift is available on its right side (in the neutron beam direction). During the run this aperture is obstructed by a removable concrete door mounted on wheels. A closed chicane with a door is used to permit the passage in case of fire;
- Muon Shielding (Figure 5.2) at ~150 m after the Sweeping Magnet, made completely with iron covering the whole tunnel cross section. The passage of personnel in case of fire is possible through an open chicane. An additional concrete layer of 3.2 m made out of standard blocks is installed after the iron to enhance the efficiency of the shielding;
- shielding at the entrance of the Experimental Area (at ~175 m), made only with concrete, to separate the area of the collimator from the measuring station. This element is 3.2 m deep again with a passage of the forklift and a closed chicane. Unfortunately in this area the tunnel has a slope of 12 % and the aperture can not be mounted on wheels for safety reasons;
- shielding at the exit of the Experimental area (at ~ 190 m), made with concrete 1.6 m deep. The passage of personnel in case of fire is possible through an open chicane;
- shielding at the end of the TT2-A tunnel (~ 50 m after the tube end) to close the Facility. At this level is installed the access door (protected by a chicane).

5.3 Collimation

Apart from the "natural" collimation made by the tube itself, there are two Collimators installed along the flying path: the first located at the end of the Primary Area at ~ 137 m, and the second at ~ 176 m.

The detailed simulations are reported in PART III.

The mechanics of the Second Collimator is made in such a way that the change of its aperture can be made with a stop of only one day.

PART II

SAFETY

1 CONTROLLED ACCESS

1.1 General Considerations

The realization of the TOF facility implies the implementation of safety systems ensuring personnel and equipment protection. The purpose of this document is to give a general overview of the access control and machine interlock safety systems and the rules to be followed to have access to the facility.

1.2 Safety Considerations

At CERN the areas under radiation control are divided in two families:

- Primary Beam Areas;
- Secondary Beam Areas.

These areas are submitted to the following safety rules:

- access to the areas under radiation control must be forbidden and nobody should be present in these areas during beam exploitation;
- should the beam be absent, the machine should be switched off and the level of resident radiation must be acceptable before access to such areas.

In order to cope with these rules an Access Control System and a Machine Interlock System are to be provided for each family of beam area.

1.2.1 Access Control Systems - ACS

The Access Control System controls the equipment (doors, separating grids, shielding walls, etc.) wrapping and parceling out a primary beam area. All this equipment is called (following the INB Regulations) Important Safety Components of the access (ISC-access).

1.2.2 Machine Interlock Systems - MIS

The Machine Interlock System manages the equipment (i.e. beam stoppers, magnets power supply, other machine equipment involved in the safety) in charge of beam circulation. All this equipment is called (following the INB Regulations) Important Safety Components of the machine (ISC-machine).

The safety concept is based on the interlock of these two systems:

- under the Machine Interlock System exploitation all the Important Safety Components of the access should be bolted in a “SAFE” position and a “VETO” signal inhibits and prevents any access procedure. In the case of an emergency, the ISC-machine is immediately stopped if a door is opened;
- in the same way, under the Access Control System exploitation, all the Important Safety Components of the machine should be stopped (“SAFE” position) and a “VETO” signal inhibits and prevents the engaging of the power supply.

1.3 Safety Systems of the TOF Project

To assure the safety in the TOF tunnel, the standard architecture of the PS was chosen. However, the supervised access was not chosen for financial reasons. Indeed, due to the limited number of intervention in the primary area, an important investment is not justified. An exceptional procedure has been applied to allow the access in this zone.

1.3.1 Secondary Beam Area

This area (Figure 1.1) is made of two sectors:

- the D sector, between the PPX1 and the PPX2. The sweeping magnet is located in this area;
- the E sector, between the PPX1 and the PPE. The Experimental Area is located in this area.

The *Equipment Layer* is made of the following items:

Secondary Beam Area Access Point equipped with:

- one *personnel* access door – PPE (Personal Protection Entry);
- a panel signaling the access mode;
- 2 doors (PPX1, PPX2) used as emergency exits (Personal Protection eXit);
- 2 search hardware systems dedicated to the patrol of the area divided in two sectors;
- hardware interfaces, switches, contacts… dedicated to the generation of the ISC-access/machine safety signals (access equipment, bending magnet, beam stoppers, PS extraction, other …);
- cabling/hardware interfaces related to the acquisition of the safety signals (access and machine equipment).

The *Control/Safety Layer* is made up of the following items:

- a hardware fail-safe;
- a synoptic, installed in TOF control room (see Figure 1.1).

The *Supervision Layer* is made of the following items:

- an Ethernet TCP/IP-based communication network;
- one workstation running the access application program;
- one PC located in the access point dedicated to the access procedures.

Access exploitation principle

During machine exploitation (ISC-machine ON), the Access Point is bolted in order to prevent any access to the area (CLOSED MODE). The access is possible by using the key on the synoptic panel. When the key is removed, the ISC-machine is set in the "sure" condition. Before turning into data acquisition exploitation, the area will be patrolled by the users.

1.3.2 Primary Beam Area

This area (Figure 1.1) is considered as a Primary Beam Area without Access Point, therefore without direct audio and video supervision. Consequently, access to this area is allowed following a specific procedure.

The *Equipment Layer* made up of the following items:

- 2 doors (D204, D201) used as entrance points;
- 2 doors (D202, D203) dedicated to the parceling of the target area;
- 1 door (D205) closes the access to the technical tunnel;
- 9 search hardware systems dedicated to the patrol of the area;
- hardware interfaces, switches, contacts… dedicated to the generation of the ISC-access/machine safety signals (access equipment, bending magnet, beam stoppers, PS extraction, other …);

- cabling/hardware interfaces related to the acquisition of the safety signals (access and machine equipment).

The *Control/Safety Layer* made up of the following items:

- a hardwired fail-safe network based on the existing safety system of the PS Primary Beam Areas;
- its communication network;
- the integration in the existing PS safety system of an additional safety chain.

The *Supervision Layer* made up of the following items:

- the existing PS-CO Ethernet TCP/IP-based communication network;
- the existing ACSPS1 workstation running the access application program.

Access exploitation principle

The absence of Access Points hampers the access procedure to the primary beam area. Any access to this area is possible using one unique key located in MCR under the responsibility of the operators. In addition, a TIS/RP technician should grant the access after the verification of the resident radiation of the area.

Of course, all grids will be equipped with emergency passage devices (in both ways) for evacuation of the area in the case of an emergency.

The activation of any emergency passage device will also stop (in addition of all machine equipment dedicated to TOF), the extraction from the PS.

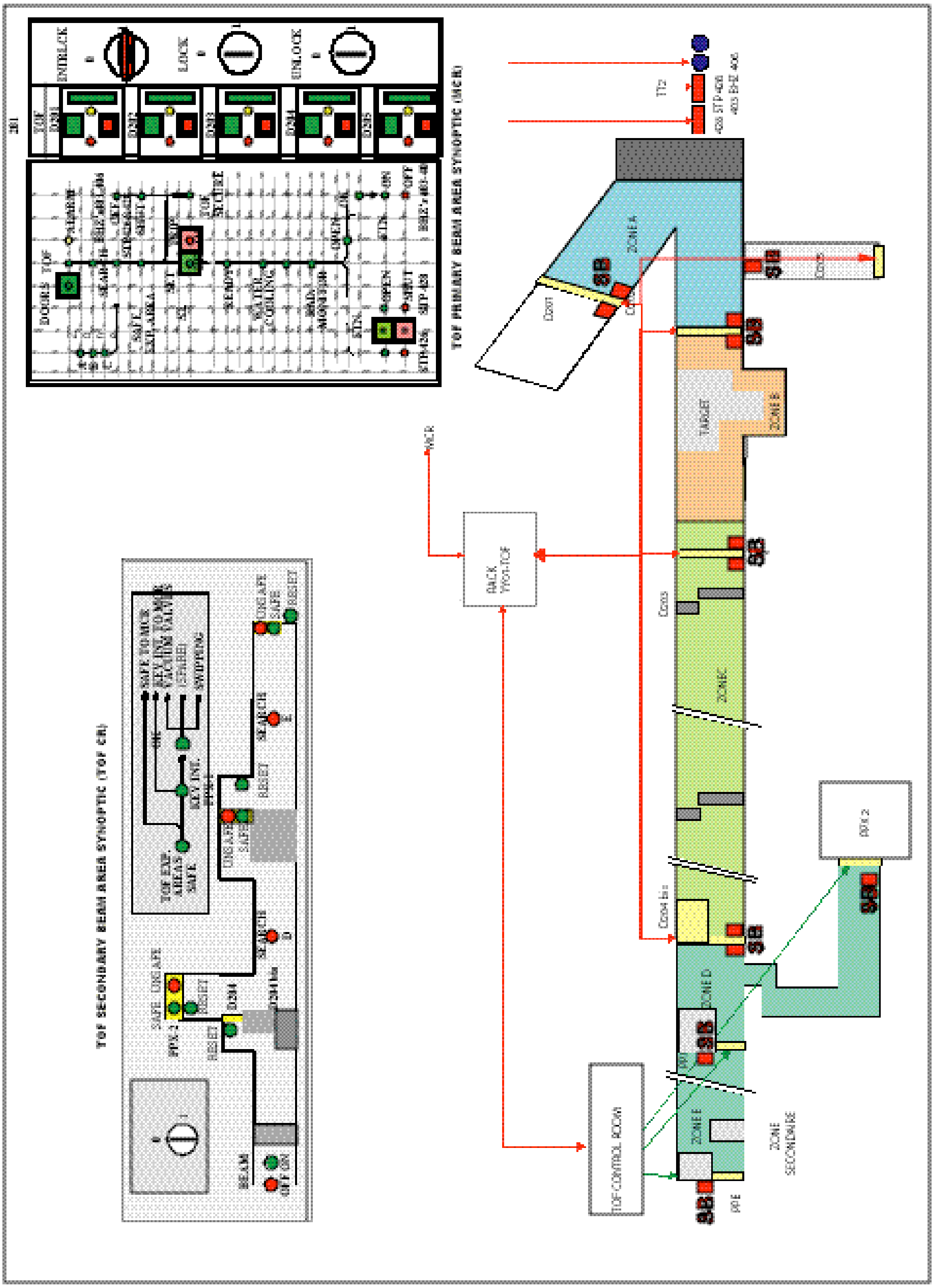

Figure 1.1: Schematic layout of the Access Control equipment location.

2 SIMULATION STUDIES ON ACTIVATION

The TOF facility using a high intensity proton beam produces through the spallation process, a high flux of charged particles, gammas and neutrons. Thus, one of the main concerns is the radioprotection aspect of such a facility. Therefore intensive simulation studies were undertaken to calculate the activity and dose at different locations of the TOF facility.

The important points of this simulation cover the following topics:

- activation of the lead target;
- activation of the cooling water;
- dose around the target area;
- dose near the sweeping magnet;
- air activation.

In the following sections the above-mentioned topics will be treated in more detail.

2.1 Spallation Target Activation

The target is made with pure lead blocks and its shape is 80×80×60 cm^3, except for the spallation area where a volume of 30×55×20 cm^3 was removed to have the nominal design dimension [3] (Figure 2.1). The exit plane is at an angle of -0.676° with respect to the vertical. The target is mounted on a steel support and is submerged in water contained in an aluminum alloy vessel. The water layer surrounding the lead block is 3 cm thick except at the exit face of the target where it is 5 cm thick. The walls of the aluminum container are 0.5 cm thick, except the exit wall that consists of a thin single metallic window [3]. This aluminum window mounted onto the water tank is 1.6 mm thick and 80 mm in diameter.

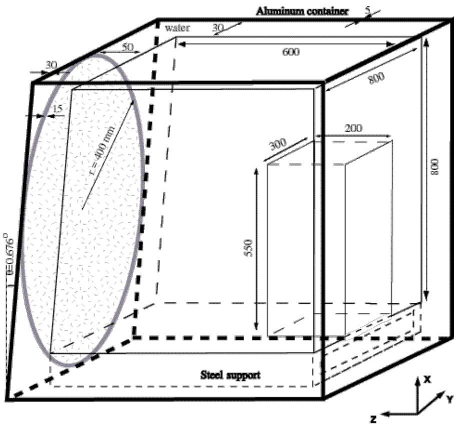

Figure 2.1: Geometry of the lead target.

In order to calculate the activity of the target the residual nuclei produced by inelastic hadronic interactions in the lead volume were scored. The intensity of the beam was assumed to be 7x10^{12} protons per bunch. Two cases were considered, the first with 1 bunch every 14.4 s (supercycle duration), the second with 4 bunches every 14.4 s. Two representative irradiation periods were considered, one lasting one month and the other nine months. The beam intensity is supposed to be constant and equal to the average value (i.e. 4.9x10^{11} and 1.94x10^{12} protons per second for 1 and 4 bunches per supercycle, respectively). At the end of the irradiation, the activity of the lead target is about 800 Ci for the one bunch scenario Figure 2.2. After one year of decay, the total activity is about 1 Ci for one month's irradiation, and about 7 Ci for nine month's irradiation. For 4 bunches the values are obviously four times larger.

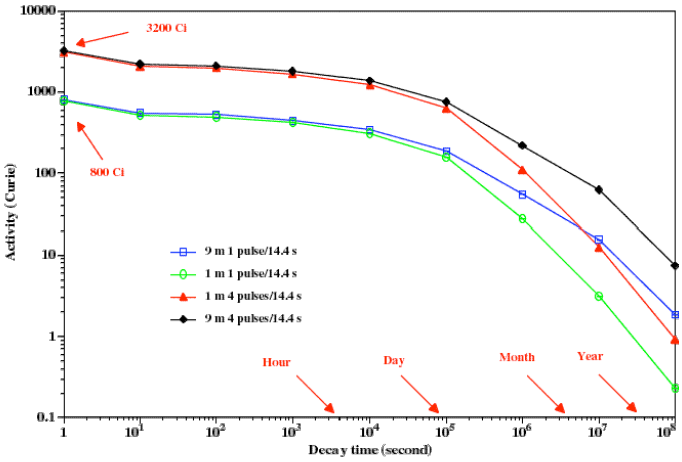

Figure 2.2: Activity of the target versus cooling time after 1 month's and 9 month's irradiation with 1 or 4 bunches per 14.4 s, 7×10^{12} protons per bunch.

The dose equivalent rate after 1 month of irradiation time and one day of cooling is estimated on the front face of the lead target to about 25 Sv/h. This result is obtained by using the ω factor giving the dose rate in contact with an extended surface in rem/h; this factor is applied to a *star density rate* (hadron inelastic interaction given per cm^3/s) calculated in Monte-Carlo programs (FLUKA [12] in our case); this star density is deposited for an irradiation period followed by a given cooling time [21].

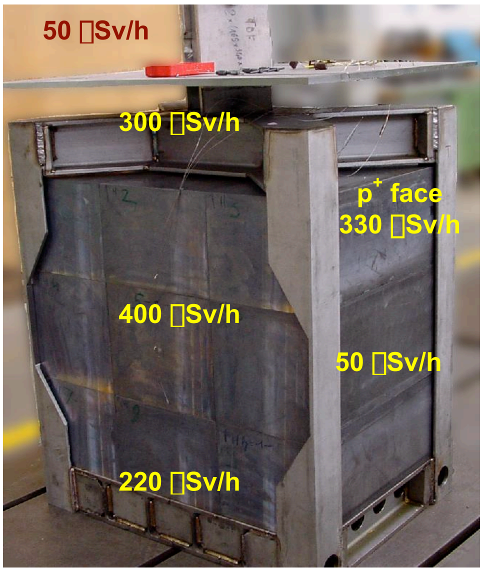

Figure 2.3: Activity of the spallation lead target after 2 months of cooling.

The dose rates obtained after different irradiation and cooling periods, for a beam intensity of 1.94×10^{12} protons/s (4 bunches scenario) are given in Table 2.1. During operation the maximum dose recorded by the Safety Division (TIS) detectors was of the order of 10 Sv/h in the target area. The target was removed at the end of the first commissioning period (14 February 2001) for inspection. After exposing the lead target to 2x10^{16} protons of 20 GeV/c and 2 months of cooling the maximum dose record was 1.1 mSv/h at the hotspot and an average of 400 μSv/h was measured in the front face of the target (Figure 2.3). The measurements are compatible with the simulations reporting a maximum dose of ~ 2 mSv/h at the hotspot. The aluminum container had a dose of 5 µSv/h and 15 µSv/h was measured on the inox screws.

I=1.94×10^{12} p/s	T_c = 1d	T_c = 10 d	T_c = 30 d
T_{irr} = 1 month	25	4	2
T_{irr} = 1 year	30	11	8

Table 2.1: Maximum dose equivalent rates on the exit face of the lead target expressed in Sv/h, for different irradiation and cooling times.

2.2 Activation of the Cooling Water

The activation of the cooling water was calculated under the same conditions described previously for the target activation. The total volume of water used in the cooling system is about 700 l; the aluminum container contains 20% of this volume. At the end of the irradiation, the activity is about 2.7 Ci for the one bunch scenario. After one year of decay, the total activity is around 5 mCi for one month's irradiation and about 20 mCi for nine month's irradiation. For 4 bunches, the values are four times larger. The activity decreases rapidly after one day because of the short half-life of most of the produced radionuclides (Figure 2.4).

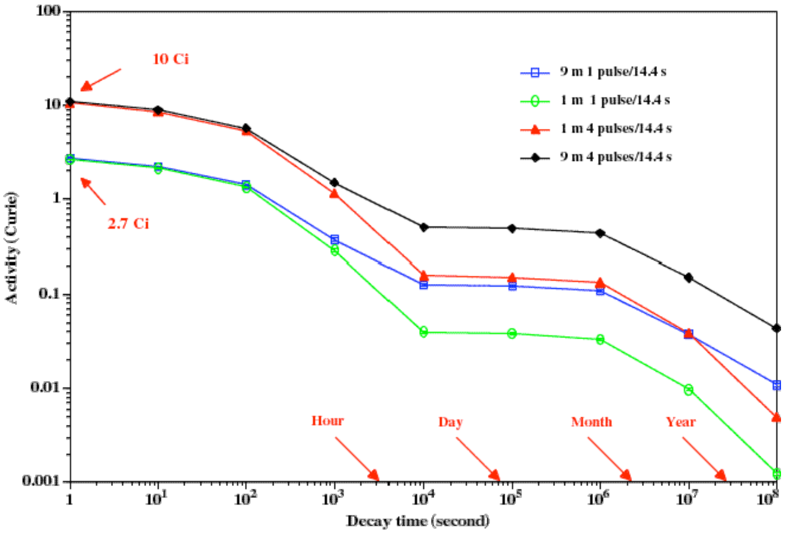

Figure 2.4: Activity of the cooling water versus cooling time after 1 month's and 9 month's irradiation with 1or 4 bunches per PS supercycle, 7×10^{12} protons per bunch.

We can reasonably assume that the specific activity of the whole water volume is five times lower than the specific activity in the water inside the container, as this water permanently circulates in the cooling system. After one day of decay, the activity is mainly due to ^{7}Be and tritium, with 53.3 d and 12.33 y half-lives respectively. The nuclei dominating the activity are given in Table 2.2 (1 month's irradiation).

TCOOLING	**RESIDUAL NUCLEI**	**Bq**	**A (%)**
Day	^{7}Be (ec mode, $T_{1/2}$=53.3 d)	1.3×10^9	96.1
	^{3}H (β^- mode, $T_{1/2}$=12.33 y)	5.3×10^7	3.9
Month	^{7}Be	9.1×10^8	94.5
	^{3}H	5.3×10^7	5.5
Year	^{7}Be	1.2×10^7	19.8
	^{3}H	5.0×10^7	80.2

Table 2.2: Radionuclides dominating the total activity of the cooling water irradiated for a period of one month.

3 RADIATION SAFETY

3.1 Target Shielding

The TOF lead target is situated at a depth of 9 m under the ISR tunnel, which is a supervised area. The dose rate allowed in this region must be less than 2.5 µSv/h; the design value for the shielding was taken at 1 µSv/h. FLUKA [12] simulations were performed to determine the shielding requirements.

The TOF target will be removed from the TT2A tunnel via a shaft set in concrete and linking a service tunnel located in-between TT2A and the ISR, which will serve as a storage area for the target. The concrete thickness between TT2A and this service tunnel is 5.5 m (Figure 3.1). FLUKA simulations were performed to estimate the dose in the ISR during the TOF operation. Only neutrons have been transported without any energy cut-off.

Simulations were performed for the neutrons transmitted through the shielded shaft. For this purpose the 130 cm diameter shaft was filled with 4.55 m of concrete, divided into 10 slices and 12 regions for simulation purposes (Figure 3.2) [22]. The density of the concrete is 2.35 g/cm^3. An average quality factor of 5 was applied to convert absorbed dose in Gray to dose equivalent in Sievert. We have considered 1 bunch and 4 bunches every 14.4 s with an intensity of 7×10^{12} protons per bunch.

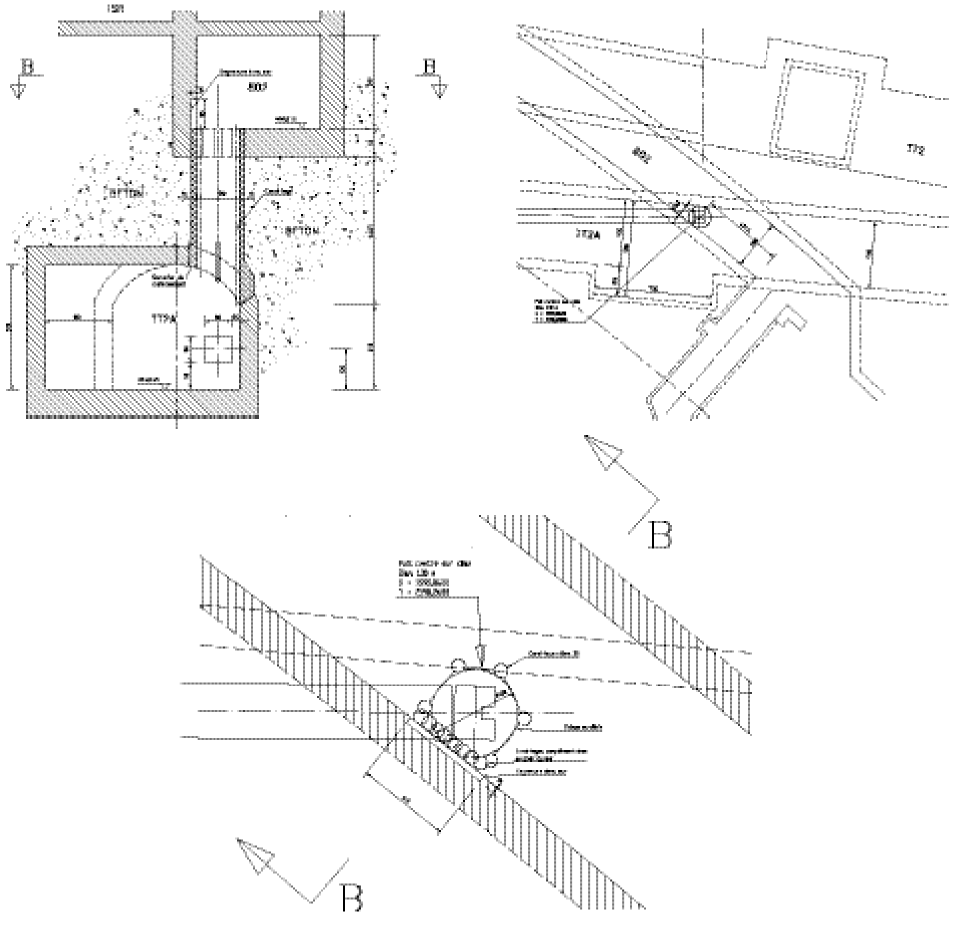

Figure 3.1: Shaft dug in concrete to extract the TOF target from the TT2A tunnel.

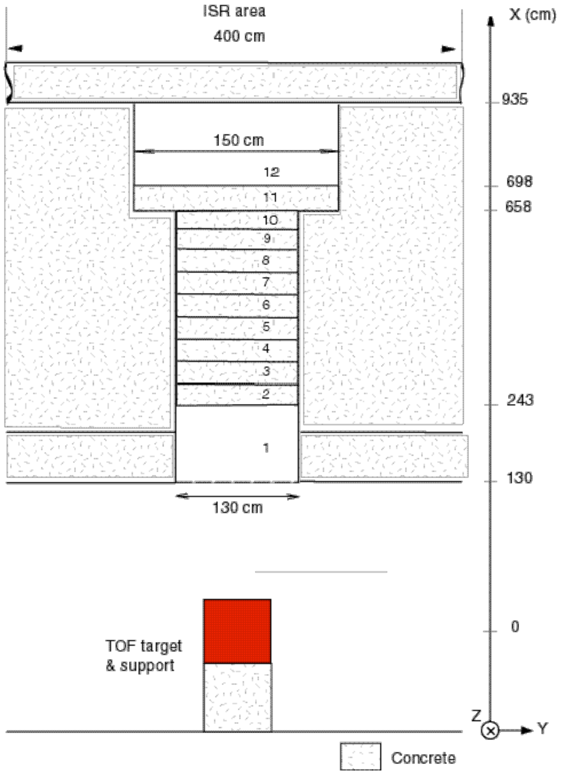

Figure 3.2: Geometry of the shaft used in the FLUKA simulation.

In region no. 1, 1.3 m above the target and before any shielding, the dose equivalent rate is about 80 Sv/h for the one bunch scenario. In region no. 12, the dose equivalent rate is around 3 mSv/h. For the 4 bunches scenario the values are obviously 4 times higher. The dose equivalent rate in the ISR with the shaft "plugged" with 4.55 m of concrete is clearly far too high. To reduce it to the design value, additional shielding has to be installed on top of the production target. Additional calculations have shown that a shielding consisting of 80 cm iron plus 2.4 m concrete placed in the service tunnel in-between the shaft and the ISR will reduce the dose equivalent rate to below 1 µSv/h.

3.2 Shielding of the Basement of Building 287

3.2.1 Initial Dose Rate Estimation

A laboratory routinely occupied by personnel is located at the same level of the TOF TT2A tunnel. This room, located in the basement of building 287 (Figure 3.3a), is linked to TT2A by a 12 m long tunnel, which serves as an emergency exit and therefore cannot be completely blocked off. The way to reduce neutron streaming from TT2A into building 287 is to install a properly designed labyrinth. As building 287 is a supervised area, the ambient dose equivalent rate in the laboratory must not exceed 2.5 µSv/h.

A collimator and the TOF sweeping magnet are located near to the tunnel aperture, about 140 m from the TOF target. The integral neutron background fluence in the tunnel (outside the neutron tube) versus the flight distance has been estimated at around 10^5 n/cm^2/3×10^{13} protons. The neutron spectrum at the entrance of the service tunnel is shown in Figure 3.3b. This neutron fluence has then been folded with the neutron fluence to ambient dose equivalent conversion factors (Figure 3.3c) given by [23]. The total dose equivalent for 4 bunches is 1.3×10^7 pSv, or a rate of 3.25 mSv/h for 4 bunches every 14.4 s (see Figure 3.3d).

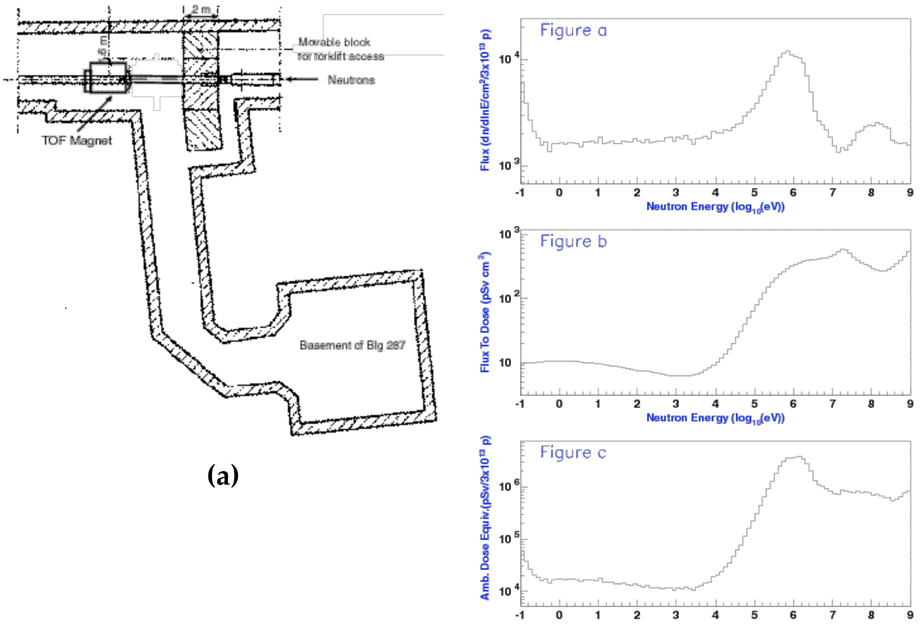

(a)

Figure 3.3: a) TT2A and service tunnel linking to the basement of building 287. b) background neutron flux in the TOF tunnel, at 140 m from the lead target c) neutron fluence to dose equivalent conversion factor d) neutron ambient dose equivalent per isolethargic bin for 4 bunches.

3.2.2 *Simple Estimate*

A first estimate of the attenuation provided by a labyrinth made of concrete and consisting of two legs each of 5.60 m long, 0.9 m wide and about 2.5 m high (cross sectional area A = 2.30 m^2) was carried out using the attenuation curves given in [24]. The resulting dose equivalent rate is estimated to be less than 1 μSv/h. The attenuation factors and results are given in Table 3.1

LEG DIMENSIONS: l = 5.60 m; A = 2.3 m^2	**ATTENUATION FACTOR**	**INITIAL DOSE RATE:** 3.25 mSv/h
1st leg	0.022	71.5 μSv/h
2nd leg	0.009	0.6 μSv/h

Table 3.1: Estimate of the dose rate in the labyrinth, in the case of 3×10^{13} protons/14.4 s.

3.2.3 *Monte-Carlo Simulation*

Due to the complexity of the problem, a Monte Carlo simulation was performed to estimate the neutron streaming in this tunnel, with the two concrete blocks of the labyrinth defined above (Figure 3.4).

At the tunnel entrance, 139 m after the lead target, the "background" neutron fluence is about 10^5 n/cm^2/3×10^{13} protons (4 bunches per PS supercycle); these neutrons are mainly fast; the dose equivalent rate is about 7.5 mSv/h using the ambient dose equivalent conversion factor given by [23] for fast neutrons (300 pSv cm^2). At the entrance of the small experimental room, the neutrons are mainly thermal, the fluence is reduced by 6 orders of magnitude, and the dose rate estimated with the conversion factor for thermal neutrons is reduced to 0.2 nSv/h.

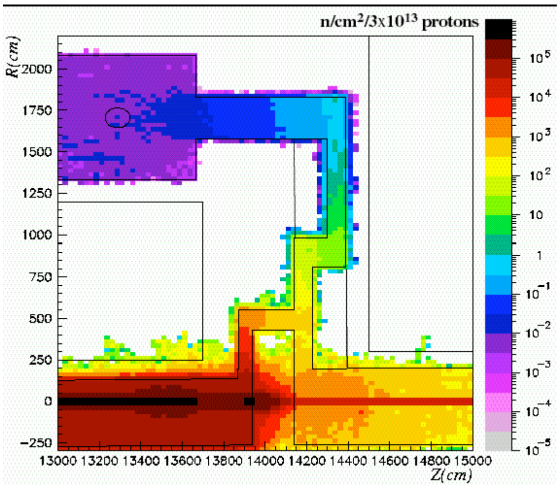

Figure 3.4: FLUKA simulation of the neutron fluence in the tunnel, with the concrete labyrinth.

The dose equivalent rate obtained by the simple calculation is a priori 3 orders of magnitude higher than the rate obtained by simulation. The first estimate was done just by considering a 12 m long straight tunnel with two concrete legs, and taking an initial dose equivalent rate of 3.25 mSv/h at the entrance situated 142 m downstream from the target. The geometry of this area is in reality more complex (as shown in Figure 3.3a), and the previous rate is obtained at 139 m, before the collimator wall (Figure 3.4). By considering the fast neutron fluence of 10^3 n/cm^2/3$\times 10^{13}$ protons, the dose equivalent rate at 142 m is 0.22 mSv/h. This rate is reduced to 44 nSv/h after the two concrete legs, and should be reduced even more by the perpendicular shape of the passage leading to the laboratory. The results given by the calculation and simulation are consistent.

3.3 Dose Rate Estimate at the Measuring Station

The measuring station is located at 187.5 m from the lead target. After the proton beam is stopped, the background in the experimental area will be dominated by γ-rays emitted by the lead target and propagating through the TOF tube. The diameter of this tube will be 1.8 cm for the capture cross-section measurements, and 15 cm for the fission cross-section measurements. Calculations were performed to determine the dose rate in this area and to design the lead shutter to be inserted at the end of the TOF tube.

Considering the dose equivalent rate of 25 Sv/h on the exit face of the target, an estimate of the rate at 187 m gives 0.5 μSv/h by considering the solid angle subtended by a surface of 10 cm in diameter. This simple calculation does not take into account the effects of the reductions and collimators at different places on the neutron TOF tube. A more detailed calculation was done by means of a Monte-Carlo simulation including the complex geometry of the n_TOF line.

After an irradiation period of 1 month, the activity of the lead target saturates around 800 Ci, emitting 2.5$\times 10^{13}$ γ/s. The photon energy distribution from the whole lead block was obtained using the activity of the residual nuclei from FLUKA and the intensity of the γ-rays corresponding to each nucleus, taken from the ENSDF database of nuclei decay modes [25]. These source photons were then transported with FLUKA from the lead target to the measuring station, taking into account the whole and detailed geometry of the 200 m long TOF tunnel. The calculated dose equivalent rate is about 1 nSv/h; this simulation was done with the photons isotropically distributed into the target and not transported from their creation point (coordinates of the residual nucleus). The actual dose rate will most likely be in-between the two values obtained by these extreme approaches.

PART III

PERFORMANCES OF THE FACILITY

1 SIMULATION OF THE BEAM CHARACTERISTICS

One of the major tasks during the design phase of the n_TOF facility has been the simulation of the physical performances of the installation. Simulating geometries like the n_TOF tunnel, with a long flight path, and with the imposed background conditions, is a very difficult and time-consuming task. To accomplish it, the most advanced computer codes FLUKA [12], EA-MC [13], and MCNPX [26] have been used, coupled together whenever needed with specially written interfaces. Moreover, the accurate representation of the tunnel geometry used in the simulation codes was automatically generated with the use of in-house translators specifically made for this purpose, based on the civil engineering plans.

1.1 Neutron Flux

The simulation of the neutron flux, one of the most important parameters of the facility, poses a serious difficulty due to the large length of the neutron flight path in the n_TOF tunnel. The solid angle is so small that only one neutron out of ~10^7 emerging from the lead target will reach the detector station at the end of the neutron tube. To solve this problem we separated the simulation process in two steps: (i) simulation of the spallation target and generation of DST's (Data Summary Tapes) of the neutrons emerging from the aluminum window and entering in the neutron tube [27], (ii) geometrical transport of the previously collected neutrons in the neutron tube.

For the first step, two simulation codes were used, the intranuclear cascade code FLUKA and the Energy Amplifier Monte Carlo code EA-MC, with the detailed geometry of the lead spallation target, and its surroundings, (modeling of the Al-window with the supporting grid). FLUKA was used for the production of neutrons with the spallation of the 20 GeV/c protons onto the solid lead target, and the transport of the generated neutrons down to the cut-off energy of 19.6 MeV. The transport of neutron with kinetic energy below the cut-off of 19.6 MeV, was performed with the EA-MC code, where neutron induced interaction cross sections are available in the nuclear databases. All the neutrons emerging the lead target from the aluminum window with a direction lying in a cone with an aperture (□ < 20º), heading toward the experimental area, were recorded into a DST file.

In the second step, the previously collected neutrons were transported geometrically towards the detector station into the neutron tube system. In the neutron transport we assumed a perfect collimation system: particles touching the collimators or the tube were *killed*. In order to enhance the statistics, we made the hypothesis that the direction of neutrons is isotropic within a small solid angle (□ 10^{-7} sr). Thus, each particle was reused several times by changing slightly its direction, in such a way to scan an area of a few cm^2 at the detector position. The program was scoring the number of occurrences of particles arriving at the detector plane for every position in the detector without touching any element of the neutron tube and collimators. The weight of each particle was properly normalized to reflect the number of times that it had been reused. The output histogram of this scanning procedure gave the integrated neutron fluence at the detector station.

The result of the flux simulation is shown in Figure 1.1. The total number of neutrons entering the experimental is plotted in isolethargic units: $dn/dlnE/cm^2/7$□10^{12} protons. One the same plot one can see also the simulation with MCNPX using a similar procedure: from the spallation of the protons on the lead target until the neutron transport to the detector area. The results were compared with those obtained using FLUKA and FLUKA+EA-MC. The three sets present a very good agreement amongst each other. At high energies, MCNPX shows a harder spectrum than what FLUKA is predicting. On the other hand, MCNPX represent better the thermal part when the *S(□,□)* treatment is enabled for light water, apart a few non-physical spikes which appear in the thermal peak, probably due to a binning affect. A gravitational cut-off will occur due to the geometry of the beam pipe for neutrons with kinetic energies lower than ~0.02 eV.

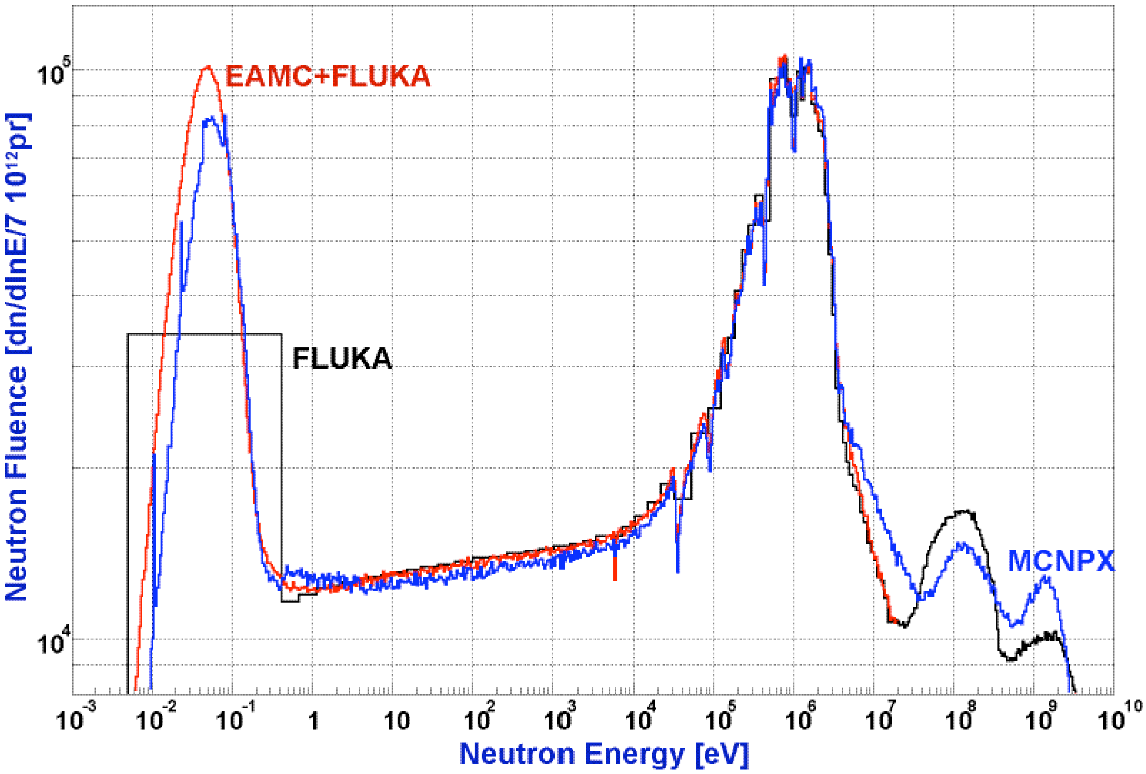

Figure 1.1: Monte Carlo simulation of the uncollimated neutron flux at 185 m using the combined codes, FLUKA-EA-MC, FLUKA and MCNP-X.

1.2 Neutron Energy Resolution

The energy resolution has been evaluated using the relation $\Delta E/E=2\Delta\lambda/(\lambda+L)$ between the energy E and the "*effective neutron path* λ" calculated at the energy of observation inside the lead followed by the 5 cm thick water moderator, and the flight path L. This effective neutron path λ can be evaluated as $\lambda=v\Delta t$, where v is the velocity of neutrons entering the TOF tube and t the time elapsed since its creation (Figure 1.2a). The effective neutron path in the lead target is a few centimeters for the lowest energies. The variance $\Delta\lambda$ has been estimated taking either the *r.m.s.* of the λ distributions, or the standard deviation from a gaussian fit of the peaks (Figure 1.2b).

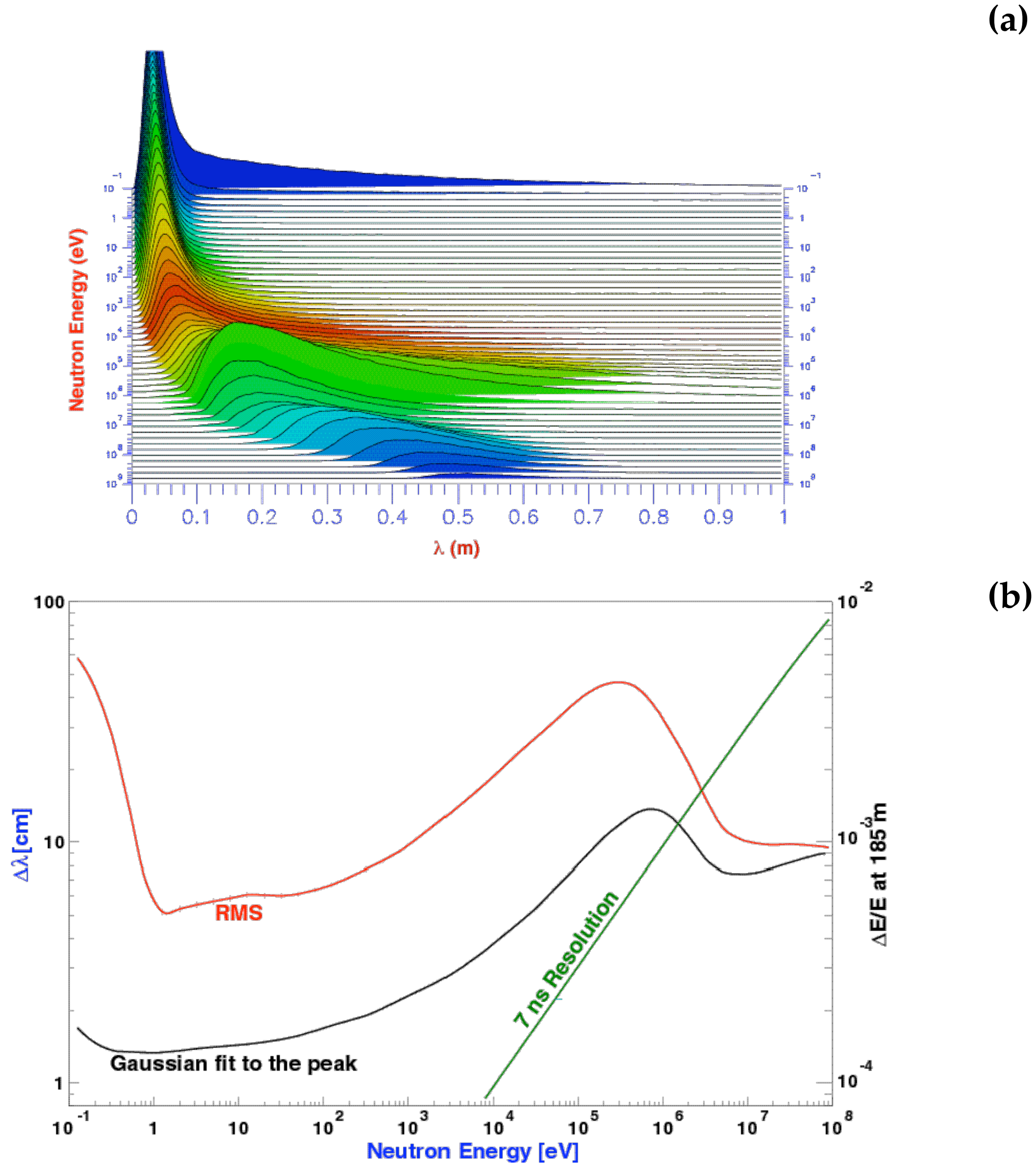

Figure 1.2: a) Monte Carlo distribution of the equivalent neutron path inside the moderator, evaluated at the energy of observation; b) Monte Carlo simulation of the energy resolution at 185 m. The 7 ns resolution due to the proton beam becomes important for neutron energies above a few MeV.

1.3 Charged-Particle and Gamma-Ray Beam Contamination

A 20 GeV/c proton beam interacting with a lead target represents a source of many charged and neutral particles [27]. As already mentioned, the fluence of charged particles is strongly suppressed by the sweeping magnet located at 145 m from the spallation module. The momentum distribution of the charged particles as resulting from simulations is shown in Figure 1.3, together with that of neutrons.

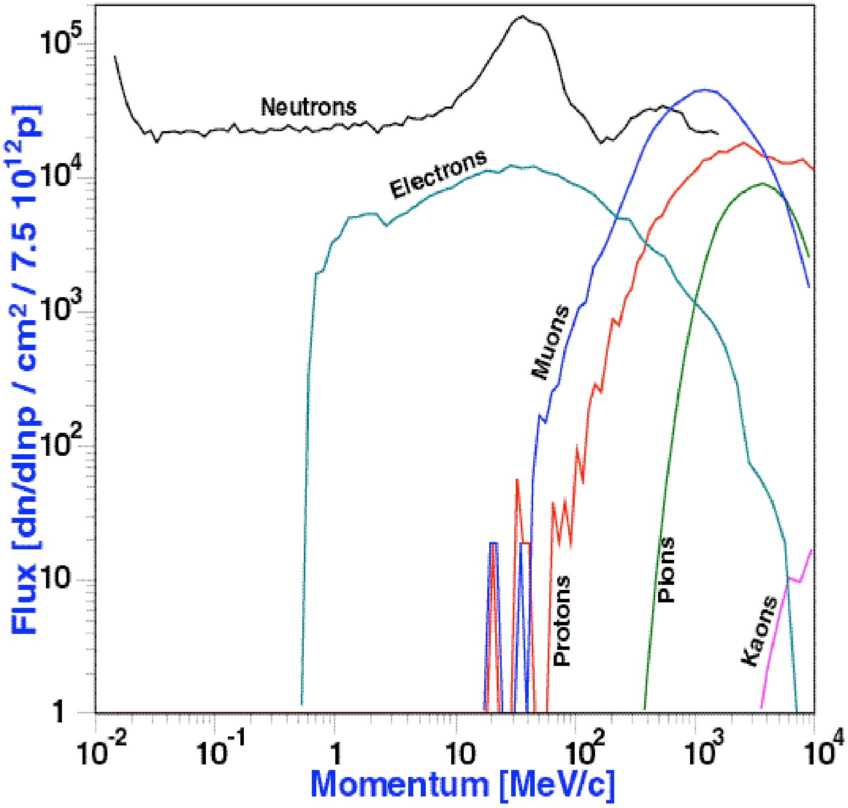

Figure 1.3: Monte-Carlo simulation of the flux of the charged secondary particles and neutrons produced by the spallation process as a function of their momentum.

During the spallation and moderation process of neutrons in the lead target, photons are produced. These photons can be well separated into two groups: a *"fast"* component resulting from the spallation process with times $t < 1\,\mu s$ and a *"slow"* component arriving at times $t \geq 1\,\mu s$ up to a few 100 μs, mainly due to thermal neutron capture by the elements present in the moderator and the lead target. The *"fast"* component, which is often called γ-flash provides a mean of accurately measuring the t_0 of each pulse.

The γ-flux of the *"slow"* component at the measuring station comes along with neutrons having energies of a few keV, but is more than an order of magnitude lower than the neutron flux (Figure 1.4a). From the energy spectrum of these photons (Figure 1.4b), 40% of the contribution is due to the neutron capture on hydrogen producing 2.2 MeV γ-rays. Another 5% contribution comes from photons with energies around 7 MeV resulting from the capture on lead, on the aluminum alloy container and on the iron target support.

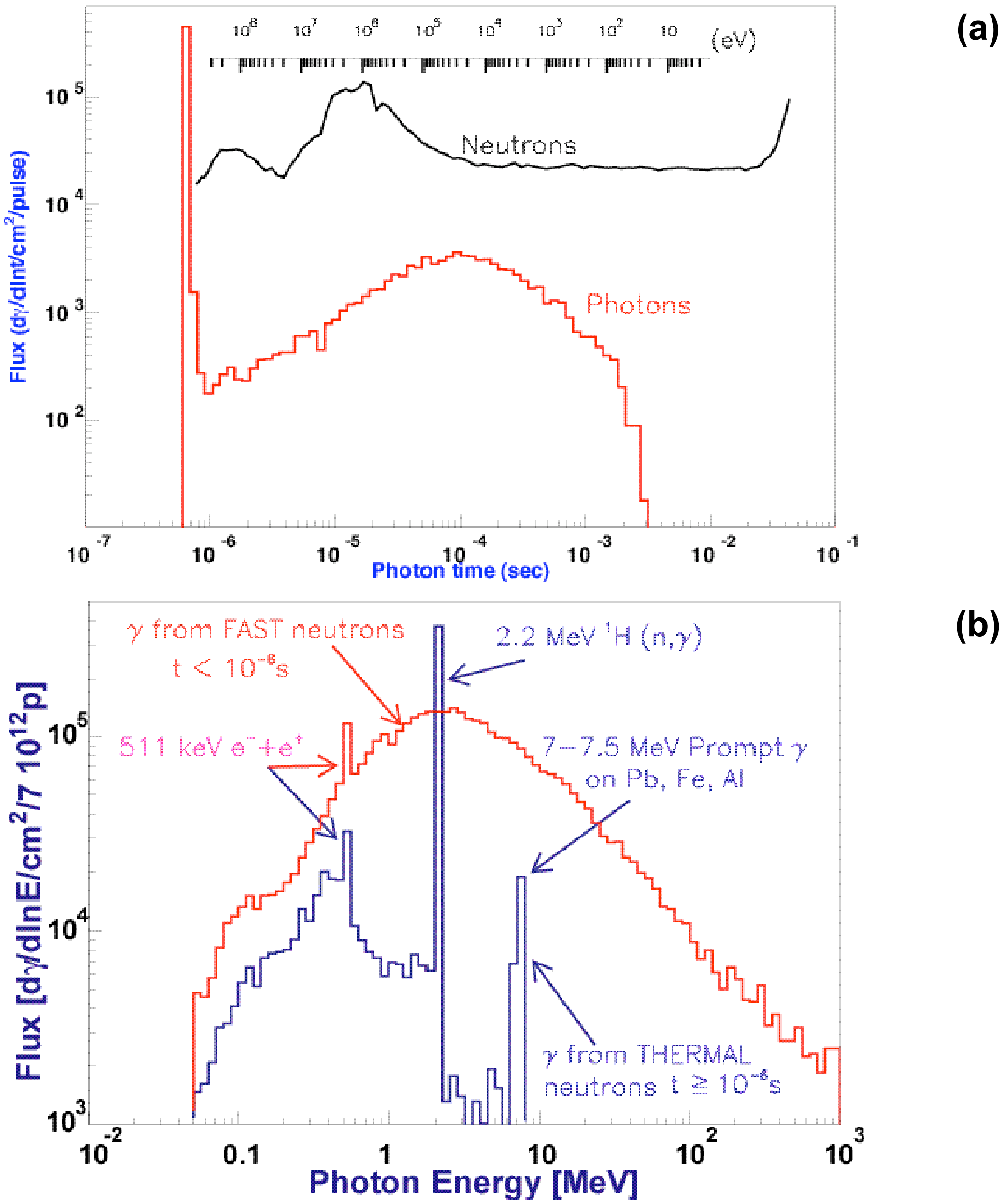

Figure 1.4: a) Prompt photon flux at the measuring station versus the arrival time. The neutron fluence and the neutron energy expected at the measuring station is also plotted. b) Energy spectrum of the prompt photons divided into fast and slow component.

2 EXPERIMENTAL SETUP

2.1 Monitoring the Neutron Beam in EAR-1

Different detectors and techniques for measuring and monitoring the neutron fluence in the experimental area (EAR-1), over the desired range have been used. Such measurements are based on "*standard*" reactions with smooth cross sections, notably ^{10}B(n,α)^{7}Li and ^{6}Li(n,t)α considered as a standard from thermal up to 250 keV and 1 MeV respectively, as well as ^{235}U(n,f) being standard from 0.15 to 20 MeV. In the high-energy domain it is possible to determine the flux by the ^{238}U(n,f) and ^{209}Bi(n,f) reactions, standards from 1-200 MeV and 35-130 MeV respectively.

The emitted alpha particles and triton fragments produced by neutron interaction can be detected inside the TOF vacuum tube by thin-windowed silicon detectors (SiMON). Four of such silicon detectors, placed back-to-back allowed coincidence measurements between both reaction products, providing thus an additional constraint to the TOF neutron energy measurement.

The measurements performed with SiMON have been complemented by measurements with PPAC detectors using the fission reaction on ^{235}U, ^{209}Bi and ^{238}U, providing also information on the spatial distribution of the neutron beam.

Other detectors placed inside the neutron escape line have been three ^{10}BF$_3$ detectors, employing the ^{10}B(n,α)^{7}Li reaction reaction for the detection of thermal neutrons.

In order to measure the profile and the homogeneity of the neutron beam arriving at the experimental area, we have developed a system of a large surface detector, based on the practically massless "*MicroMegas*" chambers.

Filters containing isotopes with so-called "*black resonances*", removing selectively neutrons with specific energies from the beam have been used to determine neutron-induced background in the experimental area. A "MULTIFILTER CHANGER" has been introduced in the TOF tube, upstream of the flux monitors.

Finally, standard integrating and counting monitors have been installed in the experimental area.

2.1.1 The n_TOF MicroMegas Detector

MicroMegas [28] is a new gaseous detector based on simple geometry with planar electrodes (Figure 2.1) developed by Nobel Laureate G. Charpak. It consists of a conversion gap where radiation liberates ionization electrons, and of a thin amplification gap. A thin 5 μm grid separates the two regions. The free electrons drift into the amplification gap where printed electrodes of any shape collect the electrons from the avalanche.

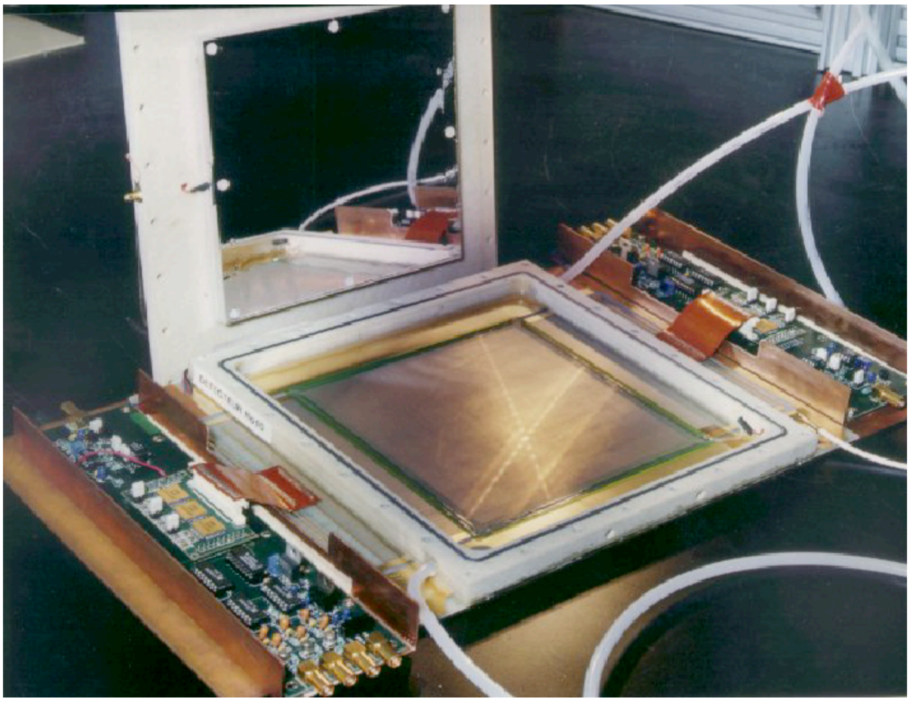

Figure 2.1: The MicroMegas detector.

The preliminary tests [29] demonstrate that it is possible to build chambers of sizes adapted to the future high-luminosity detectors, with high-count-rate capability and good time and space resolution.

In order to operate the MicroMegas detector as a neutron beam profile detector for the n_TOF facility at CERN, an appropriate neutron/charged particle converter has been employed which can be either the filling gas of the detector or a deposited target on its entrance window. Since the neutron energy range of the n_TOF facility extends from 1 eV to over 200 MeV, there is not a unique choice of an efficient converter. Interdependent parameters such as the high neutron reaction cross section, the low charged particles energy loss inside the converter, their subsequent energy-angular distribution and the range inside the filling gas should be considered and optimized.

Conversion reactions that are usually employed for slow or fast neutron detection are proton recoil, ^{10}B(n,α) and ^{6}Li(n,α). In the case of proton recoils that result from the elastic scattering of neutrons, particles are emitted in the forward direction with a simple flat energy distribution extending from zero to full incident neutron energy. Therefore, the reaction can be used for fast neutrons. The two other reactions can be used for low energy neutrons since they have the following characteristics:

- ^{10}B(n,α)^{7}Li Q = 2.792 MeV (ground state) and 2.310 MeV (excited state) (E_{Li} = 0.84 MeV and E_{α} = 1.47 MeV), with a cross section of 3840 barn for thermal neutron energies, a slope according to the *1/v* law for $E_n < 50$ keV, and with two reaction products emitted in opposite directions for thermal neutrons.
- ^{6}Li(n,α)^{3}H Q = 4.78 MeV (E_T = 2.73 MeV and E_{α} = 2.05 MeV) with a cross section of 940 barn for thermal neutron energies, a slope according to the *1/v* law for $E_n < 50$ keV, with a resonance at 240 keV and with two reaction products emitted in opposite directions for thermal neutrons.

The performance of two *MicroMegas* detectors - one with a ^{6}Li and one with a ^{10}B target - were tested using a monoenergetic neutron beam at Bordeaux in the energy range from 240 keV up to 1 MeV [30].

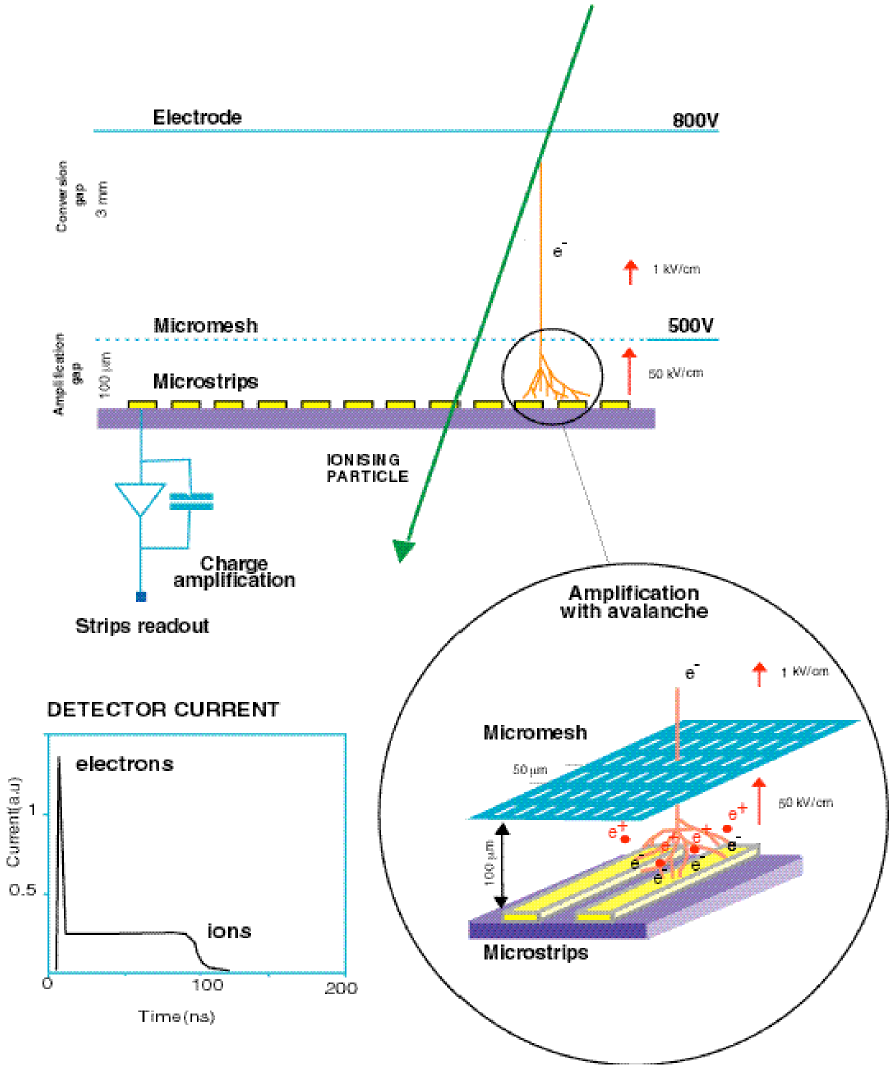

Figure 2.2: MicroMegas principle scheme.

The results indicate an excellent background rejection with full detection efficiency for the charge produced by the neutron reaction in the converter. The conversion efficiency in the solid radiator was calculated to be about 0.1% at maximum, which is reasonable for a beam profiler. With a pitch of 317.5 μm, the spatial resolution was measured to be less than 250 μm, meeting the requirements for the n_TOF experiment. The behavior was stable during the whole running period of 10 days. It can provide safe operation and an accurate measurement of the intensity and position of the incident neutron beam.

Brief Description of the MicroMegas Principle

The principle of the MicroMegas detector is shown in Figure 2.2. A drift electrode, a micromesh and an array of strips compose the detector. The charged particle ionizes the filling gas of the detector, whereas the multiplication of the produced electrons is achieved by the micromesh and detected by the strips.

As mentioned before, the ^{10}B or ^{6}Li converter is deposited on an Al foil. The principle is shown in Figure 2.3.

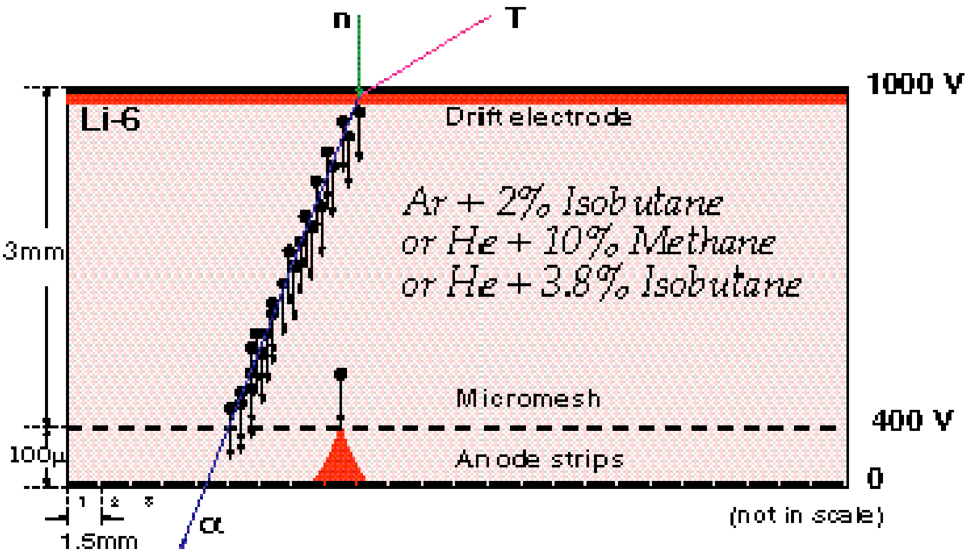

Figure 2.3: MicroMegas operating as a neutron detector.

The Vacuum Chamber

In order to achieve a very good profile of the n_TOF beam, it was decided to place the MicroMegas detector inside a vacuum chamber made of Aluminum. The chamber will be connected to the standard n_TOF tube that extends up to a diameter of 200 mm. As shown in Figure 2.4, the chamber contains 6 holes, two with 200 mm diameter for the connection to the n_TOF tube, and four with 100 mm diameter for the connections of 25 Lemo for the detector signals, the vacuum pump, the gas and the High-Voltage supplies.

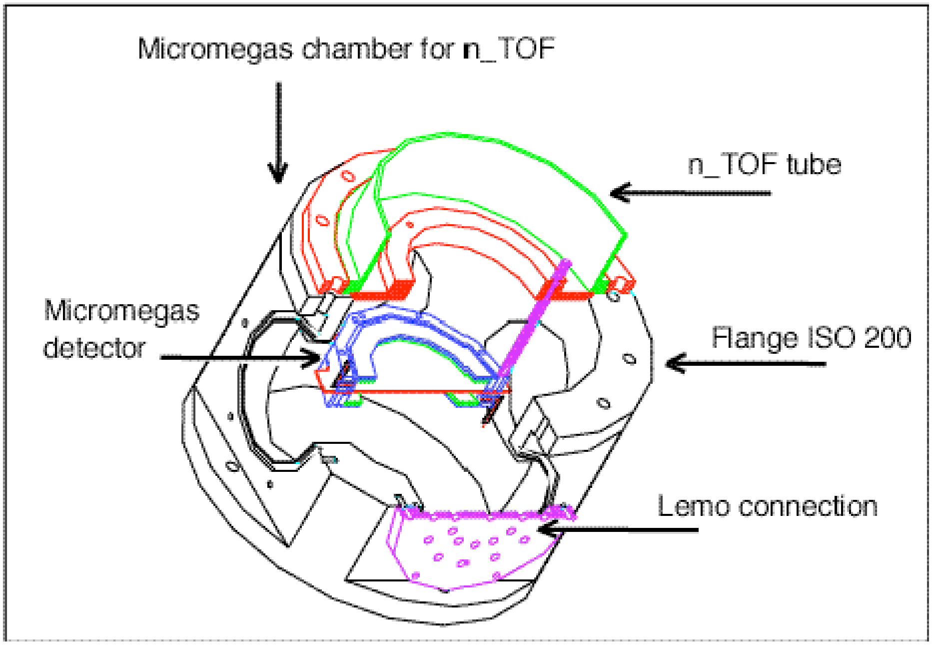

Figure 2.4: The MicroMegas vacuum chamber.

The Detector

The n_TOF MicroMegas detector shown in Figure 2.5, is a cylindrical box composed of two pieces "corps de chambre" of composite and isolated material (DELRIN). The detector is filled with a premixed gas: Ar (98%) + Isobutane (2%), He(90%) + Methane (10%) and He (96.2%) + Isobutane (3.8%). For safety reason, the percentage of Isobutane and Methane has been chosen to be low in order to respect the non-flammability of the mixed gas.

The pressure inside the detector is of the order of 1 bar. Two Kapton windows have been used to maintain the pressure inside the detector and separate it from the pressure of the vacuum chamber that is of the order of 10^{-3} bar. The Kapton windows are fixed mechanically to the DELRIN ring.

The other pieces of the detector are:

- Epoxy frame with 20 μm of Aluminum with a deposit of 0.5 μm ^{10}B or 0.5 μm of ^{6}LiF and an additional layer of 10 nm of Aluminum to protect the ^{6}LiF from oxidation.
- Nickel micromesh, 5 μm thick with openings of 37 μm every 50 μm, which is glued on the epoxy frame. The effective area is about 39 cm^2.
- The cathode is a printed-circuit-board of copper. It is composed of fifty 1.5 mm wide microstrips separated by 100 μm wide gaps (Figure 2.6).

The difference between the present arrangement and the usual MicroMegas detector is that a fast current preamplifier with 1 ns rise time will be used. This rise time is better than the 6 ns duration of the n_TOF pulse.

After the successful test in March 2000 of a MicroMegas for neutron detection, a new detector has been constructed for the measurement of the characteristics and performance of the CERN TOF facility (n_TOF-02 [31]). The detector is placed in the vacuum chamber (see Figure 2.4).

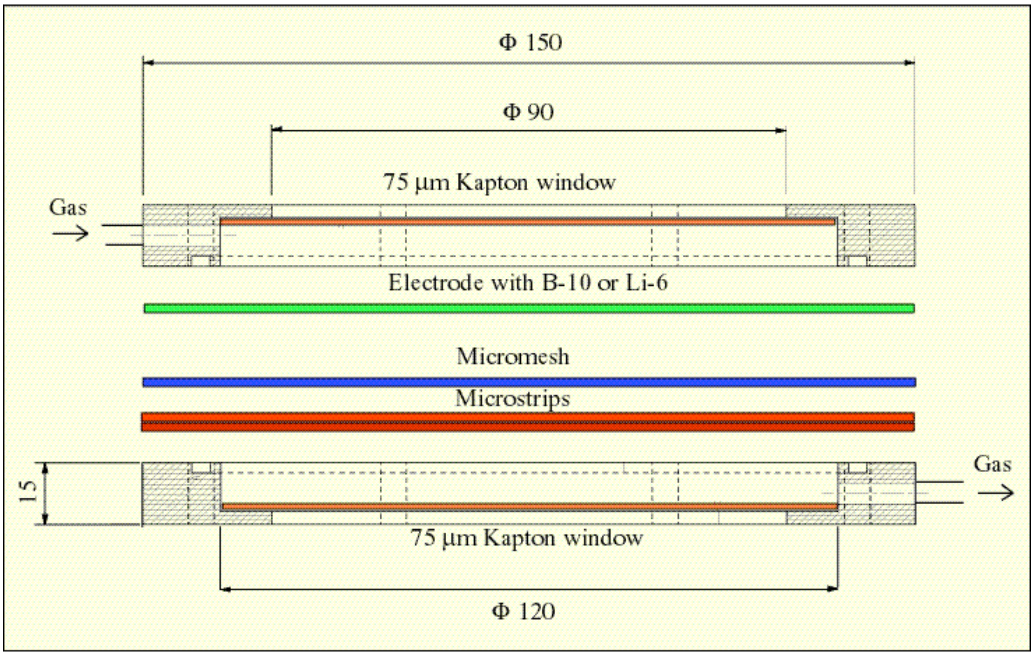

Figure 2.5: Different parts of the n_TOF MicroMegas detector.

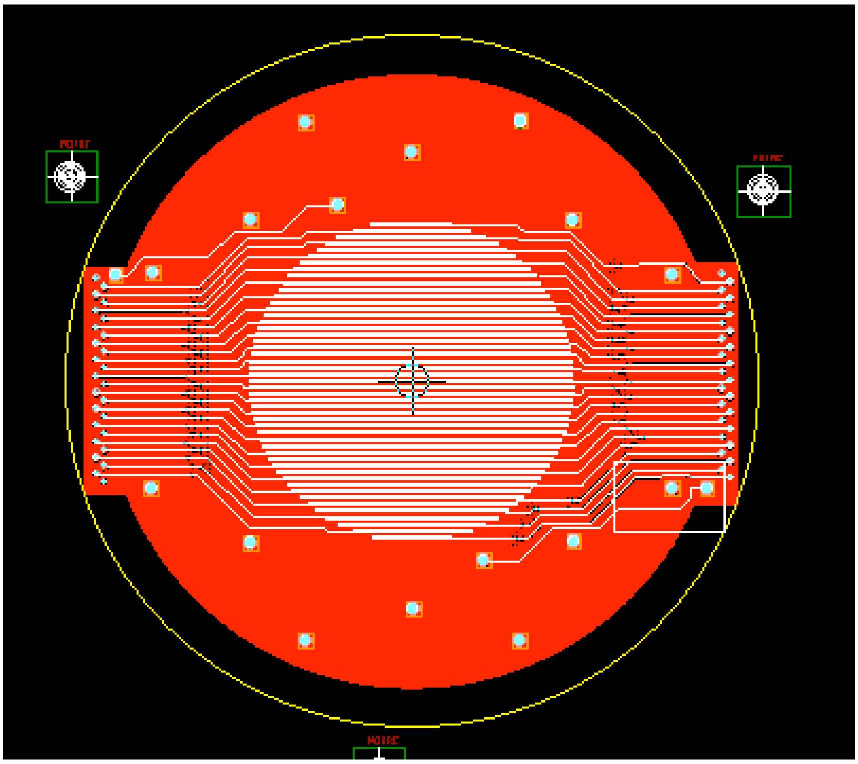

Figure 2.6: Design of the microstrip circuit.

2.1.2 Silicon Monitors (SiMON)

A neutron beam monitoring system based on Silicon detectors has been developed [32]. Four Silicon detectors, viewing a foil consisting of a pure ^{6}Li sample of 200 μg/cm^2 thickness and 6 cm diameter on a substrate of 3 μm mylar are placed inside a carbon-fiber vacuum chamber, as shown in Figure 2.7.

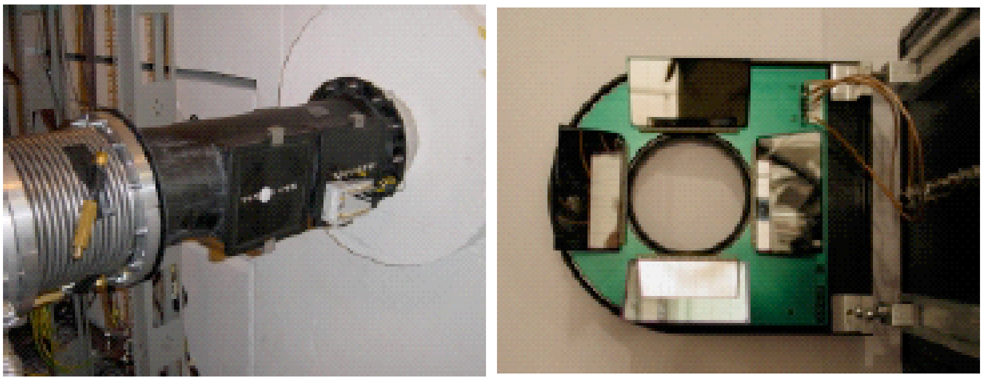

Figure 2.7: C-Fiber Chamber (left) and SiMON detectors (right).

To avoid ^{6}Li from reacting with air and falling off from the mylar, the deposit was sandwiched between two evaporated layers of C, of thickness less than 10 μg/cm^2 each. The adopted method turned out to be successful in keeping the ^{6}Li deposit in good state even after four months of operation and several air/vacuum cycles (venting operations). An advantage of the pure ^{6}Li deposit with respect to the ^{6}LiF is that a good uniformity can be achieved. The detectors and the associated electronics achieved the expected time and energy resolution expected from Monte Carlo simulations.

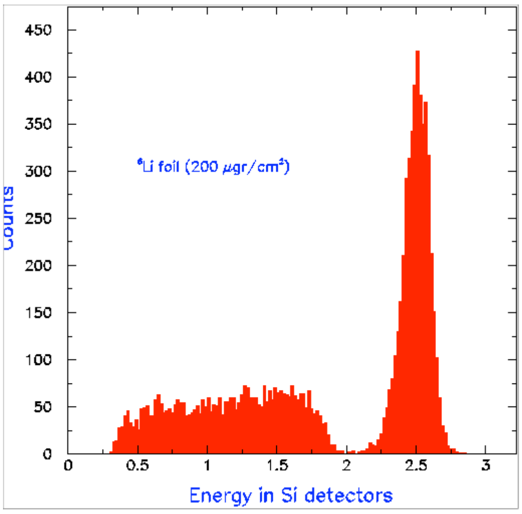

Figure 2.8: Energy deposited in the Si detectors from the products of the ^{6}*Li(n,α)t reaction, for neutron energies in the range 1 eV <* E_n *< 100 keV.*

Figure 2.8 shows the spectrum of energy deposited in the Silicon detectors taken during the first part of the measuring campaign in 2002 [32]. For the chosen thickness of the ^{6}Li deposit, tritons and alpha particles are clearly separated. To avoid threshold problems, the neutron flux analysis (and monitoring) is performed by selecting only the triton peak with a "banana" gate in a 2D plot of the energy deposited versus neutron energy.

SiMON will be used to continuously monitor the neutron beam for capture measurements. A comparison between the number of protons as derived from the number of counts in SiMON and the number of protons recorded by the n_TOF DAQ is shown in Figure 2.9

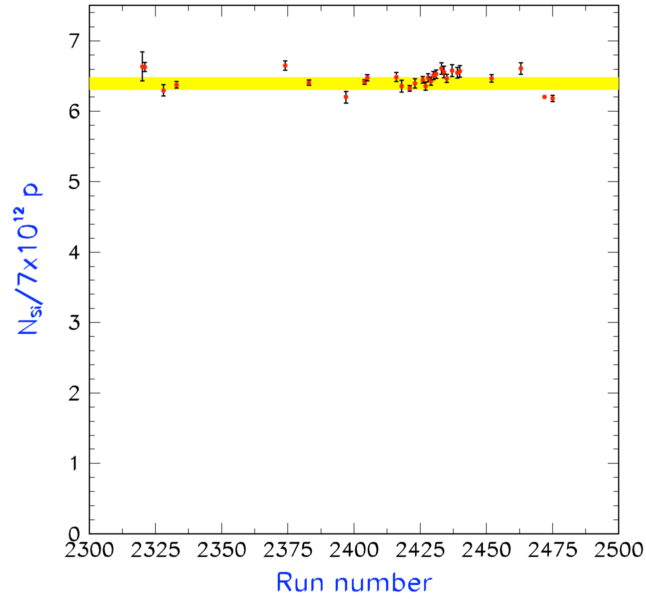

Figure 2.9: Ratio between the number of protons recorded by the n_TOF DAQ and the number of counts from SiMON. The stability of this ratio over the runs shows the reliability of the monitoring characteristics of SiMON.

The data obtained from the SiMON can also be used to obtain an absolute neutron flux determination. Due to the estimated geometric efficiency and the correction for the angular distribution of emitted tritons (this last effect also slightly affecting the shape of the neutron flux), a systematic uncertainty of the order of 10% (see section 3.1.3) has to be considered in the determination of the neutron fluence from the SiMON.

2.1.3 BF_3 Counters

The BF_3 proportional counters that we are employing are standard boron-filled detectors from CENTRONIC Limited Ref. 25EB40/50. The BF_3 proportional counter employs the $^{10}B(n,\alpha)$ reaction for the detection of thermal neutrons. Excellent characteristics are obtained, combining high detection efficiency and low background with excellent discrimination against gamma radiation. The counters have been designed to be used either with collimated beams of neutrons incident at one end of the counter or under total irradiation conditions. These counters can be employed in gamma fluxes up to typically 100 R/hr, with a maximum counting rate around 10^5 cps. The life of the counter, defined as a 10% reduction in original sensitivity, is in excess of 10^{17} neutrons/cm^2 (integrated flux units, also designated by nvt).

Construction

The counter is made of metal, filled with BF_3 gas, featuring a thin wall to minimize neutron capture (Table 2.1). The closed cylindrical body of the counter forms the cathode. The anode is a wire mounted centrally in the tube. The anode connection is brought out at one end via a suitable seal and a SHV connector. The design of the joint is such that no part of the detector exceeds the cathode tube diameter.

Dimensions: Total length: 250 mm Active length: 376 mm Connector length: 20 mm ∅ = 50.8 mm Cathode thickness: 0.7 mm	**Materials:** Body: Oxygen free copper. Electrode: ∅ 0.10 mm Tungsten. Insulation: Alumina and glass. Neutron sensitive material: Boron trifluoride. (typically 96 % ^{10}B enriched)
Electrical and Performance: Nominal operating voltage of 2695 V at 40 cm Hg gas pressure (for gas multiplication approx. 40) Plateau Length: 150 V Min. Plateau Slope: 3 % approx. per 100 V. Max. charge per pulse: $1.16\times10^{14}\times M$ coulombs, where M is the gas gain used. Operating Temperature: Limited to 80°C max. by the insulation of the connector. Life (burn up): Typically 10 % decrease at 2×10^{18} nvt with anode supply switched off.	**Typical sensitivity:** Sensitivity is a function of counter active length and pressure of the filling gas. For a thermal neutron flux of 1 nv at the nominal working voltage, the 250 mm counter sensitivity at 40 cm Hg pressure is 22 cps/nv. (nv designs flux units)

Table 2.1: Characteristics of the BF_3 counter.

Polyethylene Characteristics

The polyethylene body that contains the three BF_3 counters consists of a box of 490×490 mm^2 cross section and 475 mm in depth placed along the beam line. This structure is achieved by joining nineteen $490\times490\times25$ mm^3 plates. Six cadmium foils, $500\times500\times1.5$ mm^3, covered by additional polyethylene plates are shielding the box in order to reduce the scattered neutron background. The total dimensions of the polyethylene box are: 543 mm in width, 527 mm in height, and 528 mm in depth. Figure 2.10 shows the counters disposition inside the polyethylene.

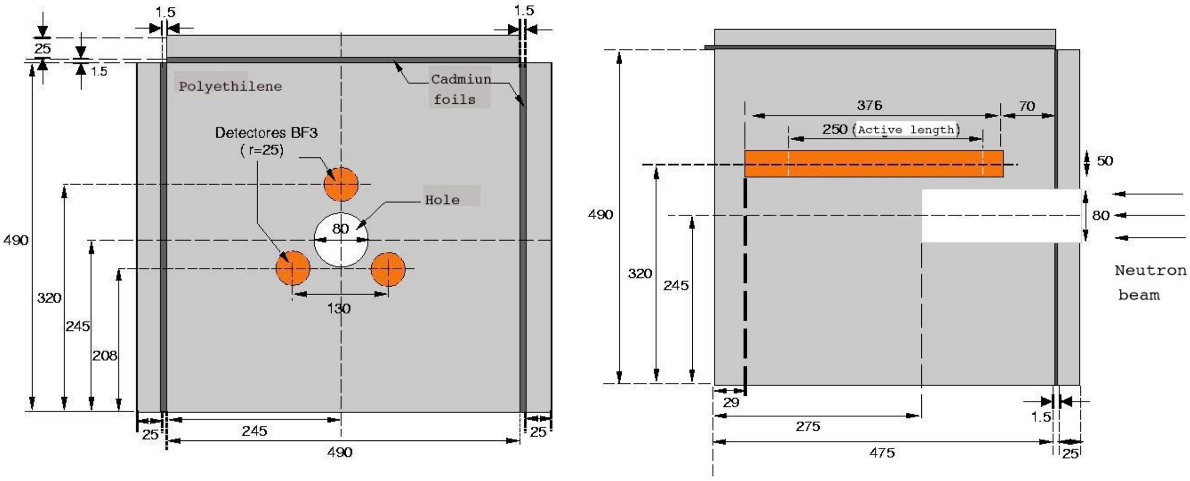

Figure 2.10: Front face (left) and longitudinal (right) cross sections.

Location at n_TOF Facility

The detector position is just at the end of the escape line, leaving a separation of half a meter between the end of the tube and the front face of the polyethylene. The distance from the lead target is approximately 197 m, and 12 m from the sample location. The exact distance from the samples is not a fundamental parameter, so short variations are not important. The critical parameter is the height of the set-up. It is necessary that he neutron beam comes into the polyethylene through the hole, so the beam center must coincide with the center of the polyethylene block. To get this fitting, the detector support must allow fine adjustment in height.

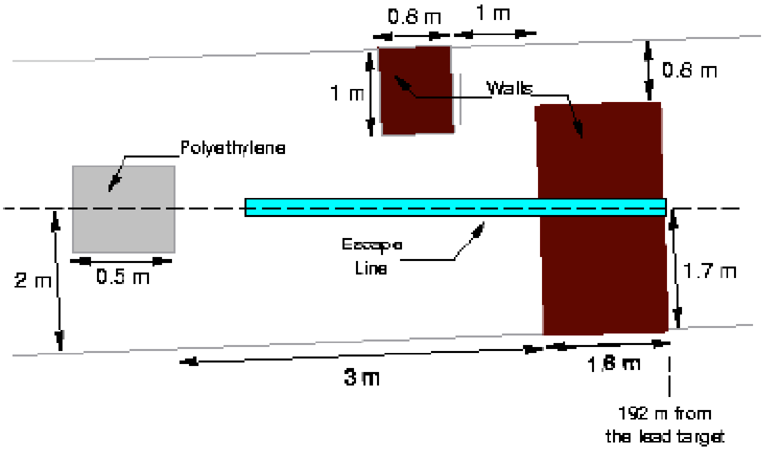

Figure 2.11: Location of the BF3 detector at the n_TOF installation.

2.2 Gamma-Ray Detection

2.2.1 *The Set of C_6D_6 Detectors: Principle of Neutron Capture Measurements with C_6D_6 Detectors*

Neutron capture experiments, performed using C_6D_6 γ-ray detectors [33], are used in combination with the pulse height weighting technique. Pulse height weighting is a method of making the detection efficiency independent of the γ-ray cascade of the (n,γ) reaction. These detectors have a low γ-ray efficiency over the range of interest between 0.1-10 MeV, but have very low sensitivity to scattered neutrons as compared to other gamma-ray detectors. However, in contrast to a 4π total absorption calorimeter, it is not possible with C_6D_6 detectors to distinguish whether the detected γ rays originate from the (n,γ) reaction, the radioactive background or from competing reaction channels like fission or inelastic scattering.

The quantity determined in a neutron capture experiment is the capture yield, i.e. the fraction of neutrons incident on a sample (with thickness N atoms per barn) and undergoing the (n,γ) interaction. The capture yield Y(E), with 0 < Y(E) < 1, for the first interaction can be written as:

$$Y(E) = (1 - e^{-N\sigma_T(E)}) \cdot \frac{\sigma_\gamma(E)}{\sigma_T(E)} \approx \begin{cases} N\sigma_\gamma & \textit{if } N\sigma_T << 1 \\ \sigma_\gamma / \sigma_T < 1 & \textit{if } N\sigma_T >> 1 \end{cases}$$

The two limiting cases are approximations for thin and thick samples, respectively. Additional terms must be added to this yield coming from neutrons that are scattered one or more times in the sample and surroundings and subsequently captured. This multiple scattering effect has to be taken into account in the R-matrix analysis code. Since the efficiency and solid angle of the detector do not exceed a few percent, the measured time-of-flight spectra need to be normalized to a well-known isotope. The standard technique is to measure this normalization using a "saturated" resonance. This refers to a resonance where the thick sample approximation is valid in the peak of the resonance and where the capture yield is no more proportional to the capture cross section but to the ratio of the capture and the total cross section. The measured resonance shape has then a flat top and from this characteristic shape the normalization constant can be extracted. Often an isotope does not have such a large resonance or is not available as a thick sample. In that case the normalization is determined by measuring the first saturated resonance of e.g. gold or silver at resonance energies of 4.9 eV (^{197}Au) and 5.1 eV (^{109}Ag), respectively. Since only the saturated resonance needs to be measured, the normalization measurement with gold or silver lasts in general much shorter than the actual measurement.

2.2.2 *The n_TOF Set-Up of C_6D_6 Detectors*

Detailed GEANT simulations [33] were performed in order to optimized a commercially available and fairly robust version as well as a more advanced design of the C_6D_6 detectors used at FZK. The simulations were performed with GEANT 3.2112 [34] including the library GCALOR [35] for neutron tracking. GCALOR is an interface to the Monte Carlo neutron code MICAP [36]. The γ-rays and neutrons were assumed to originate from a point source in front of the detector at a distance of 10 cm. Particular attention was paid with respect to neutron sensitivity, where the following improvement could be achieved:

1. BICRON version: This is a commercial detector, consisting of an aluminum cell based on the design of Nuclear Enterprise and manufactured by BICRON. Due to the results obtained in the present simulations, the neutron sensitivity of this detector has been reduced by a factor of four. Figure 2.12 shows the modified detectors.

2. FZK version: This detector was designed and manufactured by Forschungszentrum Karlsruhe and consists originally also of an aluminum cell but with much thinner walls. The neutron response of the original FZK design was further reduced by using a very thin carbon fiber cell for the scintillator which was glued directly onto the photomultiplier tube. In this way, all the parts which are not absolutely essential, were removed, including the window of the cell and the complete photomultiplier housing. Compared to the improved BICRON detector, the resulting neutron sensitivity could be reduced by another factor of four.

Figure 2.12: The modified BICRON C_6D_6 detectors.

The γ-efficiency was determined in the simulations by means of the energy deposition in the C_6D_6. Since an event was only counted if the deposited energy in the scintillator was greater than the threshold at 100 keV, the efficiency starts to decrease below 600 keV. Corresponding to the situation at n_TOF the γ-source was assumed to be 2.8 cm in front of the detector. Because of the different scintillator volumes, the γ-ray efficiency of the FZK detector is approximately 50% larger than that of the BICRON version.

The results of the simulations are summarized in Figure 2.13, which shows that the neutron sensitivity could be significantly improved. This achievement will be particularly important in measurements of resonance dominated cross sections with scattering to capture ratios of 10^4 or more. The original BICRON design suffered from the fact that it contained fairly massive aluminum parts and that the expansion volume in the form of a Teflon tube was wound around the scintillator cell, resulting in a pronounced sensitivity at the positions of the Al and F resonances.

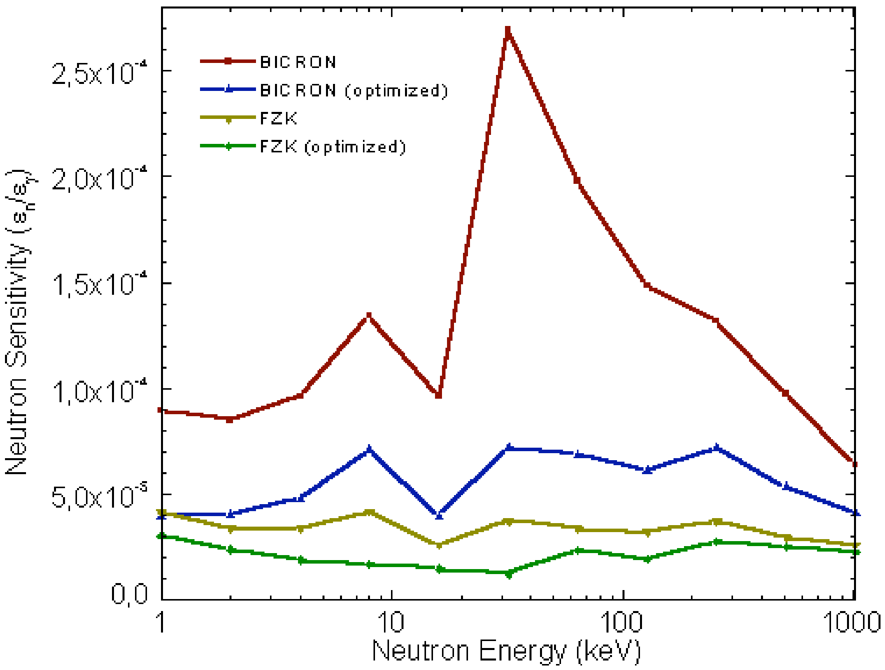

Figure 2.13: Comparison of the neutron sensitivities of the investigated designs. The neutron sensitivity is given relative to the γ-ray efficiency at 640 keV.

The simulated neutron sensitivity of the optimized FZK version was experimentally verified at the Karlsruhe Van de Graaff accelerator. Figure 2.14 shows this detector in front of the neutron target. The neutron sensitivity was measured in a TOF experiment using a neutron spectrum of E_n = 30±20 keV. The measured neutron sensitivity of $\varepsilon_n = (2.4\pm0.3)\text{x}10^{-6}$ was found in fair agreement with the simulated value of $3.7\text{x}10^{-6}$, given the fact that the experimental threshold was higher than that assumed in the simulation. A detailed description of simulations and test measurements can be found in reference [33].

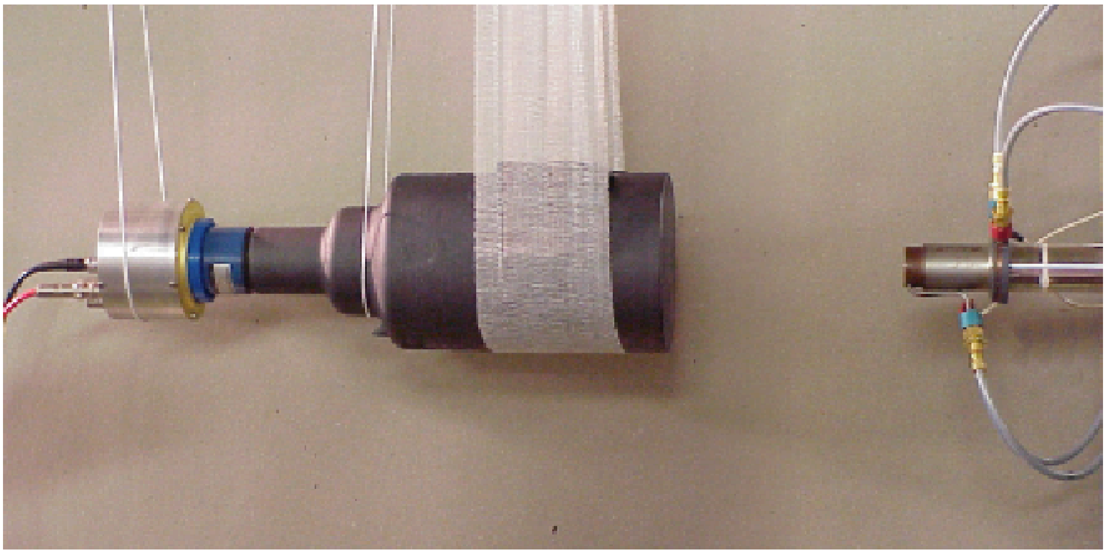

Figure 2.14: The optimized FZK detector mounted in front of the neutron production target at the Karlsruhe Van de Graaff accelerator. Note the quasi-massless suspension. The distance to the neutron target in the right part of the figure was 20 cm.

Two optimized FZK detectors have been manufactured and were successfully used during the measurement campaign 2002. Both detectors were mounted in direct contact with the beam line, in close geometry with respect to the sample. This setup allowed one to achieve an overall efficiency for capture events of about 15%. Figure 2.15 illustrates the arrangement of detectors, beam line and sample changer.

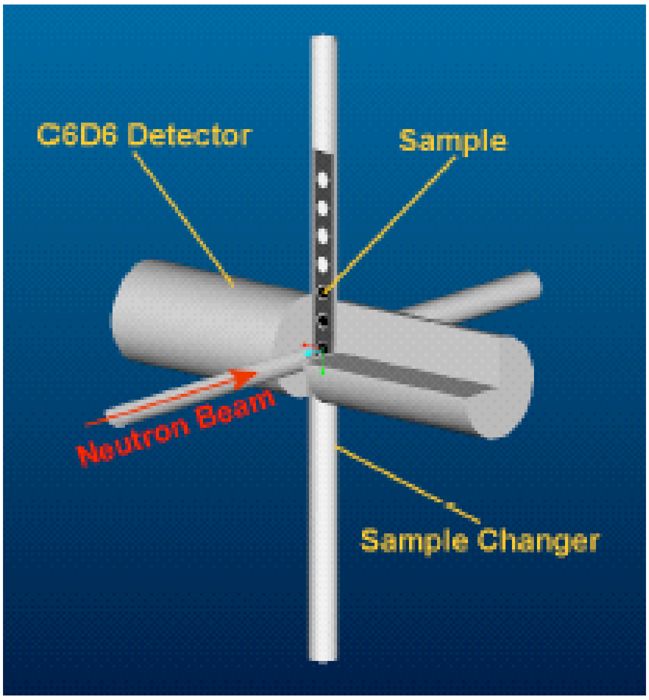

Figure 2.15: Schematic view of the experimental setup for capture measurements in EAR-1.

Determination of Weighting Functions

The working principle of the C_6D_6 detectors for (n,γ) cross-section measurements is the a posteriori manipulation of their γ-response distribution R_{ij} through the introduction of a set of weighting factors W_i such that the detection efficiency becomes proportional to the γ-ray energy E_γ :

$$\sum_i W_i R_{ij} = kE_\gamma$$

In this way the detection efficiency of the capture cascade becomes proportional to the energy of the cascade, and thus independent of the actual path, if the probability of simultaneous detection of more than one cascade γ-ray is negligible.

Obviously the accuracy of the method depends strongly on the accuracy with which the responses can be determined. Historically, and due to the difficulty to obtain mono-energetic γ-ray sources in the energy range of interest, the detector responses were initially obtained by Monte Carlo simulations. It was found later that there was a serious discrepancy between the result obtained by this method and the one obtained from transmission measurements for the well-known resonance at 1.15 keV in ^{56}Fe. After thorough investigations it became clear that the problem was originating in the Monte Carlo simulated response distributions.

This conclusion was arrived at mainly, after careful measurements at Geel [37] of mono-energetic γ-ray responses. The method employed was the coincidence technique for two-gamma cascades populated in (p,γ) resonance reactions in light nuclei. Subsequently, the measurements were repeated with a detector set-up similar to the one employed in the (n,γ) measurements. The extracted experimental weighting function giving a cross section in agreement with the standard transmission value for the 1.15 keV resonance of ^{56}Fe, was adopted for the capture measurements. However, it was also recognized that the cause for the discrepancy between the Monte Carlo simulated response and the measurement was probably due to the big influence of the materials surrounding the source (other than the detecting medium) producing secondary radiation. This cast some doubts on the universality (or even validity) of the experimental weighting function determined for the (p,γ) set-up when employed for the (n,γ) measurements. In order to take into account the systematic differences of the various target and detector set-ups only the Monte Carlo method is practicable.

At Oak Ridge [38], the Monte Carlo method was further investigated and it was found that the EGS4 [39] code gave a satisfactory result for the 1.15 keV resonance of ^{56}Fe measured with their experimental set-up. They were not able, however, to produce the same result when applied to the Geel set-up.

We have decided to re-investigated this issue more carefully. In particular whether the differences between Monte Carlo and measurement could be due to insufficient detail in the description of the measuring set-up or rather due to a poor implementation in the Monte Carlo code of the relevant physical processes in the generation and interaction of the secondary radiation.

The simulation package GEANT3 [34] was chosen and was used to investigate extensively the response of the detector set-up described in reference [40] in the photon energy range 1.2 - 8.4 MeV. The main results of this study can be summarized as follows:

- the shape of the measured response distributions is well reproduced by the simulation. The absolute value of the efficiency is well reproduced at the higher energies but there is a tendency to overestimate it at low energies (18% at 1.2 MeV). This result is not understood since at low energies one expects the Monte Carlo simulation to work better;
- at high energies the contribution to the detection efficiency of the dead materials is close to 40%. The contribution of the detector dead material is negligible as compared with the (p,γ) target backing (0.3 mm Ta).

The validity of the experimental (p,γ) weighting function for the capture measurements was investigated in reference [38] by comparing the result obtained for the 1.15 keV resonance of ^{56}Fe using different sample thickness and compositions. In order to be able to compare with these results a realistic simulation of the capture process would be necessary. Therefore a computer program was developed to generate realistic cascade events by the Monte Carlo method. For each nucleus a known low-energy level scheme can be defined consisting in a complete set of levels with known spin-parity and branching-ratios (obtained from evaluated data files, for example). At higher energies and up to the resonant state, the statistical model of the nucleus is used to generate a level scheme. Levels of appropriate spin-parity are generated from a level density formula (giving the average level spacing) by introducing fluctuations of the Wigner type. The γ-ray intensities are generated from the Giant Resonance (GR) model (Axel-Brink hypothesis) by introducing fluctuations of the Porter-Thomas type. The conversion electron process is also taken into account. Appropriate parameters for both level densities and GR can be defined for each nucleus.

In Figure 2.16 it is shown the comparison of the simulated experiment with the measurement for different samples. On one hand the dispersion of the experimental values shows the limitation of the experimental (p,γ) weighting function applied to the capture measurements. On the other hand the fact that the simulation reproduces the behavior of the experimental points is a strong evidence for the accuracy of the Monte Carlo simulations.

All this confirms the necessity of using the appropriate weighting function for each specific (n,γ) set-up, which can only be obtained by Monte-Carlo simulations. The accuracy of the simulations should be verified with a set of selected capture measurements on well known resonances. The measurements should be chosen to enhance the systematic effects of the weighting function on the extracted cross section. This can be achieved selecting resonances with very different decay patterns, that is, with different average γ-ray cascade multiplicities □(□) and energies. The proposed measurements include: the 16.2 keV [□(□) = 1.9] and the 30.4 keV [□(□) = 1.0] resonances in ^{207}Pb (S_n = 7.367 MeV), the 1.15 keV resonance [□(□) = 3.2] in ^{56}Fe (S_n = 7.646 MeV), the 4.9 eV resonance [□(□) = 4.8] in ^{197}Au (S_n = 6.512 MeV), the 5.2 eV resonance in ^{109}Ag (S_n = 6.809 MeV) and the first resonances [□(□) = 4.0] in ^{238}U (S_n = 4.806 MeV).

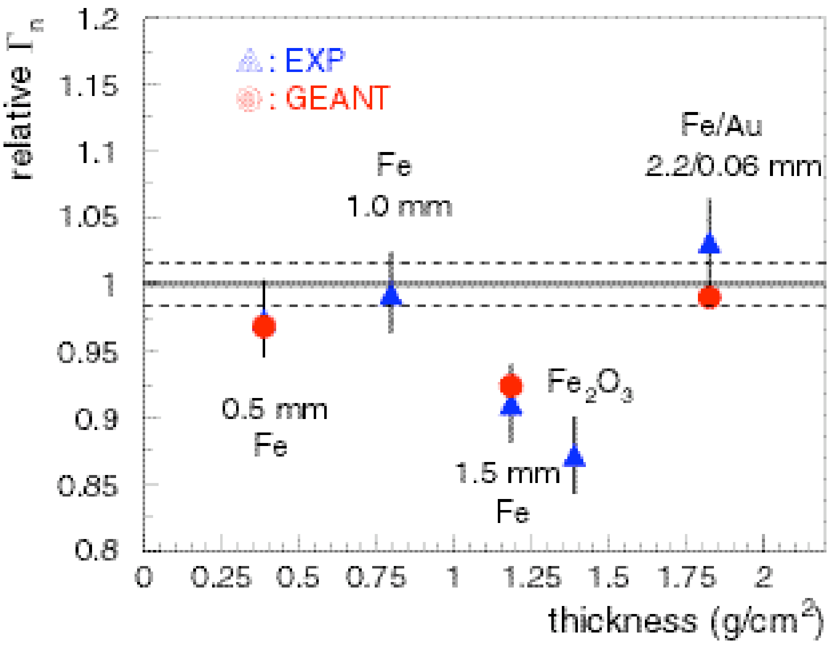

Figure 2.16: Comparison of measured [37] and simulated neutron width for the 1.15 keV resonance of ^{56}Fe obtained with the pulse height weighting technique for various sample thicknesses and compositions. The values are normalized to the transmission value.

2.2.3 BaF$_2$ Detectors and the 4π Total Absorption Calorimeter (TAC)

The best signature for the identification of neutron capture events in (n,γ) cross section measurements via the TOF technique is the total energy of the γ-cascade by which the product nucleus de-excites to its ground state. Hence, accurate measurements of (n,γ) cross sections are best to be made by using a detector that operates as a calorimeter with good energy resolution. In the γ-spectrum of such a detector, all capture events would fall in a line at the neutron binding energy (typically between 5 and 10 MeV), well separated from the γ-ray backgrounds that are inevitable in neutron experiments, and independent of the multiplicity of the γ-ray cascade.

These arguments point to a 4π detector of high efficiency, made of a scintillator with reasonably good time and energy resolution. In addition, the detector should be insensitive to scattered neutrons, since – on average – the scattering cross sections are about 10 to 100 times larger than the capture cross sections. These aspects have been combined in the design of the 4π BaF$_2$ detector shown in Figure 2.17.

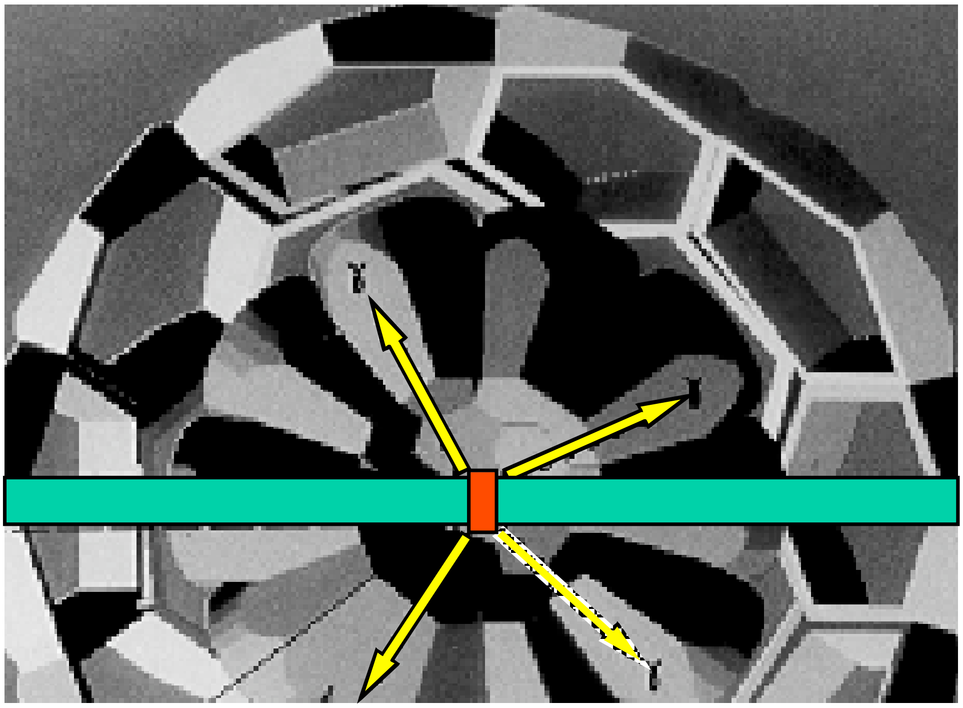

Figure 2.17: Schematic sketch of the 4π BaF$_2$ calorimeter.

The 42-element geometry chosen for this detector corresponds to the Karlsruhe array [41]. It includes 30 hexagonal and 12 pentagonal crystals forming a closed, spherical BaF$_2$ shell with an inner diameter of 20 cm and a thickness of 15 cm. Given the density of 4.88 g/cm^3 the detector exhibits an absolute γ-ray efficiency of better than 90% in the energy range up to 10 MeV. This means that γ-ray cascades following neutron capture can be detected with an efficiency of ≥ 95%. Other important features of this detector are a resolution in γ-ray energy ranging from 14% at 662 keV to 6% at 6.13 MeV and a time resolution of 500 ps.

The complex geometry of this detector was modeled in detail, including the light reflectors [42]. The cladding materials of the BaF$_2$ crystals, and the supporting structure, for a full computer simulation of the detector performance. These simulations were carried out with the GEANT package [34] complemented by the GCALOR software [35] for following neutron energies down to very low energies. The simulations were verified by comparison with experimental data obtained with the Karlsruhe array, which could be perfectly reproduced.

Figure 2.18 shows the response of the detector array to a gold sample. The open part of the spectra corresponds to true capture events in gold, while the hatched part illustrates the background due to neutrons scattered in the sample and captured in the scintillator. While of no concern in the eV range, this background becomes increasingly disturbing at higher energies. Therefore, it is foreseen to surround the sample by a 5 to 6 cm thick neutron absorber made from ^{6}LiH. The advantages of this material are that neutron captures on ^{6}Li do not produce additional γ-rays, that it is transparent to the original capture γ-rays from the sample, and that the high concentration of hydrogen ensures an efficient moderation into a neutron energy regime where the ^{6}Li cross section is large. Accordingly, the signal to background ratios in the spectra of Figure 2.18 are improved by factors of 40, 19, and 6 for energies ranging from 0.1-1 keV, 1-10 keV and 10-100 keV respectively.

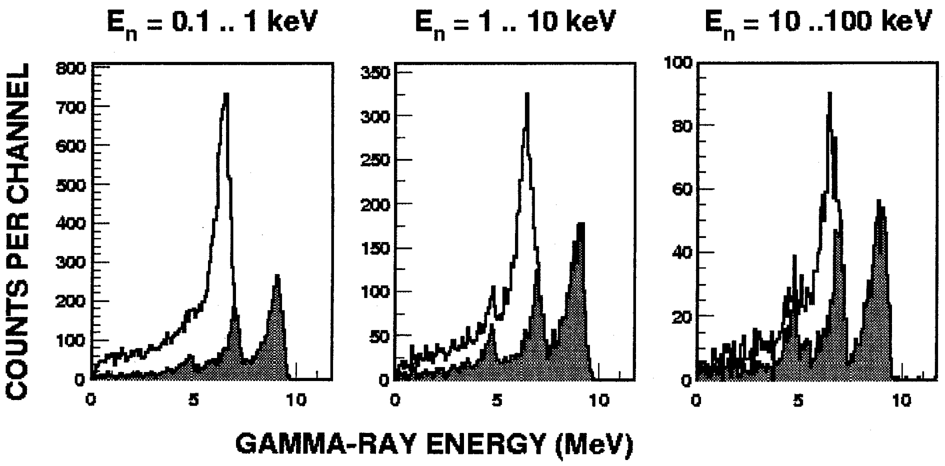

Figure 2.18: GEANT simulations of the response of the 4π BaF_2 calorimeter to a gold sample. The contributions from true capture events are indicated by the open parts, while the hatched parts correspond to background from scattered neutrons. This background can be reduced by factors of 40, 19, and 6 (from left to right) surrounding the sample with a 6 cm thick layer of ^6LiH.

First tests at the very beginning of the n_TOF campaign in 2001 revealed an unexpected obstacle. The intense, instant flash from the spallation target, caused the BaF_2 detectors to be blind for about 100 μs. Accordingly, the accessible neutron energy range would have been restricted to values below 15 keV. **This problem was drastically reduced by the improved shielding that was installed during the summer of 2001** [65]. As shown in the left panel of Figure 2.19, the detectors had recovered after 20 μs, thus allowing for an accessible neutron energy range of up to several 100 keV. Finally, further optimization of the shielding resulted in the present situation illustrated in the right panel of Figure 2.19. Now, the entire relevant energy range up to 1 MeV can be studied with the BaF_2 detector.

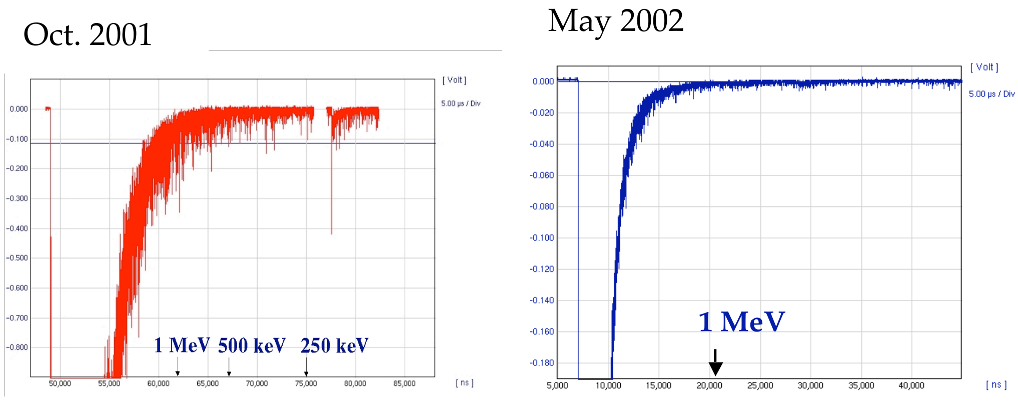

Figure 2.19: The response of the BaF_2 detectors to the instant flash from the spallation target. The left panel illustrates the status after the first installation of an iron shielding. Further improvement of this shielding led to the situation on the right, which indicates an accessible energy range up to 1 MeV.

The BaF_2 calorimeter is being constructed in the curse of 2002-2003. It is expected to be operational for the measuring campaign of 2004.

2.2.4 *HPGe detectors*

Germanium detectors are mandatory for γ-ray spectroscopy because of their high energy resolution. However, their use at n_TOF is not straightforward because of the high flux and the very low frequency of the beam. Indeed, the neutrons corresponding to (n,xn) reactions, for example, have energies between 6 and 250 MeV and appear between 1 and 5 μs after the impact of the proton beam so that the effective time per burst is 4 μs only. This yields a total effective time of some tens of seconds per year per burst. The measurement of (n,xn) cross sections is nevertheless possible, but the method has to be adapted to these extreme conditions. The solution proposed is based on a digitalization of the preamplifier signal with a 12 bit, 100 MS/s flash ADC and a pixelization of the detectors. Several tests have been performed to develop this new method.

A first test at n_TOF in June 2001 had shown that the preamplifier of the detector was blocked during more than 120 μs after the beam pulse, even at a large distance from the sample. The origin of this blocking was attributed to the high muon flux in the experimental room, which has been strongly reduced since then. Nevertheless, results of measurements with the same set of detectors at other facilities (GELINA at IRMM Geel and the cyclotron of Louvain-la-Neuve) opened interesting opportunities for measurements at these facilities, and represent major steps toward the demonstration of the applicability of the method at n_TOF. A new test was therefore performed at CERN in June 2002. In order not to perturb the running capture measurement, the detector was set at a distance of about 70 cm from the beam line. A new preamplifier, in which a current opposite to the signal is injected and resets the preamplifier, was used. This procedure is triggered by the signal of the PS with an adaptable delay, so that the detector can be ready soon after the flash. The result was encouraging. According to the intensity of the time t=0 flash, the detector was ready to register γ rays after t=2 to 6 μs, i.e. for neutron energies lower than 50 and 4.5 MeV, respectively. This was a very significant, but not fully sufficient improvement.

In September 2002, for the first time, two detectors were set as close as 12 cm from a sample. This test lasted for a few hours. The two detectors were equipped with the new preamplifier and with a conventional one, respectively. Depending on the intensity of the flash, the latter detector was blocked during up to 120 μs, exactly as before the additional iron wall was built, while the externally reset one recovered after less than 25 μs. Its behavior suggests that an energy between 10 and 40 MeV is deposited in the detector at time t=0 for each burst. Runs were performed also with an empty target frame and with the detector being placed at 24 cm from the sample, apparently without any significant change. This point deserves however further analysis. Quite recently, it has been possible (off beam) to divide the reset time of the preamplifier by a factor 2. The dead times reported above can be divided by the same factor, but this can only be checked with the beam. From the above reported observations, it appears that there is still a large flux of muons in a narrow zone around the beam pipe. FLUKA simulations are needed and will be performed in order to understand the energy deposit in the detector at time t=0, and to find solutions to lower it to acceptable values. At first glance, it is not excluded that an additional iron shielding not far from the detector may suppress completely the flash.

It is also planned to test a 5x5 segmented planar detector. The advantage would be of course that if the energy deposit is due to many interactions, it will be distributed over 25 segments and come in the range where the current injection in the preamplifier is able to reset it very quickly. On the contrary, if it is due to a few interactions, only a few segments will be blocked. Anyway, as already stated, a pixelization is mandatory at n_TOF to allow registering a sufficiently large number of γ rays in the short effective time corresponding to high energy neutrons.

To summarize, it is fair to state that HPGe detectors can be used at n_TOF below about 1 MeV, with the reset preamplifier. They could, thus, be used already now to study (n,γ) reactions, but progress is still needed to use them above this limit. An improved shielding against the residual muon flux present around the beam-line may be sufficient.

2.3 Fission

2.3.1 PTB Chamber (from the Physikalisch-Technische Bundesanstalt Institute)

Two identical parallel plate ionization chambers (Figure 2.20a) with fissile deposits, one with ^{235}U and another with ^{238}U, have been used with the main objective to determine the neutron flux over a wide energy range. These detectors are inter-comparison instruments and were provided by the PTB institute. A full description of the detectors can be found in [43].

The detectors consist of five platinum plates with fissile deposits on both sides separated by 5 mm of the electrodes made of tantalum. The thickness of the electrodes is about 0.125 mm. The circular plates are 86 mm in diameter, and the fissile deposits have a diameter of 76 mm. The overall thickness of the fission chamber is 50 mm and they work under atmospheric pressure, with a gas mixture made of 90% of Ar and 10% of CF_4. The 0.15 mm-thin windows are made of tantalum.

The total mass of ^{235}U and ^{238}U deposited is respectively 201.56 ± 0.60 mg and 197.78 ± 0.60 mg or equivalently 444 μg/cm^2/plate for the ^{235}U and 436 μg/cm^2/plate for the ^{238}U. The isotopic purity is about 99.9% for both materials.

The detection efficiency of the chambers is a slowly decreasing function of energy, from about 95% at lower energies down to 91% for energies of 150 MeV (Figure 2.20b).

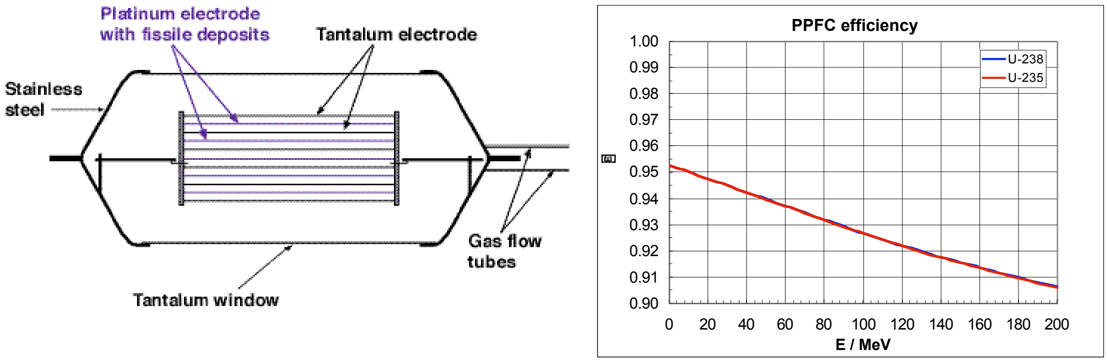

(a) (b)

Figure 2.20: a) The multi-plate fission chamber from PTB. b) Fission chamber efficiency.

Experimental Setup

During the commissioning measurements, in the experimental area, the vacuum tube was ended with a 500 μm thick aluminum window placed at a distance of 182.1 m from the window of the spallation target. The ^{238}U fission chamber was placed in air at a distance of 182.25 m and the ^{235}U fission chamber was placed at 182.35 m from the spallation target window after the ^{238}U chamber. The beam profile at the position of the detectors shows a radius of R_{beam}=1.65 cm [44, 45].

Data Acquisition System

The signals from the detectors were sent to the n_TOF control room that hosted the data acquisition system (DAQ) and the electronics. The DAQ has been specially elaborated for the commissioning measurements but it is a general purpose one, as resulting from a detailed description [46].

The DAQ concept stems from the necessity of preserving the time correlation of all the information coming from various detectors, sensors and monitors. Considering the high rates of events in the detectors induced by the proton burst, it was decided that a double system should be used: flash ADCs and multi-hit TDCs. The FADC's used was the model V676 from CAEN with 3 input channels, a sampling rate of 25 ns, and a buffer of 4096 samples, equivalent to 102.4 μs sampling range. One FADC was used for each chamber, recording in the first channel the raw signal from the detector and on the second the discriminated from the CFD. The TDC's used were the model CAEN V767B, with 128 input channels, a time resolution of 0.8 ns and a buffer capable of recording up to 32k events. The active range of the TDC's is 800 μs, but with a use of periodic signal of 300 μs connected in one of the TDC channels, we could discriminate signals down to 300 ms, well below the thermal neutrons. One TDC was used for each detector, recording the arrival time of the discriminated signal from the CFD relative to the forerunning pulse from the PS. The threshold set on the CFD's was carefully chosen to discriminate the alphas from the fission fragments.

Moreover, the DAQ was accommodating all the information coming from all the beam transformers (for the intensity of the proton beam), beam profile monitors, thermocouples and the fission events on scalers with various time windows for later cross checking. This information was used in the data processing for rejecting the "bad" events. The DAQ was triggered with the forerunning pulse from the PS, which was set a few μs before the gamma flash.

2.3.2 *Parallel Plate Avalanche Counters (PPACs)*

Parallel Plate Avalanche Counters (PPACs) have been known for many years as a precise timing instrument but were scarcely used before the considerable development of heavy ion physics. A PPAC consists of two thin parallel stretched foils with a very low gas pressure in between. Particles traverse the detector perpendicular to the planes. The principle of operation is the same as a multiwire proportional chamber. The gap between the foils must be small, a few millimeters, in order to maintain a high electric field, for reducing the time spread and achieving good time resolution. The electric field has to be uniform to insure the same operating regime on the whole active surface of the detector. Copper coated epoxy resin for printed circuit board, on which thin aluminized plastic foils are glued, is very well suited for this purpose. The copper layer is used for electric connections. Time determination is obtained on a central anode made of 1.5 micron thick mylar foil aluminized on both sides. Cathodes placed on each side of the anode are made from 1.5 micron thick mylar foils also, with deposited aluminum strips 2 mm wide. One cathode gives the X position, the other with strips deposited perpendicularly, gives the Y position. Each strip is connected to a cell of a delay line, each cell giving a 2 ns delay. The positions in X and Y are then given by the delay observed at the end of the line, with a resolution of 2 mm at worse.

These detectors are built to operate with pressures ranging from 1 up to 20 mbar. Under these low pressure conditions, a few hundred volts applied between the plates (typically 300 V/cm/mbar) is sufficient to reach the proportional regime. Released electrons gain enough energy to induce immediate secondary ionization in the homogeneous electric field, forming a Townsend avalanche. It seems that pure hydrocarbons are best suited for these detectors and higher gains can be reached with isobutane. Multiplication factors of thousands are obtained with 100%

efficiency in a wide domain of energy losses. For large energy losses like those obtained from fission fragments (FF), pulse height saturation can occur. Therefore, a relatively low voltage can be set, which allows operating the detector far from the sparking limit. A 2 to 3 ns rise time pulse is collected due to the high velocity of electrons and the good homogeneity of the electric field. Only the fast component of the signal due to the motion of electrons is used. The slow part from the positive ions is eliminated by differentiation of the signal. The best timing performances may not necessarily correspond to the fastest output rise time, since at very low gas pressure, pulse fluctuations can become important. Time resolutions of the order of 250 ps (FWHM) are obtained with such detectors even for large dimensions.

PPACs possess a number of attractive features. They are the thinnest available time and position sensitive detectors, eliminating problems due to auto-absorption. They can be built in large dimensions, they are not sensitive to radiation damage, and the fast removal of positive ions provides them a high rate capability as position detectors (more than 2 MHz frequency).

The n TOF Set-up of the PPAC Detectors

The samples are placed in a stack where each of them sees two PPACs [5]. The neutron beam traverses perpendicularly the whole assembly constituted by PPACs and samples as shown in Figure 2.21.

A sample made of material spread as a layer of 300 $\mu g/cm^2$ and with few cm in diameter is placed perpendicular to the neutron beam direction. The target is deposited on a thin substrate to allow the detection of the two fission fragments in coincidence. Two $20 \times 20\ cm^2$ PPACs (perpendicular to the beam) are placed on each side of the target. They are able to detect and measure the position of the two fission fragments emitted in coincidence by the fissionable nuclei with practically 100% efficiency (when their angle of emission is small enough to allow fission fragments to escape from the target and traverse the backing and the mylar foils of the PPACs). The distance between the PPACs and the 300 $\mu g/cm^2$ target is of 15 mm. From measurements of the position, it is possible to deduce the angle of emission of both fragments. The corresponding solid angle can be determined within a few per cent for each target, and is of the order of 50% of 4π at least, depending on the target and backing thicknesses.

The sample and the PPACs are mounted in an aluminum chamber connected to the neutron TOF tube since they operate at very low gas pressure (7 mbar isobutane). Tightness is insured by Mylar windows. High voltage cables, signals from PPACs, and gas-flow are connected through a flange.

Materials with "standard" fission cross sections, like ^{235}U, ^{238}U and ^{209}Bi, are used both for normalization of the relative fission yields as well as for flux monitoring. A total of 10 samples, including those used as flux monitors and standards, can be measured at once.

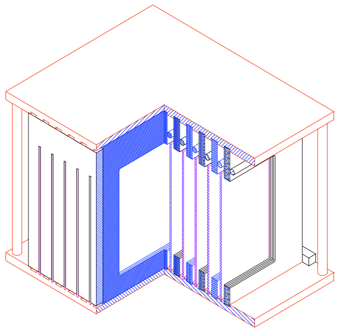

Figure 2.21: A schematic draw of the 10 PPAC detectors.

Gas Circuit and Regulation

The gas enters between the PPAC electrodes to insure good sweeping of the ions created by the fission fragments and then fills the aluminum chamber. The pressure is maintained at 7 mbar and a steady flow of 2 liters per hour with a gas regulation placed near the chamber (Figure 2.22). The differential regulation maintains a constant differential pressure between the vacuum tube and the detector device through a pressure sensor connected to both, the vacuum and the gas circuit. The primary pump is situated close to the regulation crate, in order to maintain constant gas flow. The exiting gas will be rejected into the atmosphere through an evacuation pipe.

A bypass, closed under regular conditions, can be opened for pumping or filling, in order to avoid pressure differences which could damage the windows. All these operations are automatically controlled either locally or remotely.

Specific safety circuits (Figure 2.22) are activated in cases of any failure of the regulating devices. Lower- and higher-pressure thresholds prevent over- or under-pressure in the system, for instance if the primary pump breaks down. Any crossing of these thresholds closes automatically the valves, thus separating the PPAC device. In case of power failure, valves are automatically closed isolating the detectors, and locks prevent these valves from re-opening when the power is restored. If the pressure in the chamber increases, a bypass valve is opened preventing any pressure difference. If the vacuum breaks down, flatting of the chamber with air is avoided by means of electromagnetic and pneumatic valves in parallel to the bypass activated by power failure. Due to the differential regulation a constant pressure of 7 mbar is kept between the detector and the vacuum chamber.

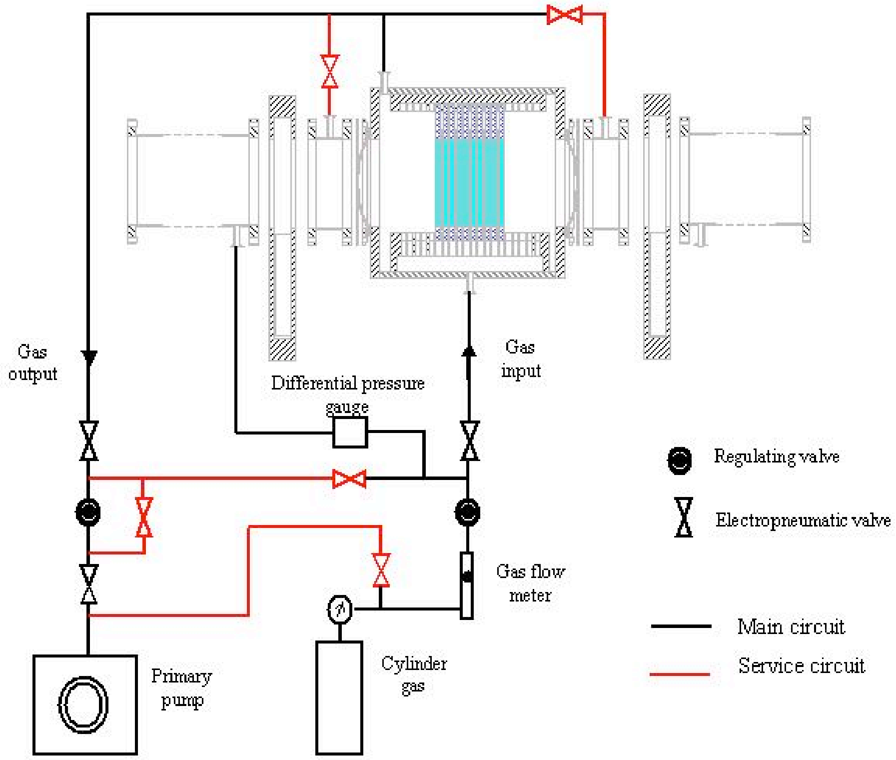

Figure 2.22: The PPACs gas regulation system.

The Spatial Resolution

The detectors are made of 2 mm wide Al strips deposited on 0.9 mm Mylar foils. This allows achieving a spatial resolution of few millimeters with avalanche parallel plate detectors. The PPAC anodes are connected to current preamplifiers delivering signals of 10 ns total width with a time resolution of < 1 ns. This anode signal enters a 1 GHz Flash ADC of 8 bits resolution and provides the neutron arrival time. The strips of the cathodes are connected to delay lines with each delay cell inducing a 5 ns delay, allowing thus a position determination from the delayed signals collected at each end of the delay lines. The signal amplitude and the detection of the two fission fragments in coincidence are used for discriminating fission and alpha particles. The solid angle covered by a PPAC pair is almost 4π. However, when the fission fragments are emitted tangentially, self-absorption in the sample, energy losses in the backing, and energy losses in the entrance windows of the PPAC have to be considered. Table 2.2 shows the importance of these effects for different sample thickness. We concluded that 300 μg/cm^2 thick samples constitute an optimal compromise.

	Detection probability for Fission Fragments with more than 10 MeV residual energy inside the PPAC		Limiting angle (angle between fragment and target surface)	
Target thickness	Facing the target	Through backing	Facing the target	Through backing
100 μg/cm^2	93%	83%	4.6°	9.1°
300 μg/cm^2	91%	81%	6.7°	10.7°
500 μg/cm^2	90%	80%	7.9°	12.4°
800 μg/cm^2	87%	77%	10.6°	14.8°
500 μg/cm^2	82%	69%	14.8°	17.8°
1000 μg/cm^2	78%	65%	16.3°	21.7°
1500 μg/cm^2	69%	56%	21.7°	26.2°
2000 μg/cm^2	61%	49%	28.6°	34.0°

Table 2.2: Detection efficiency of coincident fission fragments as a function of sample thickness.

2.3.3 Fission Ionization Chamber (FIC)

The measurement of fission reactions with a counter based on the absorption of the fission fragment in gas has been foreseen at the n_TOF Facility at CERN [3]. After the good results achieved during the second n_TOF Commissioning [44, 45] by using a Parallel Plate Induction Fission Chamber from PTB [43], it has been decided to build a dedicated counter based on the same principle but optimized for the facility. This kind of detector [47, 48, 49, 50] is simple and easy to operate. In Figure 2.23 the configuration of the detector is sketched. Apart from the windows, made with Kapton foils 125 μm thick, all metallic parts are made out of aluminum or aluminum alloy. The occupancy along the TOF tube in the direction of the neutron beam is about 50 cm and the overall arrangement is such that there is no mass on a circular cross-section larger than that of the neutron beam. The TOF tube sector reserved to FIC is actually a cross-shaped tube with two flanges of diameter ø=200 mm in the tube direction, and two others reserved for the mounting of the detector body. One of these flanges has two sealing: the first to ensure the vacuum tightness, the second to define the volume where the gas is confined and where the ionization chambers are mounted.

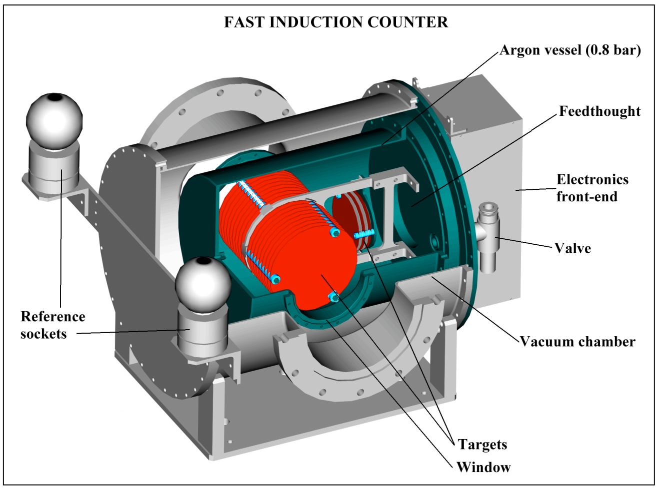

Figure 2.23: An artistic view of the FIC detector.

The detector is filled with gas (90% Ar, 10% CF_4) at 0.72 bar. No gas circulation is needed. The targets directly exposed to the neutron beam are stacked on the supports together with the other electrodes. A total of 16 targets and 18 electrodes could be mounted together leaving a distance of 5 mm between layers. There is also another stack of electrodes (3 targets and 4 electrodes) mounted perpendicularly to the previous one, that could be equipped with reference isotopes to evaluate the background produced by scattered neutrons. In both stacks one place is reserved for a “dummy” target (support without deposit).

In the configuration for the 2002 run [51], the counter is equipped with the following available targets:

- Isotope ^{234}U: 7 targets, total mass ~ 37.7 mg in the main line;
- Isotope ^{234}U: 1 target, total mass ~ 5.4 mg in the back ground line;
- Isotope ^{235}U: 1 target, total mass 5.06 mg in the main line;
- Isotope ^{238}U: 2 targets, total mass ~ 20 mg in the main line;
- Isotope ^{238}U: 1 target, total mass ~ 10 mg in the back ground line.

The detector cover is screwed on the flange and the tightness made by an o-ring squeezed between these two parts. An additional cylindrical case is surrounding the detector body to minimize the possibility of accidental break of the windows, during the transport. This part is removed once the detector is installed on the line. The fissile isotopes are deposited on both sides of 100 μm thick aluminum foils with diameter ø=72 mm in the form of a chemically stable U_3O_8 oxide. The radioactive deposits have a diameter of ø=52 mm. The samples, made by painting successive layers starting from a uranile solution and baking at a temperature of about 800 °C present a stable and uniform U_3O_8 oxide compound Table 2.3 gives the total mass and activity of the eight ^{234}U target composition.

Isotope	**Relative content**	**Mass (mg)**	**Activity (Bq)**	**Activity (in units of L_A)**
^{234}U	99.84 %	42.93	10.12 MBq	14455
^{235}U	0.082 %	0.035	3 Bq	0
^{236}U	0.046 %	0.02	0.5 Bq	0
^{238}U	0.03 %	0.013	0.2 Bq	0

Table 2.3: Composition and activity of the U-isotopes in the ^{234}U targets mounted in FIC for the 2002 run [51].

All electrodes (Figure 2.24) are electrically connected to the feed-through located on the flange. The targets are held at ground potential by the preamplifier input whilst the facing electrodes are at -300 V potential.

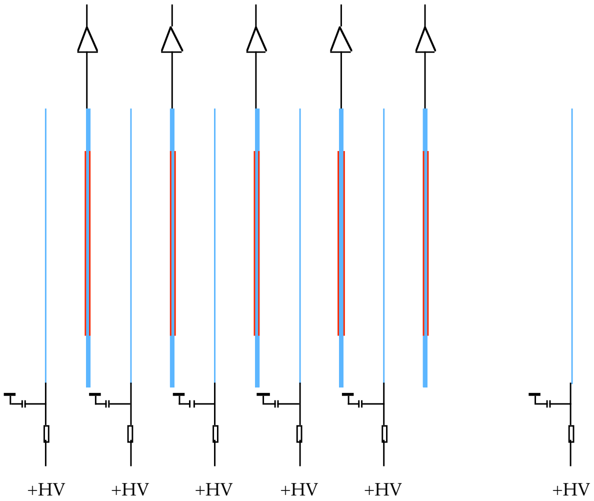

Figure 2.24: Electrical connections of the Detector.

Immediately after the feed-through, are located two boards (Figure 2.25): the Front-End Electronics and the HV Distribution Board. The Front-End is a Transimpedence Amplifier followed by a Line Driver to transmit the signal in differential mode to the Control Room (at ~ 80 m).

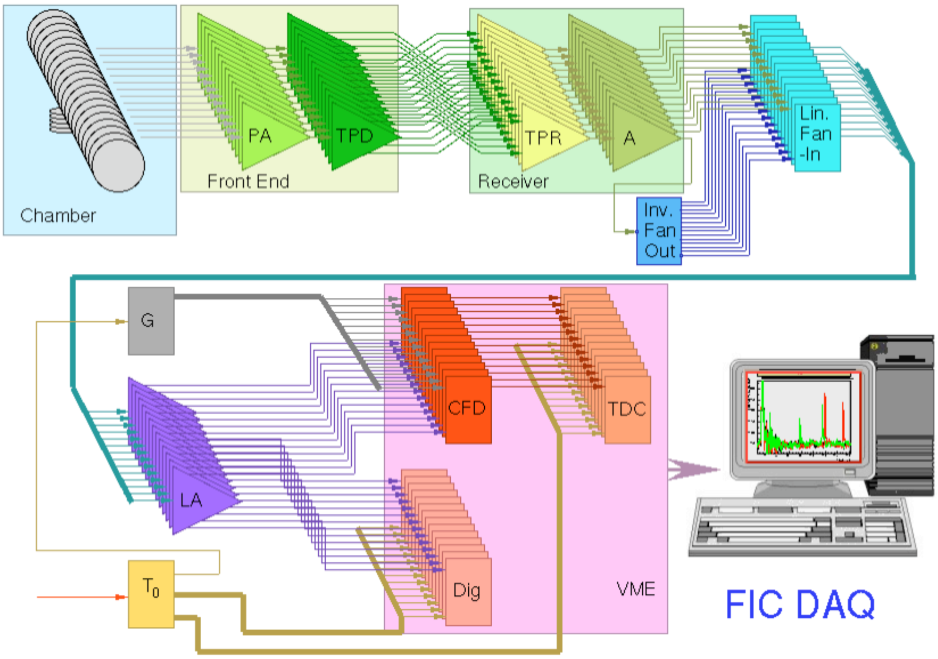

Figure 2.25: Layout of the Electronics and connections to the DAQ. At the receiving end, a Differential Receiver distributes the signals to various NIM Modules to drive a Constant Fraction Discriminator. The discriminated signals provide the stops to the TDC having a resolution of 0.8 ns. The TDCs used can record events over a time window of 200 ms (or more) without dead time. The pulses waveforms are also digitized by using FADC with a sample rate of 40 MHz.

Figure 2.26 shows the pulse height distribution of ^{235}U events as it was recorded with the Flash-ADC. One can notice the clear separation between the fission fragments and the alphas together with the white noise. Based on the pulse height distributions for every individual channel the discrimination threshold was carefully chosen to a value as it is shown in the figure. Figure 2.27 shows the histogram of fission events from the ^{234}U, ^{235}U and ^{238}U isotopes used versus the incident neutron energy during the October 2002 run [52]. During 4 weeks of run, with a total of 6.7x10^{17} protons the detector collected 6.5x10^{6} fission events on ^{234}U, 3.2x10^{7} on ^{235}U and 1.8x10^{6} on ^{238}U.

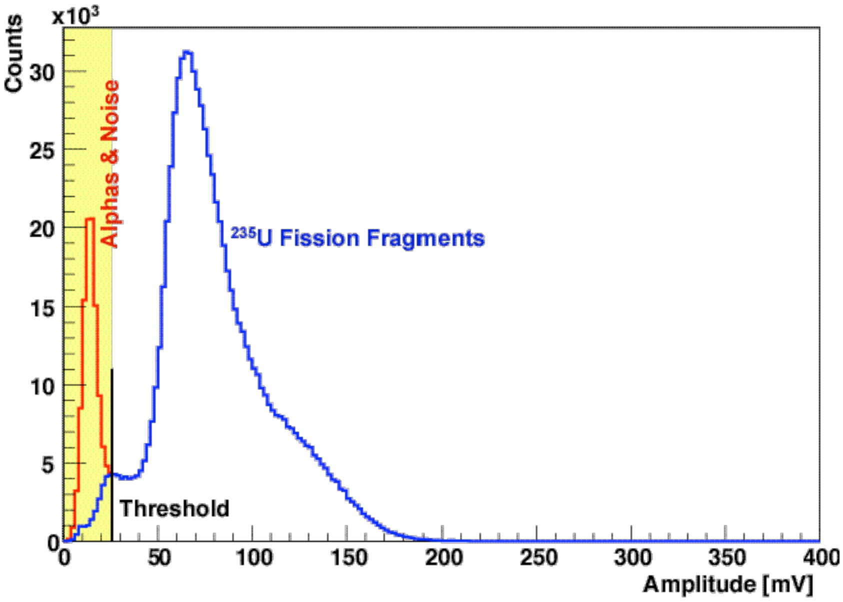

Figure 2.26: Pulse height distribution of ^{235}U fission events. The discrimination threshold set on the CFD is also visible.

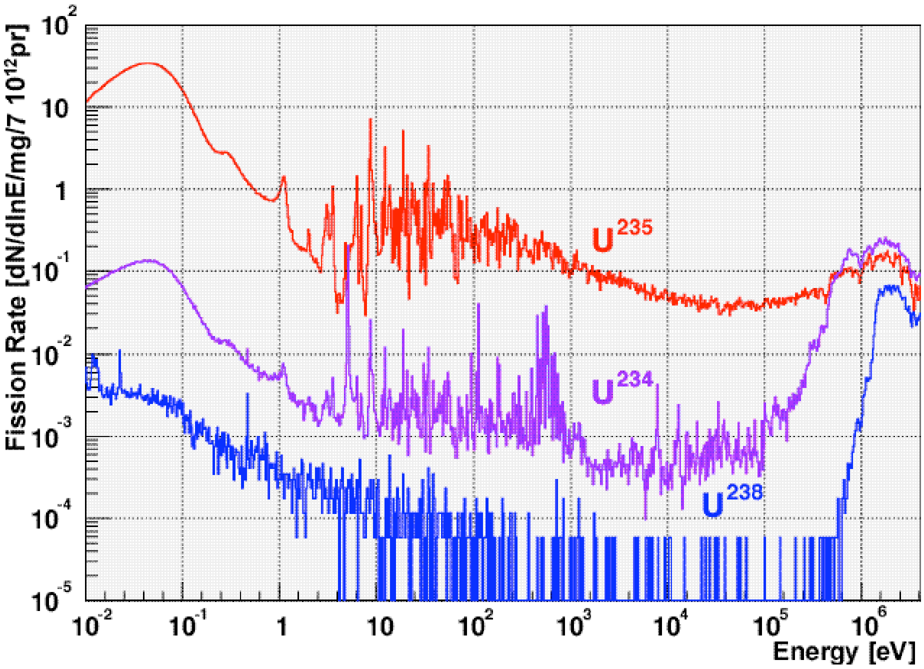

Figure 2.27: Fission event rate of ^{234}U, ^{235}U and ^{238}U plotted isolethargically versus a typical proton bunch of 7 10^{12} protons [52].

2.4 The Data Acquisition Systems

Two different and independent data acquisition systems have been developed which match the specific characteristics of the PS proton and the n_TOF neutron beams.

2.4.1 DAQ-A

An innovative, general purpose Data Acquisition System (DAQ) has been developed [53] by considering the CERN n_TOF beam repetition rates[1], the expected number of event rates and the characteristics of the detector signals. We achieved a highly flexible and adaptable DAQ that accommodates the various detector requirements without any loss of efficiency or dead time, in a user-friendly software environment. Without compromising the possibility to record all information, the present system has the novel and unique feature to sample and store exclusively the full analogue waveform of the detector signals for each channel and beam burst by using on–line zero-suppression [53]. Additional data reduction is achieved by recording the data in compressed "tar" file format, providing typically a reduction of a factor of two. This on–line zero-suppression yields respectable data reduction factors shown in Figure 2.28 for the C_6D_6 and the silicon detector and for different samples in the beam having different reaction rates.

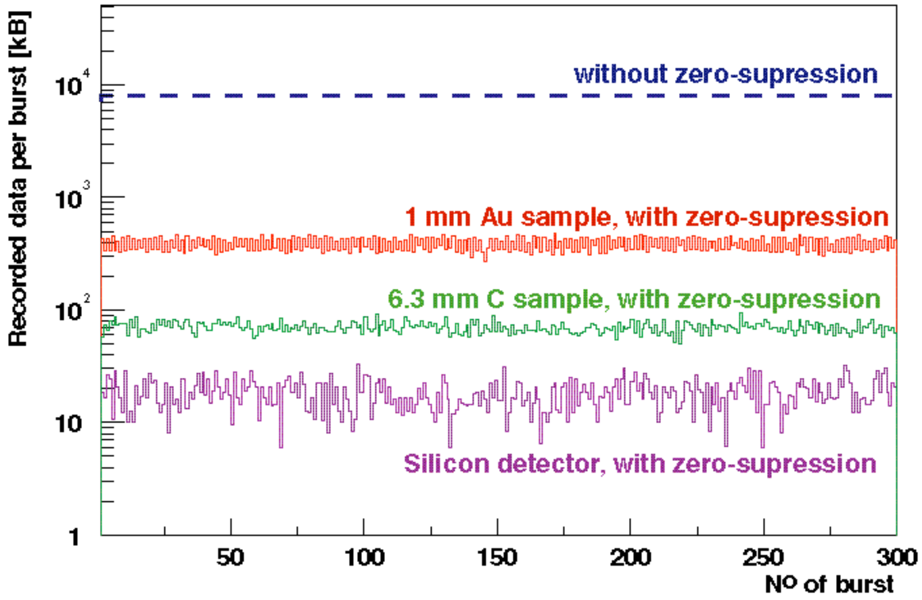

Figure 2.28: The data reduction due to the zero-suppression is presented for the C_6D_6 detectors in the case of the 1 mm ^{197}Au sample with ~ 350 signals per burst and in the case of the 6.3 mm C sample with ~ 70 signals per burst. The reduction of the Silicon data with ~ 10 signals per burst is also shown.

The sampling is performed by Flash-ADC (FADC) modules that provide for a time-tag and which allow full pipelining (digital conversion not blocked by data readout). This DAQ architecture permits the complete reconstruction of the detector response in off-line analysis with the advantage of the possibility to resolve pile-up or background events. The n_TOF DAQ system is able to synchronously collect the data of all detectors and transfer them after each burst through a Gigabit switch to the CERN CDR facility for fast data storage.

---

[1] At the TOF neutron facility the detectors are active for 16 ms during a PS burst, i.e. at the maximum repetition of 2.4 s, covering neutron energies down to below 1 eV.

The Front-End Electronics

The n_TOF Data Acquisition System consists of Digitizer modules based on FADCs with a repetition rate up to 2 Gsamples per second (Gs/s). The detector signal characteristics define the sampling rate and the dynamic range to be used. The various detector requirements imposed the use of two types of FADCs.

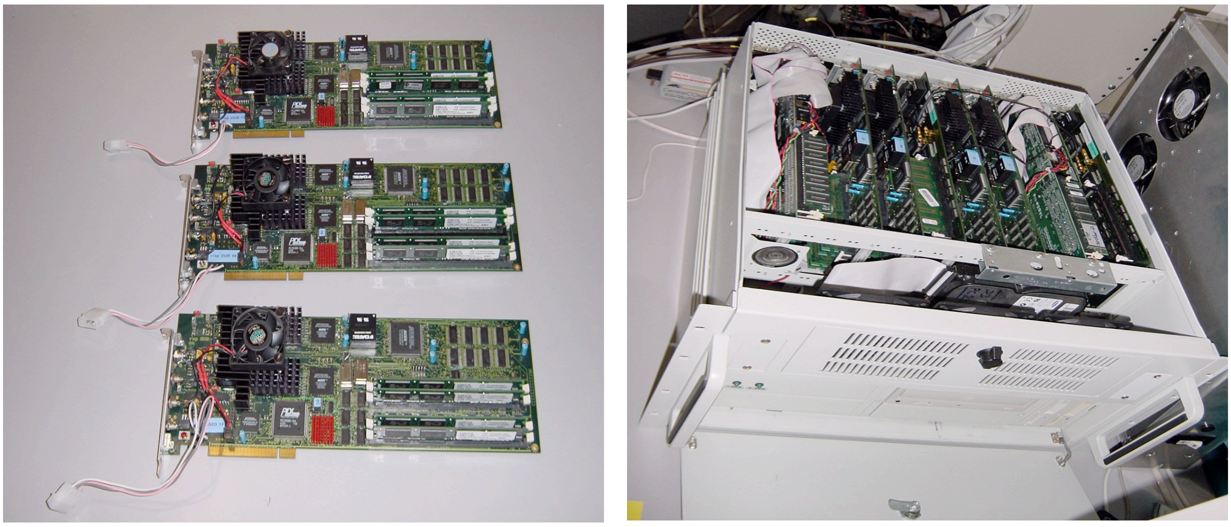

Figure 2.29: The ETEP digitizer modules (left) and the chassis (right).

One type, ETEP (Figure 2.29), has a single dynamic range from 0 to –500 mV and sample rates of 1 Gs/s down to 62.5 Ms/s (binary division), with memory depth up to 512 Mbytes and with zero-suppression applied prior of writing to memory. We apply this first type on all standard n_TOF detectors [53] and due to its unique large memory depth it can be also used in our experiments at other neutron sources, providing for a very long recording time.

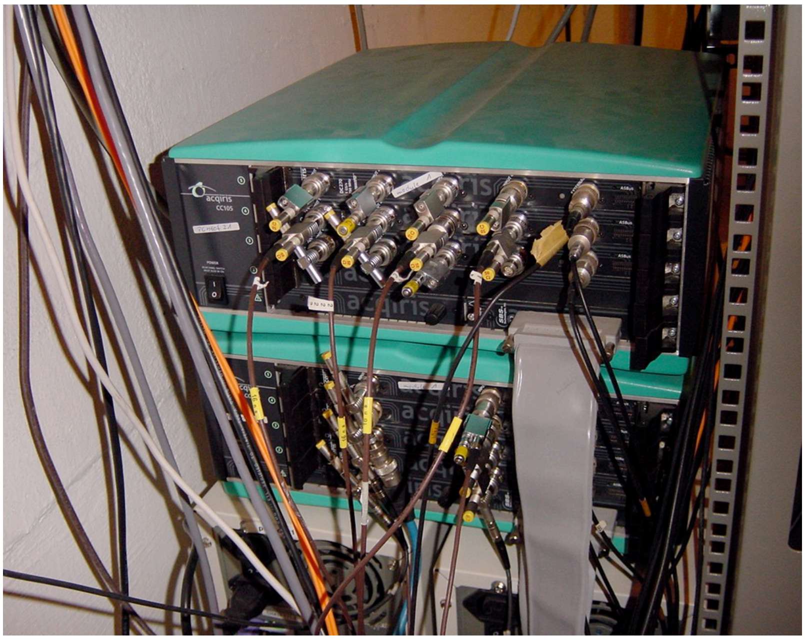

Figure 2.30: The ACQIRIS digitizer modules and the chassis.

The other type, ACQIRIS (Figure 2.30), has several dynamic ranges between ±5 V down to ±5 mV and sample rates from 2 Gs/s down to 1 Ms/s (steps of 1, 2 and 5), with memory depth up to 16 Mbytes and with zero-suppression applied by software after writing to the memory of the associated PCs. This second type, due to its flexibility is used for detector commissioning and for multipurpose applications requiring the features of a multichannel digital oscilloscope combined with large memory.

The hardware specifications for both types of digitizer modules, the "slow control" and the networking features are presented in references [53] and [54].

Both types of digitizer modules have been commonly developed between the n_TOF Collaboration and industry. The conceptual design of a digitizer in PCI format, the on-line zero–suppression mechanism, the large memory feature, the horizontal data path for event monitoring (SPY [53]), the clock generator and its fan-out and the 200 MHz FADC front-end design have been the n_TOF contribution to the first type. The software zero-suppression mechanism and its associated driver have been the n_TOF contribution to the second type.

The DAQ system has been operational with 16 channels since November 2000. During 2001, we used 36 channels of the second digitizer type. The application of the first type of digitizers has shown that they can operate according to the specifications with the exception of the presence of excessive noise on the input channels and of an uncertainty of 8 sampling clock periods in the inter-module synchronization. The offset circuitry in front of the digitizer inputs combined with a high efficient input protection circuitry has been developed by the n_TOF Collaboration and will be incorporated in the DAQ system during future measurement campaigns in order to eliminate the input noise. Our industrial partner has localized the synchronization problem at the clock multiplexing integrated circuit and the digitizing mode of the FADC (binary) and will provide the improvements to all digitizer modules.

The DAQ Architecture

The architecture of the DAQ system has been extensively described elsewhere [53, 54, 55, 56] and only a brief overview of the improvements will be presented here for completeness.

During the April 28 to June 11 2001 run period, the DAQ system consisted of four data streams equipped with 36 digitizer channels employing 4 PCs and a fifth stream containing the "slow control" information and the beam information relevant to n_TOF provided by the PS control system, employing 2 PCs. All this equipment was situated in the experimental area and the data transfer to the n_TOF control room (CR) was performed via an optical Gigabit switch (Figure 2.31). The PC server in the CR has been upgraded to a 500 Gb disk server in March 2001. At the same time the 200 GB disk server situated in the CDR area has been also replaced by a 500 Gb disk server. Additionally we had a 100 Mb Ethernet switch installed in the CR to improve the access to the 500 GB disk server for monitoring purposes. For the run control, the event monitoring and the on-line analysis we employed three PC Workstations in the CR and for the data analysis ten PCs in offices connected mainly to the CERN LXPLUS cluster.

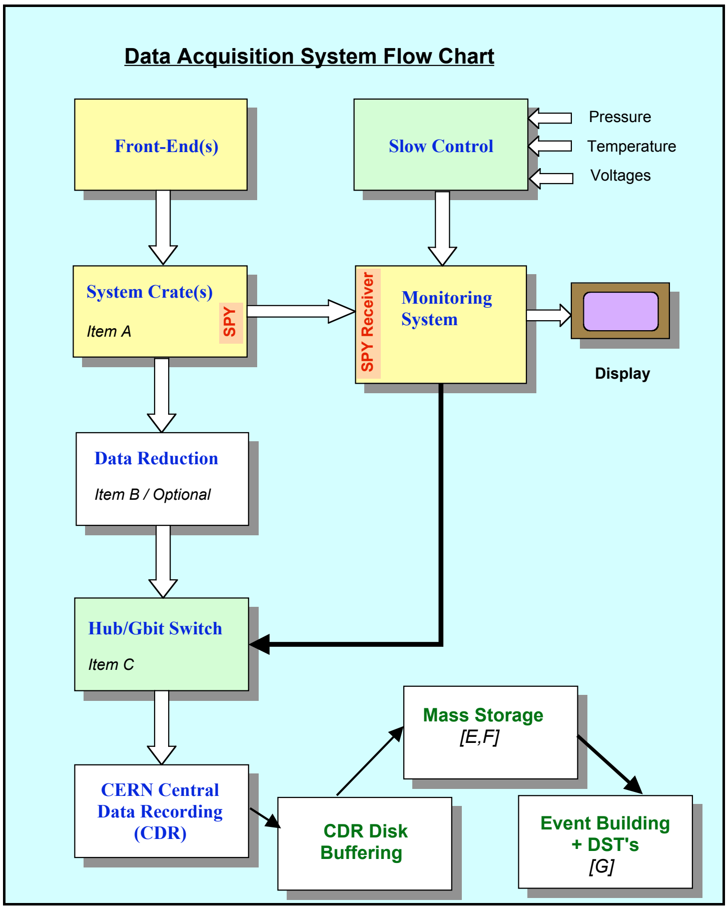

Figure 2.31: The block diagram of the n_TOF DAQ.

Monitoring and Synchronization across Multiple Data Streams (SPY)

The monitoring and synchronization across the various data streams has been extensively described elsewhere [53]; therefore only an overview is presented here.

The SPY and SPY RECEIVER modules together with their drivers have been delivered by ETEP in July 2001 with a delay of several months. The modules and drivers have been successfully tested since then and the implementation of the drivers and associated software is under progress.

Because of the delay in delivery, the n_TOF Collaboration elaborated after intensive software optimization an alternative software solution replacing the horizontal hardware path for the on-line event building and monitoring. The penalty of this solution was the difficulty to meet the appropriate speed for running with the repetition rate of 2.4 s per burst.

Trigger (GATE) Fan-out

The prompt beam pulse from the PS, suitably attenuated and delayed generates the trigger pulse at the CR. It is sent via a high quality coaxial cable to the experimental area where it is used to make the GATE signal, which is kept active during the whole acquisition period of 16 ms and is interlocked with the busy signals of the processor and the monitoring chassis via a PC parallel port to NIM converter module[2]. A special fan-out unit distributes the GATE signal to the individual digitizer modules via equal length cables. The skew of each output is < 200 ps in respect to all other outputs.

---

[2] Designed and constructed by the n_TOF Collaboration.

Slow Control and Beam Data

The "Slow Control" system at present comprises the setting and monitoring of the CAEN high voltage system crate, the sample changer positioning system, and the beam information from the PS control system. The data stream from the "Slow Control" contains apart from the high voltage data and the sample position in the sample changer also the beam information acquired via a different PC communicating via Ethernet with the PS beam monitors (beam intensity via beam transformer readings). The utilization of a dedicated PC for the beam information was imposed by synchronization constraints, since this beam information is available at the PS beam monitor module only during a short time interval within the PS bursts.

The *"Monitoring Processor Chassis"* [53] can acquire upon request the "Slow Control" data via a LABVIEW interface [57] including further data on low voltages, currents, temperature, pressures, etc.

Performance of DAQ and the Data Rates

The digitizers are acquiring data during 16 ms for each proton burst. The stored data amounts to 8 MB per channel and proton pulse, due to the 500 Ms/s sampling rate of the digitizers. With an 8 Ms acquisition memory per channel and a repetition rate of the proton beam pulse of 2.4 s the designed system has no dead time. The transfer of these 8 MB to the PC memory takes ~ 0.7 s on the PCI bus. The zero-suppression algorithm[3] takes ~ 0.7 s. The data of the five data streams amounting to 10 Mb on average are transferred via the Gigabit Switch to the disk buffer in the CR in 0.1 s; the transfer from the CR to the CDR takes another 0.1 s. We like to emphasize that the system was performing without dead time also at a peak data rate of 18 Mb/s. The data storage at the CDR is transparent to us, since the system has a disk buffer server at the CDR location and is using CASTOR software [58]. An interesting feature of this software is that data from the experiment is kept always in two copies throughout the transfer process until its safely stored on tape.

System Features

Our digitizers are situated in the experimental area, organized in data streams and controlled by PCs. Each stream corresponds of up to 8 channels; the data are conveyed through Gigabit Ethernet interface cards via a Gigabit switch to the disk server situated in the CR and then transferred to the CDR disk server and tapes. Since all this electronics is, under normal running conditions, inaccessible, we have foreseen two independent channels for controlling those DAQ PCs (chassis) including the "Monitoring Processor Chassis" from the CR.

The first channel consists of TCP/IP terminal server units (Passport), which permit the control of the DAQ PCs via their serial ports. The access is via a terminal protocol, which permits the low-level control of the booting process and soft-restarts.

The second channel permits remote power-on and power-off, remote reset and reading of the status signal of each individual PC. In the case of the first FADC type (ETEP) the reading of the status of the auxiliary power supplies (±5 V). This is achieved by adding a connector at the rear of each PC conveying these signals to a "PC status multiplexer" (PSM)[4] for all PCs in the experimental area, including the "Monitoring Processor Chassis". The PSM is controlled via a PC workstation situated in the CR. The status signal(s) from each PC are included in the Slow Control data.

---

[3] Before code optimization; after optimization. 0.4 s (with 800 MHz PC); 0.65 s from digitizer to PC memory and zero-suppression 0.3 s (with 1.8 GHz PC).

[4] Designed and constructed by the n_TOF Collaboration.

The DAQ Software

The software was extensively presented in reference [53] and has been operational since November 2000. A major improvement [55] was required since then by the introduction of the CASTOR software for data recording in the CDR. The additional disk server in the control room required also some adjustments. After the first experience with the data visualization and monitoring program it was found necessary to proceed to a major re-write of this software [55,56] in order to permit direct and user-friendly on-line information on the quality of the data.

2.4.2 DAQ-B

Commissioning Data Acquisition System

The n_TOF facility at CERN was commissioned successfully in November 2000 and in April 2001. For the commissioning phases an innovative, multi-purpose Data Acquisition System (DAQ) was developed [59]. Due to the particularity of the n_TOF neutron beam, proton pulses arriving every 1.2s producing a high neutron flux at the measuring station over a wide range of time (~150ms), the DAQ system had to fulfill several requirements [60]. We needed to have time-correlated information from various sources: electronic modules (VME, VXE, CAMAC etc.) with different setups for each measurement, beam information from the CERN Proton Synchrotron (PS) [61] database and asynchronously recording information from the slow control system based on SCADA for temperature behavior of the lead target. The goal was to create a versatile and user-friendly DAQ system to cope with the above tasks. Versatile, for being able to handle various configurations and experimental conditions. Moreover it had to be able to access different electronic modules and external information, allowing a programmable multilevel triggering system. The program had to be also user friendly, to permit the operator through a graphical user interface (GUI), to configure the system by defining and modifying the module parameters, visualize online and offline the spectra and perform simple operations on the collected data.

Program Architecture

Figure 2.32 shows the general layout of the DAQ system. The program is composed of 3 separated units: (i) *RunControl*, (ii) *DAQcore* and (iii) *Monitor*, which inter-communicate with a messaging mechanism based on TCP/IP sockets, and exchanging the raw data through the use of shared memory, available on Unix Sys.V operating systems.

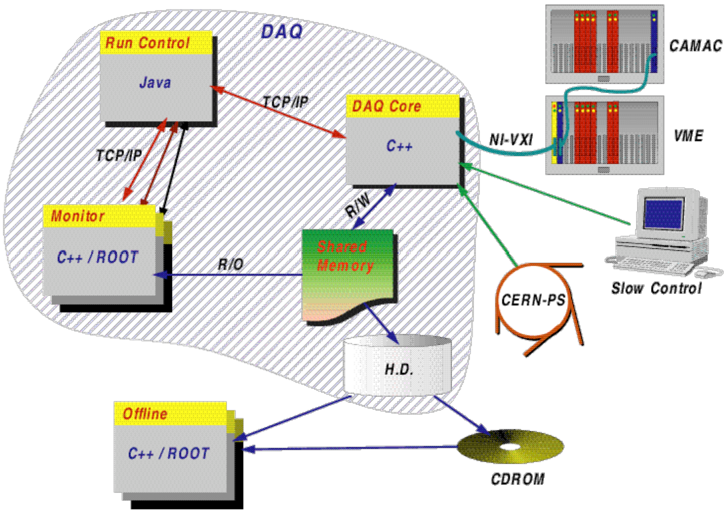

Figure 2.32: General layout of the Data Acquisition System B.

Run Control

The *RunControl* is the interface program written in Java™ that controls and monitors the acquisitioning procedure. It is the communication link between the *Monitor* and *DAQcore* programs. It provides the graphical user interface based on Java AWT, with several static and dynamic dialog boxes, for configuring and programming the software modules for each experimental setup. The program holds a library of all programmable components that are created and linked by the developer. The operator can use the predefined modules, to create a set of modules for each running condition, modifying only the necessary parameters.

DAQ Core

The *DAQcore* is the heart of the DAQ program; it is a background process where the user has no direct control on it. It is responsible for the communication of the DAQ program with the hardware. The program waits for messages from the *RunControl* or trigger signals from the devices while the acquisition is running.

The program is based on the idea of reusable components, called modules. Each module represents a software driver (C++) used in the program to communicate with a specific type of device. There are several module drivers that can control various devices i.e. accessing data from the CERN-PS database (PSDB) [61] (proton intensity, beam position, transformer readout etc), synchronous or asynchronous timers, CAMAC modules (user programmable or predefined ones), VME modules, other programs (i.e. SCADA that was used for the slow control) or information via the WWW etc. Currently the program is coupled with the National Instruments VXI PCI interface [62] for communicating with the VME crates, and with the CAMAC modules through a CBD-8210 [63] board. Due to the object oriented structure of the program the code that controls a module is decoupled from the rest of the program. Hence, the creation of new components is focused only in the basic methods that control the specific device. These methods are the initialization of the device, collection of the data, trigger signal detection and optionally filling a histogram or a graph in ROOT [64], in case immediate visualization of the data is required. Moreover, all the parts of the code that are responsible for the communication with the hardware are well separated, thus it is easy for one to change the NI-VXI interface and write a code to control a different unit.

The DAQcore handles all the remaining operations, memory allocations, data transfer, storing and recalling from the data file. An integrated interface between the *RunControl* GUI and the core of the DAQ program allows the exchange of data and setting of variables that are defined by the programmer (i.e. base address, operation mode etc.) through a high level interface which is dynamically created as a dialog box by the program, and made available to the operator.

During the initialization of the program, a shared memory space is allocated. The space is large enough (defined by the user in *RunControl*) to hold the maximum amount of data that can be collected by all the defined modules. The data collected from the modules (software or hardware) remain in this storage until the arrival of another event. In the intermediate time between events, this shared memory is accessible in R/O mode from the *Monitor* processes.

During the acquisition time, the program is checking all the modules for a trigger signal, which marks the availability of new data. All the modules that are related to this trigger signal are queried and their data are collected. The raw data are transferred from the modules memory, to the shared memory in a Data Encapsulated Format. Immediately after the collection of all the data the shared memory is dumped to the hard disk and a message is send via TCP/IP to notify the *RunControl* for the existence of new data.

The acquisition process continues until either the user stops it by pressing the stop button in the *RunControl* program, or if stop selection criteria arrives (i.e. depending on data size, number of events or time passed). For each run, two files are created (*i*) an info file (extension `.nfo`) and (*ii*) the data file (extension `.dat`). The info file contains all the information in human readable text format for the current run (run number, title, user comments, module configuration etc.) while the data file contains the raw data in binary format.

Monitoring Program, Online and Offline

The online visualization of the acquisition process is done through a separate program called *Monitor*. The operator can open one or more *Monitor* processes, which are connected as clients to the *RunControl*. The program is written in C++ sharing the same software module libraries with the *DAQcore*. Even though it's main purpose is to visualize the collected data during the acquisition, it provides a very powerful user interface based on ROOT [64] with high quality graphics, fitting routines, graphics editor and printing capabilities. The monitoring program communicates via TCP/IP with the *RunControl*, and it is notified for every change that occurs in the configuration setup, the arrival of new events and the position in the shared memory where new raw data are located.

The program accesses the shared memory initially created by the *DAQcore*, in a Read Only mode, and when a new event is present it updates all the active plots. The use of the shared memory to access the data, avoids data traffic over the network and it speeds up a lot the data exchange, with the disadvantage that the *Monitor* program must physically co-exist on the same computer with the *DAQcore*. To minimize dead time the *Monitor* program updates its display only in periods of inactivity (in the interval time between events). In high event rates, the display is "*frozen*" and in this case the user must update it manually.

The *Offline* replay is a C++ program for replaying the collected data, event by event as during the acquisition time. Allowing the user to create more sophisticated plots and trace back the events. The user interface is almost the same with the *Monitor* program except that the data are read back from the data file instead of the shared memory.

Performances

The DAQ program was initially tested during the n_TOF commissioning period (1 month run in November 2000, and 2 weeks in April 2001). During the commissioning period we have used a setup consisting of VME, CAMAC and special modules. On the VME crate, 3 Multihit TDC's (CAEN V767B) and 5 Flash ADC's (V676) were installed for recording the arrival time of the pulses and the pulse shape respectively. On the CAMAC crate we had several scalers for recording the integral number of events, I/O registers for controlling the request of the proton beam, state of the magnet, and a home made X-Y scanner device for positioning the detectors. With the use of a special camera a digitized image of the proton beam was processed and the beam position and profile were recorded.

Figure 2.33 shows the timing signals used for the n_TOF commissioning. The t_{PS} is the pre-pulse signal by the CERN-PS to notify the arrival of a pulse, which is also used as the starting signal on the modules. t_o is the unknown time zero when the proton beam is hitting the spallation target. After a flight path of 185 m and time t_{gamma}= 616 ns the gamma flash was observed and the thermal neutrons arrives at times of 150 ms after the proton pulse. The PS-DB was updated with the transformers values, after a few hundreds of ms. Thus, a delay line of t_{stop}=t_{PS}+300 ms was used as a trigger for the DAQ to collect the data from all the modules. Moreover, a special module was communicating with the slow control system based on SCADA recording the thermocouple values. This module was triggered in asynchronous mode every 14 s.

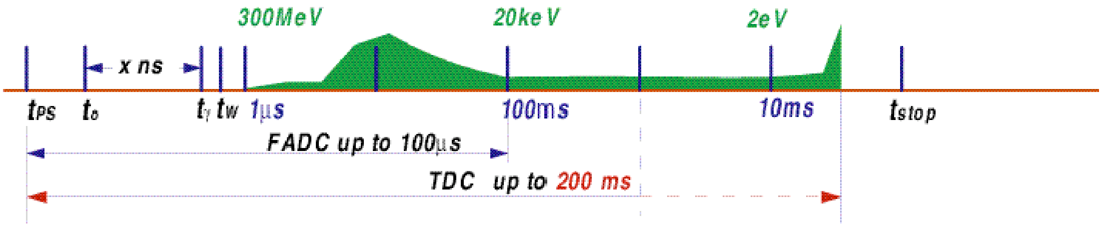

Figure 2.33: n_TOF Commissioning Time Signals.

The *DAQcore* was proven to be very stable without any problem that would occur in data loss. The maximum sustainable transfer rate was of the order of a ~ 10 Mb/s, while the manual of NI-VXI indicates a rate of 23 Mb/s. To calculate the overall performance one has to add also the time spent for processing, drawing and communication between the programs. The program currently runs under Linux; since Linux is a multitasking operating system, the dead time of the program depends on the time-sharing between the active applications. Due to the time slicing of ~ 10 ms between processes from the OS, the program could handle maximum ~ 1000 daqevents per second.

In the current version of the DAQ program, the *DAQcore* holds in the shared memory only one daqevent[5]. Thus, this rate of ~ 1000 trig/s is much higher than the pulse rate at n_TOF of 1-2 triggers per 1.2 s. In the newer version, the program will be able to store in the shared memory multiple numbers of events allowing higher trigger rates.

Another important feature of the DAQ is that all the information recorded during the runs, are accessible via WWW through a web portal, creating a detailed electronic logbook (eLogBook). In this way, the user can visualize the current status and the *eLogBook* from anywhere through a web browser.

The DAQ system has proven to be very robust, and flexible beyond our initial goals. It is versatile and user friendly enough, to be used as a general-purpose acquisition system that can be adapted easily to other experimental setups. The program was used successfully in the Commissioning phase [44, 45] for the determination of the neutron fluence with PTB fission chambers, measurement of the temperature behavior of the lead target, for the validation of the hypothesis that the neutron background was generated by muons [65] and air activation in the experimental area [66].

Currently it is used on a daily basis for the measurement of the ^{234}U fission cross section with the FIC detector [4]. Apart from the measurements with a pulsed source, the DAQ was used also in environments with continuous beam like at the PTB neutron facility and for gamma spectroscopy with HPGe detector.

---

[5] The term daqevent (trigger) refers a signal that will notify the DAQ program to collect the data from the active modules, in the case of n_TOF, this is the arrival of the proton bunch, which can produce several thousands of neutron events on the detectors, which are considered as an event for the DAQ.

3 EXPERIMENTAL DETERMINATION OF THE BEAM CHARACTERISTICS

The detection systems presently available at n_TOF have been described in details in the previous section. A summary of the results obtained for flux measurements, for the resolution and for the background conditions are reported herewith. A detailed description of the techniques used and of the results obtained will be reported in a **paper which is under preparation** [6]

3.1 Measurements of the Neutron Flux

A series of measurements has been performed in order to determine the neutron fluence in the experimental area. The first of these measurements has been performed during the commissioning phase with the PTB detectors [44, 45]. Other measurements have been performed with SiMON [32], with the C_6D_6 gamma-ray detectors [33], and with PPACs detectors [5].

The data obtained with the two PTB chambers will be used as a kind of reference for comparison of results obtained with other detectors.

All the measurements reported here refer to the configuration used for capture measurements, namely with a **second collimator diameter** of **1.8 cm**.

A summary of the results obtained is shown in Figure 3.1 below. The results of the measurements will be described in the following paragraphs.

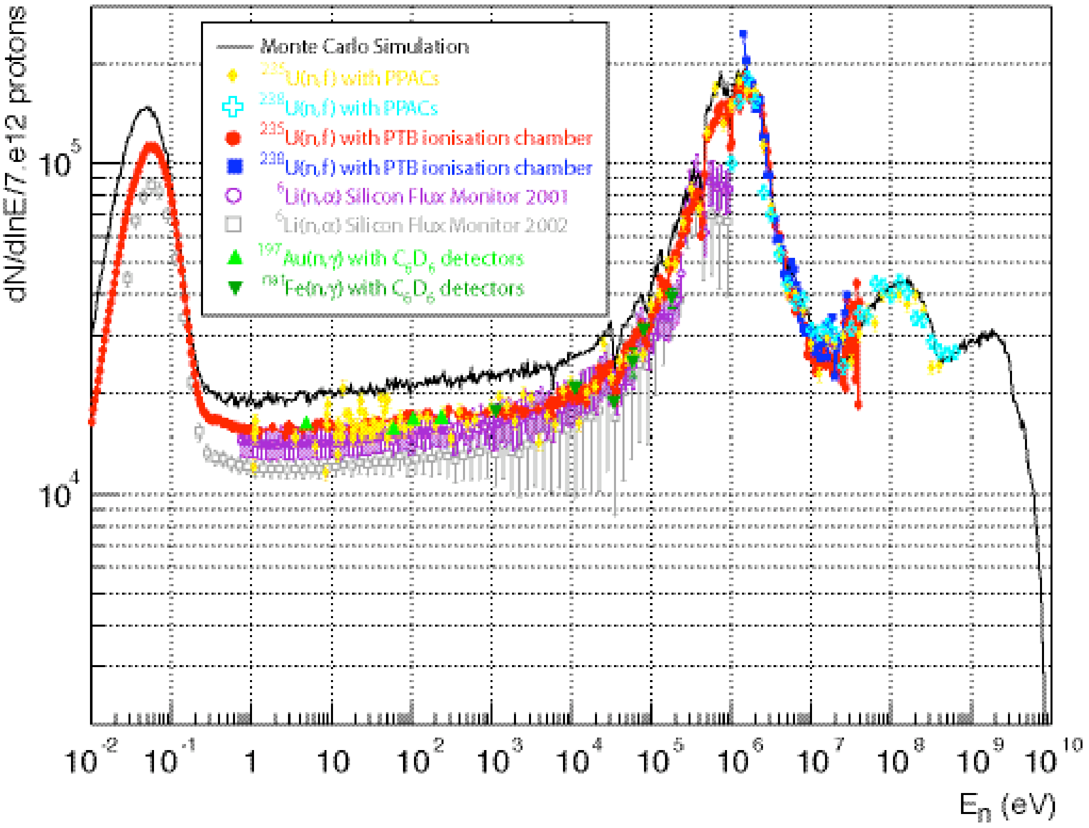

Figure 3.1: Neutron flux in EAR-1 as measured with different experimental techniques. A comparison is shown with the Monte Carlo simulations.

3.1.1 *PTB Measurements*

The measurement performed with two identical parallel plate ionization chambers [43] used a deposit of 197.78 ± 0.60 mg of ^{238}U and 201.56 ± 0.60 mg of ^{235}U, equivalent to 436 µg/cm^2/plate and 444 µg/cm^2/plate, respectively. The detection efficiency for the chambers varies slowly as a function of energy, i.e from about 95% at low energies, down to 91% for neutron energies of 150 MeV. During the measurements, the vacuum tube in EAR-1 was terminated with a 500 µm thick aluminum window, placed at 182.1 m from the window of the spallation target. The ^{238}U and the ^{235}U chambers were placed in air at a distance of 182.25 m and 182.35 m respectively. The beam profile at the position of the detectors shows a circular shape with a radius of 1.65 cm.

During the measurement campaign [44, 45], a total number of 8.6×10^{17} protons were delivered by the PS in 155,000 pulses (both parasitic and dedicated). The average proton intensity was 5.5×10^{12} protons/pulse.

A large set of data was collected, consisting of $1.6\text{x}10^5$ events obtained with the ^{238}U chamber from the fission threshold up to 50 MeV, and $6.6\text{x}10^6$ events with the ^{235}U chamber over the energy range from 0.01 eV up to 50 MeV. A sample of the raw data obtained is shown in Figure 3.2.

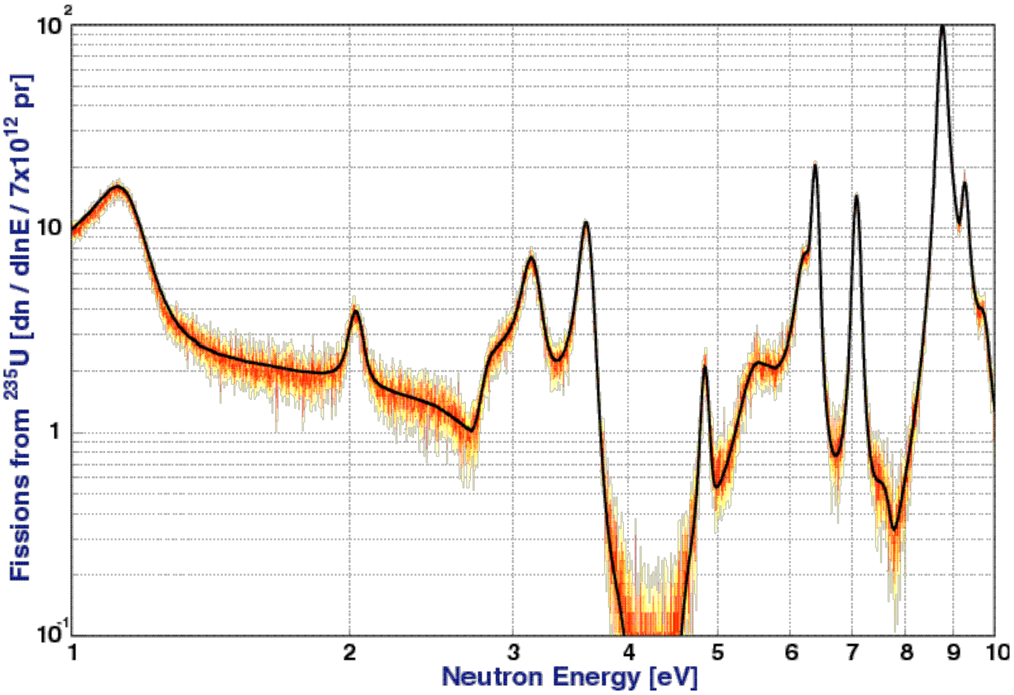

Figure 3.2: Reaction rate of ^{235}U fission events in the 1-10 eV neutron energy region measured with the PTB chambers. The solid line is deduced from the ENDF-B6 evaluation.

Some corrections due to transmission through the platinum and tantalum plates and electrodes need to be applied in order to deduce the neutron flux from fission event rates. In addition, corrections are needed to account for the distortion of the flux due to the ^{238}U chamber placed in front of the ^{235}U chamber and to the multi-layer structure of the chamber itself.

The resulting measured neutron flux is shown in Figure 3.3, and compared with Monte Carlo simulations.

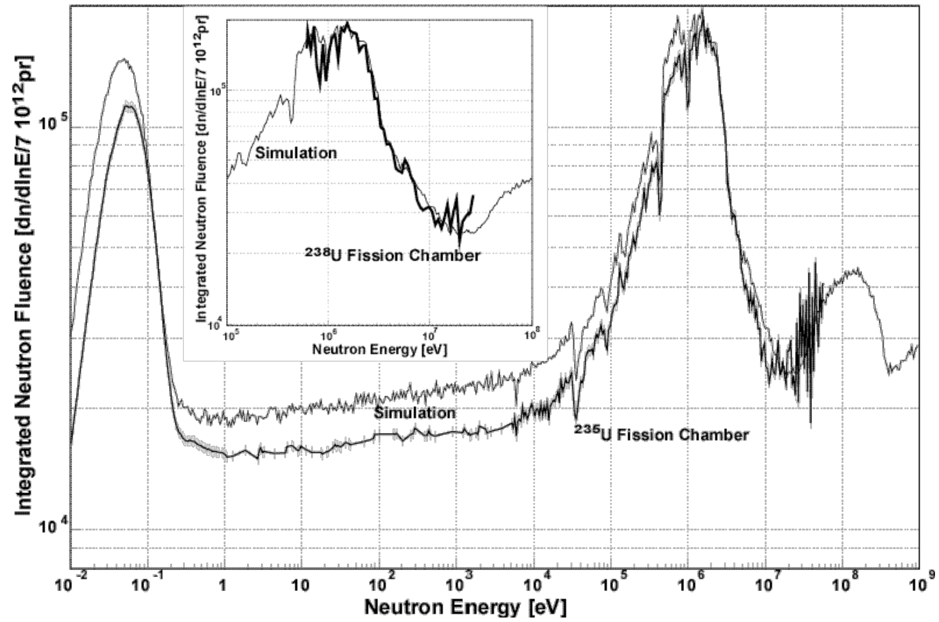

Figure 3.3: Integrated neutron fluence as a function of neutron energy from ^{235}U and ^{238}U fission chambers compared with simulation.

One can observe the flat shape of the spectral function of n_TOF ranging over a wide energy domain, i.e. from 1 eV up to 10^4 eV, which confirms the expected isolethargic character. Some local depletions appear both in the simulated fluence and in the experimental data. They are due to the presence of various materials in the neutron beam, in particular the aluminum of the windows separating the target from the beam line and the one at the end of the neutron line and the oxygen contained in the 5 cm thick water moderator. In the high-energy region (above 1 MeV) where the collimation effect is minimal the agreement between the simulated and the measured data is excellent. Below 1 MeV the simulation starts to deviate from the measured data, establishing a maximum discrepancy of 20% for energies below ~100 keV. This factor remains almost constant in the epithermal and thermal region, while the spectrum shape including all the resonances follows very closely the simulated one. For energies below 0.1 eV the gravitational cut-off affects the measured data while this effect is not included in the simulations. Considering the challenging problem of simulating a geometry like the n_TOF tunnel, with all the assumptions used in such a simulation (beam profile, moderator thickness, windows, beam line components alignment, etc.), a discrepancy of 20% can be considered satisfactory.

3.1.2 Flux from C_6D_6 Measurements

The capture data was measured with two C_6D_6 FZK-type detectors placed in a 90° geometry in close contact with the C-fiber sample changer [33]. The information on the sample thickness and the total number of protons for the samples analyzed is summarized in Table 3.1:

Sample	**Thickness (at/b)**	**Number of protons**
Au 0.1×45 mm^2	6.3x10^{-4}	6.7x10^{15}
Fe 0.5×45 mm^2	4.2x10^{-3}	1.4x10^{17}
Fe 2.0×45 mm^2	1.7x10^{-2}	5.7x10^{17}

Table 3.1: Sample thickness and total number of protons for each sample.

According to the principles of the Pulse Height Weighting Technique (PHWT), the raw detector counts were multiplied by a weight depending on the energy deposited in the detector.

In order to obtain the shape of the neutron flux as a function of the energy we analyzed several known resonances of Au and Fe using the R-Matrix fitting code SAMMY [67].

The TOF histograms of weighted counts N_w are converted into yield data Y^{exp} according to the relation: $N_w = Y^{exp} \cdot N_n \cdot E_c$, where N_n is the total number of neutrons in the TOF bin and E_c is the γ-cascade energy, which represents the detection efficiency according to the PHWT principles. The number of neutrons per bin, N_n, is precisely the number we seek to extract. For convenience an initial value for N_n was assumed from the neutron intensity parameterization

$$I_n = 15215 \cdot E^{0.0200372} \cdot (n/7 \cdot 10^{12}\, p)$$

which fits the ^{235}U PTB data in the range 1 eV – 5 keV, and the recorded number of protons.

The experimental yield is then fitted with SAMMY, which calculates the theoretical yield from the known resonance parameters. The fit function used is: $Y^{exp} = A \cdot Y^{th} + B$, where the normalization factor A and the background function B are varied. The other varied parameter is the energy of the resonance to allow for the energy-TOF calibration. The theoretical yield calculated by SAMMY includes the broadening due to the thermal motion and the shape of the resolution function (see section 3.2), and takes into account the multiple scattering in the sample. In this way the normalization factor A represents a correction to the initial neutron flux if the assumptions of the PHWT are fulfilled and in particular if the Monte Carlo simulation accurately reproduces the measurement.

In fact it is necessary to apply several systematic corrections related to the principles of the PHWT: (i) the loss of counts due to the use of a low energy threshold in the C_6D_6; (ii) the detection of more than one γ-ray per cascade; and (iii) the loss of γ-rays in the cascade due to the conversion electron process. The combined effect of all three can be estimated from a realistic simulation of the experiment using capture cascades generated from the statistical nuclear model.

Additionally, as mentioned before, we have found inconsistencies in the recorded proton intensity between runs and a relative correction factor has to be applied based on the data measured with SiMON. For normalization, we used the counts recorded in the silicon detectors #1 and #2 with amplitudes corresponding to the tritium peak and TOF corresponding to the neutron energy range 1 eV – 10 keV.

First, an analysis was performed on the data sorted without t_0 correction in order to obtain the correct normalization with sufficient statistics. The fits obtained for the 1.15 keV resonance in both Fe samples for the summed statistics of both detectors is shown in Figure 3.4.

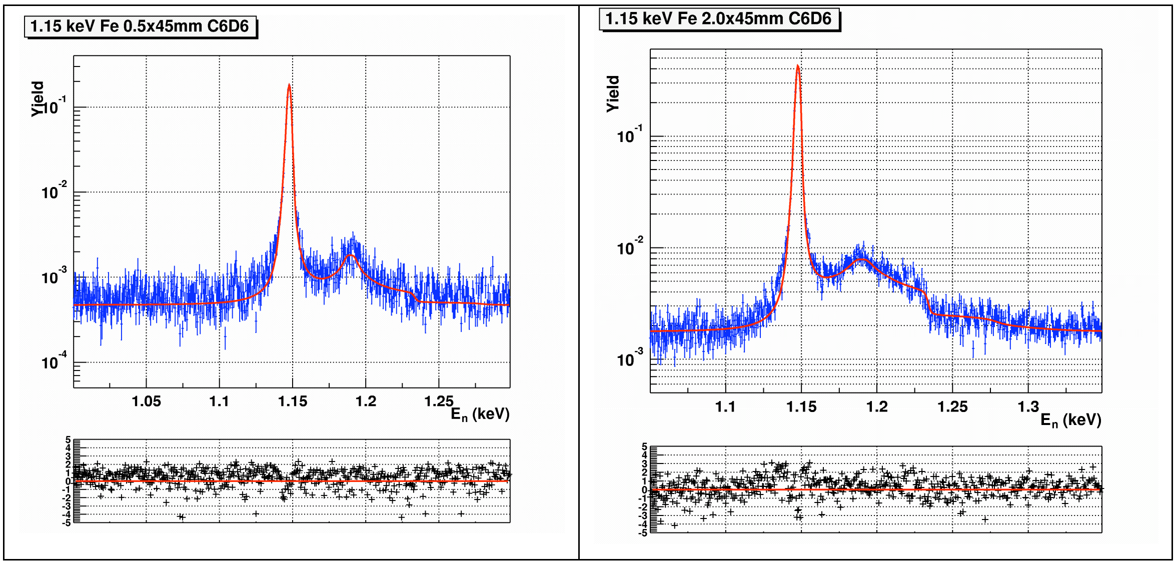

Figure 3.4: SAMMY fits to the 1.15 keV ^{56}Fe resonance for both samples.

The resulting normalization factor obtained from the fit to the thin-sample data, together with the result for the saturated 4.9 eV resonance in ^{197}Au is presented in Table 3.2. In the table, are also given the correction factor due to the electronic threshold f^{thr} and the correction factor of the Si-Monitor relative to the Au measurement f^{Si}.

Sample	Resonance	A	f^{thr}	f^{Si}	A^{corr}
Au 0.1×45 mm^2	4.9 eV	0.991(6)	1.045(11)	1	1.036(13)
Fe 0.5×45 mm^2	1.15 keV	0.998(13)	1.005(11)	1.012(16)	1.015(24)

Table 3.2: normalization factor from SAMMY and threshold and SiMON corrections.

The uncertainty on A includes the SAMMY fit uncertainty and a 0.3% uncertainty (non-systematic) from the weighting function, estimated from the realistic simulation of the measurement. The uncertainty on f^{thr} includes the statistics of the realistic simulation plus 1% uncertainty (systematic) from the method. The uncertainty on f^{Si} is dominated by the statistics of the Au measurement.

An important issue concerning the determination of the absolute flux is the accuracy of the normalization factor. It is not easy to quantify the several systematic uncertainties affecting the result: mainly the accuracy of the Monte Carlo simulation code, the knowledge of the exact geometry, and the accuracy of the proton intensity for the Au measurement (for instance, the counting rate of the two detectors differed by 8%). A fair estimate of the systematic uncertainty on the absolute flux determination is therefore of the **order of 10%**.

In order to establish the neutron flux shape in a wider energy region other resonances of Au and Fe were analyzed. In the case of the high-energy Fe resonances, the thick iron sample with t_0 correction for both detectors and the full statistics were used. The results were normalized to the value at 1.15 keV for the thin iron sample. In the analysis of the high-energy resonances, an additional uncertainty related to the correctness of the shape of the resolution function has to be considered (see section 3.2). The flux derived from all the resonances analyzed is collected in Table 3.3 and compared to the one extracted from the PTB ^{235}U fission chamber, showing a good agreement as illustrated in the Figure 3.5.

E_R (eV)	I_n (n/7 10^{12}p)□10^4
4.9	1.63(2)
60.3	1.56(2)
107.0	1.68(6)
240.5	1.70(5)
1.15□10^3	1.78(4)
1.12□10^4	2.09(8)
3.42□10^4	1.89(7)
5.92□10^4	2.5(2)
8.08□10^4	3.14(15)
1.81□10^5	3.9(3)

Table 3.3: Neutrons per nominal bunch at several resonance energies.

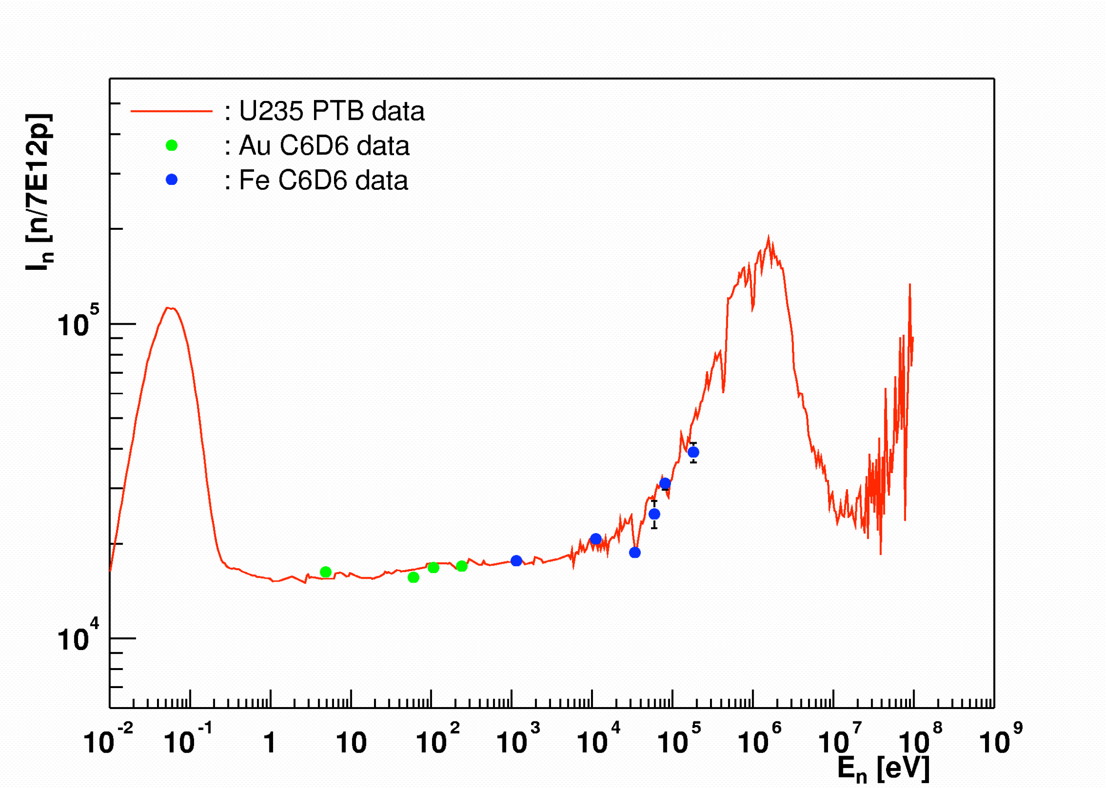

Figure 3.5: Number of neutrons per nominal bunch from the present analysis combined with the PTB ^{235}U fission data.

3.1.3 Flux from SiMON

The neutron fluence in EAR-1 can be deduced from the data taken with the SiMON detectors. Figure 3.6 shows the calibrated energy deposited in the Si detectors as a function of the apparent neutron energy (reconstructed from the time-of-flight data). Tritons and alpha particles can be clearly identified in the plot, on the basis of the total energy deposited in the Si.

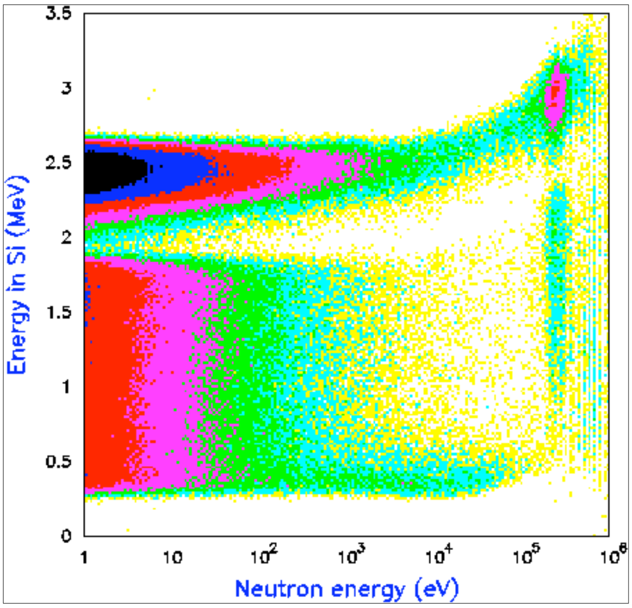

Figure 3.6: Energy deposited in Si detectors as a function of the reconstructed neutron energy. The two loci, corresponding to tritons and alpha particles, are well separated.

After applying proper cuts to identify and isolate the triton peaks, the yield from the (n,α) reaction can be derived. However, in order to derive the neutron fluence, the estimate of the geometric efficiency requires some consideration. In fact, the Si detectors ensure only a partial coverage of the emission solid angle and the angular distribution of emitted tritons exhibits a strong anisotropy for neutron energies above 10 keV.

To estimate the geometric efficiency of the system, we have performed simulations with GEANT4 [34], with a detailed software replica of the apparatus. Tritons were generated according to the angular distribution from the ENDF/B-VI evaluation. The resulting efficiency is shown in Figure 3.7.

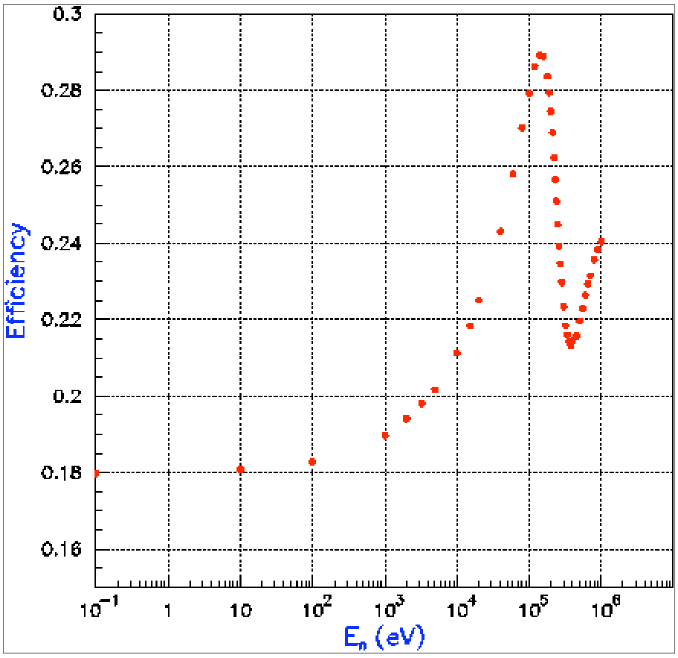

Figure 3.7: Geometric efficiency, as obtained from simulations of the Si Monitor.

The reconstructed isolethargic flux, integrated over the whole beam profile, and normalized to 7.10^{12} protons is shown in Figure 3.8.

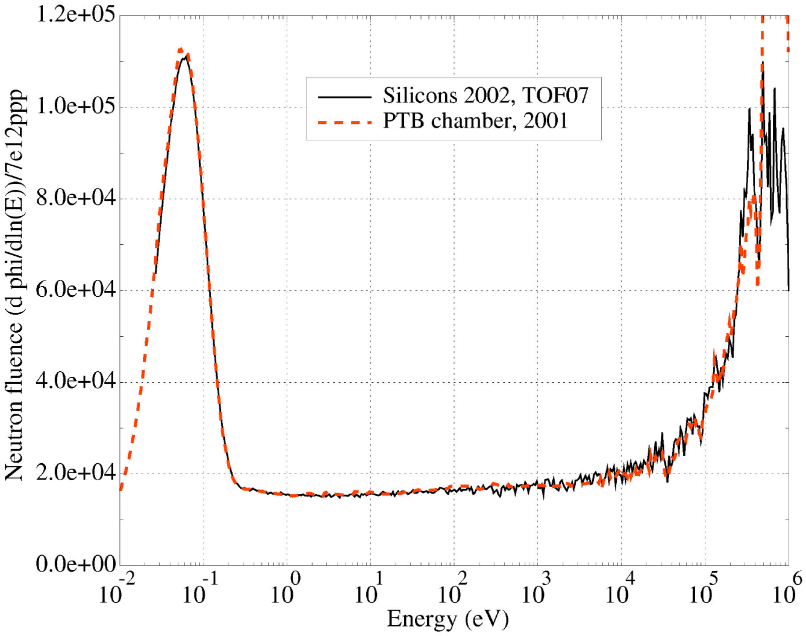

Figure 3.8: The integrated isolethargic neutron flux measured with the Si Monitor.

Several systematic uncertainties affect both the absolute normalization and the shape of the neutron flux. The most important are associated with

- The uncertainty in the ^{6}Li(n,α)t cross section. This can be evaluated by comparing the values reported in the various nuclear data libraries. The fluctuations turn out to be less than 1% for energies below 10 keV, but rise **up to 5%** in the energy range 10 keV – 500 keV. The JENDL-3.2 library was adopted in the present analysis.
- Geometrical efficiency. A detailed replica of the apparatus was implemented in the simulations. However, small differences between the real and simulated set-up cannot be excluded. In particular, the foil-Si distance and the angle of the Si detector may in reality be slightly different than simulated. We performed a test by changing some parameters in the simulations, and under realistic assumptions, the effect is of **a few percent** both on the absolute scaling of the flux and on the shape. In particular, the region from around 100 keV of reconstructed neutron energy may be more sensitive to differences in geometrical details.
- Thickness of the ^{6}Li deposit, and its uniformity. The target laboratory of LNL, that prepared the various foils used for SiMON certifies that the total mass of the deposit and its uniformity is accurate in **within 3%** [32]. The effect of this uncertainty concerns only the absolute normalization of the neutron fluence and not its energy behavior.
- Number of protons used in the normalization. A comparison of several runs shows that non-statistical fluctuations of **up to 5%** are observed in the ratio between the number of events in the Monitor and the number of protons recorded in the run. Such fluctuations are associated to the recorded number of protons and straightforward corrective actions have been taken to solve this problem, which however, results in an uncertainty in the absolute value of the presently determined flux.

A combination of the effects discussed above leads to an estimated uncertainty of 7% in the absolute value of the neutron fluence for energies up to 1 keV. Above 1 keV, the uncertainty in the angular distribution and in the cross sections leads to an overall **estimated uncertainty of the of 10%**.

3.1.4 Flux from PPACs

The Parallel Plate Avalanche Chambers (PPAC) technique is a powerful method based on measurements in coincidence of fission fragments induced by the neutron beam on ^{235}U, ^{238}U and ^{209}Bi standard targets [5]. These elements have been chosen to cover the energy range of interest 1 eV to 250 MeV. In the present report, we show that fluence can be provided up to 1 GeV due to the low "gamma flash" sensitivity of the PPAC.

The PPAC method allows for a determination of the XY position of the neutron interaction in the target and the emission angle of the fragment, providing useful information to calculate the spatial dependence of the fluence as a function of the neutron energy and to determine the solid angle of the experimental set up.

During the first experimental tests in 2001 [5], three targets have been mounted perpendicular to the beam axis in a scattering chamber (Figure 3.9). Their main features are summarized in Table 3.4.

Element	**Thickness** μg/cm^2	**Total number of atoms in target** (per cm^2)	**Active area** mm^2	**Backing**	
				Mylar foil μm	**Al** μg/cm^2
^{235}U	94	4.11x10^{17} ± 3%	172 ± 3	1.5	38
^{238}U	100	4.71x10^{17} ± 11%	186 ± 7	1.5	38
^{209}Bi	300	8.64x10^{17} ± 10%	2800	1.5	27

Table 3.4: Targets used for flux measurements with the PPAC technique.

The total number of atoms in ^{235}U and ^{238}U targets has been determined by the RBS method, scanning the target with an alpha beam. For the ^{235}U element, a better precision is obtained by measuring also the alpha radioactivity of the target.

PPAC of 20 x 20 cm^2 surface, built at IPN-Orsay, have been used to detect fission fragments. They are made of two stages to provide simultaneously time and position parameters (t, X, Y). A fast signal collected on the central electrode (anode) determines the time at which the fission occurred. (X,Y) position measurements are provided by stripped cathodes, on both sides of the anode, by using the delay line readout method.

These detectors were placed parallel to the targets. They operate with isobutane at a pressure of 7 mbar and an anode bias of 580 V. A description of a PPAC is shown in Table 3.5.

Cathode		**Gap**	**Anode**			**Gap**	**Cathode**	
Mylar foil μm	Al strips μg/cm^2	C_4H_{10} mm	Al μg/cm^2	Mylar foil μm	Al μg/cm^2	C_4H_{10} Mm	Al strips μg/cm^2	Mylar foil μm
1.5	38	3.2	38	1.5	38	3.2	38	1.5

Table 3.5: PPAC configuration.

Five detectors and three reference targets have been mounted in the scattering chamber as shown in Figure 3.9.

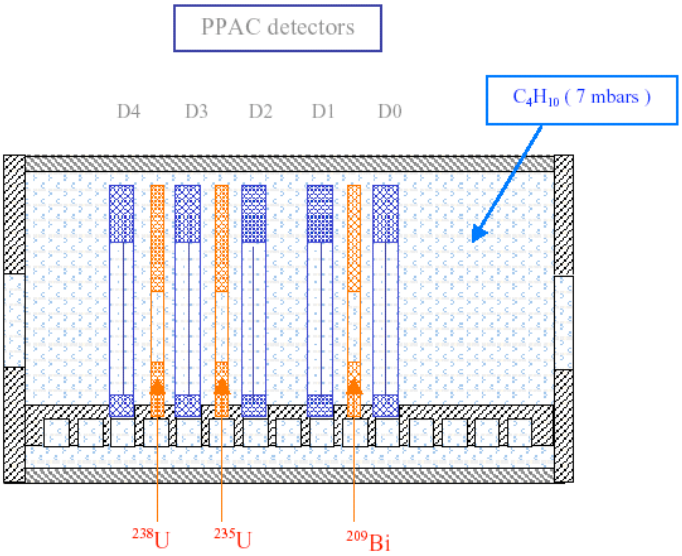

Figure 3.9: Schematic view of the experiment.

The 5 signals (1 per anode and 2 per cathode) from each detector were processed by the Aquiris flash ADCs, at a sampling rate of 500 MHz, driven by a PC-Linux computer. The memory depth, 8 Mbytes per channel, was large enough to measure neutron energies down to 0.7 eV.

The so called "gamma flash", observed as the "first event" of each beam pulse, produces only a very weak anode signal (20 ns wide) in the PPAC, followed by a plateau 1 μs length (Figure 3.10). Thanks to the very efficient peak extraction method described in the reference [5], the signal analysis can be then performed up to 1 GeV. On the other hand, the "gamma flash" is used to calibrate the anode signal, i.e. neutron energy, for each event in a given beam pulse.

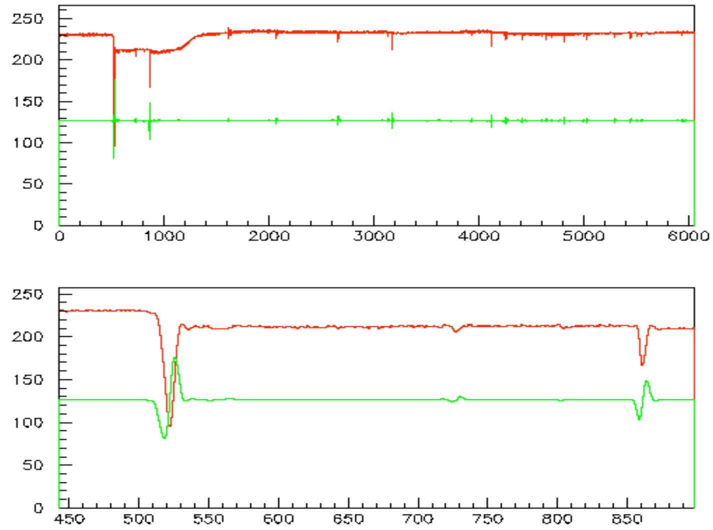

Figure 3.10: Red (upper) curve: Anode signal following the “γflash”, Green (lower) curve: filter derivative. Upper part: full movie frame. Lower part: zoom on the 2 first peaks.

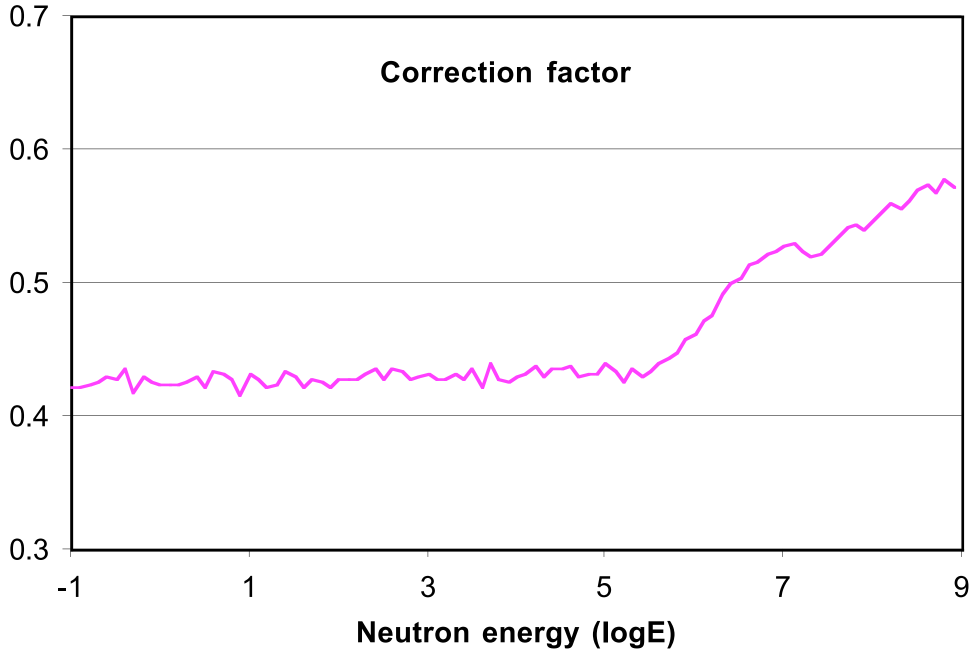

Figure 3.11: Part of the neutron flux intersected by the ^{235}*U target as a function of the neutron beam energy.*

Fission events are characterized by the detection of both fragments in two adjacent counters surrounding the target. This allows a high discriminating power against other types of reactions taking place at energies higher than 1 MeV. The knowledge of the impact position on the target is a powerful tool to determine the beam intensity locally as a function of the energy. Unfortunately, in the 2001 experiments [5], the uranium targets (1.5 cm in diameter) were too small compared to the beam size to obtain this information. Consequently, we have applied a correction factor depending on the neutron energy to determine the integrated flux. This correction takes into account the neutron flux distribution at the spallation target given by simulations [27], and the geometrical collimator effects (Figure 3.11).

In this calculation, a 6.5 m distance has been assumed between the sample and the exit face of the last collimator. A 0.5 m variation of the distance results in a 4.4% modification of the correction factor for the range below 100 keV.

Localization in the PPAC does not only allow to know at which position on the target the fission fragments have been emitted, it also allows to calculate the emission angle and then the true solid angle of the experimental set up. In Figure 3.12, the number of fission fragments detected as a function of their emission angle is represented. One can verify that the angular distribution of the fission fragments is isotropic as expected up to 66 degrees at least, and then the decrease at larger angles reflects the loss of efficiency due to large energy losses in the target and in the Mylar foils of PPACs. Consequently, to get the best as possible precision on the fluence determination, whatever the mass, Z, and energy of the fission fragment, only emissions at angles lower than 66° have been considered. This means that 40% of the true fission events have been eliminated, and accordingly corrected for the flux determination. The solid angle accuracy is of the order of 2%.

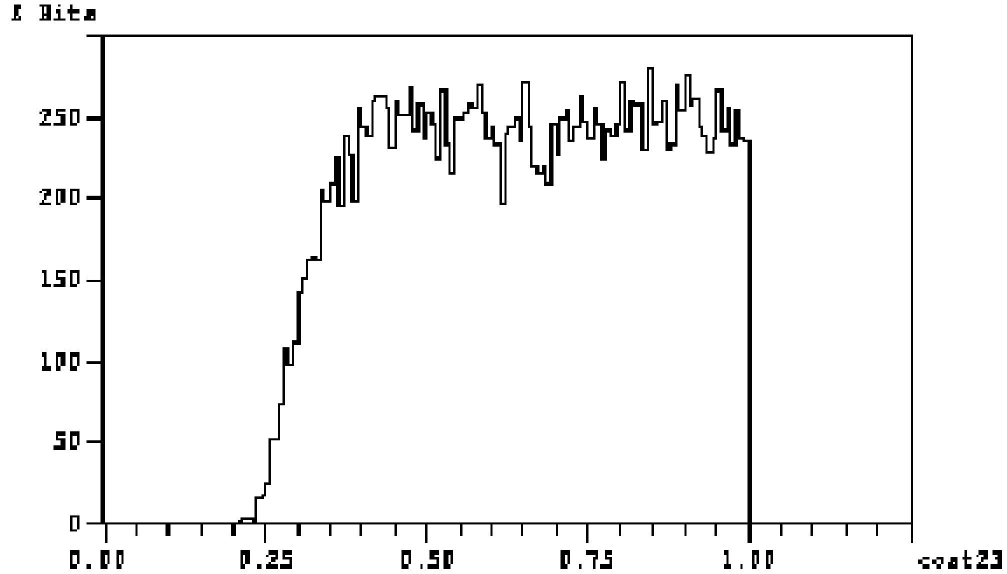

Figure 3.12: Counting rate of detected fission fragments as a function of the cosine of their emission angle from the target.

Fission events from a given target are identified by setting conditions [5]. The uncertainty introduced by the different conditions is very small.

We have calculated the neutron flux by using the cross sections from the databases ENDF/B-VI for energies lower than 20 MeV [68] and from reference [69] at higher energies. The final fluence calculation is shown in Figure 3.1 in a dn/dln(E) scale. The precision of the results depends essentially on the knowledge of the fission cross sections and from the simulation on the beam fraction intersecting the fission targets.

In conclusion, we have obtained the neutron fluence from 0.7 eV up to 1 GeV in a single measurement. The analysis technique allows for identification of fission events removing all problems due to contaminations from reactions in the foils or in the gas. A very good agreement is obtained between ^{235}U and ^{238}U experimental data in the energy range between 1 MeV to 1 GeV. We have been able to take into account the position information to calculate the solid angles and to reconstruct the impact position on the target. This last information will be very useful to deduce the beam profile as a function of the neutron energy.

A comparison with the results obtained with other techniques shows a very satisfactory agreement, in particular with the data obtained with PTB chambers (see Figure 3.1).

3.2 Energy Resolution: Experimental Determination

The n_TOF energy resolution has been investigated extensively in Monte Carlo simulations (see Part III, section 1). Here we report on the experimental determination of this quantity.

A complete determination of the resolution, in the entire energy range, is essentially impossible. However, the results of the Monte Carlo simulations can be verified experimentally for a number of cases. Once this is done, the results of the simulation can be adopted with confidence in the full energy range. This is the approach we have followed in our measuring campaign.

A premise is necessary when dealing with the determination of the resolution. In fact, several components contribute to the total resolution in a time-of-flight experiment. In particular, the time distribution of neutrons in a given energy interval is affected by:

- the time-width of the proton beam pulse;
- the moderation-time in the target-moderator assembly;
- the thermal motion of the nuclei in the sample (Doppler broadening);
- the time response of the detector.

Here we deal only with point 2. In fact, only this component of the resolution is unknown, *a priori*, while all the other quantities are either known, negligible, or can be easily evaluated.

Monte Carlo simulations of the spallation-moderation process in the n_TOF target assembly have shown that the shape of the TOF distribution, for a given neutron energy interval, can be characterized by an asymmetric peak and a tail to longer times [70]. The width of the peak increases with increasing neutron energies.

On the other hand, the resolution broadening of the neutron resonances in Fe is dominated by thermal broadening (Doppler) up to a few keV. At higher energies, the moderation time-distribution of neutrons in the target-moderator assembly dominates and determines the shape of the Resolution Function (RF). Hence, in the analysis of discrete resonances of Fe, the parameters of the measured cross section will be sensitive to the exact shape of the RF. We have analyzed a few isolated resonances in iron in order to investigate the shape of the RF and compare it to the results of Monte Carlo simulations.

To start with, the shape of the MC simulated RF has been fitted with an analytic function. From the available functions in the present version of SAMMY [67] (an R-matrix analysis code), the function best suited to represent the n_TOF RF is the so-called RPI function. This function consists of a χ^2 function with six degrees of freedom, plus two exponential terms. The RPI function has a total of 27 parameters in order to allow the adjustment of the shape with the energy. In the analysis, we have used only the seven energy-independent parameters to fit the shape at specific neutron energies. In Figure 3.13, we show the fits of the MC statistics accumulated for several neutron energy intervals, around the energies of selected isolated neutron resonances.

Both the MC results obtained with the code FLUKA+CAMOT (as provided with the web utility n_TOFU) and those obtained with FLUKA only (as provided by lambda) are shown in Figure 3.13. Taken into account the statistical dispersion of the points, the agreement between both the simulations and the fitted function is good.

The parameters determined in this way are used to analyze some of the resonances of ^{56}Fe. The results of the fits obtained with SAMMY for some resonances are shown in Figure 3.14. During the fit, the parameters of the resonance are kept fixed except for the energy, which is allowed to vary. From this analysis it can be immediately seen that the shape of the RF is correct. This represents the experimental evidence that the MC simulations are capable of representing correctly the n_TOF RF, at least in the energy range from 10 keV up to 200 keV.

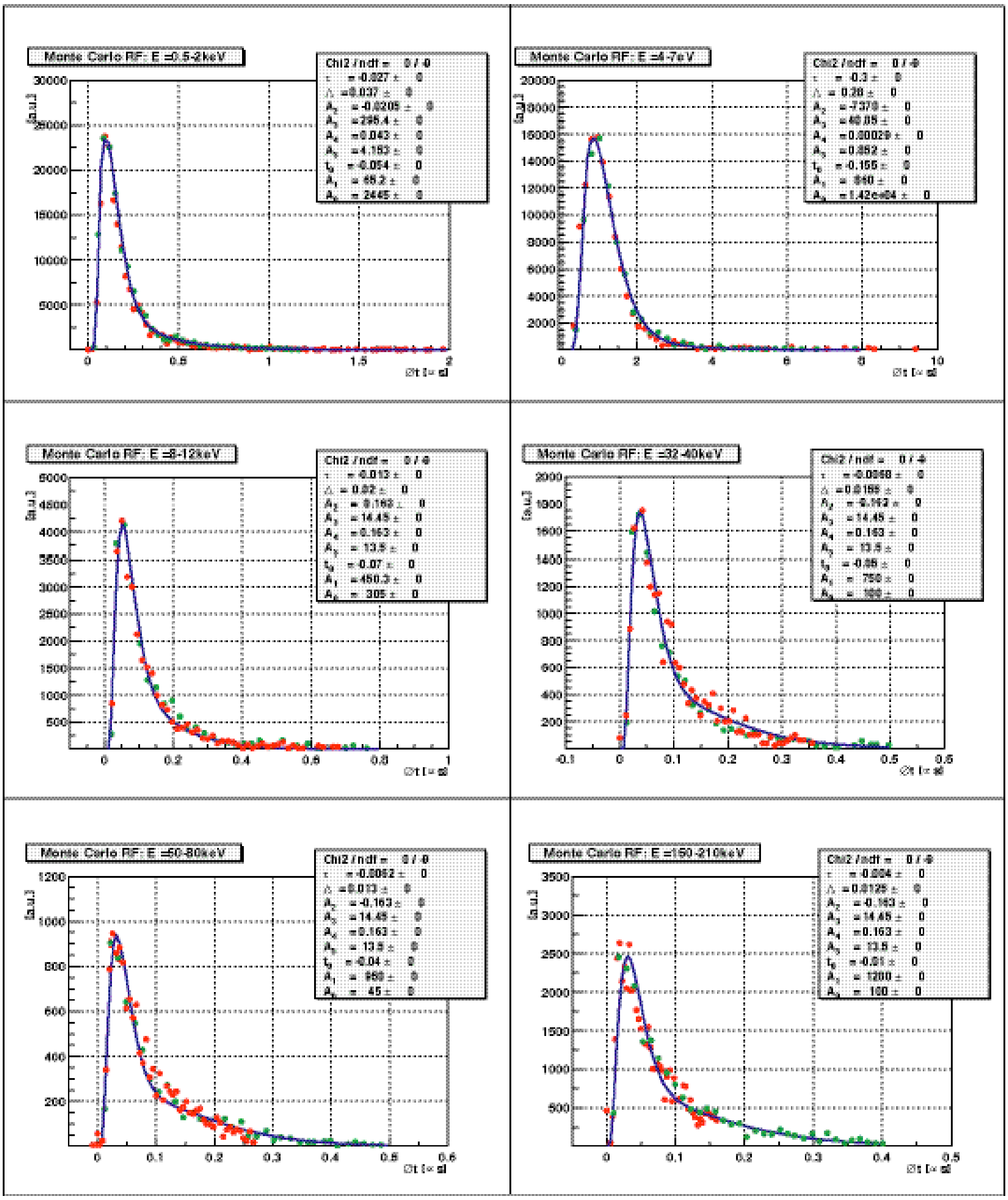

Figure 3.13: RF as simulated with FLUKA (red) and FLUKA+CAMOT(green). The RPI function fit is shown in blue with the parameters in the inset.

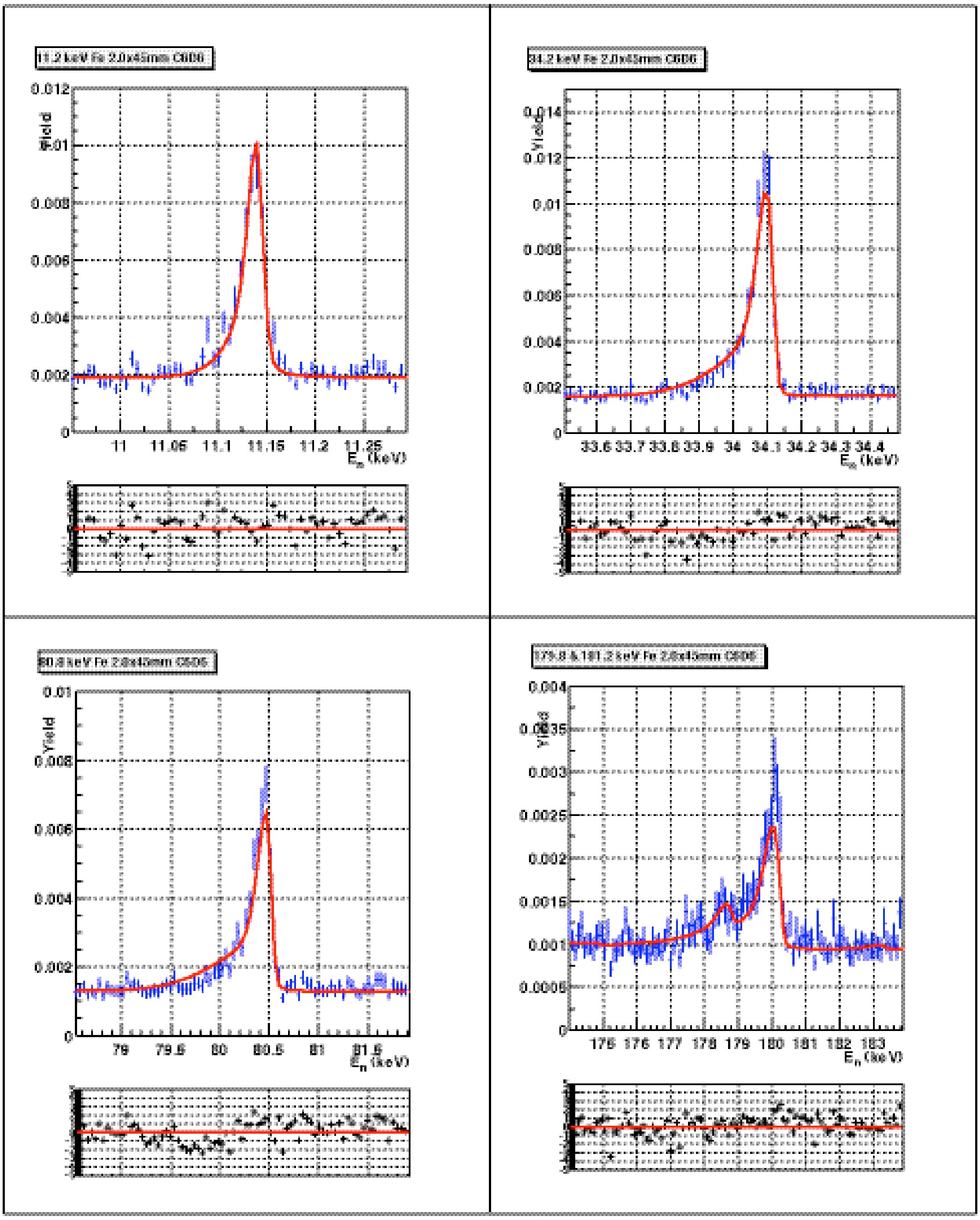

Figure 3.14: SAMMY fit to four resonances in Fe.

In an attempt to quantify the accuracy of the RF determination, the following considerations can be made.

As can be deduced from the observation of the figures, it seems that the RPI functions used are overestimating the amount of the low energy tail. In principle we can use the measured resonance shape to deduce the correct RF, and in fact SAMMY allows to adjust the parameters of the RPI function. An attempt was made to fit some of the parameters (□□,t_0,A_1) for the 80.8 keV resonance in ^{56}Fe with the result shown in the Figure 3.15.

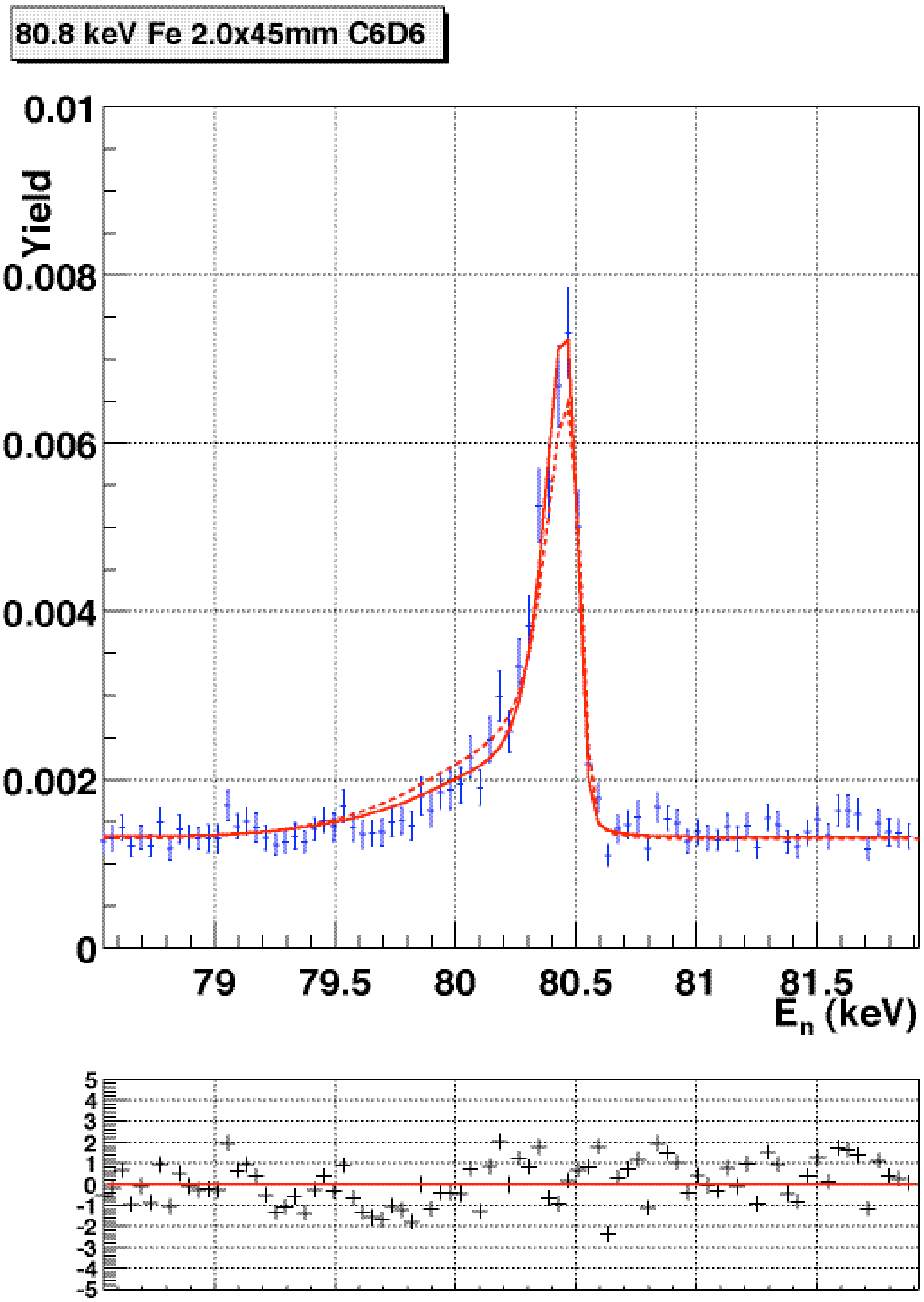

Figure 3.15: SAMMY fit to the 80.8 keV resonance in ^{56}Fe.

The reduced χ^2 of the fit improves from 1.38 to 1.06, but the normalization factor only changes by – 3.5% which gives a measure of the systematic deviation associated to the exact shape of the RF. The situation will be more critical of course in the case of overlapping resonances as is the case of the doublet at 180 keV. The change of the FWHM resolution represented by the change in the parameters amounts to – 10%. In any case it can be seen that for the 80.8 keV resonance the fitted shape of the RF is not completely satisfactory. The reason for this is partly the limited statistics but mainly the fact that the RPI function is on the one had too complex and on the other it is not in fact the most adequate to describe the resolution of n_TOF. The proper adjustment of the shape of the RF should be done after implementation of the new RF shapes in SAMMY.

After the reliability of the simulations is confirmed, a simple relation which allows to evaluate the n_TOF energy resolution can be formulated. This is the following:

$$\frac{\Delta E}{E} = \frac{2}{L}\sqrt{(\Delta L)^2 + 1.913 \cdot E \cdot (\Delta T)^2}\ ,$$

where E is the energy at which the resolution is to be estimated, L is the TOF length, and ΔL is the width of the RF (for example its FWHM). The second term in the square-root represents the contribution due to the time-width, ΔT, of the proton pulse. In this relation L and ΔL are expressed in cm, E in eV, and ΔT in μs. The conversion from a time distribution to a distance distribution is realized simply by the relation $\Delta L = v\Delta t$, where v is the velocity relative to neutrons with energy E.

At n_TOF, L = 187.5 m, $\Delta T \approx 14.1$ ns and a fit to the MC simulations of the RF in the energy range from 1 eV to 1 MeV results into

$$\Delta L = 2.75 + 0.0468\sqrt{E}\ ,$$

again with ΔL in cm when E is in eV.

For the numerical RF simulations, two on-line utilities are available on the http://cern.ch/n_TOF web-site (following the links: `lambda` and `n_TOFU`).

3.3 Spatial Profile of the Neutron Beam

In order to operate the MICROMEGAS detector as a neutron beam profile detector for the n_TOF facility at CERN, an appropriate neutron/charged particle converter has been employed which can be either the detector's filling gas or target with appropriate deposit on its entrance window [30]. Since the neutron energy range of the n_TOF facility extends from 1 eV to 250 MeV, there is not a unique choice of an efficient converter. Inter-dependent parameters such as the high neutron reaction cross section, the low charged particles energy loss inside the converter, their subsequent energy-angular distribution and the range inside the filling gas has been considered and optimized (see Figure 2.3 of Part III).

The neutron distribution is based on the detection of one outgoing charged particle from the reactions, ^{10}B(n,α)^{7}Li and ^{6}Li(n,α)^{3}H (i.e. an alpha or a triton). Thus, such a nucleus should leave the target, entering the conversion gap of the detector, with sufficient energy to create enough ionization in the gas.

3.3.1 Data Analysis and Experimental Results

As already mentioned, the CERN n_TOF facility provides a direct correlation of the neutron time of flight to its energy, an additional time measurement in the neutron detection allows the determination of the beam profile and the neutron flux as a function of the neutron energy. Since the neutron beam start signal has a RMS of 7 ns, a time resolution of few ns is required. In order to operate under these conditions, the anode strips were readout through 50 fast current preamplifier (rise time of 1 ns) associated with the innovative n_TOF Data Acquisition System based on 1 GHz flash ADCs (rates of 180 MHz).

The n_TOF Data acquisition system has a zero suppression algorithm incorporated which removes unnecessary information from the recorded data. In order to preserve all the information needed, a number of pre-samples before the threshold passing must be recorded and a number of post-samples as well. This permits the observation of a base line shift, pulse pile-ups, double pulses, etc. Each signal has been analyzed in detail: the base line and RMS, the start and end time, the amplitude of the signal and in particular the total area of the signal which is proportional to the energy deposited on the strip.

A particle passing through Micromegas (recoils, alphas and tritons) creates some electrons that are amplified and then detected by one-dimensional strips. The particle is inducing some signal on all the strips over which it has traveled. An example of the signals recorded for one burst (10^{12} protons) are reported in Figure 3.16. This figure shows clearly the different time of the created electron. The first signal corresponds to the electron created close to the mesh and the last one the electron created just after the drift electrode [71]. The detail of the data analysis procedure can be found in reference [72].

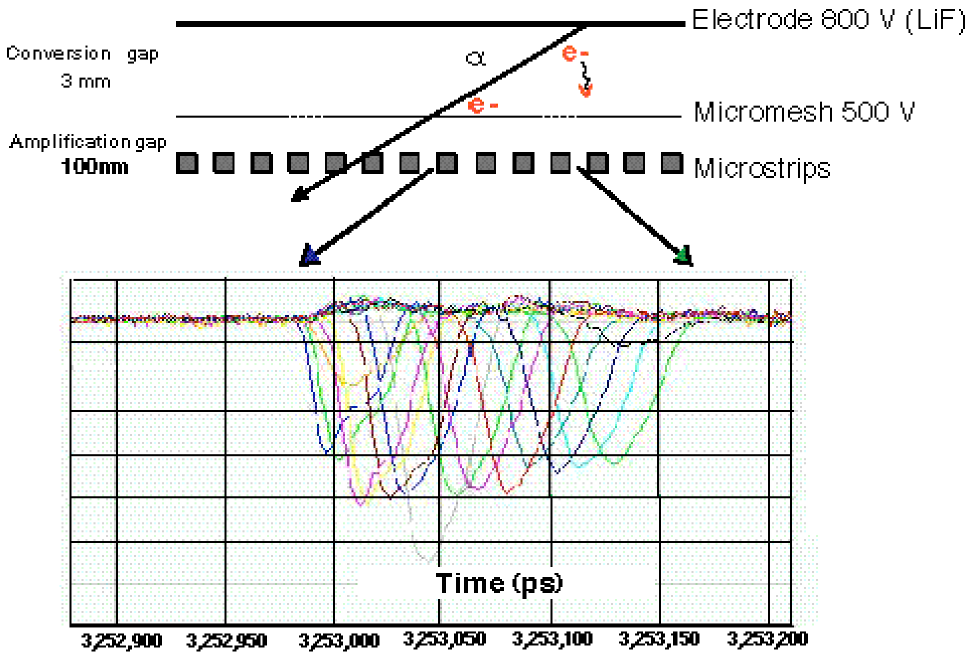

Figure 3.16: An example of the signal recorded during the run for 10^{12} protons.

Three different measurements have been performed, one with horizontal strips (vertical profile), one with vertical strips (horizontal profile) and one with the strips at 30° in respect the horizontal position. The results for neutron energy range between 10 and 100 eV and for the three positions of the detector are reported in Figure 3.17.

The projected profiles were obtained from 10 eV to 100 MeV. Above 100 MeV the analysis becomes difficult because all the particles arrive at very close time. As a consequence, there is a non-negligible quantity of pile-up and determining the first pulse in the cluster becomes impossible. In this case the projected profiles are no more reliable.

An example of the horizontal projection of the n_TOF neutron beam profile at the exit of the “sample changer” for three neutron energy ranges (from 10 eV to 10 keV, from 10 keV to 1 MeV and from 1 MeV to 10 MeV) are shown in Figure 3.18. It is worth noting the difference of the half width of the n_TOF beam profile between the low energy range and the high-energy range (significantly smaller, as reported in Table 3.6).

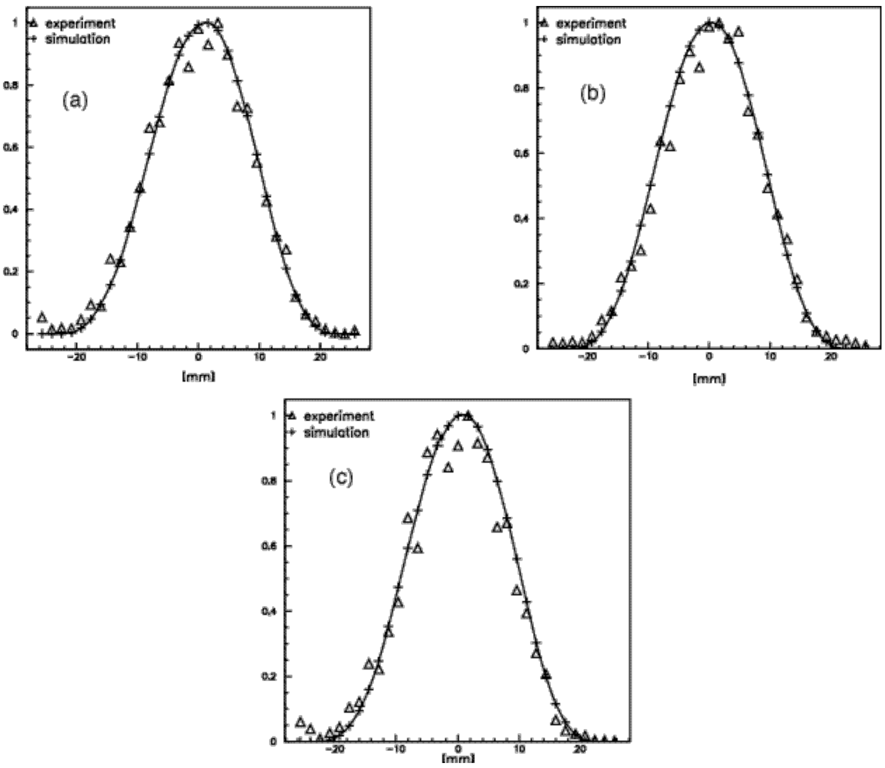

Figure 3.17: (a) Horizontal, (b) Vertical, (c) 30° projected profiles and simulation normalized to the maximum value between 10 and 100 eV at 186 m.

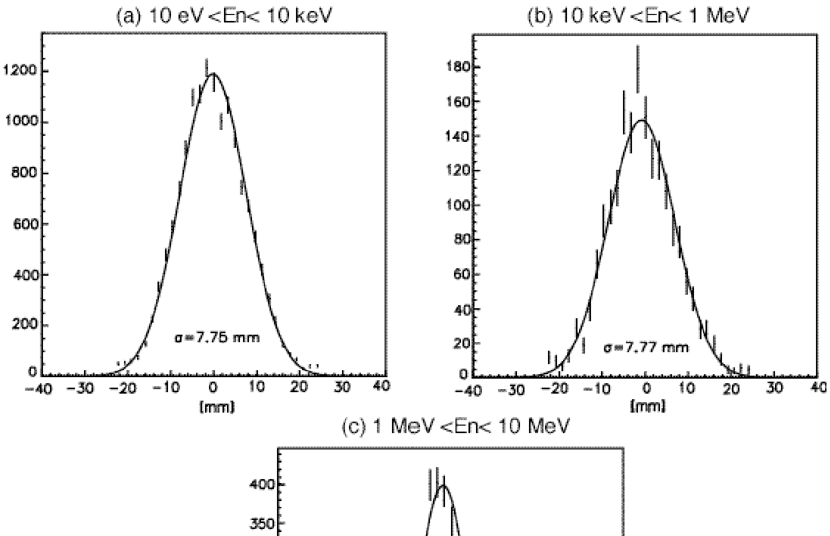

Figure 3.18: Experimental horizontal projection of the n_TOF neutron beam profile at the exit of the "sample exchanger" for three neutron energy ranges (a) from 10 eV to 10 keV, b) from 10 keV to 1 MeV and c) from 1 MeV to 10 MeV).

The time converted to equivalent neutron energy of the relative flux seen by Micromegas detector are reported in Figure 3.19. Two plots are illustrating the result obtained with the ^{4}He + iC_4H_{10} and Ar + iC_4H_{10} respectively.

Figure 3.19 shows clearly the 1/v response at low energies and the resonance at 250 keV characteristic of the ^{6}Li converter. At higher energy (several MeV) there is a large bump as a consequence of the increase of neutron fluence in this energy (spallation peak) and also the increase of detector efficiency provided by the detection of recoil nuclei from the filling gas. Several dips are observed in the energies corresponding to the different elastic resonances of the ^{16}O. This is the result of the dispersion of neutron of those energies from the main beam by the oxygen present in the water used for cooling of the lead target. The shift, observed in the figure between the two plots, is the result of the presence of the elastic resonance of the ^{4}He (n,n') ^{4}He reaction.

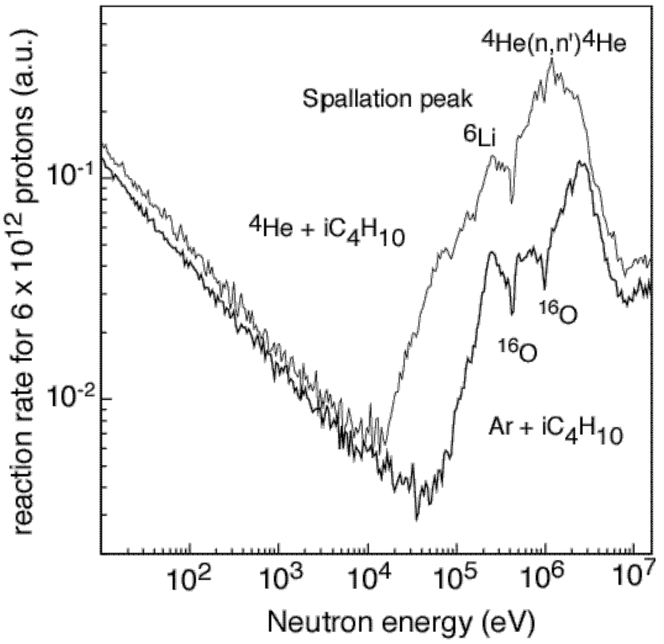

Figure 3.19: Relative flux (counts rate) of the n_TOF neutron beam seen by Micromegas detector as a function of the neutron energy.

3.3.2 Comparison with Simulations

The detail of the simulation of the n_TOF beam profile is given in Part III section 2.3. The simulated profiles have been projected with the same binning as the one defined by the strips of Micromegas for the three directions x, y and 30^0 (see Figure 3.17).

After normalization to the maximum value[6], the maximum discrepancy that could be observed is 20% in an energy region of low statistics (10 to 100 keV). The strips are anyway not exactly the same and the sensitivity of each strip is then variable. Some of them have for example more insulated spacers (to keep the width of the amplification gap) glued to them, which is changing their sensitivity. In the energy range 10 to 100 eV, this discrepancy is reduced to only 10% since the reaction rate is much higher (Figure 3.19).

To conclude, the shape of the different projections are in good agreement, and the simulation of the profile can be used for example to estimate the number of incoming neutrons for capture, fission and (n,xn) cross-section experiments.

---

[6] The comparison is focused on the spatial distribution of the beam.

3.3.3 *Analytic Approximation of the Beam Profile*

From the three different measurements that we made with different orientations of the strips, it is possible to reconstruct a simple analytic beam profile B(x,y) shape.

This analytic function must have several important features of the beam. The neutron beam is produced by some incident protons bunches on a lead target. Considering that the spallation cascade in the target is axially symmetric and that the 10° between the proton beam and the n_TOF beam line has a small effect [27], we assumed that the center of the beam is the center of symmetry. Then, it is possible to make for the three histograms of the strip occupancy a symmetry with respect to their center in order to double the points of measurement on one side and to choose an analytic function with a center of symmetry. Moreover, it can be shown that with this collimation system taken as perfect and the detector placed at 186 m, the beam is totally cut off at the radius r = R_{max} = 21.4 mm. The first derivative of the beam profile has to be zero at the center (r = 0) and at the edge (r = R_{max}).

The following function is chosen to approximate the beam were μ_x, μ_y, σ_x and σ_y are a free parameters:

$$B(x,y) \propto \exp[-\frac{1}{2}\{\frac{(x-\mu_x)^2}{\sigma_x^2}+\frac{(y-\mu_y)^2}{\sigma_y^2}\}] \quad \mathit{for}\ r=\sqrt{x^2+y^2} \leq R_{\max}$$

$$B(x,y) = 0 \quad \mathit{for}\ r > R_{\max}$$

where μ_x, and μ_y are the centers along the x- and y-axis. This expression combines all the features of the n_TOF beam and has the possibility to be slightly deformed thanks to the presence of the independent parameters σ_x and σ_y.

The energy deposit on the strips of the detector is proportional to the integral of the beam over the strips. It is then possible to adjust the free parameters μ_x, μ_y, σ_x and σ_y and compare the integral of the B(x,y) function over each strip with the values obtained experimentally [71]. The values of the parameters calculated with the experimental projected profiles at 186 m are reported in Table 3.6. The simulation results are also reported in the table for comparison. The upper energy limit in this table is only 30 MeV.

An important uncertainty occurs in the 10 to 100 keV energy range (see Table 3.6). It is mainly due to the fact that we have a poor statistics in this energy range (see Figure 3.18), it is the place where the reaction rate is the lowest (see Figure 3.19). Concerning the center of the beam, a shift (indicated by $\Delta\mu$) of about 0.5 to 1.5 mm in both planes has been observed experimentally and confirmed by the simulations.

	Experimental				**Simulation**	
Energy range	σ_x [mm]	$\Delta\mu_x$ [mm]	σ_y [mm]	$\Delta\mu_y$ [mm]	σ_x [mm]	σ_y [mm]
10 eV – 100 eV	7.6	0.5	7.2	0.4	7.7	7.7
100 eV – 1 keV	7.4	0.8	7.3	0.6	7.7	7.6
1 keV – 10 keV	7.4	1.4	7.6	1.2	7.7	7.6
10 keV – 100 keV	7.9	2.6	7.4	2	7.7	7.6
100 keV – 1 MeV	7.5	0.9	7.0	0.7	7.6	7.4
1 MeV – 10 MeV	6.6	0.5	6.4	0.4	6.8	6.7
10 MeV – 30 MeV	6.4	0.7	6.1	0.6	6.1	6.0

Table 3.6: Values of parameter σ_x and σ_y at 186 m obtained by fitting experimental data and simulations.

3.4 Background Conditions for (n,γ) Measurements

There are several sources of background that can distort a neutron capture measurement with C_6D_6 detectors [38]. At high neutron energies (short times of flight) the main contributions are the ultra-relativistic particle flash (mainly gamma-rays and muons), high-energy neutron recoils in the detectors and neutron inelastic reactions occurring at the samples placed in the neutron beam. Such components of the background mainly affect the neutron energy region above a few hundred of keV in the count rate of the C_6D_6 detectors as a function of the neutron energy.

The background in capture cross-section measurements with C_6D_6 detectors at neutron energies below a few hundred of keV consists of gamma rays produced by several mechanisms. The three most important components have been identified:

- environmental background with no sample placed in the neutron beam. It is an intrinsic characteristic of the facility and depends on the intensity of the neutron fluence in the experimental area;
- gamma-ray background produced by neutrons scattered by the sample and captured in materials at or in the vicinity of the detectors (detector itself, beam pipes, experimental area walls, etc.). This component of the background is related to the ratio of capture to elastic cross section of the sample material. At n_TOF, the background associated to neutron capture events in the detector “dead” materials has been minimized by using low neutron sensitivity detectors, equipped with thin aluminum or carbon fiber canning;
- in-beam gamma rays scattered at the samples and detected in the C_6D_6. This component depends on the atomic number Z of the sample material.

A series of measurements for investigating the different background components was performed with two different types of C_6D_6 detectors [65]: one commercially available Bicron detector with reduced aluminum canning and two carbon fiber canning detectors with ultra-low neutron sensitivity. The magnitude of the background was measured for five cases:

- in absence of any sample in the neutron beam, for the evaluation of the environmental background;
- on a C sample with a large elastic cross section, negligible (n,γ) cross section and low Z (i.e. low gamma ray scattering cross section);
- on a Pb sample with a large elastic cross section, low (n,γ) cross sections and high Z (i.e. large gamma ray scattering cross section);
- on a Fe sample as intermediate case;
- with a Fe sample in the beam and a detector placed at different positions inside the experimental area.

The experimental setups used in the different measurements are shown in Figure 3.20. To be noticed in the Setup 2 are the two positions of the two carbon fiber C_6D_6 detectors: one with both detectors placed at 90^0 degrees and the other one with the detectors shifted backward 7.8 cm with respect to the sample position.

Table 3.7 contains the technical details for the C and Pb samples used for the measurements.

Sample	Diameter (mm)	Thickness (mm)	Mass (g)	No. of atoms
^{nat}C	20	6.35	3.933	1.972×10^{23}
^{nat}Pb	20	1.0	3.607	1.048×10^{22}
^{nat}Fe	45	2.0	25.00	2.696×10^{23}

Table 3.7: Characteristics of the samples used for the measurements [65].

Figure 3.21 shows the count rate distribution per average proton pulse (i.e. $7\text{x}10^{12}$ protons) of the carbon fiber canning C_6D_6 as a function of the time of flight (bottom) and time of flight neutron equivalent energy (top). A logarithmic binning of 50 bins/decade was used for representing all the neutron energy distribution presented all through this section, while 100 bins/decade were used for the time distributions. A threshold of 200 keV in the energy deposition on the C_6D_6 was adopted.

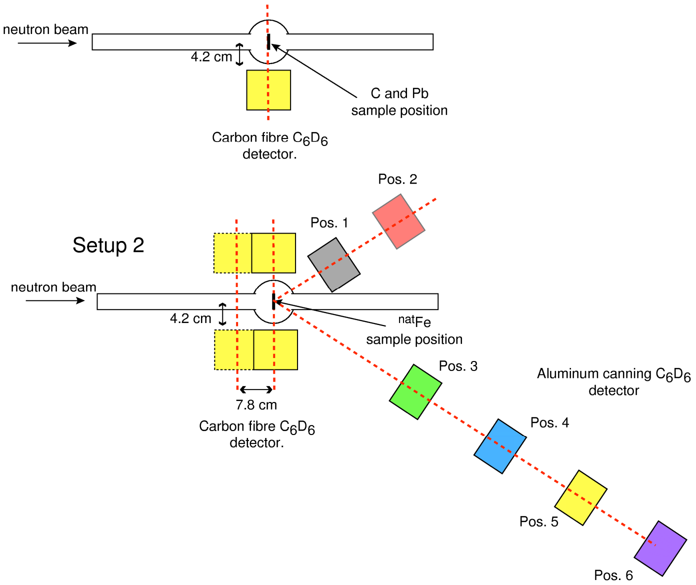

Figure 3.20: Schematic description of the different C_6D_6 experimental setups.

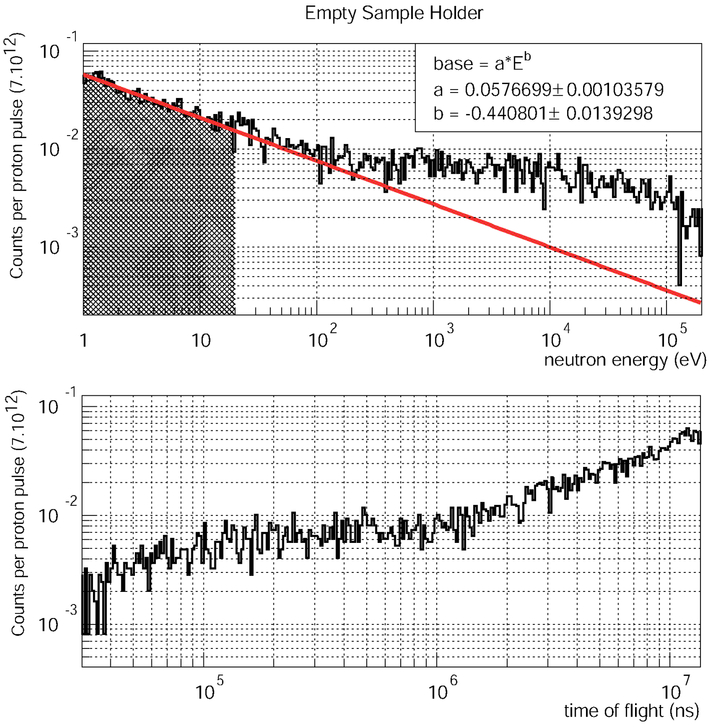

Figure 3.21: Count rate distribution of the carbon fiber C_6D_6 detector per average proton pulse in absence of any sample in the beam. Top: count rate as a function of the neutron energy. Bottom: count rate as a function of the time of flight. A binning of 50 bins/decade was adopted for the neutron energy dependent rate distribution and 100 bins/decade for the time dependent rate distribution.

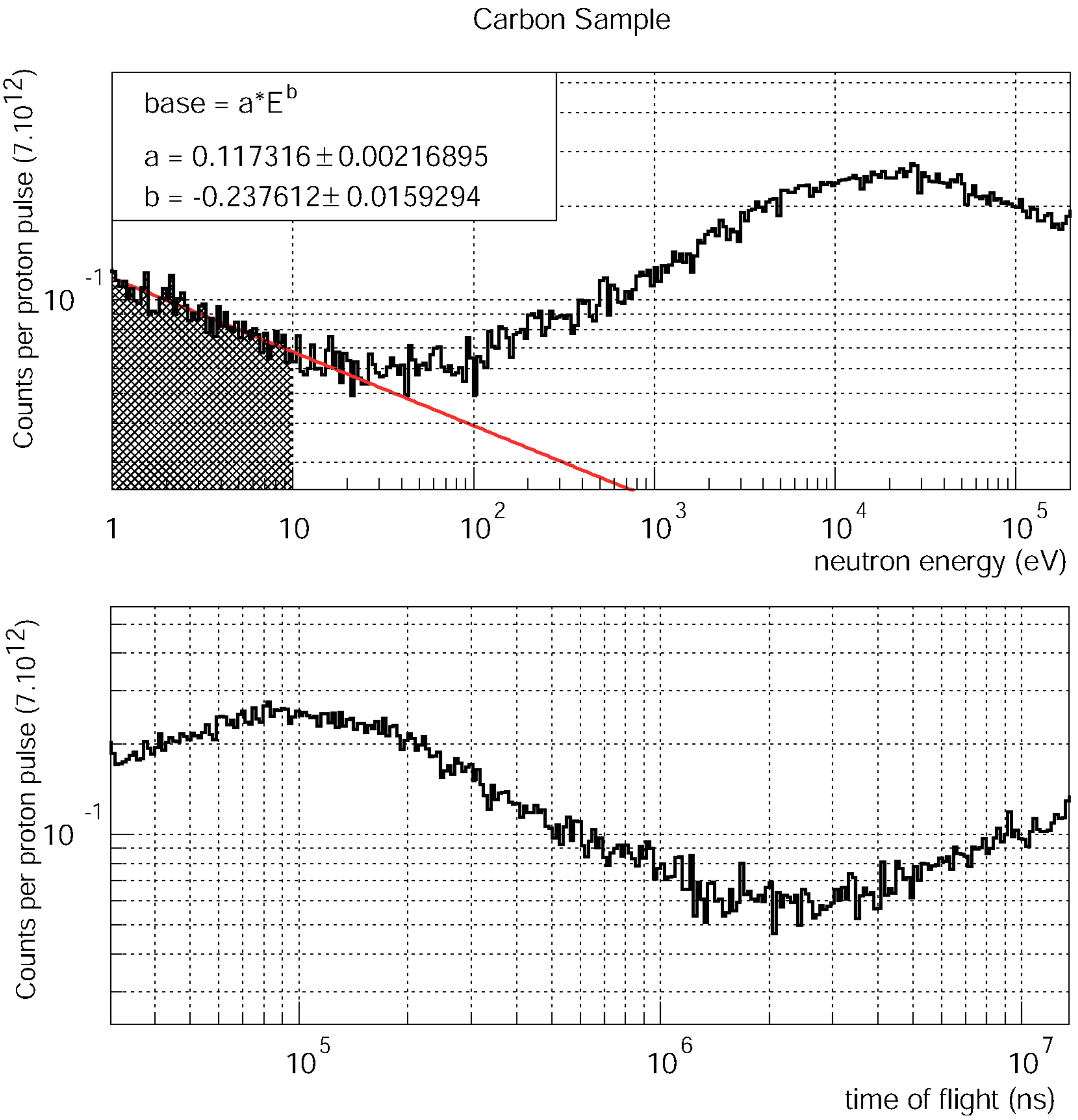

Figure 3.22: Count rate distribution of the carbon fibre C_6D_6 detector per average proton pulse for a C sample in the beam. Top: count rate as a function of the neutron energy. Bottom: count rate as a function of the time of flight. A binning of 50 bins/decade was adopted for the neutron energy dependent rate distribution and 100 bins/decade for the time dependent rate distribution.

Two components are distinguished in the TOF equivalent neutron energy spectra: one at lower neutron energies showing a power law dependence on the neutron energy and a second one with a more complex structure as a function of the neutron energy. The two components are observed in the rate distributions when the C and the Pb samples are placed in beam as well. Figure 3.22 shows the rate distribution in the carbon fiber C_6D_6 detector for the measurement with the C sample, as a function of the neutron energy (top) and time of flight (bottom).

Figure 3.23 shows the equivalent distributions for the Pb sample. A small Ag contamination in the natural Pb sample was identified through the 5.2 (n,γ) resonance visible in the Pb neutron energy spectrum. A lower threshold of 200 keV in the C_6D_6 deposited energy was adopted. The empty sample rate distribution was subtracted from both C and Pb measurements with a normalization given by the ratio of counts in the SiMON detectors. In this way, only the contributions associated to the samples remain.

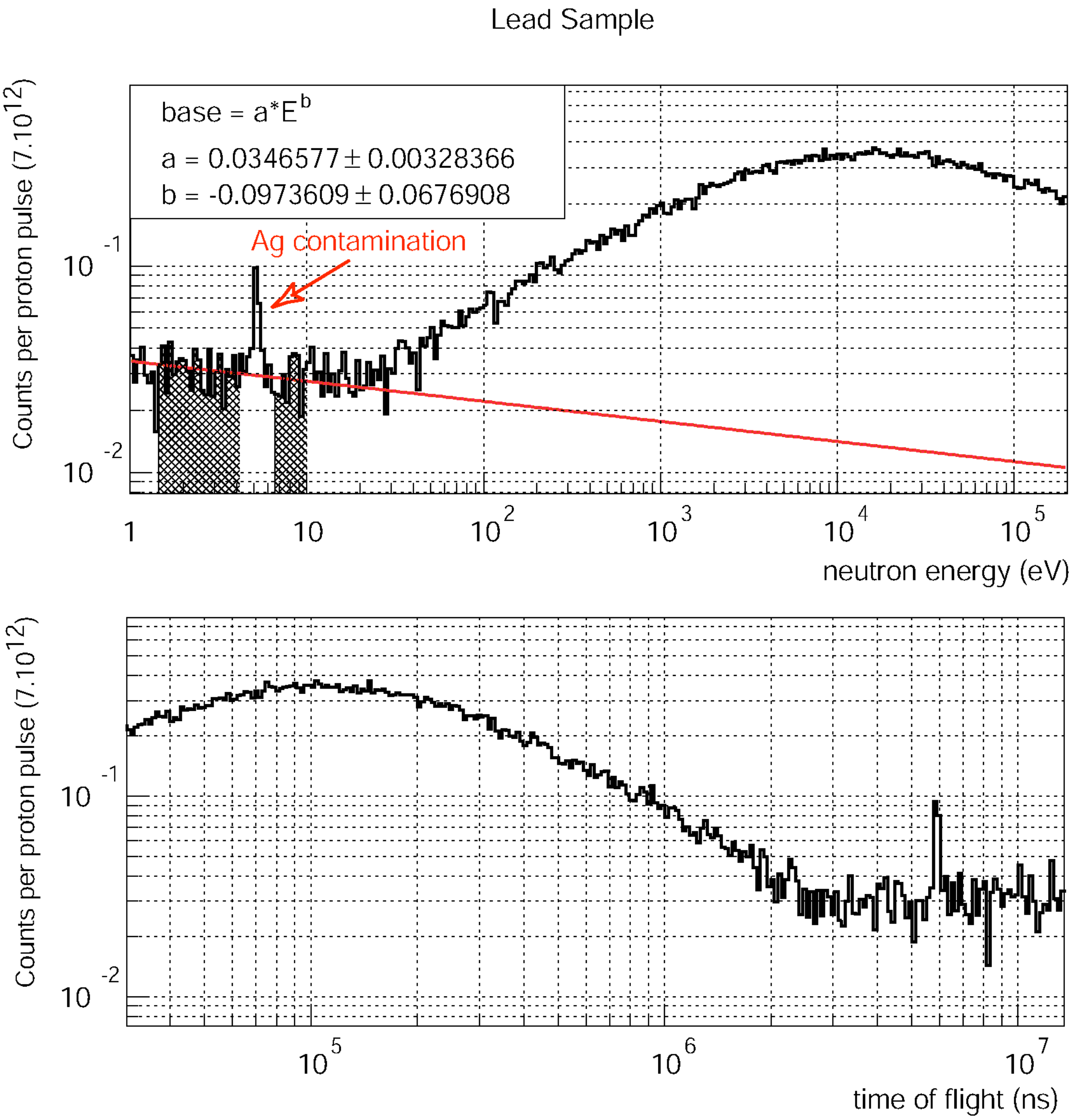

Figure 3.23: Count rate distribution of the carbon fiber C_6D_6 *detector per average proton pulse for a Pb sample in the beam. Top: count rate as a function of the neutron energy. Bottom: count rate as a function of the time of flight. A binning of 50 bins/decade was adopted for the neutron energy dependent rate distribution and 100 bins/decade for the time dependent rate distribution.*

Comparing the results for the empty sample holder with respect to the C and Pb in the Figure 3.22 and Figure 3.23 respectively, it can be observed that the low energy contribution to the background follows a complete different scaling law than the contribution at higher neutron energies. The contribution at lower neutron energies is a factor of 5 smaller for the Pb measurement. By taking into account the different number of atoms in the samples (18.81 times more atoms for C than for Pb), the effect is compatible (within a factor of 2) with the difference in the neutron elastic cross sections of the two isotopes. However, the maximum of the background component at 20 keV neutron energy is about 30 times higher for Pb than for C, after rescaling to the same number of atoms. Such an effect cannot be explained by neutron cross section differences. In fact, as it will be shown below, the count rate in the 20 keV neutron energy region can be associated to in-beam scattered gamma-ray, which is strongly dependent on the atomic number of the scattering material.

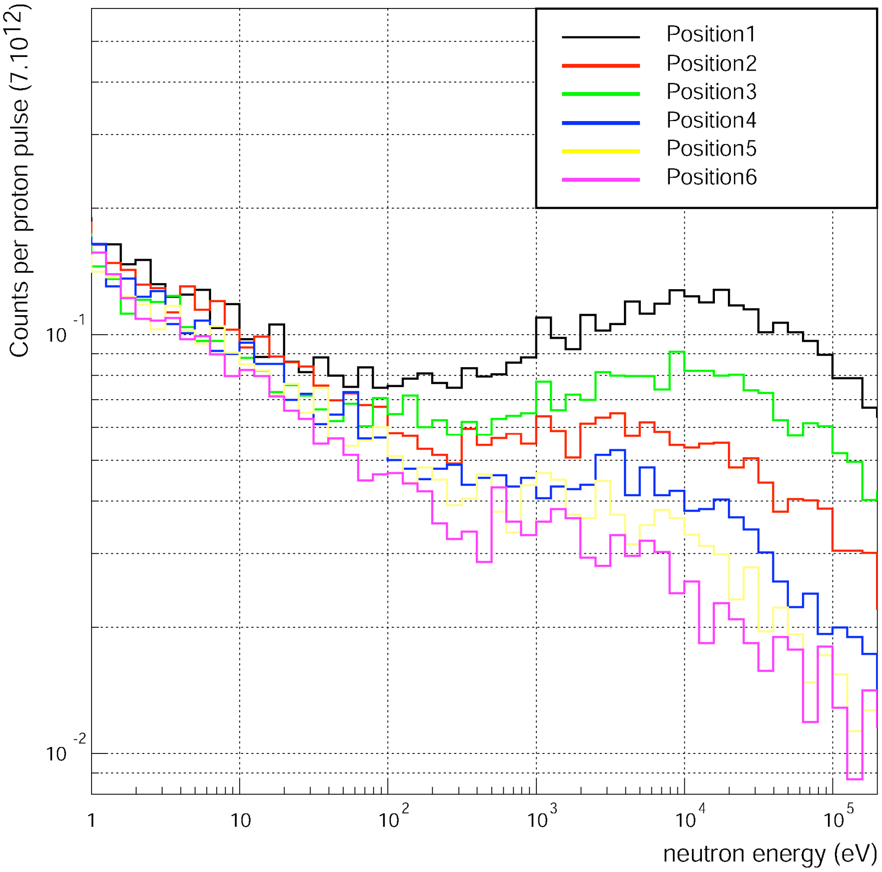

Figure 3.24: Count rate distribution of the aluminum canning C_6D_6 detector per average proton pulse at different positions in the experimental area. The positions are defined in Figure 3.20. A binning of 10 bins/decade was adopted.

To confirm the interpretation of the low energy count rate distribution as due to neutron scattered around in the experimental area, a series of measurements was performed with the Bicron detector placed at different positions inside the experimental area and the C sample placed in the beam. Figure 3.24 shows the count rate of the C_6D_6 detector at the positions defined in Figure 3.20. The measurements reveal that the dominant component in the neutron energy distribution between 1 eV and 20 eV is nearly independent on the distance to the sample. This is characteristic of a spatially uniform gamma background distribution originated by environmental and scattered neutrons captured in the experimental area. On the contrary, the dominant component between 20 eV and 200 keV shows a strong dependence on the distance to the sample, which indicates its origin at the center, at the sample position. This conclusion, in addition to the result shown previously, points to the existence of a in-beam gamma-ray component of the background.

In the low energy region, between 1 and 20 eV, the dependence of the count rate as a function of the neutron energy is of the form

$$Counts = a \cdot E_n^b$$

where a and b are parameters to be fitted to the spectra measured with the different samples. A least-square analysis produced the results shown in Table 3.8. Before fitting, the empty-sample distribution representing the environmental background was subtracted from both the C and Pb count rate distributions, by normalizing to the ratio of count rates in the Silicon Flux monitor of the respective measurements.

	Energy interval for the least squares fit	***a***	***b***
No sample	0.724 eV – 20.eV	0.0551(10)	-0.441(14)
C sample	0.724 eV – 10. eV	0.1126(21)	-0.238(16)
Pb Sample	1.51 eV – 4.17 eV, 6.92 eV – 10. eV	0.0335(32)	-0.099(67)

Table 3.8: Ccoefficients of the least squares fit of the background component due to scattered neutrons to the power law $a \square E_n^b$

In the case of Pb, the region for the least squares fit had to be split in two parts in order to exclude the Ag contamination at about 5.2 eV.

In order to confirm the presence of in-beam gamma-ray generating capture events in the detectors, a simulation of the gamma-ray generated in the spallation target area was performed. The result of this simulation is shown in Figure 3.25.

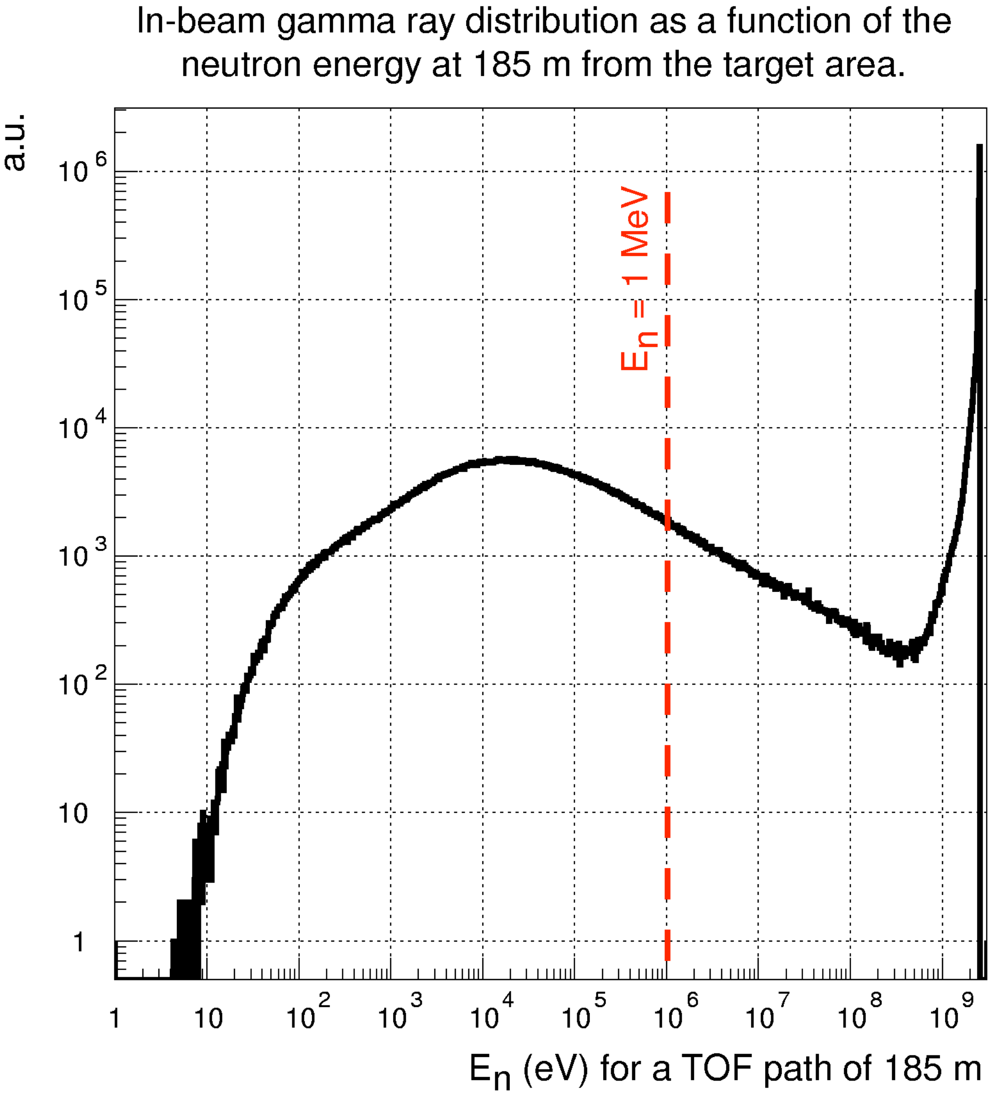

Figure 3.25: Monte Carlo simulated in-beam gamma ray energy distribution originating at the spallation target area as a function of the TOF neutron energy at 185 m.

As can be seen in Figure 3.26, in addition to the strong prompt emission, gamma-rays are emitted also at much later times, from the target-moderator assembly, corresponding to low neutron energies. In addition, the shape of the distribution matches with the observed distribution (bump in the 20 keV neutron energy region). The same set of simulations show that for TOF longer than 1.4 μs (corresponding to neutron energies below 1 MeV, at 185 m), the gamma-ray spectrum is dominated by the **2.2 MeV γ-ray from the neutron capture in hydrogen**. The γ-ray spectrum is shown in Figure 3.26.

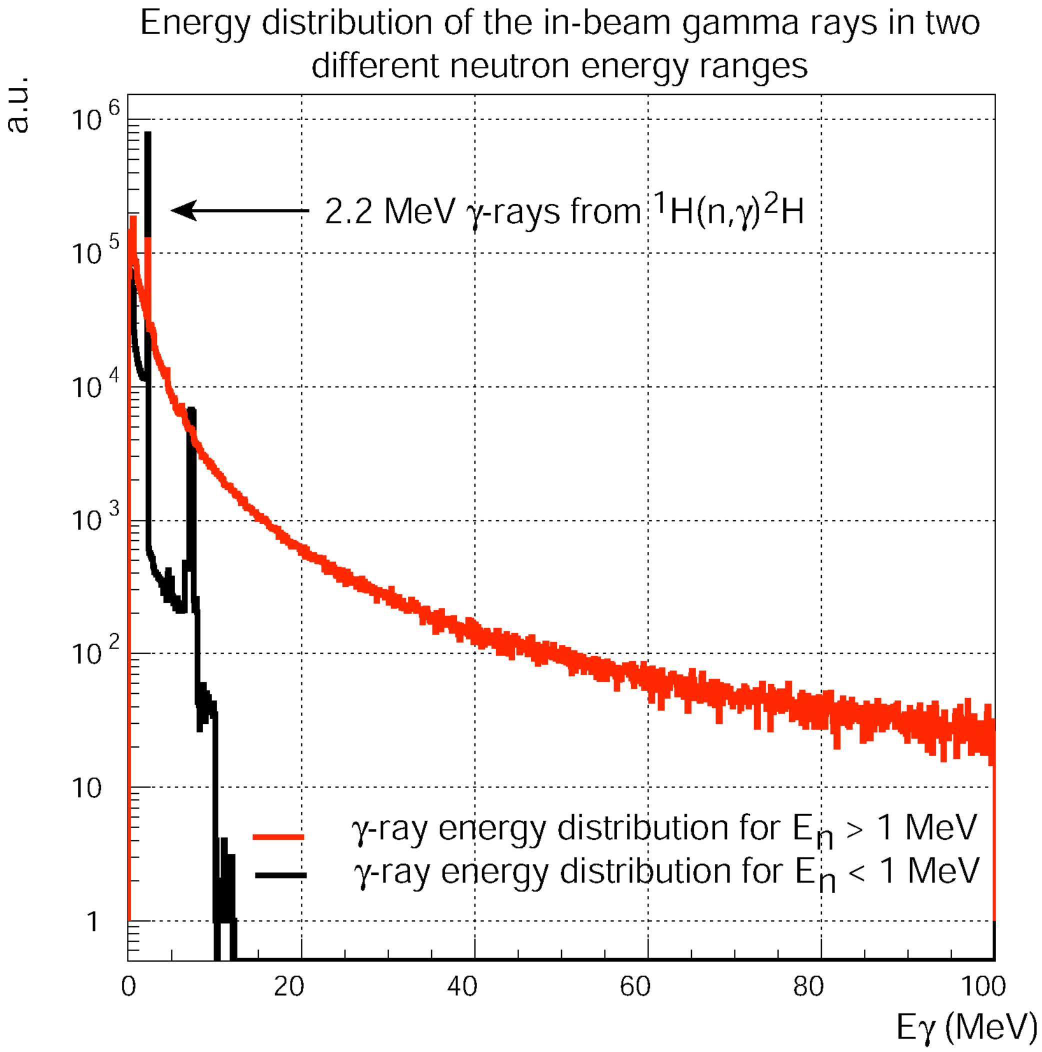

Figure 3.26: Gamma-ray spectra originating at the Pb spallation target for two different neutron energy ranges.

The scattered in-beam gamma ray background shows a dependence on the scattering angle, larger at lower Z scattering materials (for which Compton scattering dominates) and lower at larger Z materials (for which pair creation starts to play an important role). Figure 3.27 shows the count rate of one carbon fiber C_6D_6 detector as a function of the neutron energy for two different detector positions during a ^{nat}Fe(n,γ) measurement. It can be observed in the figure that the in-beam gamma ray component between 20 eV and 200 keV is strongly suppressed (about factor of 5) with respect to the same measurement with the detector placed at the 90° position. However, the count rate losses in the ^{56}Fe(n,γ) resonance at 1.1 keV were only 30%. For this reason, a standard C_6D_6 setup for (n,γ) measurements has been adopted in which the detectors are placed at angles larger than 90° with respect to the beam axis.

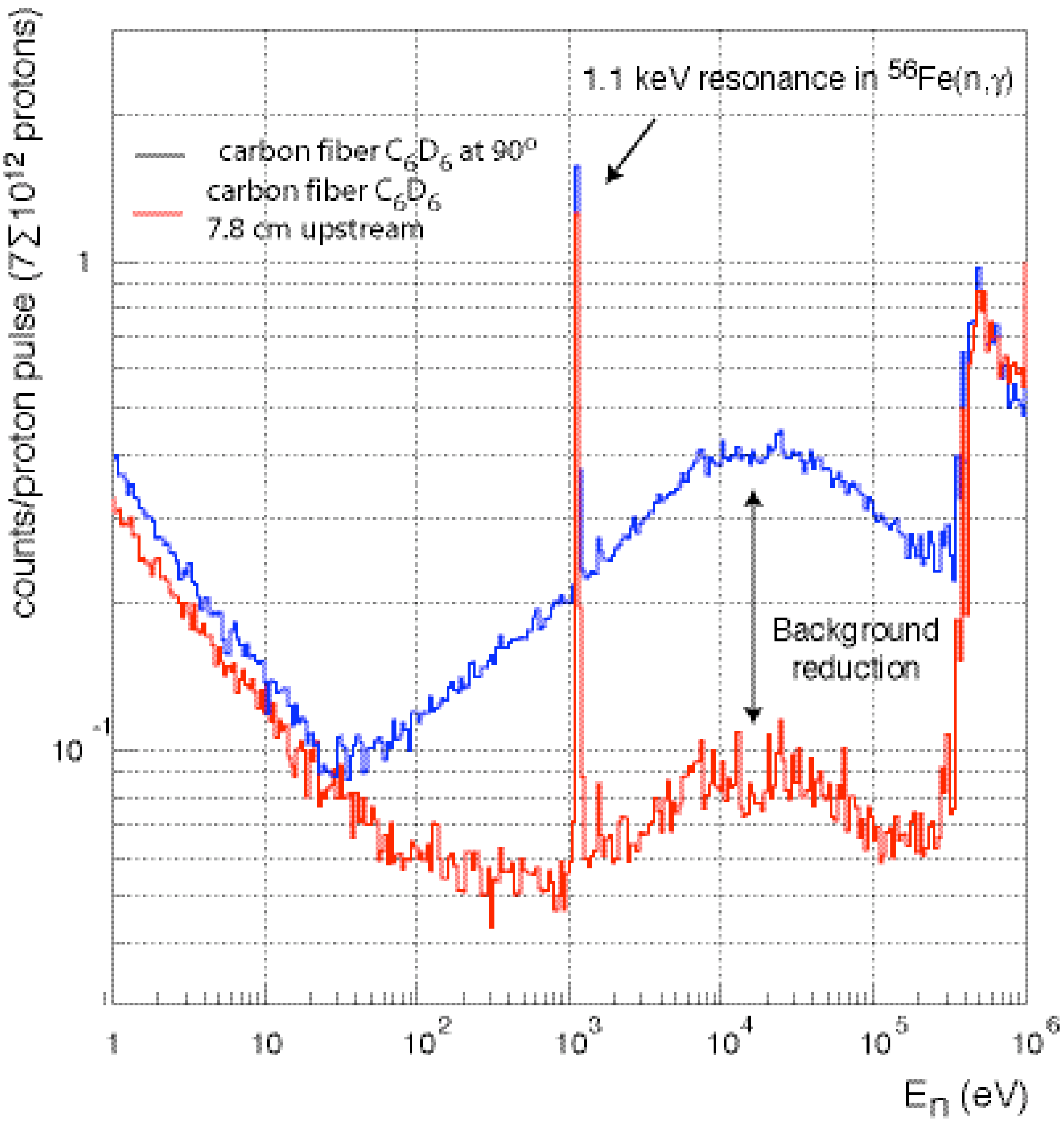

Figure 3.27: Comparison between the count rates in a ^{nat}Fe(n,γ) measurement of one carbon fiber C_6D_6 detector placed at 90^{o} and 7.8 cm backwards with respect to the sample.

The integrated count-rate in the energy region 20 eV – 200 keV are reported in Table 3.9. The renormalized count rates for Pb takes into account of the different total number of atoms present in the C and Pb samples ([C]/[Pb] = 18.8)

	Counts for 7×10^{12} protons (neutron energy region: 20 eV – 200 keV)
Empty sample holder	0.7
C sample	25.6
Pb sample (renormalized)	704.5

Table 3.9: Integral count rates per proton pulse due to in-beam gamma rays at neutron energies between 20 eV – 200 keV. A threshold of 200 keV in the deposited energy has been used.

In summary, a series of measurements with C_6D_6 detectors were performed for identifying the background components in capture measurements between 1 eV and 200 keV. The count rate of the C_6D_6 detectors was recorded for C, Pb, and Fe samples placed in the neutron beam as well as for an empty sample holder position. Two background components were identified:

- one due to environmental or sample-related scattered neutrons and captured in the experimental area. Such a contribution is dominating in the entire energy range in absence of any sample or between 1 - 20 eV for the samples studied.
- one dominating at neutron energies between 20 eV and 200 keV due in-beam gamma rays scattered by the samples.

The following considerations are in order:

- The background component associated to the neutron scattering and subsequent capture increases with the elastic scattering cross section of the sample materials studied.
- The in-beam gamma ray background component showed a large dependence on the atomic number of the sample materials, as well as large angular dependence.
- The in-beam gamma ray background was suppressed by a factor of 4 by shifting the C_6D_6 detector 7.8 cm backwards with respect to the normal to the beam axis at the sample position. Such a setup is the standard for (n,γ) measurements with C_6D_6 detectors.
- After correcting the count rate spectra for the gamma ray detection efficiency of the C_6D_6 detectors, a further suppression of a factor of 4 is achieved for a $^{nat}Fe(n,\gamma)$ cross section measurement.

The count rates due to background in a carbon fiber C_6D_6 detector between 1 eV – 20 eV and 20 eV – 200 keV are summarized in Table 3.10.

	Counts for 7×10^{12} protons	
	1 eV – 20 eV	**20 eV – 200 keV**
Empty sample holder	2.1	0.7
C sample	5.4	4.7
Pb sample (renormalized)	40	64
Ratio of counts Pb/C	7.4	13.6

Table 3.10: Count rates in a carbon fiber C_6D_6 detector placed at 90^o with respect to the beam axis due to background in two different neutron energy regions.

CONCLUSION

The concept of the n_TOF neutron beam made use of the specifically high flux of neutrons attainable using the spallation process of 20 GeV protons on a lead target and the remarkable beam density of the CERN-PS. The main advancement offered by this facility lies exactly in its useful, initial neutron rate of three orders of magnitude higher than in the most performing electron linacs and in the up to three orders of magnitude better energy resolution extending the presently available energy range of the resolved resonance region in neutron induced cross section measurements. The extra flux can be used in experiments either to improve beam-downstream the resolution for a given flux, or alternatively to increase beam-upstream the flux for a given energy resolution.

The small repetition rate of less than a Hertz excludes time overlaps due to successive proton bunches and provides a rejection power of many orders of magnitude for the accidental background due to radioactive samples such as minor actinides, fission fragments and the isotopes of the U or Th fuel cycle.

Different forms of shielding and the geometry of the experimental area have been optimized, in order to keep the background to a level compatible with the operation of large calorimeters. The experimental area is equipped with all necessary infrastructure to provide flexible and safe operation in the running of the individual measurements. The extended program of measurements for determining the background level in the n_TOF measuring station confirmed the results of the simulation studies. The background related to the neutrons arriving through the beam-pipe is the dominant component in the experimental area, neutrons scattering on the samples under study representing the most significant background. A further improvement of this background can be achieved by lining of the experimental area with borated and even better Li enriched polyethylene.

Special effort has been dedicated to the geometry, material and size of the neutron beam collimators, in order to allow a large flexibility in the choice of the size and the intensity of the neutron beam. Different targets and different detectors may be used in a variety of configurations according to the requirements of each specific measurement. The experimental area includes the “counting room”, where the electronics, the data acquisition system and the computer are hosted, including a room for the spare detectors and workspace for the personnel.

Finally, this facility allows to study systematically and accurately neutron induced reactions in the energy interval between 1 eV and 250 MeV with a quality superseding that of the presently available nuclear data and satisfying thus the demanding requests in frontier research and industrial requirements.

GLOSSARY

ACS	Access Control System
ADC	Analog to Digital Converter
ADS	Accelerator-Driven Systems
BCT	Beam Current Transformer
BPM	Beam Position Monitor
C6D6	Deuterated Benzene (liquid scintillator)
CAMAC	Computer Automated Measurement and Control
CDR	Central Data Recording
DAQ	Data Acquisition System
EAR-1	Experimental Area-1
FADC	Flash Analog to Digital Converter
FIC	Fission Ionization Chamber
FWHM	Full Width at Half Maximum
FTN	n_TOF Proton Transfer Line
FZK	Forschungszentrum Karlsruhe
HPGe	High-Purity Germanium (detector)
IPN-ORSAY	Institut de Physique Nucléaire d'Orsay
ISR	Ion Storage Ring
LHC	Large Hadron Collider
MC	Monte Carlo
MCA	Magnet C type A
MCR	Main Control Room of the PS
MIS	Machine Interlock Systems
ND	Nuclear Data
NEL	Neutron Escape Line
n_TOF	The neutron time-of-flight facility at CERN
PCI	Personal Computer Interface

PHWT	Pulse Height Weighting Technique
PLC	Programmable Logic Controller
PPAC	Parallel Plate Avalanche Counter
PPE	Personal Protection Entry
PS	Proton Synchrotron
PS-CO	PS – Control Operator
PTB	Physikalisch-Technische Bundesanstalt (fission chamber)
QD	Quadrupole
QFS	Quadrupole Focusing Sector
RBS	Rutherford Back Scattering
RC	Reaction Chamber
RF	Radio Frequency
RMS	Root Mean Square
RPI	Rensealer Polytechnic Institute
SCADA	Supervisory Control And Data Acquisition
SG	Service Gallery
SiMON	Neutron monitoring system based on Silicon strip detectors
TAC	Total Absorption Calorimeter
TCP/IP	Transmission Control Protocol / Internet Protocol
TCR	Technical Control Room
TDC	Time to Digital Converter
TIS	Technical Inspection and Safety
TLD	Thermo Luminescense detector
TOF	Time-Of-Flight
VME	Versatile Module Europe
VXE	VME subfamily
WCM	Wall Current Monitor
WWW	World Wide Web

APPENDIX

CERN n_TOF: Basic Parameters

The Proton beam

Proton beam momentum:		**20 GeV/c**
Beam size at the target position		
	(horizontal)	7.8 mm
	(vertical)	5.6 mm
Intensity	dedicated	7 x 10^{12}
[proton/pulse]	parasitic	4.5 x 10^{12}
Repetition frequency (typical)		1 pulse / 2.4 s
Pulse width		6 ns (rms)
n/p		300

The spallation module

The target	
Material	Lead
X, Y, Z (external dimensions)	80 x 80 x 60 [cm^3]
Niche dimension	55 x 20 x 20 [cm^3]
Beam direction (Z-axis)	coplanar in YZ plane 10 degrees in X-direction
Window	
Material	Aluminum alloy
Diameter	80 cm
Thickness	1.6 mm
Grid thickness	40 mm
Equivalent mass thickness	6.17 mm
Cooling & Moderation	
Material	Water
Thickness at the exit face	5 cm

The TOF tube

Sector-Material	**Thickness [mm]**	**Length [m]**	**Internal Diameter [cm]**
1-Al Alloy	8.0	4.135	80
2-Stainless Steel	7.9	65.75	80
3-Stainless Steel	6.4	68.35	60
4-Stainless Steel	4.8	61.372	40
Total Length		**199.607**	

CERN n_TOF: Basic Parameters

Collimators

First collimator

Segment-Material	Internal- External radius [cm]	Length [m]	Initial co-ordinate [m]
1-Iron	5.5 - 25.0	1	135.54
2-Concrete	5.5 - 25.0	1	136.54

Second collimator : capture mode

Segment-Material	Internal- External radius [cm]	Length [m]	Initial co-ordinate [m]
1-Borated polyethylene 5%	0.9 - 20.0	0.5	175.35
2-Iron	0.9 - 20.0	1.25	175.85
3-Borated polyethylene 5%	0.9 - 20.0	0.75	178.10

Second collimator : fission mode

Segment-Material	Internal- External radius [cm]	Length [m]	Initial co-ordinate [m]
1-Borated polyethylene 5%	4.0 - 20.0	0.5	175.35
2-Iron	4.0 - 20.0	1.25	175.85
3-Borated polyethylene 5%	4.0 - 20.0	0.75	178.10

The neutron beam profile in EAR-1 (collimator for capture mode)

Energy range		x-dimension [mm]	y-dimension [mm]
1 eV - 100 eV		7.6 ± 0.5	7.2 ± 0.4
100 eV - 1 keV		7.4 ± 0.8	7.3 ± 0.6
1 keV - 10 keV		7.4 ± 1.4	7.6 ± 1.2
10 keV - 100 keV		7.9 ± 2.6	7.4 ± 2.0
100 keV - 1 MeV		7.5 ± 0.9	7.0 ± 0.7
1 MeV - 10 MeV		6.6 ± 0.5	6.4 ± 0.4
10 MeV - 30 MeV		6.4 ± 0.7	6.1 ± 0.6

CERN n_TOF: Basic Parameters

The neutron fluence in EAR-1

Energy range	Uncollimated [n/pulse/cm2]	Capture mode [n/pulse]	Fission mode [n/pulse]
< 1 eV	**2.0E+05**	**3.1E+05**	**2.0E+06**
1 eV - 10 eV	2.7E+04	4.5E+04	2.9E+05
10 eV - 100 eV	2.9E+04	4.7E+04	3.1E+05
100 eV - 1 keV	3.0E+04	5.1E+04	3.3E+05
1 eV - 1 keV	**8.6E+04**	**1.4E+05**	**9.3E+05**
1 keV - 10 keV	3.2E+04	5.4E+04	3.6E+05
10 keV - 100 keV	3.9E+04	7.1E+04	4.7E+05
100 keV - 1000 keV	1.1E+05	2.3E+05	1.5E+06
1 keV - 1 MeV	**1.8E+05**	**3.5E+05**	**2.3E+06**
1 MeV - 10 MeV	8.3E+04	2.4E+05	1.7E+06
10 MeV - 100 MeV	2.8E+04	7.2E+04	5.1E+05
> 100 MeV	4.4E+04	1.2E+05	5.6E+05
1 MeV - > 100 MeV	**1.6E+05**	**4.4E+05**	**2.7E+06**
Total	**6.2E+05**	**1.2E+06**	**8.0E+06**

Note: 1 pulse is 7E+12 protons. Collimated fluence (fission and capture modes) is integrated over the beam surface.
The numbers shown here are those from Monte Carlo simulations, validated with various measurements (see text).

Energy resolution @ 187.5 m (collimator for capture mode)

Neutron Energy	p-beam pulse width FWHM [cm]	moderation FWHM [cm]	ΔE/E
1 eV	0.0	3.0	3.0E-04
10 eV	0.1	3.0	3.2E-04
100 eV	0.2	3.3	3.5E-04
1 keV	0.6	5.1	5.5E-04
10 keV	2.0	7.9	8.7E-04
30 keV	3.4	10.2	1.1E-03
100 keV	6.2	18.0	2.0E-03
1 MeV	19.5	34.1	4.2E-03
10 MeV	61.7	16.9	6.8E-03
100 MeV	195.0	14.5	2.1E-02

REFERENCES

[1] C. Rubbia et al., *Conceptual Design of a Fast Neutron Operated High Power Energy Amplifier*, CERN/AT/95-44 (ET), (29 September 1995); see also C. Rubbia, *A High Gain Energy Amplifier Operated with fast Neutrons*, AIP Conference Proc. 346, Int. Conf. on ADT Technologies and Applications, Las Vegas, (1994). For more details on the TRU's incineration see also C. Rubbia et al., *Fast Neutron Incineration in the Energy Amplifier as Alternative to Geologic Storage: the case of Spain*, CERN report CERN/LHC/97-01 (EET), Geneva, (17 February 1997) and C. Rubbia et al., *A realistic Plutonium elimination scheme with Energy Amplifiers and Thorium-Plutonium Fuel*, CERN report CERN/AT/95-53 (ET), Geneva, (12 December 1995).

[2] Under contract number FIKW-CT-2000-00107, (February 2000).

[3] C. Rubbia, et al., *A high resolution spallation driven facility at the CERN-PS to measure neutron cross sections in the interval from 1 eV to 250 MeV*, CERN/LHC/98-02 (EET) and CERN/LHC/98-02 see also C. Rubbia et al., *A high Resolution Spallation driven Facility at the CERN-PS to measure Neutron Cross Sections in the Interval from 1 eV to 250 MeV: a relative Performance Assessment*, CERN/LHC/98-02 (EET)-Add. 1, Geneva, (15 June 1998).

[4] P. Cennini et al., *Handling of the Radioactive Samples for the Fast Induction Chamber (FIC) for the measurement of Fission Reactions at the n-TOF Facility at CERN*, Technical Note CERN-TIS-2002-039-RP-TN, (August 2002).

[5] C. Stéphan, L. Ferrant, B. Berthier, S. David, L. Tassan-Got, C.O. Bacri, F. Rejmund, C. Moreau and the n-TOF Collaboration, *Neutron induced fission cross section measurements*, Journal of Nuclear science and Technology, Supplement 2, (2002), 276.

[6] The n_TOF Collaboration, *The performance of the n_TOF time-of-flight high energy spallation source at the CERN-PS*, in preparation (2003).

[7] M. Giovannozzi, *Alternative Layout of the Transfer Line for the Time-Of-Flight Neutron Facility at CERN-PS*, CERN/PS/CA/Note 99-17, (1999).

[8] S. Andriamonje et al., *Feasibility Study of a Neutron TOF Facility at the CERN-PS*, CERN/PS 98-065 (CA), Geneva, (5 November 1998).

[9] M. Giovannozzi, *New Transfer Line in the TT2 Tunnel for the Time-Of-Flight Neutron Facility at CERN-PS*, CERN/PS/CA/Note 98-23, (1998).

[10] G. Arduini, M. Giovannozzi, K. Hanke, J-Y. Hémery, M. Martini, *MAD and Beam Optics description of the TT2/TT10 transfer lines. Part I: optics without emittance exchange insertion*, CERN/PS/CA/Note 98-14, (1998).

[11] H. Grote, F. C. Iselin, *The MAD program – User's Reference Manual*, CERN/SL/AP 90-13, (1990).

[12] A. Ferrari and P.R. Sala, *Intermediate and High Energy Physics Models in FLUKA: Improvements, Benchmarks and Applications*, Proc. of Int. Conf. on Nuclear Data for Science and Technology, NDST-97, ICTP, Miramare, Trieste, Italy, (19-24 May 1997).

[13] Y. Kadi et al., *The EA-MC Monte Carlo Code Package*, Proc. Of the 5th Meeting on Shielding Aspects of Accelerators, Targets and Irradiation Facilities (SATIF5), Paris (18-21 July 2000).

[14] S. Andriamonje et al., *Neutron TOF facility (PS213) Technical Design Report*, CERN/INTC/2000-004, Editor: E. Radermacher.

[15] D. Cano-Ott et al., *First parameterisation of the neutron source at the n_TOF and its influence on the collimation system*, DFN/TR-03/II-00.

[16] A. Bignami, C. Coceva, and R. Simonini, *Monte Carlo simulations for the moderator of the pulsed neutron target of the Geel Lina*", EURATOM Report EUR 5157 (1974).

[17] A. Abánades et al., *Results from the TARC experiment: spallation neutron phenomenology in lead and neutron-driven nuclear transmutation by adiabatic resonance crossing*, Nuclear Instruments and Methods in Physics Research, A 478 (2002) 577-730.

[18] B. Langeseth, G. Pluym, B. de Raad, *Magnetic Measurements on the Bending Magnets of the Beam Transport System of the CERN PS*, PS Int. (EA)60-14, (1960).

[19] M. Giovannozzi, M. Sassowsky, *Sweeping Magnet for the Time Of Flight Facility at the CERN PS*, CERN/PS/CA/Note 99-12, (1999).

[20] A. Fontaine, H. Schönbacher, M. Tavlet, *Compilation of radiation damage test data*, CERN 98-01, (1998).

[21] M. Höfert et al., *The prediction of radiation levels from induced radioactivity discussion of an internal dump facility in the PS*, DI/HP/185 Health Physics Group, (27 January 1975).

[22] V. Lacoste et al., *Activation Studies and Radiation safety for the n_TOF Experiment*, SL-Note-2000-045 (EET), (27 July 2000). See also Proc. Of the 5th Meeting on Shielding Aspects of Accelerators, Targets and Irradiation Facilities (SATIF5), Paris (18-21 July 2000).

[23] A.V. Sannikov, E.N. Savitskaya, *Ambient Dose and Ambient Dose Equivalent Conversion Factors for High-Energy neutrons*, CERN/TIS-RP/93-14, (1993).

[24] IAEA Technical Report Series no. 283, *Radiological safety aspects of the operation of proton accelerators*, IAEA Vienna (1988).

[25] J.K. Tuli, *Evaluated Nuclear Structure Data File – A Manual for Preparation of Data Sets*, Thomas W. Burrows, *The program RADLST*, National Nuclear Data Center, Brookhaven National Laboratory, Upton, NY 11973, (29 February 1988).

[26] H.G. Hughes et al., *MCNPX for Neutron-Proton Transport*, Mathematical and Computation Topical Meeting, American Nuclear Society, (27-30 September 1999), Madrid, Spain.

[27] V. Vlachoudis et al., *Particle distribution entering the vacuum tube from a 80□80□60 cm*^{3} *lead target*, SL-Note-2000-029 (EET), (30 March 2000). See also the MC-2000 Conference Proceedings, Lisbon (23-26 October 2000).

[28] Y. Giomataris, et al., *Micromegas: a high granularity position sensitive gaseous detector for high particle-flux environments*, Nucl. Instr. and Methods A 376 (1996) 29-35.

[29] G. Charpak et al., *First beam test results with Micromegas, a high-rate, high-resolution detector*, CERN-LHC/97-08 (EET), DAPHNIA-97-05.

[30] S. Andriamonje et al., *Experimental studies of a MICROMEGAS neutron detector*, Nucl. Instr. & Methods A 481 (2002) 36-45.

[31] n_TOF-02, CERN/INTC 2000-016, February 2000

[32] S Marrone, et al., *A low-mass neutron flux monitor for the n_TOF facility at CERN*, in preparation for Nuclear Instruments and Methods A (2003)

[33] R. Plag, M. Heil, F. Kaeppeler, P. Pavlopoulos, R. Reifarth, and K. Wisshak, *An optimized C_6D_6 detector for studies of resonance-dominated (n,□) cross sections*, Nuclear Instruments and Methods A (2002), in press.

[34[GEANT, *Detector description and simulation tool*, CERN Program Library W5013 (1994).

[35] Handler, et al, *Unix Version of CALOR89 for Calorimeter Applications*, SDC-92-00257 (May 1992).

[36] O. Johnson and T. A. Gabriel, *A User's Guide to MICAP: A Monte Carlo Ionization Chamber Analysis Package*, ORNL/TM-10340 (January 1988).

[37] F. Corvi, G. Fioni, F. Gasperini, P. B. Smith, *The weighting function of a neutron capture detection system*, Nuclear Science & Engineering, 107 (1991), 272.

[38] F. G. Perey, J. O. Johnson, T. A. Gabriel, R. L. Macklin, R. R. Winters, J. H. Todd, and N. W. Hill, *Response of C_6D_6 and C_6F_6 gamma-ray detectors and the capture of the 1.15 keV resonance of ^{56}Fe*, Proceedings of the International Conference on Nuclear Data for Science and Technology, Mito, Japan, 30 May-3 June 1988, p. 379 (1988).

[39] EGS4: *Monte Carlo Simulation of the Coupled Transport of Electrons and Photons*, SLAC-PUB-6499.

[40] J. L. Tain et al., *Accuracy of the pulse height weighting technique for capture cross section measurements*, Journal of Nuclear Science and Technology, Supplement 2, (2002), 689.

[41] K. Wisshak, et al., Nuclear Instruments Methods A 292, 595 (1990)

[42] M. Heil, et al., Nuclear Instruments and Methods A 459, 229 (2001)

[43] D.B. Gayther, *International Intercomparison of Fast Neutron Flux-Rate Measurements Using Fission Chamber Transfer Instruments*, Metrologia 27, 221-231, (1990).

[44] C. Borcea et al., *Results from the Commissioning of the n_TOF Spallation Neutron Source at CERN*, CERN-SL-2002-051.

[45] C. Borcea et al., *First results from the neutron facility (nTOF) at CERN*, Appl. Phys. A 74 [Suppl.], S55 – S57 (2202).

[46] V. Vlachoudis, *A multi-purpose DAQ system developed for the n_TOF commissioning*, EET Internal Note 2001-03, (2001).

[47] F. Casagrande, P. Cennini, X.li, *The Argon Gas Detectors for the Fission Measurement in FEAT*, NIM in Physics Research, A 372 (1996) 307-310.

[48] P. Cennini et al., *Fission Fragment Detector to be installed at the Measuring Station in the TOF Facility*, SL-Note-99-026 EET (16-02-99).

[49] P. Cennini, V. Lacoste, *Proposal for a Fission Detector based on the measurement of the ionization produced by the absorption in gas of the Fission Fragments*, SL-Note-2000-006-EET (03-01-00).

[50] K.H. Gruber et al., *New High resolution Fission Cross-Section Measurement of* ^{233}U *in the 0.4 eV to 700 keV Energy Range*, Nuclear Science and Engineering 135, 141-149 (2000).

[51] The n_TOF Collaboration, *A Detailed Study of Hyperdeformed States of Uranium in the* $^{234}U(n,f)$ *Reaction*, CERN/INTC 2002-022, P145-Add.1 (11-04-02).

[52] P. Cennini et al., *Fast Ionisation Chamber for Fission Process Studies on the High-Resolution Neutron Time-of-Flight Facility at CERN*, in preparation (2003).

[53] The n_TOF Collaboration, *n_TOF Technical Report*, CERN/INTC 2000-018, (3 November 2000).

[54] H. Wendler et al., *The n_TOF General Data Flow*, n_TOF Note 200502, (May 2000).

[55] D. Cano-Ott et al., *The n_TOF data access package*, n_TOF Note 210402, (April 2000).

[56] H. Wendler, E. Schaefer, B. Betev, P. Pavlopoulos, R. Plag, V. Ketlerov (eventuellement D. Cano-Ott, T. Papaevangelou), *The n_TOF one Gigasample data acquisition system with real-time data reduction and event monitoring*, to be published in NIM-A.

[57] LabView, National Instruments Software, http://www.ni.com/

[58] CASTOR: *CERN Advanced Storage Manager*, http://castor.webcern.ch/castor

[59] V. Vlachoudis, *A multi purpose DAQ system developed for the n_TOF commissioning*, in Proceedings of CHEP 2001, Edited by H.S. Chen, Science Press New York, pg. 562, (2001).

[60] P. Cennini, *The Data Acquisition System for the TOF Facility: Guidelines*, SL-Note-99-040-EET, (21 April 1999).

[61] http://wwwpsco.cern.ch

[62] National Instruments, *PCI-MXI-2 User Manual*, (January 1996).

[63] A. Smoliakov, *CBD-8210 Interface library based on NI-XVI software.*

[64] http://root.cern.ch

[65] The n_TOF Collaboration, *Study of the Background in the Measuring Station at the n_TOF Facility at CERN: Sources and Solutions*, CERN/SL/Note 2001-046, CERN/INTC 2001-038.

[66] V. Lacoste, *Gamma Background Measurement in the n_TOF Experimental Area*, Internal Note, CERN/SL/EET 2000-006.

[67] N. M. Larson, *A Code System for Multilevel R-Matrix Fits to Neutron Data Using Bayes' Equations*, Oak Ridge National Laboratory Report ORNL/TM-9179/R5, (2000).

[68] ENDF/B-6, OECD NEA Data Bank; IAEA-NDS-110, IAEA Nuclear Data Section, Vienna, Austria.

[69] P.W. Lisowski, A. Gavron, W.E. Parker, J.L. Ullmann, S.J. Balestrini, A.D. Carlson, O.A. Wasson, N.W. Hill, *Fission cross sections in the intermediate energy region*, Proceedings of a specialists' meeting on neutron cross section standards for the energy region above 20 MeV, Uppsala, Sweden, (21-23 May 1991).

[70] C. Coceva, M. Frisoni, M. Magnani, and A. Mengoni, *On the figure of merit in neutron time-of-flight experiments*, Nuclear Instruments and Methods, A 489 (2002), 346-356.

[71] S. Andriamonje et al., *The Micromegas neutron detector for CERN n_TOF*, to be published, Nuclear Physics B, Proceedings of the International Conference on Advanced Technology and Particle Physics, Como, Italia, (2001).

[72] J. Pancin et al, *Measurement of the n_TOF Beam Profile with a Micromegas detector*, to be published in Nucl. Instr. & Methods A (2002).